Title
Epitranscriptomic and Epigenetic Engineering as Novel Therapeutic Approaches in Glioma

Author
Pianka, Sean Thomas

Publication Date
2021

Peer reviewed|Thesis/dissertation

UNIVERSITY OF CALIFORNIA

Los Angeles

Epitranscriptomic and Epigenetic Engineering as Novel Therapeutic Approaches in Glioma

A dissertation submitted in partial satisfaction of the requirements for the degree Doctor of Philosophy in Neuroscience

by

Sean Thomas Pianka

2021

ABSTRACT OF THE DISSERTATION

Epitranscriptomic and Epigenetic Engineering as Novel

Therapeutic Approaches in Glioma

by

Sean Thomas Pianka

Doctor of Philosophy in Neuroscience

University of California, Los Angeles, 2021

Professor Albert Lai, Chair

Glioma is the most common form of primary brain cancer and suffers from a paucity of efficacious therapies. Decades of research have successfully characterized glioma subtypes based on genetic, epigenetic, and molecular signatures that act as important prognostic indicators. Here, we present two novel approaches to designing therapeutics that convert malignant glioma and glioblastoma subtypes into more treatment-amenable subtypes. We first describe how the $IDH1^{mut}$ → D-2-HG ⊣ FTO axis establishes a unique epitranscriptomic profile that we term G-RAMP, which results in reduced tumor cell proliferation in both patient tumor samples and patient-derived gliomaspheres via inhibition of the anti-apoptotic regulator ATF5. G-RAMP was characterized using MeRIP-Seq unbiased screening of N^6-methyladenosine (m6A) enrichment sites in $IDH1^{mut}$ gliomas, and small molecule inhibitors of FTO were employed to recapitulate $IDH1^{mut}$ growth phenotypes in more malignant $IDH1^{wt}$ lines. Our second approach utilized dCas9-DNMT3a epigenetic editing platforms to induce high-density methylation of the *MGMT* promoter and exon 1 region. *MGMT* methylation is a positive prognostic indicator in gliomas that predicts patient tumor responses to the standard-of-care antineoplastic agent temozolomide. We demonstrate that unmethylated *MGMT* gliomas can be converted to exhibit *MGMT* methylated profiles, which results in decreased expression of *MGMT* and enhanced sensitivity to temozolomide. The utilization of epitranscriptomic and epigenetic engineering approaches thus represent two novel means of effecting subtype conversions in glioma that demonstrate promising potential as neoadjuvant therapies.

The dissertation of Sean Thomas Pianka is approved.

Harley I. Kornblum

Linda M. Liau

David A. Nathanson

Matteo Pellegrini

Albert Lai, Committee Chair

University of California, Los Angeles

2021

For my parents

TABLE OF CONTENTS

ACKNOWLEDGEMENTS

I am first and foremost grateful to **Tie Li** of the Lai lab for his innumerable contributions to this work, both materially and in the interpretations of our findings. He is my teacher and my friend, who patiently guided me through my doctorate research and taught me how to operate successfully in the arena of glioma biology. I also owe much to **Bryan Kevan**, a friend from Pomona College and another Lai lab member, for his tireless work on the numerous bioinformatics approaches we employed. **Blaine Eldred**, also of the Lai lab, was a steadfast lab partner whose excellence made our animal studies possible. **Haowen Liang**, also of the Lai lab, brought his commensurate technical and aesthetic skills to the fore in the design of the figures presented herein. I am also deeply grateful to Dr. **David Nathanson**, **Jennifer Salinas**, **Jonathan Tsang**, and all the other members of the wonderful Nathanson lab who were instrumental in the sourcing of gliomaspheres and the implementation of our *in vivo* experiments. I express sincere thanks to Dr. **Harley Kornblum** and Dr. **Michael Condro** of the Kornblum lab for providing outstanding guidance in the use of gliomaspheres established in their laboratory and all manner of imaging equipment and reagents that they freely shared. I also wish to thank Dr. **Matteo Pellegrini** and Dr. **Marco Morselli** of the Pellegrini lab, as well as Dr. **Giovanni Coppola**, Dr. **Riki Kawaguchi**, and Dr. **Fuying Gao** for their teaching and support regarding the early interpretation of our bioinformatics results. I am also unendingly grateful to Dr. **Linda Liau** for the scientific insights and career advising she so magnanimously provided. I extend my warmest appreciation to Dr. **Carlos Portera-Cailliau** whose mentorship and friendship throughout my time in the UCLA-Caltech MSTP continues to be a source of immense personal and academic support. I thank **Susie Esquivel**, **Josephine Alviar**, and **Phuong Macadangdang** of the UCLA-Caltech MSTP administration for their attentive and indispensable help in coordinating my medical and graduate education. I also thank Dr. **Felix Schweizer** and **Jenny Lee** of the UCLA Interdepartmental Ph.D. Program for Neuroscience for their tremendous work in creating and facilitating a fantastic graduate training experience. Finally, this work would not have been possible without the unwavering support and camaraderie of Dr. **Albert Lai**, who taught me what it truly means to be a mentor and scientific explorer, and whose compassionate and pragmatic teachings will continue to be invaluable on my journey as an aspiring physician scientist.

Research reported in this publication was supported by the National Cancer Institute of the National Institutes of Health under Award Number F30CA247525, the UCLA Tumor Cell Biology Training Program under USHHS Ruth L. Kirschstein Institutional National Research Service Award Number T32CA009056, the UCLA Brain Research Institute Graduate Student Research Grant, and the Lothar-Anne Rosenthal Fellowship. The content is solely the responsibility of the authors and does not necessarily represent the official views of the organizations listed herein.

CURRICULUM VITAE

Education:

UCLA David Geffen School of Medicine, MSTP, Los Angeles, CA **2015-Present**
MD-PhD Candidate, *Interdepartmental PhD Program in Neuroscience, GPA: 4.0, Class of 2023*

Pomona College, Claremont, CA **2010-2014**
Magna Cum Laude, B.A., Neuroscience major, GPA: 3.9, Class of 2014

Phillips Exeter Academy, Exeter, NH **2005-2010**
Cum Laude, GPA: 3.7, Class of 2010

Positions and Employment:

Dates	Position	Institution	Principle Investigator
08/2011 – 05/2013	Undergraduate Researcher	Pomona College	Jonathan King, PhD Roberto Garza-Lopez, PhD
05/2012 – 08/2012	Undergraduate Researcher	University of Hong Kong	Sam-Po Law, PhD
06/2013 – 05/2014	Undergraduate Researcher	UCSD	Gregory Light, PhD
05/2014 – 08/2015	Post-Baccalaureate Researcher	UCSD	Gregory Light, PhD
05/2016 – 08/2016	Graduate Rotation Student Researcher	UCLA	Peyman Golshani, MD-PhD
05/2017 – Present	Graduate Student Researcher	UCLA	Albert Lai, MD-PhD

Fellowships & Grants:

2020 – Present Ruth L. Kirschstein NRSA for Individual Predoctoral MD/PhD Degree Fellows (F30)
2019 – 2020 T32 in Tumor Cell Biology, *University of California at Los Angeles, CA*
2018 – 2019 Brain Research Institute Pre-Doctoral Grant, *University of California at Los Angeles, CA*
2018 Cold Spring Harbor Laboratory Summer Fellowship, *American Brain Tumor Association*
2016 – 2017 Lothar-Anne Rosenthal Fellowship, *University of California at Los Angeles, CA*

Professional Societies:

2017 – Present *Society for Neuro-Oncology*

Academic Honors & Awards:

2020 *Sigma Xi, National Honor Society*
2014 *Phi Beta Kappa*, *National Honors Society*
2014 *Magna Cum Laude*, *Pomona College*
2014 Senior Prize in Neuroscience, *Pomona College*
2014 Pomona College Scholar & Distinction in the Senior Exercise/Thesis, *Pomona College*
2013 Summer Research Fellowship in Neuroscience, *Pomona College*
2012 East Asia Research Grant, *Pomona College*

Other Experiences:

2018	Graduate Teaching Assistant, Cellular Physiology, *University of California, Los Angeles*
2017 – Present	Undergraduate Student Research Mentor (Lai lab), *University of California, Los Angeles*
2015 – 2017	Medical Volunteer (student-run homeless clinic), *University of California, Los Angeles*
2014 – 2015	Psychiatry Department Staff Research Associate, *University of California, San Diego*
2013 – 2014	Biochemistry Teaching Assistant, *Pomona College*
2013 – 2014	Organic Chemistry Teaching Assistant, *Pomona College*
2011 – 2012	Mathematics Teaching Assistant, *Pomona College*

Selected Publications:

Liu LY, Ji MS, Nguyen NT, Chow FE, Molaie DM, **Pianka ST**, Green RM, Liau LM, Ellingson BM, Nghiemphu PL, Cloughesy TF, Lai A. Patterns of long-term survivorship following bevacizumab treatment for recurrent glioma: a case series. *CNS Oncol.* 8(2): CNS35. 2019.

Cooper, YA*, **Pianka, ST***, Alotaibi, NM, Babayan, D, Salavati, B, Weil, AG, Ibrahim, GM, Wang, AC and Fallah, A. Repetitive transcranial magnetic stimulation for the treatment of drug-resistant epilepsy: A systematic review and individual participant data meta-analysis of real-world evidence. *Epilepsia Open*. 2018. 3: 55–65. *Denotes co-first authorship and equal contributions

Perez VB, Tarasenko M, Miyakoshi M, **Pianka ST**, Makeig SD, Braff DL, Swerdlow NR, Light GA. Mismatch negativity is a sensitive and predictive biomarker of perceptual learning during auditory cognitive training in schizophrenia. *Neuropsychopharmacology*. 2017. DOI: 10.1038/npp.2017.25.

Tarasenko M, Perez VB, **Pianka ST**, Vinogradov S, Braff DL, Swerdlow NR, Light GA. Measuring the capacity for auditory system plasticity: an examination of performance gains during initial exposure to auditory-targeted cognitive training in schizophrenia. *Schizophrenia Research*. 2016. 172(1-3): 123-30.

Selected Presentations:

Pianka ST, Li T, Lai A. IDH1^{MUT} induces N^{6}-methyladenosine (m6A) RNA hypermethylation via D-2-HG in glioma. Poster presented at the *Society for Neuro-Oncology Annual Meeting*. 2019. Phoenix, AZ.

Pianka ST, Li T, Cox C, Ji M, Eldred BS, Lai A. Epitranscriptomic regulatory mechanisms underlying phenotypic differences in glioma. Poster presented at the *11th Annual Neurology Science Day*. 2019. Los Angeles, CA.

Pianka ST. Targeted methylation of the MGMT DNA repair enzyme increases chemotherapeutic efficacy. Presented at the *Cold Spring Harbor Laboratory Brain Tumor Course*. 2018. Cold Spring Harbor, NY.

Pianka ST, Perez VB, Light GA. Neuroplasticity-based cognitive training in schizophrenia: predicting patient responses using a neurological marker. Poster presented at the *Pomona College Summer Undergraduate Research Program Poster Conference*. 2013. Claremont, CA.

Pianka ST, Su IF, Law SP. Understanding developmental dyslexia in children in a Chinese-Cantonese lexical context. Poster presented at the *Pomona College Summer Undergraduate Research Program Poster Conference*. 2012. Claremont, CA.

DISSERTATION INTRODUCTION

Over the last thirty years, we have gained a rich scientific understanding of glioma, especially with regard to their diverse subtypes defined by unique genetic, epigenetic, and metabolic signatures, mechanisms of *de novo* gliomagenesis and therapeutic resistance, and daunting degrees of intratumoral heterogeneity. Despite these discoveries, gliomas (and glioblastoma in particular) remain some of the most clinically intractable oncologic conditions known to humankind. The median overall survival for glioblastoma patients is a mere 15 months, and this number has not meaningfully advanced in decades. The most notable advances in novel therapeutic development for glioma have so far been made in the arenas of immunotherapy and the utilization of transcranial alternating electric fields, two approaches that have demonstrated promising efficacy. Classic precision medicine approaches also continue to be a staple method for the identification and testing of new drug targets; and while this strategy has proven effective in many cancers, the innate heterogeneity and rapid proliferative potential of gliomas makes identifying consistently sensitive targets extremely difficult. With incidences on the rise and a paucity of efficacious treatment options available, it behooves us to think even more creatively in our exploration of new avenues to surmount the monumental treatment challenges facing our field and our patients.

Here, I introduce a new paradigm for precision medicine approaches to novel therapeutic discovery: instead of fighting an uphill battle to design drugs focused on proportionally rare and longitudinally transient targets within a constantly shifting molecular landscape, why not harness the power of genetic, epigenetic, and epitranscriptomic engineering to "level the playing field," reducing heterogeneity between tumors and forcing the most malignant glioma subtypes to recapitulate phenotypic characteristics seen in subtypes we know are already amenable to therapy? I am basing this theoretical approach on the fact that some gliomas are highly sensitive to our standard-of-care interventions, including *IDH1*^{mut} gliomas and the subset of glioblastomas with methylated *MGMT* promoters. The presence of either signature at diagnosis is a positive

prognostic indication, as patients with *IDH1*^{mut} tumors and those exhibiting *MGMT* methylation typically live far longer than their *IDH1*^{wt} or *MGMT* unmethylated counterparts. I focused my dissertation work on utilizing global epitranscriptomic and targeted epigenetic engineering to recapitulate elements of these positive prognostic signatures. The ultimate goal of these projects was to explore the possibility of achieving what I am terming 'treatment equity' between gliomas carrying these clinically beneficial signatures and those that lack them.

In Chapter 1, I demonstrate that the *IDH1*^{mut} → D-2-HG ⊣ FTO axis induces a unique epitranscriptomic profile that underlies the slower growth rates we observe in *IDH1*^{mut} gliomas, and then show how we can translate these finding in service of attenuating growth in more malignant *IDH1*^{wt} gliomas both *in vitro* and *in vivo*. In Chapter 2, I target *MGMT* unmethylated gliomas with dCas9 fusion proteins linked to endogenous DNMT3a methyltransferases to effect high-density methylation of the *MGMT* promoter and exon 1 region, thereby downregulating MGMT expression and sensitizing previously resistant lines to temozolomide chemotherapeutic intervention. Through the various epitranscriptomic and epigenetic engineering strategies described in the ensuing chapters, I hope to provide robust examples of a new approach to precision medicine research in glioma: one where we actively harness our knowledge of unique epitranscriptomic and epigenetic patterning in less aggressive subtypes to devise synergistic treatment strategies that effectively transplant these signatures into highly malignant subtypes to interrupt tumor growth, enhance treatment response, and perhaps one day achieve better outcomes for our patients.

CHAPTER 1

The *IDH1*^{mut} → D-2-HG ⊣ FTO Axis Establishes Unique Epitranscriptomic Signatures and Mediates Reduced Proliferation in Glioma via Apoptosis

ABSTRACT

Gliomas are the most common form of primary brain tumor in adults and remain one of the most lethal of all human cancers. Gliomas are clinically stratified based on genetic and molecular subtypes, and among them *IDH1*^{mut} gliomas exhibit higher treatment amenability and superior patient outcomes compared to their *IDH1*^{wt} counterparts. The molecular underpinnings of these clinical benefits are unclear and are thus the subject of the current work. *IDH1*^{mut} gliomas produce high levels of D-2-HG, a putative oncometabolite capable of inhibiting α-ketoglutarate-dependent dioxygenases critical to a range of cellular functions. The RNA m6A demethylases FTO and ALKBH5 are shown to be sensitive to D-2-HG-mediated inhibition, which can lead to epitranscriptomic changes recently implicated in several cancers. Here we report that the *IDH1*^{mut} → D-2-HG ⊣ FTO axis establishes a unique epitranscriptomic signature defined by m6A enrichment and the downregulation of transcripts regulating glioma cell growth. We further demonstrate how targeting this pathway using genetic and pharmacologic tools reduces proliferative phenotypes in more malignant *IDH1*^{wt} gliomas both *in vitro* and *in vivo*. We established these findings in glioma patient tumor samples, patient-derived gliomaspheres, and several other glioma model systems, as well as in *IDH1*^{wt} gliomasphere intracranial xenografts in mice. MeRIP-Seq and Nanopore direct RNA sequencing were used to characterize a previously undescribed epitranscriptomic profile in *IDH1*^{mut} glioma that we term G-RAMP, and this information was used to identify a biological mechanism for reduced proliferative potential effectuated through m6A-mediated ATF5 suppression and the subsequent induction of apoptotic processes. Our work provides the first evidence that selective inhibition of the m6A epitranscriptomic regulator FTO attenuates malignant growth patterns in *IDH1*^{wt} glioma, recapitulating the clinically favorable phenotypes seen in the *IDH1*^{mut} subtype. These findings open the door to the design of novel therapeutic strategies targeting epitranscriptomic regulatory processes in glioma.

INTRODUCTION

Glioma is a highly malignant form of brain cancer and the cause of considerable morbidity and mortality. It is also the most common primary brain cancer, with an average age-adjusted annual incidence rate of 6.0 per 100,000 (Ostrom et al., 2017). Of the approximately 20,000 individuals receiving a glioma diagnosis each year in the United States, close to 50% are diagnosed with glioblastoma (Ostrom et al., 2017). Glioblastoma has an average 5-year survival rate of 5%, making it one of the most lethal human cancers (Ostrom et al., 2017). Though past genetic and molecular characterizations have defined several glioma subtypes with different degrees of malignancy and amenability to treatment (Phillips et al., 2006; Schmidt et al., 2002), the disease remains incurable and patients continue to suffer from a paucity of effective therapeutics. Among the different genetically defined subtypes, 35% of all adult diffuse gliomas (including approximately 80% of WHO Grade II-III gliomas and 12% of all glioblastomas) exhibit a characteristic R132H mutation in *IDH1* (isocitrate dehydrogenase 1) that is associated with favorable clinical attributes such as slower tumor growth and increased overall and progression free survival (Balss et al., 2008; Cancer Genome Atlas Research Network et al., 2015; Eckel-Passow et al., 2015; Ichimura et al., 2009; Kang et al., 2009; Nobusawa et al., 2009; Parsons et al., 2008; Yan et al., 2009). The survival advantages conferred by $IDH1^{mut}$ versus $IDH1^{wt}$ glioma are thus well documented in the clinical data, however, a precise understanding of the biological mechanisms underlying the reduced proliferative potential observed in $IDH1^{mut}$ gliomas remains to be fully elucidated. The goal of this study is to provide the first evidence to date that the reduced malignancy of $IDH1^{mut}$ gliomas is mediated by an epitranscriptomic perturbation altering processes critical for glioma cell survival. It is our hope that the exploration of this pathway will result in the discovery of new therapeutic strategies that can be exploited to thwart the devastating consequences imposed by the more prevalent and lethal $IDH1^{wt}$ glioma varieties.

Canonically, IDH1^{mut} forms a heterodimer with wildtype IDH1 and disrupts the oxidative decarboxylation reaction that normally forms α-ketoglutarate (α-KG) from isocitrate, instead catalyzing the conversion of α-KG to D-2-HG (D-2-hydroxyglutarate) (Dang et al., 2009). D-2-HG accumulates to supraphysiological levels within *IDH1^{mut}* cells, and acts as a competitive inhibitor of Fe(II)- and α-KG-dependent dioxygenases responsible for oxidative transformations intrinsic to numerous cellular functions. The actions of α-KG-dependent dioxygenases are varied, and include DNA demethylation via the TET (ten-eleven translocation) family of enzymes (Xu et al., 2011), histone demethylation via JHDMs (Jumonji C domain-containing histone demethylases) (Chowdhury et al., 2011; Lu et al., 2012; Xu et al., 2011), and the regulation of HIF-1α (hypoxia-inducible factor 1α) and collagen maturation via PHDs (prolylhydroxylases) (Chowdhury et al., 2011; Fu et al., 2012; Xu et al., 2011; Yalaza et al., 2017; Zhao et al., 2009). The production of D-2-HG also leads to the accumulation of reactive oxygen species (ROS) due to NADPH depletion, as NADPH is consumed in the α-KG to D-2-HG reaction (Dang et al., 2009; Gelman et al., 2018; Kölker et al., 2002; Latini et al., 2003). In glioma, D-2-HG secreted into the extracellular space also has potent effects on the tumor microenvironment, acting as an immunosuppressor of antitumor T-cell activity (Bunse et al., 2018; Richardson et al., 2019; Zhang et al., 2018). Despite the clinical evidence demonstrating that *IDH1^{mut}* is a positive prognostic indicator in glioma patients, the molecular evidence suggests that *IDH1^{mut}* paradoxically results in the promotion of oncogenic pathways and is largely understood to be a driver mutation arising early in gliomagenesis (Ichimura et al., 2009; Lai et al., 2011; Watanabe et al., 2009).

This seemingly contradictory role that *IDH1^{mut}* plays in glioma underscores the complexity of the cascading inhibitory effects mediated by D-2-HG on its abundant downstream targets. A prime example of the wide-ranging potential pathways impacted by D-2-HG is the inhibition of TET DNA demethylases that catalyze the hydroxylation of DNA 5-methylcytosine (Dang et al., 2009; Turcan

et al., 2012). TET inhibition in glioma leads to the manifestation of a hypermethylated epigenetic signature known as G-CIMP (glioma-associated CpG island hypermethylator phenotype), a phenotype associated with improved prognosis through a causal mechanism that nevertheless continues to be the subject of debate (Dang et al., 2009; Lai et al., 2011; Malta et al., 2018; Nomura et al., 2019; Noushmehr et al., 2010; Turcan et al., 2012; Waitkus et al., 2018). One prevailing theory is that G-CIMP methylation of key epithelial-mesenchymal transition genes suppresses glial dedifferentiation and thereby contributes to reduced tumor invasiveness and improved outcomes for *IDH1*^{mut} glioma patients (Malta et al., 2018; Noushmehr et al., 2010). Numerous studies have established that G-CIMP establishment is associated with improved overall survival independent of other predictors such as age and tumor grade (Brennan et al., 2013; Ceccarelli et al., 2016; Noushmehr et al., 2010; Sturm et al., 2012; Turcan et al., 2012), and stratification into “G-CIMP-high” and “G-CIMP-low” subgroups further demonstrates positive correlations between DNA hypermethylation and reductions in malignant progression (Ceccarelli et al., 2016; Nomura et al., 2019; Noushmehr et al., 2010; Turcan et al., 2012). Despite this finding that dynamic shifts in the epigenetic landscape may modulate proliferative potential and treatment amenability in *IDH1*^{mut} glioma, there remains a gap in our understanding of how the downstream effects of these epigenetic changes can be discretely separated out into their pro- and anti-tumor properties. This is largely a function of the wide variety of G-CIMP genes and their varied responses to epigenetic modulation, as well as the many other molecular pathways known to be impacted by D-2-HG that may be contributing to or impeding glioma cell proliferation.

Adding further nuance to this complexity is the discovery that D-2-HG can have pronounced effects on the abundance and distribution of chemically-modified RNA nucleotides defining unique epitranscriptomic phenotypes (Huang et al., 2019; Su et al., 2018). N^6-methyladenosine (m6A) is the most common epitranscriptomic modification in eukaryotic mRNA, and it is dynamically regulated by m6A methyltransferases (‘writers’) and demethylases (‘erasers’) (Huang et al., 2015;

Jia et al., 2011; Wang and Zhao, 2016; Wang et al., 2015a; Wei et al., 2018; Zhang et al., 2017; Zheng et al., 2013; Zhou et al., 2015). While originally discovered in the 1970s (Desrosiers et al., 1974; Perry and Kelley, 1974), it is only with the recent identification of m6A writers/erasers and the advent of epitranscriptomic sequencing methodologies (Dominissini et al., 2012; Meyer et al., 2012) that we have begun gaining insight into how m6A modifications can lead to consequential changes in fundamental cellular processes. Although the functional consequences of m6A modification are only just beginning to be explored, current evidence indicates that m6A modifications modulate a plethora of pathways effecting RNA splicing, secondary structure, export from the nucleus, intracellular localization, transcript stability, translation efficiency, microRNA processing, and RNA-protein interactions (Alarcón et al., 2015; Chen et al., 2015; Dominissini et al., 2012; Fustin et al., 2013; Geula et al., 2015; Liu et al., 2015; Meyer et al., 2012, 2015; Molinie et al., 2016; Wang et al., 2014a, 2015b, 2014b; Xiang et al., 2017; Zhao et al., 2017, 2014; Zhou et al., 2015; Zou et al., 2016). In mammals, m6A writers were identified as the methyltransferases METTL3 and METTL14 (methyltransferase-like proteins), which form a complex with WTAP (Wilms tumor 1-associated protein) to introduce m6A RNA modifications (Bokar et al., 1997; Feng et al., 2014; Knuckles et al., 2018; Liu et al., 2014; Ping et al., 2014; Wang et al., 2014b). FTO (fat-mass and obesity-associated protein) and ALKBH5 (AlkB homolog 5) perform m6A demethylase activity in RNA, and are the only two mammalian m6A erasers identified to date (Fu et al., 2013; Jia et al., 2011; Mauer et al., 2017; Wang et al., 2014a; Zheng et al., 2013). FTO tends to be localized in both the nucleus and cytoplasm (Aas et al., 2017; Ferenc et al., 2020; Gerken et al., 2007; Gulati et al., 2014; Jia et al., 2011), while ALKBH5 primarily exhibits localization to the nucleus (Du et al., 2020; Tang et al., 2018; Thalhammer et al., 2011; Toh et al., 2020; Yu et al., 2021; Zheng et al., 2013). The differences in localization suggest that the two m6A demethylases may be exerting their primary actions on different pools of RNA, and that each may govern discrete aspects of RNA processing. Interestingly, FTO and ALKBH5 expression levels vary widely between tissues and cell types, with FTO being highly expressed in brain tissue

with particularly elevated concentrations in the hypothalamus (Gerken et al., 2007; McTaggart et al., 2011), while ALKBH5 is most highly concentrated in the testis (Zheng et al., 2013). Also pertinent to our current study is the fact that FTO and ALKBH5 both belong to the family of Fe(II)- and α-KG-dependent dioxygenases inhibited by D-2-HG (Aik et al., 2014; Clifton et al., 2006; Feng et al., 2014; Gerken et al., 2007; Hausinger, 2004; Jia et al., 2011; Kurowski et al., 2003; Thalhammer et al., 2011; Xu et al., 2014, 2011; Zheng et al., 2013).

The nascent field of epitranscriptomics is currently in a period of rapid evolution, and there is increasing interest in understanding how m6A dysregulation may contribute to tumorigenesis and progression in certain cancers (Wang et al., 2017). Emerging evidence suggests that FTO and ALKBH5 may play a role in oncogenesis, though their precise oncogenic functions appear to vary with different cancer types including leukemia, glioma, breast cancer, and lung cancer (Cui et al., 2017; Deng et al., 2018a, 2018b; Huang et al., 2019; Li et al., 2017b; Su et al., 2018; Tan et al., 2015; Yan et al., 2018; Zhang et al., 2017). Of particular interest are the ways in which m6A enrichment effects mRNA transcript stabilization and degradation (Fustin et al., 2013; Huang et al., 2019; Meyer et al., 2012, 2015; Su et al., 2018; Wang et al., 2014a, 2015b, 2014b; Zhang et al., 2017; Zheng et al., 2013), thus implicating it as a novel regulator of gene expression with potentially profound clinical importance. Fascinatingly, recent studies in *IDH1*^{mut} AML (acute myeloid leukemia) revealed that FTO is sensitive to D-2-HG-mediated inhibition, and that the suppression of its m6A demethylase activity inhibits tumor cell growth in certain cancer lines (Huang et al., 2019; Su et al., 2018). The *IDH1*^{mut} occurs in 10-20% of AML patients (Mardis et al., 2009; Papaemmanuil et al., 2016), however, and in contrast to the survival benefits conferred by *IDH1*^{mut} in glioma, it is associated with more malignant AML characteristics such as increased risk karyotypes and poorer prognoses (Feng et al., 2012). This is particularly apparent in certain AML sub-populations of adults younger than 60 years old and those with normally functioning *NPM1* (Schnittger et al., 2010). Su *et. al.* found that D-2-HG inhibits FTO m6A demethylase

activity in *IDH1*^{mut} AML lines, leading to m6A enrichment in transcripts of cancer-related genes such as *MYC* and *CEBPA* (Su et al., 2018). Enrichment of m6A in these transcripts corresponded to decreased transcript stability and anti-tumor effects in the form of growth inhibition. Further evidence suggesting a role for m6A in mediating cancer cell proliferation came from Zhang *et. al.*, who found that glioblastoma stem-like cells expressing high levels of ALKBH5 were more likely to undergo tumorigenesis (Zhang et al., 2017). Increased ALKBH5 activity decreased m6A content in *FOXM1* transcripts, resulting in enhanced *FOXM1* transcription factor expression, gliomagenesis, and cell proliferation. These new and converging lines of evidence suggest that m6A enrichment is associated with targeted transcript degradation and may be protective against oncogenesis and malignant progression.

In the current study, we evaluate the molecular and clinical significance of m6A in glioma, determine its impact on transcriptional regulation, and investigate the therapeutic tractability of inhibiting the m6A demethylase FTO in *IDH1*^{wt} glioma; thereby defining an epitranscriptomic mechanism underlying the observed attenuation of proliferative potential in *IDH1*^{mut} glioma. We propose an *IDH1*^{mut} → D-2-HG ⊣ FTO axis producing a novel epitranscriptomic biomarker termed G-RAMP (glioma RNA m6A methylation phenotype) which ultimately leads to the downregulation of ATF5 (activating transcription factor 5) and the induction of apoptosis. We also show how this mechanism can be harnessed in service of reducing tumorigenicity and the overall malignancy of *IDH1*^{wt} glioma, recapitulating the clinically favorable phenotypes seen in *IDH1*^{mut} gliomas from which this therapeutic approach was derived.

RESULTS

IDH1^{mut} Patient Gliomas and Gliomaspheres Exhibit Increased D-2-HG and m6A Content

The first goal of this study was to determine if *IDH1^{mut}* gliomas exhibit enriched m6A RNA compared to their *IDH1^{wt}* counterparts. Operating with the understanding that *IDH1^{mut}* gliomas produce D-2-HG, and that this purported oncometabolite inhibits a wide range of α-KG-dependent dioxygenases including the endogenous mammalian RNA m6A demethylases FTO and AlkBH5, we sought to measure the relative m6A enrichment in RNA purified from clinical patient tumor samples, patient-derived gliomaspheres, and other glioma cell lines commonly utilized in the laboratory setting. We hypothesized that intracellular D-2-HG produced in the *IDH1^{mut}* biological context would serve as a potent inhibitor of m6A demethylase activity, thereby increasing the abundance of m6A-enriched RNA.

We obtained *IDH1^{mut}* (n=12) and *IDH1^{wt}* (n=13) fresh frozen glioma samples from the UCLA Brain Tumor Translational Resource to examine this hypothesis in the clinically relevant setting of patient tissue. Details of pathological diagnoses and patient cohort characteristics are summarized in Supplementary Table 1-S1. *IDH1* status was confirmed in these samples using immunohistochemistry and Sanger sequencing validation, and histological quality controls ensured the presence of ≥70% tumor versus normal brain tissue. Patient tissue samples were homogenized and subjected to RNA purification, followed by m6A quantification using the colorimetric EpiQuik m6A RNA Methylation Quantification Kit (*Epigentek,* Catalog #P900548, Farmingdale, NY, USA). As expected, total RNA in these patient samples exhibited differential m6A enrichment (Fig. 1a), with *IDH1^{mut}* gliomas showing significantly higher m6A levels when compared to *IDH1^{wt}* gliomas (P=0.026). While histological quality control measures ensured ≥70% tumor in each tissue sample analyzed, the residual presence of normal brain tissue and immune cell infiltrates may impact the relative m6A levels measured in a given gross tumor sample. This

is an important variable to consider in the case of *IDH1*^{mut} gliomas since intracellular D-2-HG can be secreted into the extracellular space and is known to affect the tumor microenvironment, as in the recent discovery that D-2-HG is a potent immunosuppressor of antitumor T-cell activity (Bunse et al., 2018; Richardson et al., 2019; Zhang et al., 2018). To overcome this possible confound, we quantified m6A in RNA isolated from gliomaspheres derived from *IDH1*^{mut} (*n*=4) and *IDH1*^{wt} (*n*=7) patients. These glioma stem cell lines are a highly relevant means of studying native glioma characteristics as they are directly derived from resected patient tumors and can be cultured as manipulable, non-adherent gliomaspheres both *in vitro* and *in vivo*, making them easily amenable to a variety of basic and clinical research applications. *IDH1* status for each gliomasphere line was confirmed with Sanger sequencing. Quantification of m6A RNA in these gliomasphere lines mirrored the findings we observed in fresh frozen patient tumor samples, with *IDH1*^{mut} lines showing significant m6A enrichment over *IDH1*^{wt} lines (*P*=0.042) (Figure 1-1a). Dot blot experiments using m6A-specific antibody (*Synaptic Systems,* Catalog #202-003, Goettingen, Germany) to visualize relative m6A abundance in gliomasphere RNA were consistent with the colorimetric m6A quantification assays described above (Supplementary Figure 1-S1).

Another set of variables we sought to account for was the balance between m6A writer and eraser expression in glioma cell lines, as an increase in writer expression or a decrease in eraser expression may also lead to an abundance of m6A modifications. The m6A writer complex is primarily composed of three proteins in mammals: METTL3, METTL14, and WTAP (Bokar et al., 1997; Feng et al., 2014; Knuckles et al., 2018; Ping et al., 2014; Wang et al., 2014b). This protein trimer macromolecule is responsible for the fixation of m6A RNA modifications, while the mammalian m6A demethylases FTO and ALKBH5 mediate m6A erasure activity (Fu et al., 2013; Jia et al., 2011; Mauer et al., 2017; Zheng et al., 2013). GlioVis (http://gliovis.bioinfo.cnio.es) is an online portal that provides tools for analyzing glioma gene expression data compiled in The Cancer Genome Atlas (TCGA) public resource (Bowman et al., 2017). We probed the

TCGA_GBMLGG dataset for differences in mRNA transcript counts among m6A writers and erasers as determined by RNA-Seq and microarray analyses, and stratified the results based on *IDH* status. METTL3 and METTL14 showed a slight but significant decrease in expression in the *IDH1*^{wt} cohort, while a more obvious decrease in WTAP expression was seen in the *IDH1*^{mut} cohort (Supplementary Figure 1-S2a). Since all three proteins are necessary for the m6A writer complex to function, this data suggest that there is equivocal if not minimal alteration in m6A writer complex activity between *IDH1*^{mut} and *IDH1*^{mut} gliomas. As for the m6A erasers, *IDH1*^{mut} gliomas exhibited increased FTO expression and slightly decreased ALKBH5 expression in comparison to *IDH1*^{wt} gliomas (Supplementary Figure 1-S2a). This data suggests a surprising net increase in m6A erasure expression in *IDH1*^{mut} gliomas, although we found m6A enrichment was increased in the *IDH1*^{mut} patient tumor samples and patient-derived cell lines tested in our laboratory. Moreover, transcriptomic microarray data of gliomasphere lines provided by the Kornblum lab (Laks et al., 2016) showed no differences in expression levels of m6A writers (METTL3, METTL14, WTAP) or erasers (FTO, ALKBH5) (Supplementary Figure 1-S2b). Taken together, these findings indicate that enrichment of m6A RNA in *IDH1*^{mut} glioma, in both patient tumors and patient-derived gliomaspheres, is largely governed by a mechanism independent of slight variations in m6A writer and eraser expression.

This led us to investigate what the causal role *IDH1*^{mut} plays in defining a m6A-enriched phenotype in glioma. It is well known that *IDH1*^{mut} catalyzes the conversion α-KG to D-2-HG, and that D-2-HG acts as a competitive inhibitor of α-KG-dependent dioxygenases and hydroxylases intrinsic to numerous cellular functions, including DNA demethylation via the TET (ten-eleven translocation) family of enzymes (Xu et al., 2011), histone demethylation via the JHDM (Jumonji C domain-containing histone demethylase) family (Chowdhury et al., 2011; Lu et al., 2012; Xu et al., 2011), reactive oxygen species accumulation via NADPH depletion (Dang et al., 2009; Gelman et al.,

2018; Kölker et al., 2002; Latini et al., 2003), and HIF-1α regulation and collagen maturation via PHD (prolylhydroxylase) enzymes (Chowdhury et al., 2011; Fu et al., 2012; Xu et al., 2011; Yalaza et al., 2017; Zhao et al., 2009). Other targets fall in the less elucidated arena of RNA methylation, particularly with respect to FTO and ALKBH5, the only two mammalian m6A demethylases known to date (Fu et al., 2013; Jia et al., 2011; Mauer et al., 2017; Zheng et al., 2013), and which both belong to the family of α-KG-dependent dioxygenases sensitive to D-2-HG-mediated inhibition (Huang et al., 2019; Su et al., 2018). Operating with the hypothesis that D-2-HG produced in *IDH1*^{mut} cells would lead to downregulation of RNA demethylase activity and a concomitant increase in m6A, we utilized lentivirus transduction to forcibly express *IDH1*^{mut} in glioma cell lines to provide evidence for a direct link between *IDH1*^{mut} and m6A enrichment. In addition to initial studies with HEK293T cells, we utilized immortalized human astrocytes (IHA) and U87 cells, two commonly employed malignant glioma model systems for which *IDH1*^{mut}-stabilized lines were previously established and/or investigated in our laboratory (Lazovic et al., 2012; Li et al., 2014; Turcan et al., 2012). In three independent biological repeats of HEK293T-*IDH1*^{mut} lines, m6A content was markedly increased when compared to empty vector control (*IDH1*^{wt}) HEK293T cells, as measured via m6A dot blots and quantified m6A EpiQuik measurements (Supplementary Figure 1-S3). Enrichment of m6A was consistently observed in total RNA pools as well as poly A$^+$ purified mRNA, suggesting potential alterations of the m6A mRNA epitranscriptome in the *IDH1*^{mut} context. The same finding was observed in experiments using IHA and U87 cells, with *IDH1*^{mut} expression leading to significantly higher levels of m6A-enriched RNA compared to *IDH1*^{wt} empty vector control lines (Figure 1-1b). The effect of *IDH1*^{mut} forced expression on enhanced m6A content was also generalizable to gliomaspheres, which are considered the most informative cellular model for studying glioma as they are directly derived from patient tumors. We packaged a pUltra-*IDH1*^{R132H}-EGFP plasmid or empty vector pUltra-EGFP (*Addgene*, Catalog #24129, Watertown, MA, USA) into lentiviruses and transduced native *IDH1*^{wt} HK385, HK217, and HK250

gliomasphere lines obtained from the Kornblum lab (UCLA). *IDH1^{mut}* forced expression consistently and significantly increased m6A abundance in these lines when compared to vector control *IDH1^{wt}* gliomaspheres (Figure 1-1b). We quantified intracellular D-2-HG levels using a commercially available D2HG Assay Kit (*Millipore-Sigma*, Catalog #MAK320, Burlington, MA, USA) to confirm our expected gain-of-function phenotype in all manipulated *IDH1^{mut}* lines. Intracellular D-2-HG concentrations were indeed increased across every *IDH1^{mut}* forced expression cell line versus their respective empty vector controls (Figure 1-1c). Taken together, the above data demonstrates that the introduction of *IDH1^{mut}* has a direct impact on m6A enrichment in a range of human glioma cell lines and provides additional indications that the effect may be mediated by D-2-HG production.

D-2-HG Exposure Is Necessary and Sufficient to Induce m6A Enrichment in Glioma RNA

The next goal of our study was to investigate the specific role of D-2-HG in the proposed axis linking *IDH1^{mut}* to increased m6A RNA abundance in glioma. As shown in our previous experiments, the introduction of *IDH1^{mut}* in a native *IDH1^{wt}* context induces a hypermethylated m6A RNA phenotype, and we sought to determine whether D-2-HG is the primary mediator of this induction mechanism. To do so, we first treated *IDH1^{wt}* cell lines with octyl-D-2-HG, a membrane permeable precursor of D-2-HG. Previous experiments in our lab demonstrated that octyl-D-2-HG is converted to D-2-HG intracellularly, and that dosages of 1 mM (for HEK293T) and 0.5 mM (for IHA and gliomaspheres) increased intracellular D-2-HG to levels comparable to those observed in *IDH1^{mut}* cells. Octyl-D-2-HG treatment in HEK293T cells led to m6A enrichment within 3 days, and cells undergoing continuous treatment over the course of 28 passages (approximately 70 days) demonstrated a stable enhancement of m6A content versus a DMSO treatment control condition (Supplementary Figure 1-S4). We performed subsequent octyl-D-2-HG treatment experiments on additional cell lines, culturing them in octyl-D-2-HG containing media (0.5mM) for 72 hours prior to RNA isolation and m6A quantification. Our results show that

octyl-D-2-HG treatment of *IDH1*^{wt} IHA cells leads to significantly higher m6A enrichment versus DMSO control (Figure 1-2a). The same dynamic was observed in all six *IDH1*^{wt} gliomasphere lines we tested. Even as individual *IDH1*^{wt} gliomaspheres exhibited variability in basal m6A levels, we were able to observe consistent increases in m6A enrichment in all octyl-D-2-HG treated cells (0.5mM, 72 hours) as demonstrated via EpiQuik m6A quantification (Figure 1-2a). These findings are in accordance with Su *et. al.* who first showed that D-2-HG directly induces a m6A hypermethylation phenotype in acute myeloid leukemia cell lines (Su et al., 2018). The above evidence provides the first indication that D-2-HG treatment is sufficient to increase m6A abundance in *IDH1*^{wt} gliomas, particularly in glioma stem-like cells.

To determine whether D-2-HG is necessary in the context of *IDH1*^{mut} glioma to produce m6A enrichment, we employed several pharmacological inhibitors of mutant IDH and measured their effects on D-2-HG and m6A levels. C35 (also known as AGI-5198) and AG881 are two small molecule inhibitors of mutant IDH enzymes developed by Agios Pharmaceuticals that impede the ability of mutant IDH to catalyze the conversion of α-KG to D-2-HG, thus reducing intracellular D-2-HG production (Konteatis et al., 2020; Ma and Yun, 2018; Popovici-Muller et al., 2012; Rohle et al., 2013). C35 specifically inhibits IDH1^{R132H} and IDH1^{R132C} mutants (U87 IC_{50} = 0.07 μM) (Popovici-Muller et al., 2012), and AG881 is a broad inhibitor of mutant IDH1 and IDH2 isoforms (U87 IC_{50} = 0.007 μM) (Konteatis et al., 2020). Using both *IDH1*^{mut}-expressing and empty vector control lines of IHA, U87, and HK385 cells, we first tested the efficacy of C35- and AG881-mediated inhibition on D-2-HG production. In all cases, active treatment resulted in significantly reduced intracellular D-2-HG in *IDH1*^{mut} lines, while having no effect on measured D-2-HG levels in *IDH1*^{wt} controls (Figure 1-2b). As expected, C35 and AG881 both significantly decreased the abundance of m6A in *IDH1*^{mut} lines, again while having no effect on m6A enrichment in *IDH1*^{wt} controls (Figure 1-2c). We also tested the effect of C35 and AG881 in HK252 gliomaspheres

derived from patient tumors confirmed to have de novo *IDH1*^{mut} status at time of resection. *IDH1*^{mut} gliomaspheres responded similarly to *IDH1*^{mut}-forced expression lines, exhibiting concomitant decreases in D-2-HG and m6A upon C35 or AG881 treatment (Figure 1-2d-e). Interestingly, these experiments also revealed an association between D-2-HG and m6A levels on the growth potential of gliomaspheres, with sphere volumes in C35- and AG881-treated *IDH1*^{mut} gliomaspheres showing a pronounced acceleration in growth (Figure 1-2f). Our experiments with *IDH1*^{mut} inhibition therefore provide strong evidence that D-2-HG production is necessary and positively correlated with m6A enrichment in glioma, and hint at an important underlying mechanism in which D-2-HG and m6A enrichment negatively regulate proliferative growth potential.

D-2-HG Is a Potent Attenuator of Glioma Cell Growth

Mutations in *IDH1* are commonly cited in the literature as serving an oncogenic role mediated by the putative oncometabolite D-2-HG. We hypothesized that D-2-HG, while understood to upregulate certain tumorigenic pathways, is paradoxically also a negative regulator of glioma cell growth, and that exposure to D-2-HG not only leads to m6A enrichment but is also associated with the attenuation of proliferative potential in glioma.

We first measured gliomasphere growth rates in three native *IDH1*^{wt} gliomasphere lines (HK385, HK217, HK250) transduced with lentivirus to express either *IDH1*^{mut} or an empty vector control. The gliomaspheres were disassociated down to the single cell level and allowed to proliferate under normal gliomasphere culturing conditions for 12 days. Image J was subsequently used to calculate sphere volumes in live cell images after the treatment period. The resulting changes in growth rates were in line with our hypothesis, with *IDH1*^{mut} lines exhibiting significantly smaller final sphere volumes (Figure 1-3a). We also performed similar experiments with native *IDH1*^{wt} gliomasphere lines (HK250, HK217) treated with octly-D-2-HG (0.5 mM) and meclofenamic acid

(MA) (100 μM), a selective inhibitor of the m6A demethylase FTO, and observed significant reductions in final sphere volumes in actively treated cells compared to DMSO treatment control conditions (Figure 1-3b). D-2-HG was shown to be slightly more potent than MA in inhibiting growth in these gliomasphere lines, effectively reducing final sphere volumes by 80%. MTT assays performed on native *IDH1*^{wt} IHA and U87 cells cultured for 96 hours in increasing concentrations of octly-D-2-HG (0 - 1.0mM) also showed a significant dose-dependent decrease in proliferation, beginning at 0.6 mM octly-D-2-HG treatment (Figure 1-3c). These findings align with observations made by Su, *et. al.* who demonstrated octyl-D-2-HG treatment is capable of inhibiting growth in multiple AML cell lines (Su et al., 2018).

To further validate the role of D-2-HG in attenuating growth, we investigated the effect of C35 and AG881 *IDH1*^{mut} inhibitors on proliferation and sphere growth in *IDH1*^{mut} glioma cells. Using the same gliomasphere lines described above in Figure 1-3a (*IDH1*^{mut} forced expression and empty vector control lines of native *IDH1*^{wt} HK385, HK217, HK250), we quantified the impact of C35 and/or AG881 treatment on baseline D-2-HG levels and proliferative potential. As seen in our previous experiments with C35 and AG881 treatment, *IDH1*^{mut} inhibitors have a pronounced effect on decreasing intracellular D-2-HG levels in *IDH1*^{mut} glioma lines while having no effect in *IDH1*^{wt} lines (Figure 1-3d). Additionally, this decrease in D-2-HG is associated with significant increases in sphere volumes after 15 days of continuous C35 (2μM) or AG881 (1μM) treatment. These findings show that D-2-HG acts as an inhibitor of glioma cell growth in a reversible manner and, when taken together with our results demonstrating a concomitant increase in m6A enrichment in cells exposed to D-2-HG, provide evidence for our hypothesis that there exists an anti-proliferative axis linking *IDH1*^{mut}, D-2-HG production, m6A enrichment, and reduced growth potential in glioma.

Inhibition of FTO Drives m6A Enrichment and Reduces Proliferative Potential in Glioma Cells

We next sought to determine the relative contributions of D-2-HG-mediated inhibition on FTO and ALKBH5 in terms of producing the m6A-enriched and anti-proliferative phenotypes we observed above. We therefore utilized shRNA knockdown of FTO and ALKBH5 to evaluate the specific effect of direct m6A demethylase inhibition on m6A content and glioma cell proliferation. We synthesized shRNAs targeting FTO and ALKBH5 in a piLenti-U6-shRNA-GFP-Puro system (*GenTarget Inc*., Catalog #SH-U6-GP, San Diego, CA, USA) and packaged the knockdown plasmid in lentiviruses for *in vitro* experimentation. A scrambled control (NSC) shRNA with no homology to mammalian transcriptome loci was also employed as a negative control. Transduced cell lines underwent 7 days of puromycin selection (0.8 μg/mL) followed by imaging with fluorescent microscopy after a recovery period of no more than 5 days.

In four independent biological repeat experiments using U87 lines, NSC, shFTO, shALKBH5, and shFTO+shALKBH5 cell populations showed 100% transduction efficiency post-selection as measured by %GFP positivity (Figure 1-4a). Western blot confirmed expected reductions in FTO and ALKBH5 (Figure 1-4b). Interestingly, inhibition of FTO appeared to be the driving force in m6A enrichment. U87 cells subjected to ALKBH5 knockdown showed no significant increase in m6A content compared to NSC control lines, and only cells subjected to FTO knockdown showed pronounced increases in m6A abundance (Figure 1-4c). Additional MTT data showed that after 3 days of expansion in regular media, only shFTO (± shALKBH5) exhibited reductions in proliferative potential (Figure 1-4d). We next performed additional knockdown experiments to confirm our U87 findings using native *IDH1*^{wt} HK217 and HK250 gliomaspheres. Lentiviral transduction and subsequent selection yielded comparable levels of shRNA expression efficiency and targeted knockdown in HK217 cells (Figure 1-4e-f). Qualitative dot blot assessments of m6A abundance showed a strong enrichment effect in shFTO cells and an intermediate effect in shALKBH5 lines compared to the NSC control condition (Figure 1-4g). Gliomasphere volumes

were measured 9 days after sphere disassociation following seeding at the single cell level and revealed significant growth attenuation in FTO knockdown glioma cells versus the NSC controls (Figure 1-4h). Growth inhibition was ultimately non-significant in shALKBH5 cells. The same pattern of findings was found with HK250 cells (Figure 1-4i-l). We also performed experiments in which a lentivirus was delivered to native *IDH1*^{wt} HK217 forcing expression of pMIRNA1-Flag-FTOwt or pMIRNA1-Flag-FTOmut containing two point mutations (H231A; D233A) that disrupt enzymatic function and result in no m6A demethylase activity (Jia et al., 2011). Compared to pMIRNA1-Flag-FTOmut negative control, transduced *FTO*^{wt} gliomaspheres lines exhibited significantly increased growth potential as measured by sphere volume (Figure 1-4m). These findings provide the first evidence that the regulation of m6A enrichment and associated growth inhibition are preferentially controlled by FTO over ALKBH5 in glioma.

Pharmacologic Inhibition of FTO Reduces Glioma Cell Growth In Vitro and Increases Overall Survival In Vivo

As we have shown, FTO sits in a unique position as a key mediator translating the canonical production of D-2-HG in *IDH1*^{mut} glioma into an altered epitranscriptomic landscape dominated by m6A enrichment and reduced growth potential. Therefore, we sought to investigate the possibility of utilizing small molecule inhibitors of FTO to specifically upregulate a proposed anti-tumor pathway linking D-2-HG to m6A enrichment and attenuated cell growth, without promoting other D-2-HG-mediated oncogenic pathways. The following experiments sought to determine if FTO inhibition alone would serve to decrease proliferative potential in the more malignant (and prevalent) *IDH1*^{wt} glioma subtype.

FB23-2 is a small molecule inhibitor of FTO developed by the Chen lab at City of Hope in Los Angeles (Huang et al., 2019). Huang *et. al.* showed that FB23-2 treatment results in specific inhibition of FTO m6A demethylase activity, and that this is associated with reduced proliferation

and increased apoptosis of human AML cell lines *in vitro* and *in vivo* (Huang et al., 2019). We first compared the efficacy of FB23-2 and meclofenamic acid (MA) inhibition of FTO in U87 cells and found FB23-2 to be a superior inducer of m6A enrichment (Figure 1-5a). A single 5 μM dose of FB23-2 (dissolved in DMSO) was able to achieve maximal increases in m6A RNA content after 12 hours, an effect that persisted for at least 72 hours (Figure 1-5b). U87 cells also exhibited a dose-dependent growth attenuation response to FB23-2 and MA treatment at dosages comparable to those that reliably induced m6A enrichment (Figure 1-5c), while *IDH1*^{mut}-U87 cells already under D-2-HG-mediated FTO inhibition demonstrated moderate resistance to growth attenuation (Figure 1-5d). This was in line with our hypothesis that *IDH1*^{mut} glioma cells would possess lower levels of basal FTO demethylase activity due to the presence of endogenous D-2-HG, thus reducing the growth inhibitory effect of small molecule inhibitors of FTO. This difference in sensitivity was especially pronounced in native *IDH1*^{wt} gliomaspheres and their *IDH1*^{mut}-forced expression counterparts. In HK385 gliomaspheres, growth inhibition was minimal in *IDH1*^{mut}-HK385 cells treated with FB23-2 (5 μM, 9 days) whereas *IDH1*^{wt}-HK385 cells showed ~50% growth inhibition versus an internal DMSO control condition (Figure 1-5e). Sensitivity to FB23-2 was restored in *IDH1*^{mut}-HK385 cells pre-treated with *IDH1*^{mut} inhibitors (1 μM C35; 2 μM AG881) (Figure 1-5f), providing further evidence that the presence of D-2-HG in *IDH1*^{mut} contexts activates a growth attenuation pathway that is specifically mediated by FTO. Taken together, these findings support our hypothesis that small molecule inhibitors of FTO may represent a novel treatment avenue for reducing proliferative potential in *IDH1*^{wt} glioma.

To further investigate this possibility and identify candidate gliomaspheres for *in vivo* experimentation, we next assessed the effects of FB23-2 treatment on m6A enrichment and growth inhibition in previously untested *IDH1*^{wt} gliomasphere lines (GS187, GS025, SDX130, SDX152, GS062, GS158). Out of 6 unique *IDH1*^{wt} gliomasphere lines, 5 exhibited high sensitivity

to FB23-2 defined as a 50% attenuation in sphere growth volumes following 6 days of 1 μM treatment (Figure 1-5g). The remaining gliomasphere line demonstrated 50% growth attenuation at 2.5 μM FB23-2 treatment. All lines exhibited a dose-dependent sensitivity response. Four high-sensitivity gliomasphere lines also exhibited increased m6A enrichment following 1μM of FB23-2 treatment (Figure 1-5h). Basal m6A levels were lowest in GS187, GS025, SDX130, and SDX152 gliomaspheres, and all lines showed varying levels of m6A enrichment after active treatment. We selected GS187 and SDX130 for *in vivo* treatment studies based on their sensitivity to FB23-2 in terms of both growth attenuation and m6A enrichment, and for ease of intracranial engraftment in murine models. Su *et. al.* previously showed that 12 days of FB23-2 treatment at dosages up to 20mg/kg elicits no detrimental side effects in mice, as evidenced by a lack of body weight loss or observable damage to bone marrow, spleen, or liver tissues (Huang et al., 2019). Our own pharmacokinetic studies in mice showed that a 20mg/kg dose of FB23-2 delivered via intraperitoneal injection (i.p.) was able to achieve plasma and brain tissue concentrations exceeding 1μM (Figure 1-5i). Estimated uptake across the blood brain barrier was estimated at 75.47% based on $AUC_{0\text{-}7hr}$. We therefore designed our *in vivo* treatment study to entail 20 mg/kg daily i.p. injections of FB23-2 dissolved in DMSO (or an equivalent volume of DMSO in the case of control treatments), to be delivered starting 3 days post-intracranial tumor cell injection (300,000 cells in a 2.0 μL total injection volume per mouse) in the right basal ganglia (2.0 mm depth) of female NSG mice (Figure 1-5j). The gliomasphere lines utilized in these xenograft studies were previously fixed with a *Gaussia* luciferase (GLuc) reporter to permit longitudinal tumor burden monitoring over the course of *in vivo* experiments. The *Gaussia* luciferase reporter assay is a rapid, sensitive, and non-invasive procedure that permits the monitoring and measurement of secreted reporters *in vivo*, among other applications (Tannous, 2009). Berger *et al.*, 1988 demonstrated that the levels of secreted GLuc reporter measured in conditioned media, blood, or urine linearly correlated to intracellular mRNA levels and to cell number (Berger et al.,

1988). Thus, this assay proved useful in approximating gliomasphere tumor burdens in our experimental model. Blood from xenografted mice was collected on a biweekly basis via tail vein bleeds, allowing for non-invasive tumor burden estimations over the course of our *in vivo* treatment studies.

Log-rank (Mantel-Cox) tests were used to compare survival curves between FB23-2 and DMSO treatment groups. FB23-2 treatment led to increased overall survival in both GS187 and SDX130 intracranially xenografted mice (Figure 1-5k). In GS187 xenografted mice treated with FB23-2 (n = 7) or DMSO (n = 8), log-rank analysis showed a significant difference in overall survival (P = 0.002; df = 1; Chi square = 9.554). Gehan-Breslow-Wilcoxon statistical tests confirmed this significant difference (P = 0.0035; df = 1; Chi square = 8.518). Median survival for GS187 mice treated with FB23-2 was 76.0 days and 58.5 days for DMSO-treated mice (Ratio = 1.299; 95% CI = 0.027 – 0.447). The Hazard Ratio (log-rank) was determined to be 0.282 (95% CI = 0.087 – 0.916). The observed standardized effect size for GS187 treatment versus control experiments was measured at 0.674. SDX130 xenografted mice treated with FB23-2 (n = 8) or DMSO (n = 9) also showed significant differences in overall survival following log-rank comparative analysis (P = 0.012; df = 1; Chi square = 6.244). Three SDX130 mice were removed from the study (FB23-2 = 2 mice, DMSO = 1 mouse) due to death during GLuc measurements prior to their tumor burdens reaching moribund levels. Gehan-Breslow-Wilcoxon testing showed a similarly significant difference (P = 0.034; df = 1; Chi square = 4.489). Median survival for SDX130 mice treated with FB23-2 was 56.0 days and 52.0 days for DMSO-treated mice (Ratio = 1.077; 95% CI = 0.415 – 2.791). The Hazard Ratio (log-rank) was determined to be 0.420 (95% CI = 0.152 – 1.164). The observed standardized effect size for SDX130 treatment versus control experiments was measured at 0.446. The results of these *in vivo* experiments utilizing intracranial xenografts of two independent $IDH1^{wt}$ gliomasphere lines provide evidence that targeting FTO via

pharmacological inhibition presents a viable biological mechanism to effectively reduce growth potential in glioma.

MeRIP-Seq Reveals Distinct Profiles of m6A Enriched Transcripts in IDH1^{mut} Gliomas

We demonstrated that the inhibition of m6A demethylase FTO leads to pronounced m6A enrichment and modulates growth dynamics in a wide range of glioma model systems. To begin elucidating the potential mechanisms underlying these observed phenotypes, we performed an unbiased screen of m6A-enriched transcripts across *IDH1^{mut}* and *IDH1^{wt}* U87 and IHA cell lines as well as four gliomasphere lines (*IDH1^{mut}*: HK211, HK252; *IDH1^{wt}*: HK217, HK250). To perform this screen, we utilized methylation RNA immunoprecipitation sequencing (MeRIP-Seq), a methodology combining m6A-specific immunoprecipitation and next-generation sequencing to obtain m6A localization data across the transcriptome (Dominissini et al., 2012; Meyer et al., 2012). We hypothesized that *IDH1^{mut}* glioma cells would show increased m6A enrichment in gene transcripts relevant to cell survival and growth, and that positive regulators of proliferation-related pathways would show a concomitant decrease in overall expression compared to *IDH1^{wt}* glioma cells.

We conducted MeRIP-Seq analysis using three different m6A peak calling and differential methylation analysis tools: ExomePeak, MACS2, and RADAR (Meng et al., 2014; Zhang et al., 2008; Zhang et al., 2019). We also performed RNA-Seq differential expression analysis on poly A$^+$ purified mRNA fractions from the same samples using DESeq2 (Love et al., 2014). Briefly, adapter sequences were trimmed using the FASTX Toolkit (Hannon, G.J., 2010). SortMeRNA software was then used to filter for mRNA transcripts (Kopylova et al., 2012). Transcript reads were mapped to GRCh38.p12 with STAR using transcriptome mode (Dobin et al., 2013). Uniquely mapped reads were then entered into RSEM to collate read coverage for each transcript, and a transcripts per million normalization parameter was calculated to permit differential expression

comparisons (Li and Dewey, 2011). Genes with significant differential expression were identified using EBseq software employing an empirical Bayesian hierarchical model (Leng et al., 2013). Mapped reads were visualized in Integrated Genome Viewer 2.8.9. To generate a set of differentially expressed and differentially methylated transcripts, we then subjected our m6A-immunoprecipitated mRNA and total mRNA fractions to algorithmic m6A peak calling, annotation, and $IDH1^{mut}$ versus $IDH1^{wt}$ differential expression comparisons.

We defined our final target list by intersecting the results of three independently validated m6A differential expression analysis packages: ExomePeak, MACS2, and RADAR (Meng et al., 2014; Zhang et al., 2008; Zhang et al., 2019). The three methods have different strengths and weaknesses, so our procedure intersected the three modules to search for agreement on differentially methylated sites. RADAR (RNA Methylation Differential Analysis in R) is a method based on counting events (modifications) in mutually exclusive bins across the transcriptome (Zhang et al., 2019). In a statistical setting, this is an indication that the RADAR model follows in the tradition of RNA-Seq analyses using a Poisson or negative binomial statistical framework. RADAR uses a Poisson random effect model, a more flexible model than usual for this analysis based on observed patterns in the mean-variance relationship in counts between gene transcripts. RADAR is a generally false-positive-rich model. The large number of overall bins assessed leads to the identification of many bins, by statistical chance, with a *P*-value less than 0.05. By merging 5-10 bins in a row and multiplying their respective *P*-values together to give an intersection significance of a region's differential methylation, it is possible to see large bins with a *P*-value on the order of 10^{-8} to 10^{-15}. Filters, a complex merging scheme accounting for a pre-programmed false discovery rates, and random effects are employed to reduce these false positives. ExomePeak is a MeRIP-Seq method which also uses a Poisson approach and site-specific c-tests of Poisson means to identify differentially methylated peaks (Meng et al., 2014). Mutually exclusive bins of a pre-determined length are assessed, similarly to RADAR. ExomePeak lacks

the random effect component of the RADAR model, representing a more traditional approach to regional MeRIP-Seq analysis. MACS2 is a ChIP-Seq method which can be easily repurposed to identify RNA modifications as in traditional MeRIP-Seq (Zhang et al., 2008). It relies on a sliding window model to identify regions of increased transcription. As with the previous models, MACS2 relies on a Poisson model of counts in transcriptomic regions. All three models rely on normalization strategies (using arithmetic shares within a gene or rescaling to a standard normal distribution within each gene) to permit comparative analysis of read counts across bins, as differences in read depth can inflate or deflate counts within a gene or across a transcript. All three models also employ filtering strategies based on the results from quality control or false discovery rates (FDR). The models identify significantly differentially methylated m6A peaks based on calculated $\log_2$ fold changes (logFC), and the lists of m6A-enriched peaks identified by these three models were intersected on a strict basis to produce a final output file containing our consensus genes of interest.

Only m6A peaks which all three models determined to be significantly differentially methylated were included in our downstream analyses and validation studies. The ExomePeak analysis package revealed a total of 19,159 genes exhibiting significantly differentially m6A methylated transcripts across our four *IDH1*^{mut} and four *IDH1*^{wt} lines. MACS2 revealed a total of 21,743 genes, and RADAR a total of 11,722 genes. A set of 2,012 genes demonstrated consensus agreement across the three m6A analysis packages employed, defining an unbiased selection of significantly differentially methylated peaks in which we have high confidence ($P < 0.05$; FDR < 0.1; logFC > 0.5) (Figure 1-6a). Multidimensional scaling (MDS) was applied to the pooled samples to permit graphical exploratory analysis of the data. MDS of variance-stabilizing transformation expression for the top 1000 and 2000 differentially expressed genes showed clustering of the U87 and IHA samples, and a separate cluster encompassing the gliomasphere samples (Supplementary Figure 1-S5a). MDS of fragments per kilobase of transcript per million mapped reads (FPKM)

showed a similar distribution, with U87 and IHA samples mapping to one cluster while gliomaspheres formed another (Supplementary Figure 1-S5b). We then performed principal component analysis (PCA) on these two clusters to check for unwanted variation among the included samples. PCA of the gliomasphere cluster showed adequate separation of the *IDH1*^{mut} and *IDH1*^{wt} lines based on the first three PCs after normalization (Supplementary Figure 1-S5c). PCA of the U87 and IHA cluster also showed adequate separation between *IDH1*^{mut} and *IDH1*^{wt} cells along the first three PCs (Supplementary Figure 1-S5d). The distribution of total mRNA read count bins, pre- and post-normalization read density distributions, and pre-normalization PCA results for the gliomasphere and U87 and IHA clusters are also included in supplementary figures (Supplementary Figure 1-S5c-d).

The fold enrichment distribution of m6A-containing transcripts showed a slight rightward shift in the *IDH1*^{mut} glioma cell lines compared to *IDH1*^{wt} lines, with densities depicted as a line graph overlaying a histogram representing frequencies of a given enrichment level (Figure 1-6b). Among the m6A peaks showing significant ($P < 0.05$) changes in *IDH1*^{mut} versus *IDH1*^{wt} glioma lines (a total of 5,855 peaks), 3,432 (58.6%) differentially methylated peaks exhibited m6A enrichment, whereas 2,423 (41.4%) exhibited m6A depletion (Figure 1-6c). These distributions align with our hypothesis that the *IDH1*^{mut} $\rightarrow$ D-2-HG $\dashv$ FTO axis serves to shifts the epitranscriptomic landscape of *IDH1*^{mut} glioma cells towards a more m6A-enriched phenotype. We term this set of significantly differentially m6A-methylated transcripts in *IDH1*^{mut} glioma G-RAMP (glioma RNA m6A methylation phenotype). Heatmaps depicting the top 5,000 significantly differentially methylated m6A bins (rank ordered by test *P*-value) also reveal distinct epitranscriptomic profiles for *IDH1*^{mut} and *IDH1*^{wt} glioma cell lines (FDR < 0.1; logFC > 0.5) (Figure 1-6d). Taken together, our bioinformatic analyses demonstrate that *IDH1*^{mut} glioma cells exhibit higher degrees of overall m6A enrichment, and that this enrichment occurs in a reproducible set of significantly differentially

methylated transcripts defining an *IDH1*^{mut} epitranscriptomic profile that is distinct from *IDH1*^{wt} gliomas.

To elucidate the functional characteristics of G-RAMP, we performed gene set enrichment analysis (GSEA) to identify biomolecular pathways that may be contributing to the reduced proliferative potential observed in the setting of *IDH1*^{mut} glioma. We intersected our G-RAMP list of significantly differentially methylated transcripts with three different GSEA Molecular Signature Database (MSigDb) collections ('H,' 'C2,' and 'C5') to identify gene targets for further orthogonal validation studies. Full descriptions and source publications for GSEA MSigDb gene sets can be found online (https://www.gsea-msigdb.org/gsea/msigdb/genesets.jsp). Briefly, MSigDb 'H' is comprised of 50 hallmark gene sets representing well-defined signatures of distinct biological states and processes. MSigDb 'C2' encompasses 6,290 gene sets gleaned from online pathway databases, PubMed publications, and those curated by experts in discrete domains. MSigDb 'C5' comprises 14,998 gene sets grouped based on shared gene ontology (GO) annotations, captured under three main subgroupings: molecular function (MF), biological process (BP), and cellular component (CC). The results from our MeRIP-Seq overlap analyses with GSEA MSigDb collections 'H,' 'C2,' and 'C5' are shown, ranked by the total number of MeRIP-Seq target genes involved in each gene set (Figure 1-6e).

For the GSEA-H overlap, we found a high level of concordance between our G-RAMP targets and the top gene sets found by Su *et al.* in a similar MeRIP-Seq and GSEA-H overlap analysis, performed on R-2-HG versus PBS (control) treated NOMO-1 AML cells (Su et al., 2018). This finding is of interest because R-2-HG treatments in *IDH1*^{wt} NOMO-1 cells effectively recapitulates the *IDH1*^{mut} AML phenotype, and our data shows that a similar set of genes is being differentially methylated in the setting of *IDH1*^{mut} glioma. Of particular note is the gene set comprising E2F targets involved in regulating the cell cycle, tumor suppressors, apoptosis, nucleotide synthesis,

and DNA repair and replication (Cobrinik, 2005; Maiti et al., 2005; Ogawa et al., 2002; Tategu et al., 2007; Tommasi and Pfeifer, 1995; Zwicker et al., 1996). Additional gene sets include those important for mitotic spindle assembly, G2/M checkpoint progression during cell division, and a subgroup of targets regulated by MYC. Our G-RAMP and GSEA-C2 overlap data revealed even more intersections with genes and pathways related to cell survival, proliferation, and differentiation. The top hit in our GSEA-C2 analysis was a set of genes downregulated in ME-A breast cancer cells undergoing doxorubicin-induced apoptosis (Graessmann et al., 2007). Genes associated with RNA polymerase II transcription were also prominently featured, as defined by the Reactome online database (https://reactome.org/PathwayBrowser/#/R-HSA-73857). Other top 25 gene sets captured targets of potent oncogenic transcription factors such as those upregulated in EWSR1/FLI1 fusion cells (Kinsey et al., 2006), genes downregulated during oligodendrocyte differentiation (Gobert et al., 2009), genes upregulated in response to an aminopeptidase inhibitor that induces apoptotic cell death in leukemic cells, targets of the DREAM (dimerization partner RB-like E2F and multi-vulval class B) complex regulating cell cycle-dependent gene expression (Fischer and Müller, 2017; Fischer et al., 2016; Sadasivam and DeCaprio, 2013), enhancers of the transcription factor FOXO1 which plays a role in apoptosis and cell cycle regulation (Alikhani et al., 2005; Gryder et al., 2017), genes constituting the ATM-PCC network wherein the ATM serine/threonine kinase is activated by DNA double-strand breaks to phosphorylate proteins that initiate cell cycle arrest and apoptosis (Pujana et al., 2007), genes with promoters regularly bound by the MYC oncogenic transcription factor (Zeller et al., 2003), and targets of SMAD transcriptional modulators that transduce TGF-β signals to regulate cell proliferation, apoptosis, and differentiation (Koinuma et al., 2009; Siegel and Massagué, 2003). Gene ontology analysis of our G-RAMP members performed using the GSEA-C5 MSigDb revealed a preponderance of differentially m6A-methylated transcripts in *IDH1*^{mut} glioma that fall under MF ontological classifications related to transcriptional regulation. The first gene set which captured the largest segment of our G-RAMP target list was 'Transcription Regulator Activity,' a

GO-MF classification relating to the timing and magnitude of gene transcription (GO Accession: GO:0140110). Also in our top 5 gene sets was 'Sequence Specific DNA Binding' which describes genes involved in selective and non-covalent interactions with DNA based on specific nucleotide compositions such as specific sequence motifs or types of DNA such as promoters or rDNA (GO Accession: GO:0043565), and 'DNA Binding Transcription Factor Activity' capturing genes encoding transcription factors that interact with specific motifs within *cis*-regulatory regions such as promoters and enhancers (GO Accession: GO:0003700). Of the remaining top 25 GO gene sets associated with G-RAMP, biological processes including the negative and positive regulation of chemical reactions involving nucleotides (GO Accession: GO:0045934) and other biosynthesis pathways (GO Accession: GO:0009890) figured prominently, as did the cell cycle (GO Accession: GO:0007049; GO:0022402), apoptosis (GO Accession: GO:0006915), RNA binding (GO Accession: GO:003723), and negative regulation of RNA polymerase II transcriptional functions (GO Accession: GO:0000122), among others. It is clear from our GO analysis that the *IDH1*^{mut} in glioma leads to alterations in the m6A epitranscriptomic landscape involving targets with the power to effect profound changes in cellular activity and survival, including modulation of transcription factor activity and DNA/RNA binding, interruption of fundamental synthesis pathways for critical cellular substrates such as DNA/RNA, as well as cell cycle progression and apoptosis. The constellation of gene sets uncovered in these three different GSEA overlap analyses provide strong evidence in support of our hypothesis that genes which are critical in cell fate and survival are preferentially modulated by m6A in *IDH1*^{mut} glioma to produce a phenotype with reduced proliferative potential.

To identify specific transcript targets in which m6A enrichment may be playing a direct role in modifying tumor cell survival in *IDH1*^{mut} glioma, we generated sequencing coverage plots in RADAR of target genes derived from our MeRIP-Seq datasets to provide high fidelity graphical representations of significantly differentially methylated m6A peaks, localized to specific transcript

regions. We generated plots for several dozen genes with multiple m6A peaks exhibiting significant differential methylation, and representative coverage plots at both the transcript- and peak-level are shown (Figure 1-6f). We elected to focus our attention on transcript targets that were captured in highly significant GSEA gene sets overlaps, particularly those related to apoptosis, transcription factor signaling, and oncogenic regulation. Among the differentially m6A-enriched transcripts we investigated, TRADD (tumor necrosis factor receptor type 1-associated death domain protein; NCBI Gene ID: 8717) and DAPK3 (death associated protein kinase 3; NCBI Gene ID: 1613) are representative targets involved in apoptosis, CEBPB (CCAAT enhancer binding protein beta; NCBI Gene ID: 1051) is a representative transcription factor, and TP53RK (TP53 regulating kinase; NCBI Gene ID: 112858) is a representative oncogenic regulator. To validate a potential biological mechanism linking m6A modulation with reduced proliferative potential in *IDH1*^{mut} gliomas, we next sought to employ various orthogonal approaches, namely, unbiased Nanopore direct RNA sequencing and RT-qPCR of target transcripts in glioma patient tumor samples, to verify the RADAR-derived m6A localization and enrichment patterns seen in our target transcripts and pathways of interest.

We first conducted direct RNA sequencing of *IDH1*^{mut} and *IDH1*^{wt} U87 glioma mRNA samples on an Oxford Nanopore Technologies (ONT) MinION Mk1B platform (*Oxford Nanopore Technologies*, Catalog #MIN-101B, Oxford, UK). Nanopore direct RNA sequencing offers several advantages as a methodological tool, providing the benefits of an unbiased screen capable of directly collating m6A modifications from RNA, and without the potential drawback of requiring immunoprecipitation steps that can introduce biases into constructed sequencing libraries based on variables such as RNA fragmentation efficiency, m6A antibody efficacy, and immunoprecipitation batch effects. This method thus equipped us with a valuable means of verifying the locations and differential methylation status of m6A enrichment sites in our list of target transcripts obtained through *IDH1*^{mut} versus *IDH1*^{wt} MeRIP-Seq experiments. We utilized

EpiNano version 1.2.0, a machine learning-based m6A detection and peak calling module, to parse m6A modifications in direct RNA sequencing data obtained on ONT MinION Mk1B platforms (Liu et al., 2019a). The bioinformatic pipeline behind EpiNano starts with a raw MinION MK1B sequencing signal and ends with RRACH-motif filtered results showing evidence of m6A modifications (Supplementary Figure 1-S6). The RRACH consensus motif is a known hotspot for RNA m6A modifications (R = A or G; A = m6A; and H = A, C, or U) (Dominissini et al., 2012; Harper et al., 1990; Wei and Moss, 2002; Zhang et al., 2020). The module uses errors in neural net base calling algorithms to identify nucleotide modifications at a 5-mer level of resolution, representing a sliding window five RNA nucleotides long. Detailed code and notation for the ONT EpiNano m6A analysis pipeline utilized in this study is included in Supplemental Materials (Supplementary m6A Bioinformatics 1-SMarkdown). Briefly, poly A^+ purified mRNA was loaded onto primed R9 ONT flow cells (*Oxford Nanopore Technologies*, Catalog #FLO-MIN106D, Oxford, UK). Flow cells were then inserted into a MinION MK1B platform and sequenced with MinION acquisition software version 21.02.1. Samples were run for 6 hours at -180 mV.

ONT calls their approach to sequencing 'squiggle'-cell sequencing, where raw electrical signal from the ONT platform is represented as a time series of the electrical conductivity of RNA strands as they pass through a nanopore. This 'squiggle' data is then compiled as .fast5 output files. The ONT base calling algorithm (Guppy version 3.1.5) reads the raw signal from the sequencing platform and determines the identity of nucleotide bases using ONT's extensive pooled training datasets. After neural net base calling is performed, the raw reads are compiled as .fastq output files and aligned to a reference genome, in our case the Gencode GRCh38.p13 primary assembly. Aggregate read statistics are generated using the reads aligner tool minimap2 version 2.14-r886. Minimap2 counts occurrences of mismatches, insertions, deletions and overall read quality across the parallel base called and aligned reads. The resulting .bam file contains each aligned read alongside a string representation of the base calling errors. The EpiNano module starts here,

extracting the aligned reads and tabulating statistics on the specific type of base calling errors. A 5-mer window slides through the aligned sequences and matched read quality statistics to summarize and tabulate base calling errors. It is important to note that these tabulations describe not just overall quantity of errors in the base calling at a given site, but also measure the repeated occurrences of specific errors within the same 5-mer RRACH consensus motifs across independent reads. EpiNano's machine learning modification detection is performed on these 5-mer sliding window sites using m6A models trained on data included in the module. The m6A training datasets from EpiNano are trained to identify sites that share a unique type of base calling error which has been demonstrated to be indicative of m6A methylation. The resulting m6A sites are RRACH-filtered, and by the nature of the machine learning process, each site is attached to a probability of m6A methylation. The interpretation of this probability is different from a *P*-value, but similarly illustrative of the confidence that m6A methylation is present within a given RRACH motif.

The m6A-containing RRACH motif sites generated via EpiNano are shown as scatter plot overlays on representative RADAR sequencing coverage plots (Figure 1-6g). Representative coverage plots are shown for TRADD and ATF5 (activating transcription factor 5; NCBI Gene ID: 22809) which both regulate apoptosis and are m6A-enriched in *IDH1*^{mut}, as well as ADAT3 (adenosine deaminase tRNA specific 3; NCBI Gene ID: 113179) which conversely shows m6A enrichment in *IDH1*^{wt} glioma and is involved in converting adenosine to inosine in the tRNA anticodon. Spatially, there is strong consensus between the locations of significantly differentially methylated RADAR m6A peaks (horizontal bars) and EpiNano m6A RRACH motif hits (scatter plot; red = *IDH1*^{mut}, blue = *IDH1*^{wt}). This provides strong orthogonal evidence that the unbiased screen performed using standard MeRIP-Seq methodologies is an accurate reflection of the distinct and differentially methylated epitranscriptomic profiles we observe in *IDH1*^{mut} and *IDH1*^{wt} glioma.

The IDH1^{mut}→ D-2-HG ⊣ FTO *Axis Leads to m6A RNA Enrichment and Reduced Expression of ATF5 Resulting in Increased Apoptotic Activity*

To identify a biological mechanism to help explain the reduced proliferative potential characteristic of *IDH1^{mut}* gliomas versus their wildtype counterparts, we focused our next set of analyses and experiments on G-RAMP targets that exhibited significant m6A enrichment and differential expression in *IDH1^{mut}* gliomas, particularly those involved in pathways promoting cell survival. We hypothesized that the changes in the epitranscriptomic landscape seen in *IDH1^{mut}* would lead to the downregulation of prosurvival pathways and an increase in apoptotic activity. As part of our target selection process, we utilized glioma RNA-Seq expression data from The Cancer Genome Atlas (TCGA), accessed through the publicly available GlioVis data portal and visualization tool (http://gliovis.bioinfo.cnio.es/) and stratified differential expression profiles based on *IDH1* mutation status (Bowman et al., 2017). After performing GlioVis differential expression analysis on several targets of interest gleaned from our MeRIP-Seq experiments, ATF5 emerged as a promising target for downstream study.

ATF5 belongs to the CREB (cAMP response element-binding) family of proteins, a subset of the bZIP (basic zipper) protein family (Hai et al., 1989). ATF5 is primarily involved in pathways governing cell survival, proliferation, and differentiation in a cell type-dependent manner, and typically in capacity that promotes survival and proliferation while suppressing differentiation (Dluzen et al., 2011; Liu et al., 2004; Pati et al., 1999; Yamazaki et al., 2010). A dominant-negative ATF5 isoform has also been shown to induce apoptosis in breast cancer and glioma cell lines, while having no effect on non-neoplastic breast epithelial cells or healthy neuronal and glial cells (Angelastro et al., 2006; Cates et al., 2016; Monaco et al., 2007). The intriguing evidence that ATF5 exerts prosurvival effects in glioma and not in healthy brain tissue led us to consider whether ATF5 downregulation, mediated by m6A enrichment in ATF5 transcripts, might lead to a loss of

its prosurvival, cell protective effect and explain the reduced proliferative potential observed in *IDH1*^{mut} versus *IDH1*^{wt} glioma.

In our GlioVis analysis of G-RAMP transcript targets, we found that ATF5 expression was decreased over 2-fold in the *IDH1*^{mut} (n = 429) glioma patient cohort when compared to the *IDH1*^{wt} (n = 233) cohort in a pairwise t-test (P < 6.6E-65, with Bonferroni multiple testing correction) (Figure 1-7a). Median ATF5 mRNA expression for the cohorts was $\log_2(8.36)$ in *IDH1*^{mut} gliomas (SD = 0.66), and $\log_2(9.54)$ in *IDH1*^{wt} gliomas (SD = 0.80). Additional Tukey's HSD statistical testing confirmed ATF5 suppression in *IDH1*^{mut} glioma samples, revealing a difference in mRNA expression of $\log_2(1.11)$ (P < 0.001; 95% CI: 0.99 - 1.22). When the patient cohort was stratified into ATF5 High (n = 335) and ATF5 Low (n = 332) gliomas, lower ATF5 expression correlated with significant survival benefits as measured by both standard log-rank testing and Gehan-Breslow-Wilcoxon tests (Figure 1-7b). Median survival was improved 4.14-fold in ATF5 Low glioma patients who exhibited a median overall survival of 98.2 months, compared to 23.7 months in ATF5 High patients (Hazard Ratio = 0.23; 95% CI = 0.17 – 0.31). These results provide firm evidence that ATF5 downregulation is indeed observed in *IDH1*^{mut} gliomas, and that lower expression levels attenuating the protumor survival effects of ATF5 correlates strongly with improved overall survival in patients.

To confirm these differences in ATF5 expression observed in the large-scale patient cohort data comparing *IDH1*^{mut} and *IDH1*^{wt} glioma, we performed targeted RT-qPCR on RNA isolated from fresh frozen glioma tumor samples obtained through the UCLA Brain Tumor Translational Resource. Total RNA was purified from *IDH1*^{mut} (n = 12) and *IDH1*^{wt} (n = 12) patient tumor samples and subjected to both poly A^+ mRNA purification and m6A immunoprecipitation using an anti-m6A antibody (*Synaptic Systems,* Catalog #202-003, Goettingen, Germany). The separate fractions were then used to synthesize first strand cDNA using a SuperScript II Reverse Transcriptase Kit

with Oligo(dT) primers (*Thermo Fisher Scientific*, Catalog# 18064014, Waltham, MA, USA). The levels of m6A-enriched ATF5 transcripts and total ATF5 mRNA were determined via quantitative PCR (qPCR). Prior to stratifying results based on *IDH1* status, the levels of m6A-enriched ATF5 transcripts were first normalized to a known concentration of GLuc m6A-positive control RNA that was spiked into samples prior to immunoprecipitation. Total ATF5 mRNA levels were normalized to β-actin transcript levels. In GLuc-normalized, m6A-immunoprecipitated RNA fractions, there was significantly more m6A enrichment in ATF5 transcripts isolated from $IDH1^{mut}$ versus $IDH1^{wt}$ patient tumor samples (P = 0.027) (Figure 1-7c). As originally hypothesized, increased m6A enrichment was associated with a significantly decreased overall abundance of ATF5 mRNA in $IDH1^{mut}$ glioma samples (P = 0.036) (Figure 1-7d). The finding of reduced ATF5 expression in our $IDH1^{mut}$ glioma tissue samples mirrors the results from our differential ATF5 expression analysis using TCGA cohort-level data. Additionally, we confirmed that m6A levels are enriched in ATF5 mRNA isolated from $IDH1^{mut}$ gliomas, providing a potential mechanistic explanation for ATF5 suppression as seen in this context.

We next sought to explore whether $IDH1^{mut}$ forced expression in gliomaspheres reliably induces m6A enrichment of ATF5 transcripts. HK217 and HK250 native $IDH1^{wt}$ lines were used for these experiments. Stabilization of $IDH1^{mut}$ in these cell lines was accomplished with a pUltra-$IDH1^{R132H}$-EGFP plasmid, and control transduction lines were generated with a pUltra-EGFP-only plasmid. As with the patient tumor samples described above, total RNA from these cell lines was subjected to m6A immunoprecipitation and RT-qPCR to quantify differences in the abundance of m6A-enriched ATF5 transcript. Additionally, HK217-$IDH1^{mut}$ and HK250-$IDH1^{mut}$ lines were treated with $IDH1^{mut}$ inhibitor AG881 (1 μM) or a DMSO control for 15 days to investigate the reversibility of any induced m6A modulations. Indeed, the forced expression of $IDH1^{mut}$ in these gliomaspheres produced pronounced increases in m6A-enriched ATF5 transcripts (normalized to GLuc m6A-

positive control spike in) compared to HK217-EGFP and HK250-EGFP *IDH1*^{wt} control lines (P = 0.002 in HK217; P < 0.001 in HK250) (Figure 1-7e). The pharmacological inhibition of *IDH1*^{mut} in forced expression lines significantly attenuated this effect (P = 0.031 in HK217; P = 0.002 in HK250). These results show that *IDH1*^{mut} induction is sufficient to increase the basal abundance of m6A modulations in ATF5 transcripts in glioma, and that the inhibition of D-2-HG production in this context reverses this effect.

To further elucidate the effect of increasing m6A enrichment on ATF5 transcripts and how this modulates ATF5 prosurvival functions, we next studied differences in apoptotic activity in native *IDH1*^{wt} HK217 and HK250 gliomaspheres treated with octyl-D-2-HG, MA, and the FTO-specific inhibitor FB23-2. Homozygous *IDH1*$^{mut/mut}$ BT142 cells that do not produce D-2-HG were also utilized. Gliomaspheres were cultured with octly-D-2-HG (1 mM), MA (100 μM), FB23-2 (3 μM), or a DMSO control treatment for 3 days. We employed a luminescence-based Caspase-Glo 3/7 Assay Kit (*Promega*, Catalog #G8090, Madison, WI, USA) to quantify any upregulation of Caspase 3 or Caspase 7 activity associated with apoptosis. In all three non-D-2-HG-producing gliomaspheres, Caspase 3/7 activity was significantly enhanced in comparison to the DMSO control condition (P = 0.008 with octyl-D-2-HG; P = 0.019 with FB23-2; P = 0.021 with MA) (Figure 1-7f). We also studied the effects of these treatments on apoptosis induction in U87 glioma cells using a fluorescent labeling Apoptosis/Necrosis Assay Kit (*ABCAM*, Catalog #ab176749, Waltham, MA, USA). Apoptotic cells were visualized with a green apopxin indicator (Ex/Em = 490/525 nm), necrotic and late-stage apoptotic cells were visualized with a red 7-AAD indicator (Ex/Em = 550/650 nm), and healthy cells were visualized with a blue CytoCalcein Violet 450 indicator (Ex/Em = 405/450 nm). Apoptotic activity was increased in U87 cells in all cases when compared to a DMSO control condition, with the largest increases in apoptotic indicators seen in the octyl-D-2-HG and FB23-2 treatment conditions (Figure 1-7g). A representative image of a 1 μM staurosporine (STSP) apoptosis-inducing positive control condition is also included. No

necrotic signatures were observed, suggesting that apoptosis induction is the primary means of reduced proliferative potential in these treated cell lines. Taken together, the above data provide evidence that pharmacologic inhibition of FTO results in significant upregulation of apoptotic activity. This supports our hypothesis that one biological mechanism by which the *IDH1*^{mut} → D-2-HG ⊣ FTO axis reduces proliferative potential in glioma is driven by increased m6A enrichment in ATF5 transcripts, a concomitant reduction in its expression, and the inhibition of its prosurvival functions which thus serves to promote apoptosis.

DISCUSSION

The production of D-2-HG in *IDH1*^{mut} gliomas leads to the competitive inhibition of αKG-dependent dioxygenases that regulate critical cellular functions (Bunse et al., 2018; Chowdhury et al., 2011; Dang et al., 2009; Fu et al., 2012; Gelman et al., 2018; Kölker et al., 2002; Latini et al., 2003; Lu et al., 2012; Richardson et al., 2019; Xu et al., 2011; Yalaza et al., 2017; Zhang et al., 2018; Zhao et al., 2009). The myriad downstream targets of D-2-HG provide a strong indication that the pathological consequences of *IDH1*^{mut} are likely to be widespread. Indeed, dysregulation of functional pathways effected by D-2-HG are largely understood to contribute to gliomagenesis (Ichimura et al., 2009; Lai et al., 2011; Watanabe et al., 2009). However, the clinical data clearly demonstrate that the presence of *IDH1*^{mut} confers a significant survival advantage in glioma patients (Balss et al., 2008; Cancer Genome Atlas Research Network et al., 2015; Eckel-Passow et al., 2015; Ichimura et al., 2009; Kang et al., 2009; Nobusawa et al., 2009; Parsons et al., 2008; Yan et al., 2009). This seeming contradiction highlights the paradoxical pro- and anti-tumor effects that D-2-HG engenders. The question of how D-2-HG contributes to gliomagenesis while simultaneously attenuating malignant phenotypes remains a consequential subject worthy of investigation, as the identification of these anti-tumor processes could pave the way for novel therapeutic developments that are sorely needed in glioma, particularly for the overwhelming majority of *IDH1*^{wt} glioma patients who suffer the worst clinical outcomes. A new approach to tackling this complex question arrived with the discovery that the recently identified mammalian RNA m6A demethylases FTO and ALKBH5 are both αKG-dependent dioxygenases sensitive to D-2-HG-mediated inhibition (Huang et al., 2019; Su et al., 2018). Intense interest in the biological role of m6a epitranscriptomic modifications is currently being compounded by evidence implicating FTO and ALKBH5 in various oncogenic processes (Cui et al., 2017; Deng et al., 2018a, 2018b; Huang et al., 2019; Li et al., 2017b; Su et al., 2018; Tan et al., 2015; Yan et al., 2018; Zhang et al., 2017). To date, the effects of *IDH1*^{mut} and D-2-HG on epitranscriptomic dynamics impacting tumor cell proliferation have not been systematically explored in glioma. Our

investigations sought to bridge this knowledge gap by identifying a novel epitranscriptomic signature in glioma and determining its relevance to glioma cell growth, with the ultimate aim of harnessing any anti-tumor mechanisms discovered in the process to explore a new therapeutic approach for one of the most lethal of all human cancers. Our study demonstrates that the *IDH1*^{mut} → D-2-HG ⊣ FTO axis in glioma results in specific epitranscriptomic changes contributing to reduced cell proliferation, and that directly inhibiting FTO in *IDH1*^{wt} glioma can recapitulate this clinically favorable phenotype both *in vitro* and *in vivo*.

Our experimental approach for this study relied on glioma patient tumor samples and patient-derived gliomaspheres to evaluate the epitranscriptomic landscape and tumor cell proliferation dynamics in *IDH1*^{mut} and *IDH1*^{wt} glioma. We employed clinical trial candidates that inhibit *IDH1*^{mut}-mediated D-2-HG generation as well as recently developed small molecule inhibitors of FTO to dissect patterns of m6A enrichment and cell growth. We also applied multiple unbiased screening techniques to construct epitranscriptomic profiles capturing the distribution and abundance of m6A modifications in glioma RNA, including global and targeted m6A quantification approaches, three distinct MeRIP-Seq bioinformatic pipelines, and Nanopore direct RNA sequencing technology.

ELISA-based quantifications of m6A abundance in patient tumor samples provided the first evidence that *IDH1*^{mut} gliomas exhibit significant m6A enrichment compared to their *IDH1*^{wt} counterparts. This observation was confirmed in patient-derived gliomaspheres, providing support to our hypothesis that *IDH1*^{mut} is associated with alterations in the epitranscriptomic landscape. Indeed, the forced expression of *IDH1*^{mut} in native *IDH1*^{wt} glioma cells resulted in steep increases in m6A abundance to levels on par with gliomaspheres exhibiting *de novo IDH1*^{mut} statuses, and m6A enrichment in these cases was tied to concomitant elevations in intracellular D-2-HG. We established that D-2-HG is a necessary element in the formation of the m6A-enriched phenotype

seen in *IDH1*^{mut} glioma, and that the process of m6A enrichment is reversible with the use of *IDH1*^{mut} inhibitors attenuating D-2-HG production. In fact, exposure to D-2-HG alone was sufficient to induce elevations in m6A abundance in every *IDH1*^{wt} gliomasphere tested in this study, further cementing the central importance of D-2-HG as an upstream regulator of epitranscriptomic changes in *IDH1*^{mut} glioma. This finding was consistent with evidence provided by Su *et al.*, wherein D-2-HG treatments in AML and *IDH1*^{wt} glioma model systems were shown to increase global m6A concentrations (Su et al., 2018).

D-2-HG-mediated m6A enrichment was also strongly associated with the attenuation of proliferative capacity across all glioma cell lines and gliomaspheres. Reduced proliferation rates were observed in native *IDH1*^{wt} gliomaspheres treated with D-2-HG as well as those transformed with *IDH1*^{mut} expression vectors. Blockade of D-2-HG synthesis with *IDH1*^{mut} inhibitors (or withdrawal of direct D-2-HG treatments) was able to reverse these anti-proliferative effects in all cases. Our findings indicate that the establishment of *IDH1*^{mut} coupled with canonical D-2-HG production can act to inhibit glioma cell growth. These findings are in accordance with numerous studies disputing the notion that *IDH1*^{mut} and D-2-HG play uniformly oncogenic roles in glioma (Huang, 2019). In addition to their association with improved survival in patients (Balss et al., 2008; Cancer Genome Atlas Research Network et al., 2015; Eckel-Passow et al., 2015; Ichimura et al., 2009; Kang et al., 2009; Nobusawa et al., 2009; Parsons et al., 2008; Yan et al., 2009), gliomaspheres composed of glioma stem cells derived from *IDH1*^{mut} patient tumors are well known throughout the field as being harder to establish and propagate both *in vitro* and *in vivo* (Piaskowski et al., 2011). D-2-HG aciduria is a separate condition afflicting individuals harboring germline mutation in *IDH2*^{R140Q} and *IDH2*^{R140G} that dramatically raise D-2-HG levels in the body, yet these patients are often asymptomatic are not known to exhibit increased risks for glioma or other cancers (Kranendijk et al., 2010; Struys, 2006). Even when *IDH1*$^{R132H/wt}$ or *IDH2*$^{R140Q/wt}$ heterozygosity (the canonical *IDH1* mutational signatures in glioma) are induced in transgenic

mice, no increases in the development of glioma or other tumors are observed (Huang, 2019). The downstream effects of *IDH1*^{mut} and D-2-HG are clearly complex, and prevailing theories assert that *IDH1*^{mut} inhibitors may harbor clinical benefit. Nevertheless, ongoing clinical trials in leukemias and other solid tumors employing potent *IDH1*^{mut} inhibitors that drastically reduce intratumoral D-2-HG levels have shown minimal therapeutic effects at best, with some compounds actually increasing the likelihood of developing detrimental phenotypes such as diminished sensitivity to chemotherapy and radiation therapy (Dang and Su, 2017; Deng et al., 2015; Huang, 2019; Khurshed et al., 2018; Kopinja et al., 2017; Molenaar et al., 2015; Natsume et al., 2019; Pusch et al., 2017; Rohle et al., 2013; Sulkowski et al., 2017; Tateishi et al., 2015; Turcan et al., 2013; Waitkus et al., 2018). Our finding that *IDH1*^{mut} and D-2-HG suppress glioma cell proliferation suggests caution in the utilization of *IDH1*^{mut} inhibitors as therapeutic options in glioma, as total D-2-HG blockade may disrupt other pathways that are effective anti-tumor mechanisms. Our results support this hypothesis and display similarities with work performed in AML where D-2-HG exposure was shown to inhibit cell growth in a manner that is dependent on the suppression of FTO m6A demethylase activity (Su et al., 2018).

Knockdown experiments in *IDH1*^{wt} gliomaspheres were conducted to assess the relative contributions of FTO and ALKBH5 in determining m6A abundance and relative proliferation rates. Indeed, FTO knockdown proved to be a superior inducer of m6A enrichment and cell growth suppression, and the use of an enzymatically inactivated FTO^{mut} isoform showed similar results. Conversely, ALKBH5 knockdown did not appear to meaningfully alter m6A levels or proliferation rates, suggesting that D-2-HG mediates m6A enrichment and anti-proliferative phenotypes specifically via FTO inhibition in *IDH1*^{mut} glioma. These findings formed the evidentiary basis for our experiments to test the *in vivo* efficacy of FTO inhibition as a means of treating *IDH1*^{wt} gliomas.

Results from our FB23-2 treatment studies in the context of *IDH1*^{wt} gliomasphere intracranial xenografts provide the first *in vivo* evidence in favor of targeting FTO as a novel therapeutic approach in glioma. FB23-2 is a highly selective small molecular inhibitor of FTO which previously demonstrated efficacy as an anti-tumor agent in AML (Huang et al., 2019). *IDH1*^{wt} glioma cells and gliomaspheres treated with FB23-2 *in vitro* demonstrated robust m6A enrichment and reduced proliferation rates in all cases, though with some variations in sensitivity. Out of six gliomasphere lines tested *in vitro*, four showed pronounced growth attenuations at concentrations as low as 1 μM. Pharmacokinetic studies in mice showed that 1 μM concentrations of FB23-2 were achieved in the brain at our selected dosage, and *in vivo* experiments demonstrated a positive treatment effect, with FB23-2 treated mice exhibiting significant increases in overall survival. Even though the molecular pathway targeted by FB23-2 appears to be a viable therapeutic strategy, one limitation of our study is the relative clinical utility of FB23-2. While our *in vivo* studies demonstrated a statistically significant survival advantage for FB23-2-treated mice in the context of *IDH1*^{wt} gliomasphere intracranial xenografts, the modest increases in median survival may not support the use of the current drug formulation in human studies. High concentrations of systemically delivered FB23-2 were required to achieve intratumoral therapeutic thresholds *in vivo*, and we suspect this is largely a function of rapid drug metabolism, incomplete blood-brain-barrier penetrance, and an IC_{50} that could be further optimized for glioma and *in vivo* applications. Other than increasing our sample size in future treatment studies to more clearly accentuate differences in FTO-inhibited versus control treated *IDH1*^{wt} gliomas, the recent validation of new small molecules (CS-1 and CS-2) demonstrating improved potency and FTO-specific inhibitory effects in leukemia provide us with another set of tools to enhance our treatment paradigm (Su et al., 2020). While the translational approach of the current study was focused on *IDH1*^{wt} gliomas (partly due to the difficulty of establishing slow-growing *IDH1*^{mut} animal models), additional studies are needed to investigate how synergistic treatment paradigms combining FTO and *IDH1*^{mut} inhibitors influence cell growth and malignancy in *IDH1*^{mut} glioma. This approach

would seek to block the purported oncogenic effects mediated by D-2-HG while still maintaining an epitranscriptomic state favoring tumor cell death. To provide a simple analogy: if we imagine glioma cell proliferation as analogous to forward momentum in a vehicle, then pathways that promote proliferation are the gas pedal and anti-proliferative pathways are the brake. In the context of *IDH1*^{mut} glioma, D-2-HG can thus be compared to a driver applying pressure to both the gas and the brake pedals simultaneously. In this simplified model, *IDH1*^{mut} inhibition would serve to neutralize D-2-HG and lift pressure on both the gas and the brake; while synergistic FTO inhibition replaces D-2-HG to specifically pump the brakes to slow proliferative momentum. Our current study shows that FTO inhibition alone creates enough braking power to have translatable effects even in the context of highly aggressive *IDH1*^{wt} gliomas, justifying future trials of synergistic therapeutic approaches in *IDH1*^{mut}.

Bioinformatic analysis of MeRIP-Seq data in *IDH1*^{mut} and *IDH1*^{wt} glioma cells revealed a core set of differentially m6A methylated transcripts we term G-RAMP, representing a unique and previously undescribed epitranscriptomic signature in *IDH1*^{mut} glioma. The use of Nanopore direct RNA sequencing served as a novel approach to orthogonally validate the localization and relative enrichment of m6A RRACH motif sites, and our findings demonstrated high levels of consensus with m6A sites picked up through standard MeRIP-Seq methods. A majority of differentially methylated sites identified in G-RAMP exhibited m6A enrichment, indicating that G-RAMP reflects a generally hypermethylated epitranscriptomic state. This aligns with our global m6A quantification findings in *IDH1*^{mut} patient tumors and patient-derived gliomaspheres, and provides an interesting corollary to G-CIMP, the hypermethylated epigenetic signature found in *IDH1*^{mut} gliomas associated with better clinical outcomes (Dang et al., 2009; Lai et al., 2011; Malta et al., 2018; Nomura et al., 2019; Noushmehr et al., 2010; Turcan et al., 2012; Waitkus et al., 2018). Previous work in AML lines also showed the induction of a hypermethylated m6A profile in cells treated with D-2-HG, and comparisons between our own G-RAMP GSEA analyses and those

conducted in D-2-HG treated AML cells reveals a fascinating degree of overlap (Huang et al., 2019; Su et al., 2018). Primary among them were transcripts belonging to gene sets involved in mitotic spindle assembly, responses to UV-induced DNA damage, G2M checkpoint progression, and targets of both MYC and E2F. The involvement of multiple pathways whose dysregulation is implicated in cancer development lends further credence to our assertion that the *IDH1*^{mut} → D-2-HG ⊣ FTO axis mediates transformations in the epitranscriptomic landscape that modulate cancer cell growth and survival.

Our GSEA analysis also revealed m6A changes in apoptotic pathways, within which we identified ATF5 as playing a critical role. Increased m6A enrichment of ATF5 transcripts in *IDH1*^{mut} glioma led to decreased overall ATF5 expression and the induction of apoptosis. This finding is the first evidence that perturbations in epitranscriptomic processes can increase apoptotic activity in glioma and helps elucidate one of the long-sought biological mechanisms through which D-2-HG exerts anti-tumor effects in *IDH1*^{mut}. Further support for our model was obtained in GlioVis analyses of ATF5 expression data in patient tumor samples, wherein *IDH1*^{mut} gliomas exhibited decreased ATF5 expression versus *IDH1*^{wt} gliomas. Importantly, lower ATF5 expression was correlated with improved patient survival across both low- and high-grade gliomas. Our results are in accordance with other studies demonstrating the involvement of ATF5 in pathways effecting cell survival, proliferation, and differentiation in cancer; typically mediated through its suppression of apoptosis and the maintenance of stem-like states (Dluzen et al., 2011; Liu et al., 2004; Pati et al., 1999; Yamazaki et al., 2010). ATF5 mediates its effects via interactions with cAMP response elements, amino acid response elements, and a general ATF response element (consensus sequence 5'-GTGACGTACAG-3') present in the promoters of many different cellular and viral genes (Hai et al., 1989; Li et al., 2009; Lin and Green, 1988; Peters et al., 2001; Yamazaki et al., 2010). ATF5 also binds to a unique ATF5-specific response element initially identified in rat C6 glioma cells and MCF-7 breast cancer cells (Li et al., 2009). Studies performed in rat neural

progenitor cells and PC12 pheochromocytoma cells identified ATF5 downregulation as a necessary step in normal differentiation processes (Angelastro et al., 2003, 2005; Mason et al., 2005). ATF5 downregulation and the induction of apoptotic pathways in cancer was first demonstrated in cancer cells deprived of critical growth factors, such as HeLa cells experiencing withdrawal from serum and FL5.12 cells deprived of IL-3 (Persengiev et al., 2002). Overexpression of ATF5 served to reverse the apoptotic phenotype, showing that ATF5 is an anti-apoptotic factor that can play a meaningful role in promoting cell survival. Complementing these findings in ATF5-suppressed cells was the discovery that a dominant-negative ATF5 isoform precipitates apoptotic induction in growth factor-deprived cancer cells (Angelastro et al., 2006; Cates et al., 2016; Monaco et al., 2007; Persengiev et al., 2002). Dominant-negative ATF5 also upregulates apoptotic activity in glioma and breast cancer cells cultured under normal conditions without growth factor deprivation, further highlighting the role of ATF5 as a prosurvival, anti-apoptotic factor with relevance to glioma (Angelastro et al., 2006; Cates et al., 2016; Monaco et al., 2007). Fascinatingly, ATF5 also appears to play a highly selective role in suppressing apoptotic activity in both glioma and breast cancer, where loss of function leads to the induction of apoptotic cell death in cancerous cells exclusively while having no effect on non-neoplastic breast epithelial cells or healthy neuronal and glial cells (Angelastro et al., 2006; Cates et al., 2016; Monaco et al., 2007). Dluzen *et al.* showed that this prosurvival effect of ATF5 in glioma and breast cancer is mediated by its binding to an ATF5-specific response element located alongside a negative regulatory element in the *BCL-2* promoter (P2), an interaction that stimulates BCL-2 expression and promotes cell survival under normal conditions (Dluzen et al., 2011). *BCL-2* is a primary member of the BCL-2 family of proteins that regulate the intrinsic pathway of apoptosis through modulation of mitochondrial outer membrane permeabilization (Chipuk et al., 2010; Harris and Thompson, 2000). BCL-*2* executes anti-apoptotic functions in conjunction with A1, BCL-W, BCL-XL, and MCL-1, while other BLC-2 family proteins sharing BCL-2 homology (BH) domains such as BAK, BAX, BID, BIM, BAD, BIK, BMF, HRK, NOXA, PUMA, and EGL-1 promote

apoptosis (Chipuk et al., 2010). Dluzen *et al.* confirmed the interdependency of ATF5 and BCL-2 prosurvival effects, showing that dominant-negative ATF5 cells proceeding towards apoptosis could be rescued by forced expression of BCL-2 in both rat C6 glioma cells and MCF-7 breast cancer cells (Dluzen et al., 2011). Conversely, BCL-2 depletion blocked the prosurvival effects of normal ATF5 expression, and while BCL-2 was shown to be necessary for survival in cancerous as well as non-cancerous cells, ATF5 served to promote survival only in cancerous cell types (Dluzen et al., 2011). This intriguing finding that ATF5 exerts anti-apoptotic functions in glioma cells but not in healthy brain tissue supports our proposed model that ATF5 downregulation, effected through m6A enrichment and subsequent transcript degradation, leads to marked reductions in glioma cell survival capabilities, providing a plausible explanation for the reduced proliferative potential we observed in both $IDH1^{mut}$ gliomas and $IDH1^{wt}$ gliomas subjected to FTO inhibition.

While our study provides robust evidence defining the epitranscriptomic changes leading to apoptotic sequalae arising from the $IDH1^{mut} \rightarrow$ D-2-HG $\dashv$ FTO axis, we acknowledge an important limitation requiring additional investigations. Epitranscriptomic regulation remains a comparably nascent field describing previously unknown mechanisms of gene expression regulation, and little remains known regarding how RNA modifications such as m6A direct interactions with RNA-binding proteins (RBPs). RBPs act as the ultimate downstream effectors determining transcript features and fates, and our findings thus far do not elucidate a mechanistic pathway linking m6A enrichment in G-RAMP transcripts directly to altered patterns of expression. Currently proposed models primarily implicate m6A enrichment in mRNA degradation processes, however, our understanding of the identities and functions of RBPs recognizing m6A-containing substrates (‘readers’) is continuing to evolve. The most well studied examples of proteins in this m6A reader network are the YTHDF (YT521-B homology domain-containing family) family of proteins, of which three paralogs have been shown to exhibit m6A-binding and transcript modification

capabilities (Li et al., 2017a; Shi et al., 2017, 2019; Wang et al., 2014a, 2015b). Paralogs include YTHDF1 which is thought to enhance mRNA translation (Wang et al., 2015b), YTHDF2 which has been shown to promote mRNA degradation (Du et al., 2016; Park et al., 2019; Wang et al., 2014a, 2015b), and YTHDF3 which appears to enhance both translation and degradation (Li et al., 2017a; Shi et al., 2017). Complicating matters further is the existence of conflicting evidence as to the role of each reader, and a prevailing debate over whether readers exhibit substrate specificity permitting the recognition of particular m6A-enriched transcripts. Shi *et al.* present evidence that the majority of m6A-containing transcripts bind to a single reader, but that a significant minority interact with up to three different paralogs (Shi et al., 2017, 2019). This has led to speculation that each reader may recognize distinct transcript populations within the epitranscriptome, thereby mediating different cellular processes (Anders et al., 2018; Han et al., 2019; Hesser et al., 2018; Paris et al., 2019; Shi et al., 2018). The high sequence homology between m6A motifs presents a natural challenge to this theory of sequence-specific substrate recognition, along with the absence of convincing evidence elucidating the mechanisms through which reader paralogs achieve supposedly differential effects (Patil et al., 2018; Wang and He, 2014). One theory is that the presence of m6A initiates conformational changes to secondary RNA structure, thus allowing different RBPs to recognize specific transcript substrates. In support of this hypothesis, Zou *et al*. utilized thermodynamic, spectroscopic, gel-shift, thermophoretic, and biochemical studies to show that the RRACH consensus m6A motif itself serves little purpose in determining selectivity for FTO and ALKBH5 binding. Instead, conformational changes initiated by the presence of m6A instead proposed to regulate selective transcript binding, possibly through unique FTO and ALKBH5 catalytic site-adjacent elements including the nucleotide-recognition lid domain and the L1 loop (Zhu and Yi, 2014; Zou et al., 2016). This study was limited by the fact that the substrates utilized were synthetically produced, and there may be differences in the functional role of m6A in directing conformational changes under normal physiologic conditions. Whether a similar mechanism for substrate specificity may be at play in YTHDF paralogs, or other as yet unknown

m6A reader proteins, is an open question. Countervailing arguments against the theory of selective substrate recognition among m6A readers are also strong. A recent study using PAR-CLIP (photoactivatable ribonucleoside-enhanced crosslinking and immunoprecipitation) techniques to characterize YTHDF m6A-binding sites found convincing evidence that the three known paralogs exhibit nearly identical binding preferences (Zaccara and Jaffrey, 2020). In addition, the YTHDF readers appeared to recognize the same mRNAs and initiate their degradation in a redundant manner (Zaccara and Jaffrey, 2020). While our study did find that m6A enrichment promoted reductions in overall ATF5 transcript expression, we did not investigate the precise mechanisms mediating ATF5 transcript degradation. Future studies using PAR-CLIP methods specified to each YTHDF paralog will be the first step in disentangling the network of readers that may be producing differential actions on G-RAMP member transcripts.

Additional studies are also required to identify other potential anti-tumor targets within G-RAMP to gain a deeper understanding of how this epitranscriptomic profile impacts specific cell survival functions in such a wide constellation of possible pathways. Ideally, further refinements of our G-RAMP member list would be accomplished using high throughput MeRIP-Seq analysis of large numbers of *IDH1*^{mut} and *IDH1*^{wt} glioma patient tumor samples. This is made difficult by the fact that the quantity of mRNA starting material required for such experiments is restrictively high, particularly in such valuable patient tissue samples. Direct RNA sequencing and algorithmic m6A peak calling using Nanopore technologies offers one potential workaround as they require lower amounts of mRNA inputs. The advent of new m6A analytical tools adapted for Nanopore platforms such as MINES (Lorenz et al., 2020) and nanoRMS (Begik et al., 2021) are promising developments for this approach. Other recently developed high throughput bioinformatic approaches such as MAZTER-Seq also obviate the need for m6A immunoprecipitation steps and increase the feasibility large scale epitranscriptomic profiling of glioma patient tumor samples. These approaches will also allow us to correlate G-RAMP findings in patients with any associated

survival data, a necessary step to conclude with confidence that the establishment of G-RAMP via FTO inhibition produces an anti-proliferative phenotype with real world clinical relevance.

Finally, we are directing future investigations to explore how m6A enrichment of ATF5 and other G-RAMP members effect interactions with reader proteins to gain insight into the mechanics of m6A-induced transcript degradation. One approach would entail performing large scale PAR-CLIP studies for each YTHDF paralog using both *IDH1*^{mut} and *IDH1*^{mut} mRNA inputs to characterize the readers associating with m6A-enriched target transcripts. Next-generation sequencing of these transcripts will allow us to subsequently identify specific hotspots interacting with each m6A reader protein. Another complementary approach to further dissect this pathway entails the application of recently developed CRISPR/Cas9-based tools permitting targeted epitranscriptomic editing (Liu et al., 2019b). These fascinating tools couple deactivated Cas9 (dCas9) either to a single chain m6A methyltransferase comprising a METTL3 and METTL14 composite to effect m6A deposition, or alternatively FTO or ALKBH5 to remove m6A modifications. These fusion proteins can be guided to specific m6A loci using a single strand guide RNA (sgRNA) designed to exhibit homology to RRACH motif-adjacent sequences. The design of sgRNAs allowing site-specific m6A deposition or removal would be guided by the results of PAR-CLIP studies highlighting mRNA sequence regions that serve as substrates for m6A-specific RBPs. Additional m6A target sites could be identified using miCLIP (m6A individual-nucleotide-resolution cross-linking and immunoprecipitation) sequencing-based approaches (Linder et al., 2015), as well as a novel site-specific m6A quantification method developed by Liu *et al*. coupling m6A antibody crosslinking with probe elongation (Zhou et al., 2018). Targeted epitranscriptomic editing using these combined approaches would equip us with a powerful tool to quantify the contributions of specific m6A loci in determining the stability of G-RAMP transcripts and provide critical insight into the precise mechanisms governing alterations in glioma cell functions.

In conclusion, our study assessed the effect of *IDH1*^{mut} and D-2-HG on m6A enrichment in glioma, identified a unique epitranscriptomic signature mediating a downstream mechanism governing apoptosis induction, and successfully harnessed this mechanism to reduce proliferative potential and improve survival in *IDH1*^{wt} glioma. To our knowledge, this is the first study to date investigating the impact of *IDH1*^{mut} and D-2-HG on epitranscriptomic dynamics and proliferative potential in glioma. We describe the significance of m6A epitranscriptomic profiles in *IDH1*^{mut} glioma and showed that inhibition of the m6A demethylase FTO provides a viable therapeutic target in *IDH1*^{wt} glioma. Our study also proposes a previously undescribed mechanism for reduced proliferative potential in *IDH1*^{mut} glioma based on the *IDH1*^{mut} → D-2-HG ⊣ FTO axis that enriches m6A content in ATF5 transcripts, thereby downregulating ATF5 expression and inducing apoptosis. We also define a novel epitranscriptomic biomarker (G-RAMP) in *IDH1*^{mut} glioma, which may contain a trove of additional molecular targets for therapeutic and mechanistic investigations. Finally, our work provides new evidence that attenuating malignant growth patterns in *IDH1*^{wt} glioma and effectuating the clinically favorable phenotypes seen in *IDH1*^{mut} gliomas is achievable through targeted epitranscriptomic modulation, opening a new realm of treatment strategies for one of the most lethal of all human cancers.

METHODS

Patient Tissue Sample Acquisition

Clinically annotated *IDH1*^{mut} (*n*=12) and *IDH1*^{wt} (*n*=13) fresh frozen patient glioma tumors were acquired through the UCLA Brain Tumor Translational Resource, and under approval of the UCLA Institutional Review Board. Histological quality control was performed on every sample to confirm ≥70% tumor tissue versus normal brain. *IDH1* status was determined via immunohistochemistry and/or Sanger sequencing.

TCGA Genetic Analyses

Gene expression data for 282 *IDH1*^{wt} and 30 *IDH1*^{mut} glioblastoma samples were downloaded from the TCGA data portal for analysis (https://portal.gdc.cancer.gov/projects/TCGA-GBM). Log2 Lowess normalized signals collapsed by gene symbol were utilized, with all data originally derived using an Agilent 244K Custom Gene Expression Array (*Agilent Technologies*, Catalog #G4502A-07, Santa Clara, CA, USA).

Gliomasphere Microarray Analyses

Total RNA was isolated from gliomasphere cultures and subjected to poly A^+ purification for mRNA. A NanoDrop ND-1000 spectrophotometer (*NanoDrop Technologies*, Wilmington, DE, USA) was used to determine concentration and quality of RNA samples, followed by confirmatory assays using an Agilent 2100 Bioanalyzer (*Agilent Technologies*, Santa Clara, CA, USA). Purified mRNA was then reverse transcribed, labeled, and prepared per the manufacturer's protocols prior to hybridization to an Affymetrix high-density oligonucleotide HG-U133A Plus 2.0 Human Array to analyze gene expression levels for 47,400 transcripts/variants, including 38,500 genes (*Affymetrix*, Santa Clara, CA, USA).

Cell Culture and Treatments

IDH1^{mut} and *IDH1*^{wt} expression was induced in previously established U87 and HEK293T cells using *IDH1*^{R132H}-pLPCX and *IDH1*^{wt}-pLPCX retroviral constructs, with blank-pLPCX transduced lines acting as vector controls (Lazovic et al., 2012; Li et al., 2013; Li et al., 2014). *IDH1*^{mut} and *IDH1*^{wt} expression was confirmed in all cell lines with immunoblotting. Immortalized human astrocytes (HAC) with stabilized expression of hTERT, E6, and E7 were provided by Dr. Russell Pieper (University of California, San Francisco) (Sonoda et al., 2001). *IDH1*^{MUT} (*n*=5) and *IDH1*^{WT} (*n*=7) patient-derived gliomaspheres were provided by Dr. Harley Kornblum (University of California, Los Angeles) (Laks et al., 2016; Garrett et al., 2018). U87, HEK293T, and HAC cell lines were maintained in DMEM cell culture medium supplemented with 10% fetal bovine serum and penicillin/streptomycin, cultured at 37 °C and 5% CO_2. Gliomaspheres were maintained in DMEM/F12 supplemented with B27, heparin, EGF, and bFGF (Laks et al., 2016). Octyl-D-2-HG and octyl-L-2-HG were purchased from *Cayman Chemical* (*Cayman Chemical,* Catalog #16374 & 21123, Ann Arbor, MI, USA). *IDH1*^{mut}-inhibitors C35 and AG881 were purchased from *Xcess Biosciences, Inc.* (*Xcess Biosciences, Inc.,* Catalog #M60068-2s, San Diego, CA, USA) and *Selleck Chemicals* (*Selleck Chemicals*, Catalog #S8611, Houston, TX, USA), respectively. FTO inhibitors FB23-2 and meclofenamic acid (MA) were obtained from *MedChemExpress* (*MedChemExpress*, Catalog #HY-127103, Monmouth Junction, NJ, USA) and *Cayman Chemicals* (*Cayman Chemicals*, Catalog #70550, Ann Arbor, MI, USA), respectively (Huang et al., 2019). All pharmaceutical treatment agents were dissolved in dimethyl sulfoxide (DMSO) (*MilliporeSigma*, Catalog #472301, Burlington, MA, USA), and cells were treated with indicated concentrations and time courses. Equimolar quantities of DMSO were used as treatment control conditions across all described experiments.

Total RNA and mRNA Isolation

Total RNA was purified from cellular samples using either AllPrep DNA/RNA Mini Kits or RNeasy Mini Kits (*Qiagen,* Catalog #80204 & 74104, Valencia, CA, USA). A PolyATract mRNA Isolation

Systems (*Promega*, Catalog #Z5300, Madison, WI, USA) kit was used to purify mRNA from total RNA samples.

m6A RNA Dot Blot

Total RNA and poly A^+ purified mRNA from samples were subjected to m6A dot blots using m6A-specific antibody purchased from *Synaptic Systems* (*Synaptic Systems*, Catalog #202003, Goettingen, Germany). Briefly, mRNA was isolated from total RNA using Dynabeads mRNA Purification Kits (*Thermo Fisher Scientific*, Catalog #61006, Waltham, MA, USA) per the manufacturer's instructions. At least 20.0 μg of total RNA was used for each sample. Purified mRNA was diluted to a concentration of 2.0 ng/μL, and then heated at 70 °C for 10 minutes to disrupt secondary RNA structures. 2.0 μL of mRNA was then added directly to Hybond-N+ membrane optimized for nucleic acid transfer, followed by 15 minutes of UV-light exposure to induce crosslinking. Membranes were washed in 10.0 mL of TBS with 0.05% Tween 20 (TBST) wash buffer for three 10-minute rounds. Membranes were then incubated in blocking buffer (TBST w/ 5% milk and 2.0% BSA) for 1 hour at room temperature, followed by incubation with anti-m6A antibody in a 1:2000 in 10.0 mL of fresh blocking buffer overnight at 4 °C. Three rounds of 10-minute TBST washes were then followed by incubation with donkey anti-rabbit IgG-HRP (1:5000 dilution) in 10.0 mL of blocking buffer for 1 hour at room temperature. After an additional three rounds of 10-minute TBST washes, membranes were incubated in 0.125 mL/cm^2 of ECL Western blotting substrate for 5 minutes (in darkness) at room temperature prior to film exposure and developing.

Quantification of m6A

Quantification of m6A in total RNA was achieved using EpiQuik m6A RNA Methylation Quantification Kits (Colorimetric) (*Epigentek*, Catalog #P900548, Farmingdale, NY, USA)

according to the manufacturer's directions. m6A content was calculated relative to synthetic positive (100% m6A) and negative (0% m6A) control oligonucleotides, provided in the EpiQuik kit. Briefly, a minimum of 200 ng of purified RNA was added to the provided strip-well plate frame, followed by incubation at 37 °C for 90 minutes. Capture antibodies for m6A were then added to the solution and incubated for 60 minutes at room temperature, followed by the addition of corresponding detection antibodies and 30 minutes of incubation at room temperature. After the addition of enhancer solution and several rounds of washing per the manufacturer's protocol, detection solution was added followed by 10 minutes of incubation at room temperature away from light. A stop solution was utilized to halt the enzymatic reaction and the 450 nm absorbance immediately read on a Wallac Victor2 microplate reader (*Perkin Elmer*, Waltham, MA, USA). Relative m6A content is proportional to measured OD intensities for each sample, and were calculated using the following formula: $m6A\% = \frac{(Sample\ OD - NC\ OD) \div S}{(PC\ OD - NC\ OD \div P} \text{ x } 100\%$ (where NC OD = 450nm absorbance for negative m6A control RNA, PC OD = 450 nm absorbance for positive m6A control RNA, S = ng of sample RNA, P = ng of PC RNA). Two-tailed Student's *t*-tests were used to compared means between groups, with statistical significance set at $p<0.05$.

Intracellular D-2-HG Quantification

Intracellular D-2-HG was quantified using enzymatic assays originally described by Balss, *et al.* 2012, and who we thank for generously providing key reagents that are also commercially available in the D-2-HG Assay Kit (*MilliporeSigma*, Catalog #MAK320, Burlington, MA, USA) (Balss et al., 2012). All experiments were performed in triplicate, unless otherwise specified. Briefly, cells were harvested and lysed prior to splitting each sample into two aliquots for D-2-HG quantification and total protein quantification using the Pierce BCA Protein Assay Kit (*Thermo Fisher Scientific*, Catalog #23225, Waltham, MA, USA), respectively. Deproteination of the D-2-HG quantification aliquot was achieved using 3.0 μL of Proteinase K (*Qiagen*, Catalog #19131,

Hildren, Germany) per 100.0 μL of cell lysis solution. 25.0 μL of lysate was then added to 75.0 μL of assay solution containing 0.1 μg of the enzyme D-2-HG dehydrogenase (HGDH), 100.0 μM NAD+, 5.0 μM resazurin, and 0.01 U/mL diaphorase in 100.0 mM HEPES (pH 8.0). In the presence of D-2-HG, HGDH converts D-2-HG to α-ketoglutarate (α-KG) in a NAD+ dependent manner. The reduction of NAD+ to NADH enables the conversion of resazurin to fluorescent resorufin, which was then quantified via fluorometric detection (λ_{ex} = 540 nm, λ_{em} = 590 nm) on a Wallace Victor2 1420 Miltilabel HTS Counter (*PerkinElmer*, Waltham, MA, USA). D-2-HG quantification (pmole/μg protein) of a given sample was based on a standard curve of known D-2-HG concentrations. Two-tailed Student's *t*-tests were used to compared means between groups, with statistical significance set at $p<0.05$.

$IDH1^{mut}$ and $IDH1^{wt}$ Forced Expression

Lentiviruses were produced using pUltra-$IDH1^{mut}$-EGFP, pUltra-$IDH1^{wt}$-EGFP or blank pUltra-EGFP plasmids (*Addgene*, Catalog #24129, Watertown, MA, USA) packaged with pMD2.G VSV-G envelope plasmid (*Addgene*, Catalog #12259, Watertown, MA, USA) and pCMVR8.74 packaging plasmid (*Addgene*, Catalog #22036, Watertown, MA, USA) in HEK293T cells cultured in regular DMEM. Plasmids were transfected into HEK293T using X-tremeGENE HP DNA Transfection Reagent (*MilliporeSigma*, Catalog #XTGHP-RO, Burlington, MA, USA). HEK293T cells were allowed to incubate for 48 hours, at which time the lentivirus-containing media was harvested, aliquoted, and stored at -80 °C. Target glioma cells were disassociated to the single cell level and seeded in gliomasphere-compatible media (absent penicillin/streptomycin). Cells were transduced with lentivirus-containing media and regular culture media in a 1:5 ratio. 1.0 μg/mL of polybrene was added to facilitate transduction efficiency. Cells remained in lentivirus-containing media for no more than 48 hours, at which point media was replaced with standard

culture media. After 12-15 days, all cells exhibited 100% GFP positivity indicating successful transduction. Sequencing and western blot analyses provided orthogonal confirmation.

Immunoblotting

Cells or tissues were lysed in 1x Pierce RIPA lysis buffer (*Thermo Fisher Scientific,* Catalog #89900, Waltham, MA, USA) with proteinase inhibitor in a 1:100 dilution (*Thermo Fisher Scientific,* Catalog #EO0491, Waltham, MA, USA). Purified protein content from the lysates was measured using the Pierce BCA Protein Assay Kit (*Thermo Fisher Scientific,* Catalog #23225, Waltham, MA, USA). Protein was denatured at 100 °C for 10 minutes with Laemmli Sample Buffer. Equal concentrations of protein were then electrophoretically fractionated in 4–15% precast polyacrylamide gels (8.6 x 6.7 cm, for use with Mini-PROTEAN Electrophoresis Cells) (*Bio-Rad Laboratories*, Catalog #4568084, Hercules, CA, USA) and transferred to nitrocellulose membranes. The membranes were then subjected to immunoblot assays following a similar protocol as described above for m6A dot blots. One alteration was that blocking buffer was performed in TBST with 5% dry milk. Specific primary antibodies include rabbit anti-IDH1^{mut} (1:1000) (*Dianova*, Catalog #DIA-H09, Hamburg, Germany), polyclonal rabbit anti-FTO (1:5000) (*Novus Biologicals*, Catalog #NB110-60935, Centennial, CO, USA), rabbit anti-ALKBH5 (1:2000) (*Novus Biologicals*, Catalog #NBP1-82188, Centennial, CO, USA) and mouse anti-α-tubulin (1:2000) (*MilliporeSigma*, Catalog #T6199, Burlington, MA, USA). Secondary antibodies used include goat anti-rabbit IgG-HRP (1:5000) (*Abcam*, Catalog #ab6721, Waltham, MA, USA) and goat anti-mouse IgG-HRP (1:5000) (*Thermo Fisher Scientific,* Catalog #62-6520, Waltham, MA, USA).

FTO and ALKBH5 Knockdown

Plasmids for pLenti-FTO-shRNA-GFP (5'-TTTCTCACACTGCACAAGCATGGCTGCTT-3'), pLenti-ALKBH5-shRNA-GFP (5'-CGTGTCCGTGTCCTTCTTTAGCGACTCTG-3') or pLenti-

NSC-shRNA-GFP (5'-AACAGGCACACGTCCCAGCGT-3') were constructed on a pLenti-U6-shRNA-GFP-Puro vector backbone (*GenTarget, Inc.*, Catalog #SH-U6-GP, San Diego, CA, USA). Lentiviruses containing these constructs were packaged with pMD2.G VSV-G envelope plasmids (*Addgene*, Catalog #12259, Watertown, MA, USA) and pCMVR8.74 packaging plasmids (*Addgene*, Catalog #22036, Watertown, MA, USA) in HEK293T cells cultured in regular DMEM. An FTO^{mut} isoform containing point mutations (H231A; D233A) that disrupt enzymatic activity (pMIRNA1-Flag-FTOmut) and FTO^{wt} (pMIRNA1-Flag-FTOwt) expression vectors were also produced in this manner (Jia et al., 2011). Plasmids were transfected into HEK293T using X-tremeGENE HP DNA Transfection Reagent (*MilliporeSigma*, Catalog #XTGHP-RO, Burlington, MA, USA). HEK293T cells were allowed to incubate for 48 hours, at which time the virus-containing media was harvested, aliquoted, and stored at -80 °C. U87 cells were seeded at 50% confluency in 6-well plates and allowed to recover overnight. Lentivirus-containing media was prepared in a 1:10 dilution with regular culture media (without penicillin/streptomycin). 1.0 μg/mL of polybrene was also added. After three days of viral incubation, puromycin selection (0.8 μg/mL) was performed for 7 days. In gliomaspheres, spheres were disassociated to the single-cell level using TrypLE Express Enzyme (1X, with phenol red) (*Thermo Fisher Scientific*, Catalog #12605036, Waltham, MA, USA) and gentle pipetting. Disassociated cells were seeded in regular gliomasphere culture media (without penicillin/streptomycin). Lentivirus-containing media was added to the cultures in a 1:5 ratio with regular gliomasphere culture media and 1.0 μg/mL of polybrene. After 3 days of incubation, 1.0 μg/mL of puromycin was applied for 7 days to select for successfully transduced cells. GFP imaging was used to validate transduction efficiency, and western blot analyses were used to confirm successful target knockdown.

Cell Proliferation Quantification

For adherent cell lines (U87, HAC, HEK293T), MTT assays were employed to test cell proliferation rates as previously described (Franken et al., 2006; Hermisson et al., 2006; Remington et al., 2009). Briefly, a uniform number of cells were cultured in 24-well plates under specified times and treatment durations, and then exposed to pre-mixed 3-(4,5-dimethylthiazol-2-yl)-2,5-diphenyltetrazolium bromide (MTT) solution (0.5 mg/mL in regular culture media). Cells were incubated at 37 °C for 1 hour. The MTT solution was then removed, and the MTT-reduced formazan product was extracted from the cells following lysing with 300 mL of DMSO. Formazan concentrations were measured at 560 nm absorbance using a Wallac Victor2 microplate reader (*Perkin Elmer*, Waltham, MA, USA) with a background subtraction of 660 nm absorbance. Three independent experiments were performed for each experimental condition. Data were analyzed in Prism 9 and results presented as a 'mean±SEM.' For gliomaspheres, sphere volumes measured at predetermined timepoints were used to determine cell growth rates. Briefly, live images of gliomaspheres in culture were taken using a Leica DMi8-440 inverted fluorescent microscope (*Leica Microsystems*, Wetzlar, Germany). Sphere volumes in live images were then calculated using Image J. A minimum of 100 spheres were imaged for each experimental condition, and volumes were averaged and analyzed in Prism 9 with results presented as a 'mean±SEM' with a unit of mm^3. Unless otherwise stated, two-tailed Student's *t*-tests were used to compared means between groups, with statistical significance set at $p<0.05$.

MeRIP-Seq Differential Expression and m6A Methylation Analyses

A minimum of 400 μg of total RNA from patient tumor, gliomasphere, or glioma cell culture was subjected to poly A^+ purification to isolate ≥10 μg of mRNA using the Dynabeads mRNA Purification Kit (*Thermo Fisher Scientific*, Catalog #61006, Waltham, MA, USA). Transcripts were fragmented into ~100nt segments as described by Molinie *et. al.*, 2017 (Molinie et al., 2017). Dynabeads were coupled to m6A-specific antibodies (*Synaptic Systems*, Catalog #202003,

Goettingen, Germany) using the Dynabeads Antibody Coupling Kit (*Thermo Fisher Scientific*, Catalog #14311D, Waltham, MA, USA). Washing, elution, extraction, and cleanup of m6A-enriched mRNA was performed per the manufacturer's protocols, described in further detail in the abovementioned publication (Molinie et al., 2017). TruSeq Stranded mRNA Library Preparation Kits (*Illumina*, Catalog #20020594, San Diego, CA, USA) were used for all sequencing library preparations, with unique adapter indices ligated to each sample to allow for multiplexing (TruSeq RNA Single Indices Set A, *Illumina*, Catalog #20020492, San Diego, CA, USA). Library quantification and quality control was performed using KAPA Library Quantification Kits (*Roche*, Catalog #KK4828, Basel, Switzerland). For each sample, we performed high throughput sequencing on a m6A-immunoprecipitated fraction (MeRIP-Seq) as well as a mRNA-only fraction (RNA-Seq). Sequencing was conducted at the UCLA Neuroscience Genomics Core on *Illumina* Hi-Seq4000 system. Each sample underwent 75nt paired-end sequencing, giving a read depth of ≥30 million per multiplexed sample.

To perform an unbiased screen of m6A-enriched transcripts across our samples, we performed MeRIP-Seq analysis using three independently validated m6A peak calling and differential methylation analysis tools: ExomePeak, MACS2, and RADAR (Meng et al., 2014; Zhang et al., 2008; Zhang et al., 2019). We also performed RNA-Seq differential expression analysis on total mRNA fractions from the same samples using DESeq2 (Love et al., 2014). Differential expression modules required extensive use of packages from the Bioconductor and R CRAN databases, the most important of which include *samtools* version 0.1.19 for filtering BAM/SAM files, *sam2tsv* for file conversion, *minimap2* version 2.14-r886 for readalignment, *GenomicFeatures* version 1.44.0 and *GenomicRanges* version 1.34 for genomic range intersection, and *minfi* version 1.28.4 and *limma* version 3.48.0 for microarray model evaluation. Extended analyses required extensive use of the *tidyverse* version 1.2.1 environment for manual charting and plotting. For our MeRIP-Seq analyses, adapter sequences were first trimmed using the FASTX Toolkit (Hannon, G.J.,

2010). SortMeRNA software was then used to filter for mRNA transcripts (Kopylova et al., 2012). Transcript reads were mapped to the Gencode GRCh38.p13 primary assembly with STAR using transcriptome mode (Dobin et al., 2013). GTF annotation files were obtained through the Gencode website (https://www.gencodegenes.org/human/). Uniquely mapped reads were then entered into RSEM to collate read coverage for each transcript, and a transcripts per million normalization parameter was calculated to permit differential expression comparisons (Li and Dewey, 2011). Genes with significant differential expression were identified using EBseq software employing an empirical Bayesian hierarchical model (Leng et al., 2013). Mapped reads were visualized in Integrated Genome Viewer 2.9.4. To generate a set of differentially expressed and differentially methylated transcripts, we then subjected our m6A-immunoprecipitated mRNA and total mRNA fractions to algorithmic m6A peak calling, annotation, and *IDH1*^{mut} versus *IDH1*^{wt} differential expression comparisons using ExomePeak version 1.8.0, MACS2 version 2.2.7.1, and RADAR version 0.2.4, executed through R (Meng et al., 2014; Zhang et al., 2008; Zhang et al., 2019). The regions identified by these three models were then intersected on a strict basis. Only regions upon which all three models agree were determined to be significantly differentially methylated, and these sites were further matched up with gene-level RNA-seq results for further validation, obtained using DESeq2 version 1.32.0. Rtracklayer version 1.28.10 was used to coordinate visualizations between R and the Integrated Genome Browser. Detailed code and notation for the running of these models and the execution of our differential expression and methylation analysis as well as figure generation are included in Supplemental Materials (Supplementary m6A Bioinformatics 1-SMarkdown). Gene Set Enrichment Analysis (GSEA) was performed on MeRIP-Seq and RNA-Seq data outputs to extract biomolecular pathway enrichment information for *IDH1*^{mut} and *IDH1*^{wt} glioma samples.

Oxford Nanopore Technologies (ONT) Direct RNA Library Preparation and MinION Sequencing

Libraries were prepared for MinION direct RNA sequencing using the Direct RNA Sequencing Kit (*Oxford Nanopore Technologies*, Catalog #SQK-RNA002, Oxford, UK) per the manufacturer's protocol version DRS_9080_v2_revK_14Aug2019. Briefly, 500ng of poly A^+ purified mRNA was adapter ligated using ONT RT Adapter and T4 DNA Ligase (*New England Biolabs*, Catalog #M202T, Ipswich, MA, USA). Reverse transcription was performed on adapter ligated mRNA using SuperScript III Reverse Transcriptase (*Thermo Fisher Scientific*, Catalog #18080044, Waltham, MA, USA) and purified with RNAClean XP magnetic beads (*Beckman Coulter*, Catalog #A63987, Brea, CA, USA) washed in freshly prepared 70% ethanol. The RNA:cDNA product was next ligated to ONT RNA Adapters and purified using RNAClean XP beads washed twice in Wash Buffer provided by ONT. The product was eluted in ONT Elution Buffer and mixed with ONT Running Buffer in preparation for flow cell loading. Samples were then loaded onto primed R9 ONT flow cells (*Oxford Nanopore Technologies*, Catalog #FLO-MIN106D, Oxford, UK). The flow cell was then inserted into a MinION MK1B platform (*Oxford Nanopore Technologies*, Catalog #MIN-101B, Oxford, UK) and sequenced with MinION acquisition software version: 21.02.1. Samples were run for 24 hours at -180 mV.

Oxford Nanopore Technologies EpiNano Base Calling, Filtering, and m6A Modification Mapping

Detailed code and notation for the ONT EpiNano m6A analysis pipeline is included in Supplemental Materials (Supplementary m6A Bioinformatics 1-SMarkdown). The processes utilized for m6A base-calling, filtering, mapping and feature extraction are identical to the protocol described by Liu *et al*., 2019 unless otherwise stated (Liu et al., 2019a). All packages are also available for download as part of EpiNano (github.com/enovoa/EpiNano). EpiNano version 1.2.0 was used for this study. The workflow for EpiNano relies mostly on a *Nextflow* version 20.04.1 pipeline called *MasterOfPores*, which is built upon *docker* version 19.03 and *singularity* version 3.2.1. Further refinement of the raw signal from the ONT MinION MK1B platform was performed using *nanopolish* version 0.12.4. Briefly, reads were locally base-called using Guppy 3.1.5.

Reads were then filtered using NanoFilt with the settings “-q 0 -headcrop 5 -tailcrop 3”. Minimap2 was employed using the settings “-ax map-ont”. The mapped reads were next converted to mpileup format with Samtools version 1.4. Feature extraction (mean per-base quality, mismatch frequency, insertion frequency, and deletion frequency) in BAM alignment files were then converted to tab delimited formats using sam2tsv. Current intensity information for individual reads in the fast5 files was extracted using h5py version 2.7.0 in Python. Sequences were slid with a window of 5 bp, and a mean and standard deviation of current intensities was calculated for each 5 bp sliding window. We relied on the same machine learning training datasets used to identify 5-mer windows containing m6A modifications (RRACH consensus sequences) described by Liu *et al*., 2019 and available on GitHub (github.com/enovoa/EpiNano) (Liu et al., 2019a). All the above-mentioned processes were performed on a remote server running Ubuntu 18.04 Bionic Beaver with a 16-core 2.3GHz Intel Xeon processer, 128GB of RAM, and a NVIDIA Quadro K5200 GPU with 8GB of video RAM. Calculations were done in R version 3.5.1, Python version 3.7.7, and RStudio version 1.4.11. Documentation of data analysis pipelines was compiled in RMarkdown version 2.8 (Supplementary m6A Bioinformatics 1-Markdown).

Gene-Specific m6A RT-qPCR

Gene-specific m6A RT-qPCR was performed by coupling m6A-immunoprecipitation and RT-PCR techniques. GLuc m6A-positive control mRNA and CLuc m6A-negative control mRNA were spiked into 10 μg of total RNA from samples. Immunoprecipitation of m6A-RNA was performed as descripted in the MeRIP-Seq protocol, but without any RNA fragmentation steps. The pulled down m6A-RNA was subjected to first-strand cDNA synthesis using a SuperScript II Reverse Transcriptase Kit with oligo-dT primers (*Thermo Fisher Scientific*, Catalog# 18064014, Waltham, MA, USA). Briefly, 1 μL of Oligo(dT) was combined with 1 μL of 10mM dNTP mix, 10 μL of m6A-immunoprecipitated RNA and sterile nuclease-free water for a final volume of 12 μL. The mixture

was heated to 65 °C for 5 minutes and chilled on ice. 4 μL of 5X First-Strand Buffer, 2 μL of 0.1 M DTT, and 1 μL of RNaseOUT was then added to the mixture. The contents were mixed and then incubated at 25 °C for 2 minutes. 1 μL of SuperScript II RT was then added to the mixture to establish a final volume of 20 μL. The mixture was incubated at 25 °C for 10 minutes and then 42 °C for 50 minutes. The RT reaction was inactivated at 70 °C for 15 minutes. Next, 2 μL of the RT product was added to a PCR reaction mixture of 5 μL of 10X PCR Buffer (200 mM Tris-HCL (pH 8.4), 500 mM KCl), 1.5 μL of 50 mM $MgCl_2$, 1 μL of 10 mM dNTP mix, 1 μL of forward primer (10 μM), 1 μL of reverse primer (10 μM), 0.4 μL of Taq DNA polymerase, and sterile nuclease-free water for a final volume of 50 μL. The mixture was then added in triplicate to a 96-well plate, and a denaturing step was performed by heating the mixture to 94 °C for 2 minutes. Real-time quantitative PCR data collection and analysis were performed on a CFX Connect Real-Time PCR Detection System (*Bio-Rad Laboratories*, Hercules, CA, USA).

Primers utilized in these experiments include the following:

Gene	**Forward Primer**	**Reverse Primer**
ACTB	5'- CCAGAGGCGTACAGGGATAG-3'	5'-CCAACCGCGAGAAGATGA-3'
ATF5	5'-GCTCAGAGGGAAGAGTGTCG-3'	5'-CAAGGCGAAAGTGGAAGACT-3'

Apoptotic Activity Measurements

For quantification of changes in apoptotic activity in octyl-D-2-HG, FB23-2, and MA treated cells, the Caspase-Glo 3/7 Assay Kit (*Promega*, Catalog #G8090, Madison, WI, USA) was used. The assay is a homogenous luminescent assay that captures Caspase 3 and Caspase 7 activities. This is achieved with a luminogenic substrate containing the tetrapeptide sequence DEVD. The substrate is cleaved by caspases, thus generating a luminescent luciferase signal proportional to the amount of caspase activity present in the samples. The manufacturer's protocol was followed

in the execution of all experiments. Briefly, cells were cultured in white-walled 96-well plates and treated with the specified compounds in triplicate. 100 μL of Caspase-Glo 3/7 Reagent was added to each well. Plates were placed on a shaker at 300 rpm for 30 seconds and incubated at room temperature for 3 hours. Luminescence for each sample was then measured on a Wallac Victor2 microplate reader (*Perkin Elmer*, Waltham, MA, USA).

For visualization of fluorescently labeled apoptosis activity in octyl-D-2-HG, FB23-2, and MA treated cells, the Apoptosis/Necrosis Assay Kit (*Abcam*, Catalog #ab176749, Waltham, MA, USA) was used, following the manufacturer's protocol. Briefly, cell lines were cultured in regular media in 24-well plates and treated with the specified compounds in triplicate. After three days, the plated cells were washed twice with 100 μL of provided Assay Buffer and resuspended in 200 μL of Assay Buffer with 2 μL of Apopxin Green Indicator (100X stock), 1 μL of 7-AAD Necrosis Indicator (200X stock), and 1 μL of CytoCalcein 450 Indicator (200X stock). Cells were incubated at room temperature for 60 minutes, followed by two 100 μL Assay Buffer washes. Cells were then imaged under a fluorescent microscope. Apoptotic cells were visualized using the FITC channel (Ex/Em = 490/525 nm). Necrotic cells were visualized using the Texas Red channel (Ex/Em = 550/650 nm). Healthy cells were visualized with a violet channel (Ex/Em = 405/450 nm).

Animal Procedures

Female NOD SCID gamma (NSG) mice (8-10 weeks old) were used for all experiments requiring intracranial xenografting of patient-derived glioma stem cell lines. Cell lines cultured in regular gliomasphere culture media were spun down at 300 g for 4 minutes and then disassociated using TrypLE Express Enzyme (1X, with phenol red) (*Thermo Fisher Scientific*, Catalog #12605036, Waltham, MA, USA) and gentle pipetting. Cell concentration calculations were performed on fractions resuspended to the single cell level, with a final concentration of 300,000 cells / 2 μL

media prepared for each mouse and held on ice to await intracranial injection. NSG mice were placed into an isoflurane anesthesia induction chamber, and then affixed on a steady isoflurane flow via a nose cone coupled to a stereotactic stage. The incision area was shaved and sterilized with three rounds of betadine and ethanol scrubs. A 2 cm diagonal scalp incision was then made from the near the left eye posterior to the right rostrum. A stereotactic needle mount was then moved into position directly over the skull plate fusion landmark bregma where it was zeroed. The needle was then moved 1 mm anterior and 2 mm lateral (to the right) over the right basal ganglion injection site. A fine bit drill was then used to create a burr hole. The needle was then loaded with 300,000 gliomasphere cells suspended in a final injection volume of 2 μL. The stereotactic needle driver was zeroed upon the bevel reaching the surface of the brain within the burr hole. The needle was then lowered into the skull at a rate of 0.1 mm / 5 seconds until a depth of 2.5 mm was achieved. After 30 seconds, the needle was then raised at a rate of 0.1 mm / 5 seconds until reaching a final depth of 2.0 mm, thereby leaving behind a small cavity for tumor cell injection. The 2 μL tumor cell suspension was injected into the brain at a rate of 0.1 μL / 10 seconds. When finished, the needle was allowed to sit in the brain for 30 seconds before being drawn up at a rate of 0.1 mm / 10 seconds. The burr hole was then plugged with bone wax before closing the scalp incision with a tissue adhesive. Xenografted mice were then removed from the stereotactic head mount and isoflurane nose cone and transferred to a clean cage over a heating pad for individual monitoring until awake. Xenografted mice were allowed to recover for three days before being randomized into either FB23-2 or DMSO treatment groups. FB23-2 (*MedChemExpress*, Catalog #HY-127103, Monmouth Junction, NJ, USA) was dissolved in DMSO for a final stock concentration of 50mM and was delivered via intraperitoneal (i.p.) injection (20 mg/kg) daily. Injection volumes were calculated each day based on individual mouse weights. DMSO control treatments were delivered in a similar fashion, with i.p. injection volumes scaling with animal weights. Mice were checked on a daily basis and euthanized by CO_2 inhalation upon the display

of symptoms indicative of excessive glioma tumor burden, including but not limited to, recurrent seizures, paralysis, hunched posture, decreased grooming and/or eating activity, and labored breathing. All treatment deliveries and censorship events were verified by two independent handlers. Overall survival (days) was calculated for each mouse at the time of censorship.

Gaussia Luciferase Tumor Burden Estimation

Within the confinement of a laminar flow hood, mice were individually restrained and prepped with antiseptic isopropyl wipes for tail vein bleeding. The lateral tail vein was then lanced with a single-use steel lancet and 6.6 uL of venous blood were collected using a freshly tipped p10 pipet. Blood samples were promptly mixed with 2 uL of 50 mM EDTA to prevent coagulation and temporarily stored in PCR strips and on ice, but not for more than 2 hours. Once all experimental and negative-control blood samples had been collected, an opaque 96-well plate was prepared. To each well, 8 uL of 5 mM NaCl in 1x PBS and 2 uL of blood were added, followed by homogenization. Blood samples were plated in triplicates, to allow for averaging of sample values. Separately, fresh substrate Coelenterazine (CTZ) was prepared and allowed to incubate in the dark at room temperature for 30 minutes. Substrate CTZ (100 uM CTZ) is a 1:100 dilution of 10 mM stock CTZ in salted PBS (5 mM NaCl). Enough substrate CTZ was produced to allow 100 uL to be added to each well containing sample in addition to 1.5 mL of substrate CTZ used for priming the luminometer injector. 10 mM CTZ aliquots were produced by adding 1.179 mL of acidified ethanol to 5 mg of stock CTZ. Acidified ethanol was produced by adding 2 drops of 1 M HCL to 10 mL of molecular grade ethanol. Stock CTZ was stored at -80 °C and away from light for long term storage. *Gaussia* luciferase readings were performed on a CLARIOstar luminometer and analyzed using MARS Data Analysis Software packages (*BMG LABTECH*, Cary, NC, USA). Before each use of the luminometer, the injector was rinsed twice with 70% ethanol and then primed with fresh substrate CTZ. Next, the luminometer was programmed to read luminescence following a flash kinetics model wherein readings are integrated over a 1 second interval. The 96-

well plate containing samples was then loaded into the luminometer for program execution. Raw luminometer readings were multiplied by a coefficient of 5 to account for the 1:5 dilution of 2 uL of blood in 8 uL of salted PBS. *Gaussia* luciferase reporter assay readings were taken weekly for each mouse.

Survival Analysis

Overall survival data was collated in Prism 9. Comparisons of survival curves between groups was accomplished using log-rank (Mantel-Cox) tests and Gehan-Breslow-Wilcoxon tests, allowing for the calculation of *P* and Chi square values. 1 degree of freedom (df) was used in all survival analyses, and the threshold for significance was set at $P < 0.05$. Median survival times, log-rank Hazard Ratios, and 95% CI intervals were also calculated. Kaplan-Meier survival curves were generated using Prism 9.

FIGURES

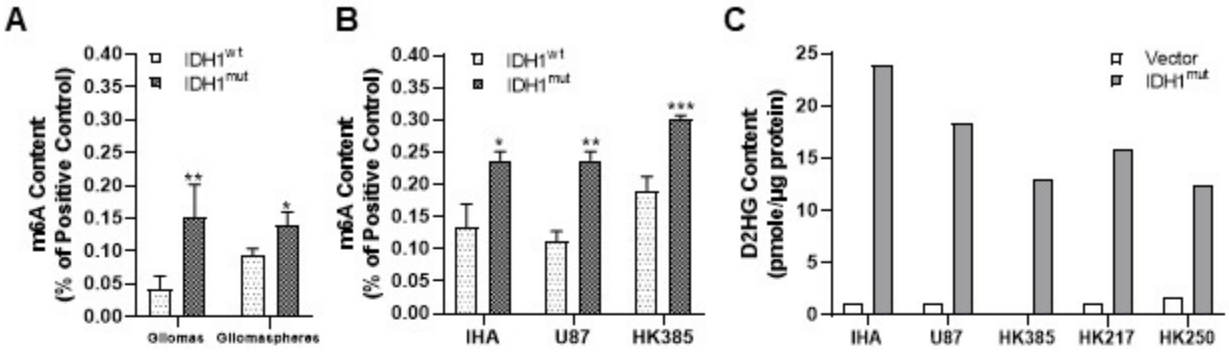

Figure 1-1. *IDH1^{mut}* patient gliomas and gliomaspheres exhibit increased D-2-HG content and m6A enrichment. A) Quantification of m6A content in total RNA isolated from patient tumor samples and patient-derived gliomaspheres using EpiQuik, normalized to GLuc positive controls. B) Quantification of m6A content in RNA isolated from empty vector control IHA, U87, and HK385 gliomas and *IDH1^{mut}* forced expression lines. C) Intracellular D-2-HG content in *IDH1^{mut}* versus native *IDH1^{wt}* empty vector control glioma cell lines and gliomaspheres. All experiments were conducted in triplicate. Results are presented as Mean ± S.E.M. Pairwise Student's t-tests: **P* < 0.05, ***P* < 0.01, ****P* < 0.005.

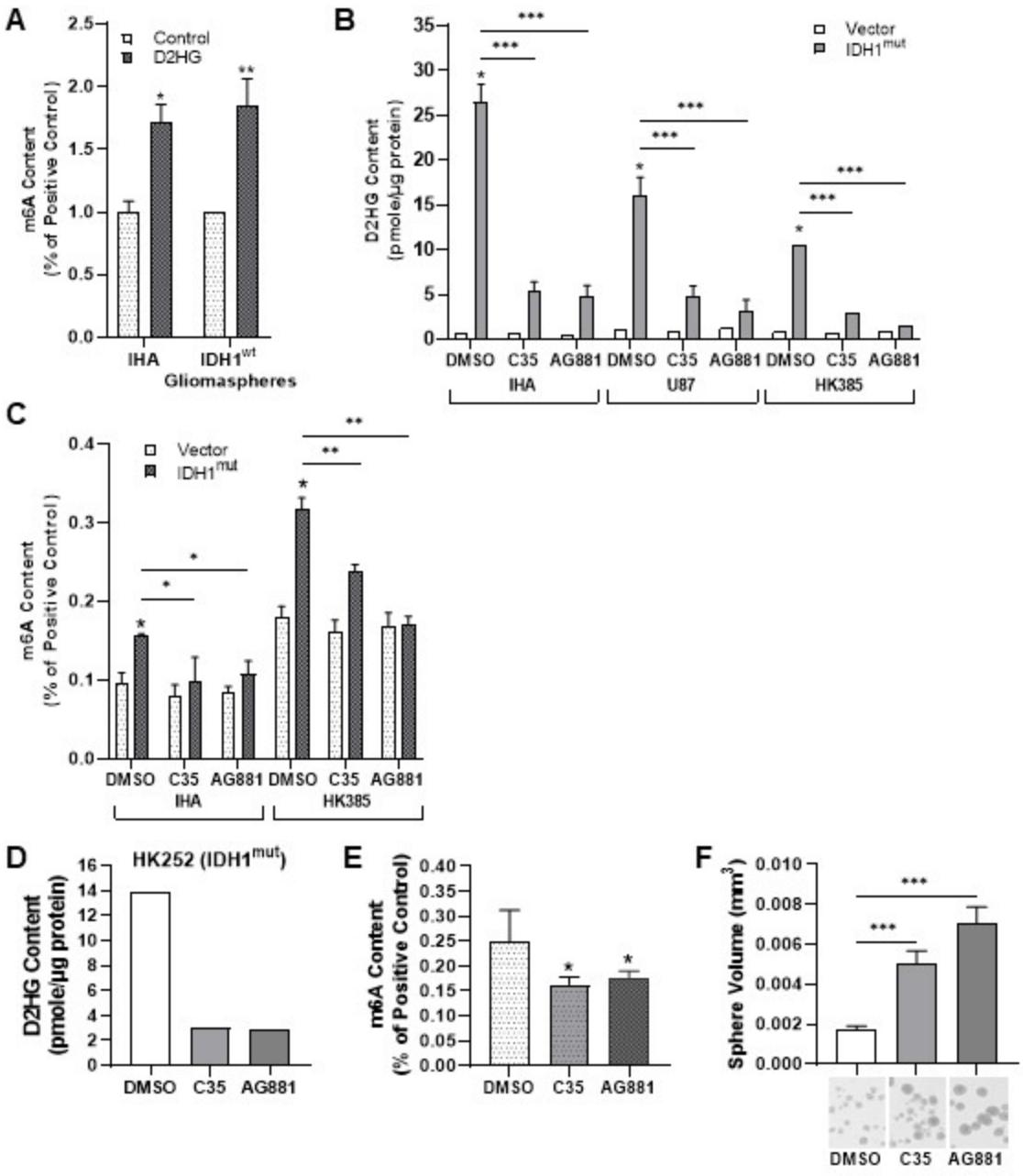

Figure 1-2. D-2-HG is sufficient to increase m6A abundance in *IDH1*^{wt} glioma and necessary to induce m6A enrichment in *IDH1*^{mut} glioma. A) EpiQuik m6A quantification of D-2-HG-treated glioma and gliomasphere lines. B) D-2-HG content in *IDH1*^{mut} and *IDH1*^{wt} glioma cell lines and gliomaspheres treated with *IDH1*^{mut} inhibitors C35 and AG881 versus DMSO control treatment. C) EpiQuik m6A quantification of *IDH1*^{mut} and *IDH1*^{wt} glioma cell lines and gliomaspheres treated with *IDH1*^{mut} inhibitors C35 and AG881 versus DMSO control treatment. D) D-2-HG content in HK252

native *IDH1*^{mut} gliomaspheres treated with C35 or AG881 versus DMSO. E) Quantification of m6A in HK252 native *IDH1*^{mut} gliomaspheres treated with C35 or AG881 versus DMSO. F) Sphere volumes measuring proliferation potential and representative images of HK252 native *IDH1*^{mut} gliomaspheres treated with C35 or AG881 versus DMSO. All experiments were conducted in triplicate. Results are presented as Mean ± S.E.M. Pairwise Student's t-tests: $*P < 0.05$, $**P < 0.01$, $***P < 0.005$.

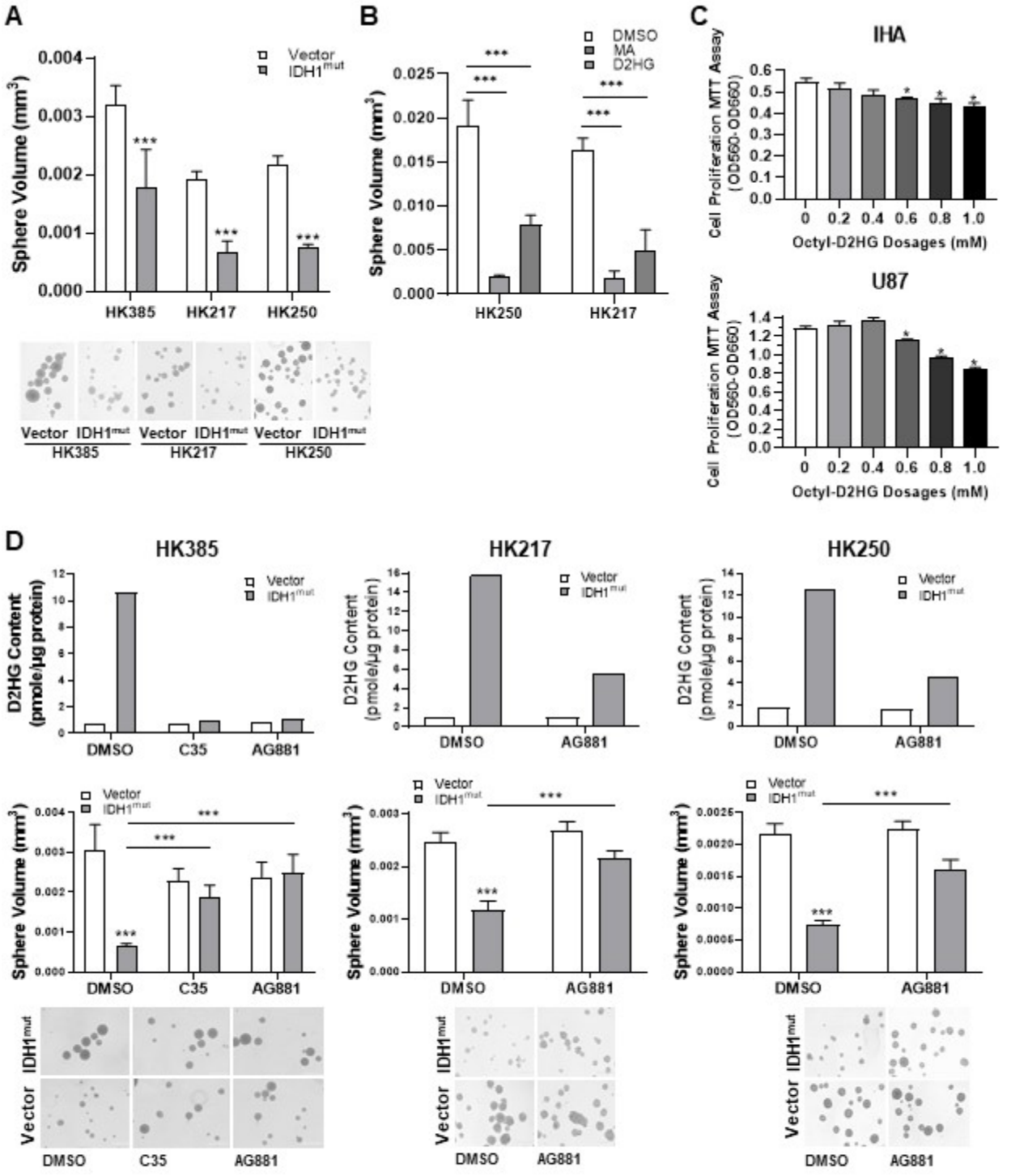

Figure 1-3. D-2-HG attenuates glioma cell growth in *IDH1*^{mut} and *IDH1*^{wt} glioma. A) Sphere volumes measuring proliferation potential and representative images in native *IDH1*^{wt} gliomaspheres (HK385, HK217, HK250) and identical cell lines undergoing *IDH1*^{mut} forced

expression. B) Sphere volumes in native *IDH1*^{wt} gliomaspheres (HK250, HK217) treated with D-2-HG, MA, or DMSO control. C) MTT cell proliferation assays in IHA and U87 glioma cells quantifying cell proliferation following different D-2-HG dosing concentrations. D) D-2-HG content and corresponding sphere volumes measuring proliferation in native *IDH1*^{wt} gliomaspheres (HK385, HK217, HK250) transduced with either empty vector control or *IDH1*^{mut}, and undergoing treatment with C35, AG881, or DMSO control. All experiments were conducted in triplicate. Results are presented as Mean ± S.E.M. Pairwise Student's t-tests: **P* < 0.05, ***P* < 0.01, ****P* < 0.005.

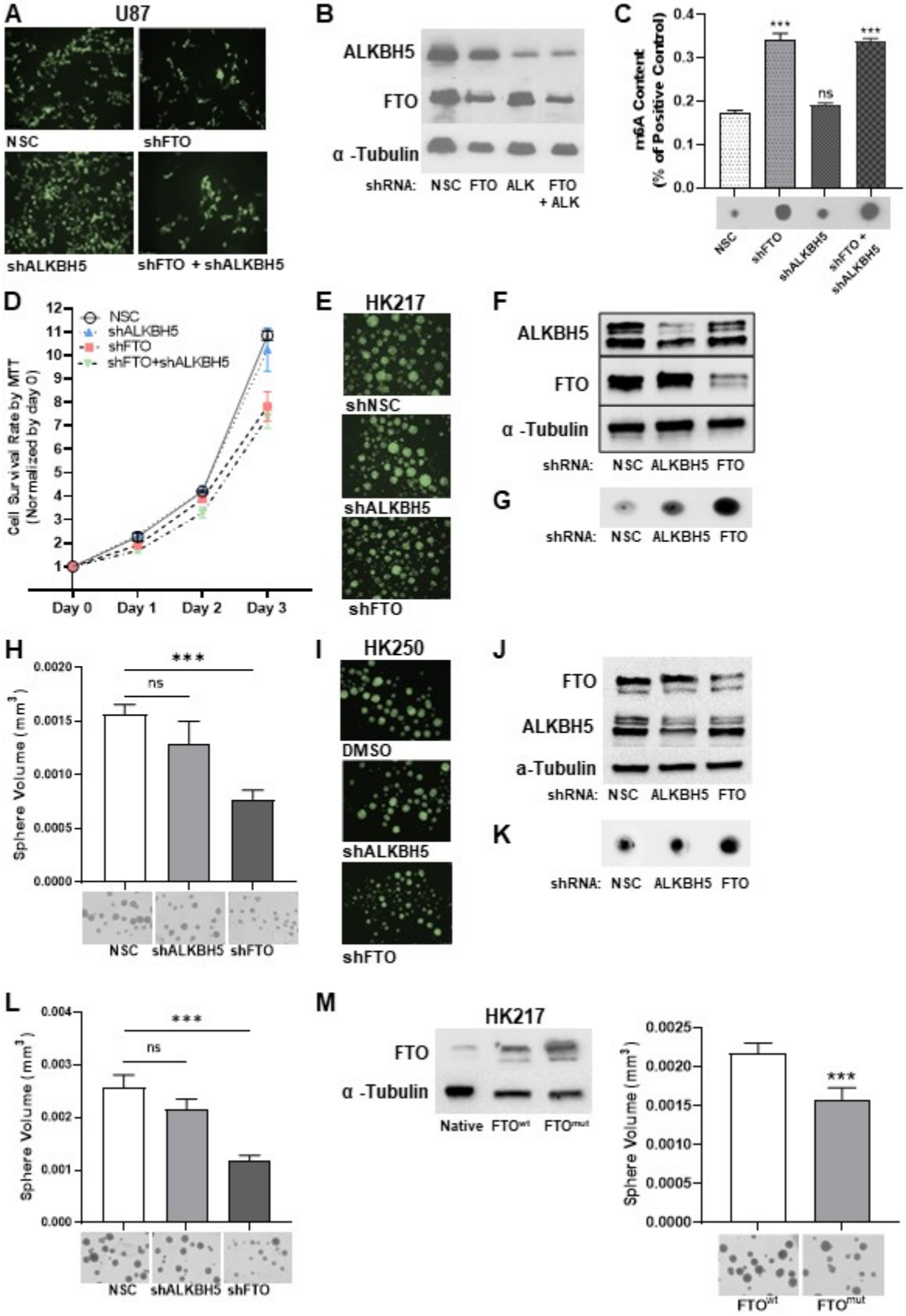
A
U87
NSC
shFTO
shALKBH5
shFTO + shALKBH5
B
ALKBH5
FTO
α -Tubulin
shRNA: NSC FTO ALK FTO + ALK
C
m6A Content (% of Positive Control)
0.4
0.3
0.2
0.1
0.0
***
ns
***
NSC
shFTO
shALKBH5
shFTO + shALKBH5
D
NSC
shALKBH5
shFTO
shFTO+shALKBH5
Cell Survival Rate by MTT (Normalized by day 0)
12
11
10
9
8
7
6
5
4
3
2
1
Day 0
Day 1
Day 2
Day 3
E
HK217
shNSC
shALKBH5
shFTO
F
ALKBH5
FTO
α -Tubulin
shRNA: NSC ALKBH5 FTO
G
shRNA: NSC ALKBH5 FTO
H
Sphere Volume (mm3)
0.0020
0.0015
0.0010
0.0005
0.0000
***
ns
NSC
shALKBH5
shFTO
I
HK250
DMSO
shALKBH5
shFTO
J
FTO
ALKBH5
a-Tubulin
shRNA: NSC ALKBH5 FTO
K
shRNA: NSC ALKBH5 FTO
L
Sphere Volume (mm3)
0.004
0.003
0.002
0.001
0.000
***
ns
NSC
shALKBH5
shFTO
M
HK217
FTO
α -Tubulin
Native
FTOwt
FTOmut
Sphere Volume (mm3)
0.0025
0.0020
0.0015
0.0010
0.0005
0.0000
***
FTOwt
FTOmut

Figure 1-4. Knockdown of *FTO* drives m6A enrichment and reduces proliferative potential in glioma. A) Representative fluorescent images of U87 glioma cells expressing shRNA targeting *FTO*, *ALKBH5*, or *FTO*+*ALKBH5* compared to a scrambled (NSC) shRNA control. B) Western blots showing FTO and ALKBH5 protein expression compared to α-Tubulin in U87 shRNA knockdown lines. C) EpiQuik quantification of m6A in U87 shRNA knockdown lines with representative m6A dot blots. D) MTT cell survival assays in U87 shRNA knockdown lines. E) Representative fluorescent images of HK217 $IDH1^{wt}$ gliomaspheres expressing shRNA targeting *FTO* or *ALKBH5* compared to NSC control. F) Western blots showing FTO and ALKBH5 protein expression compared to α-Tubulin in HK217 shRNA knockdown gliomaspheres. G) Representative m6A dot blots in HK217 shRNA knockdown gliomaspheres. H) Sphere volumes and representative images measuring proliferative potential in HK217 *FTO* and *ALKBH5* knockdown gliomaspheres versus NSC control. I) Representative fluorescent images of HK250 $IDH1^{wt}$ gliomaspheres expressing shRNA targeting *FTO* or *ALKBH5* compared to NSC control. J) Western blots showing FTO and ALKBH5 protein expression compared to α-Tubulin in HK250 shRNA knockdown gliomaspheres. K) Representative m6A dot blots in HK250 shRNA knockdown gliomaspheres. L) Sphere volumes and representative images measuring proliferative potential in HK250 *FTO* and *ALKBH5* knockdown gliomaspheres versus NSC control. M) Western blots of FTO protein expression compared to α-Tubulin and sphere volumes measuring proliferation in HK250 gliomaspheres expressing catalytically inactive FTO^{mut} compared to FTO^{wt}-expressing and empty vector controls. All experiments were conducted in triplicate. Results are presented as Mean ± S.E.M. Pairwise Student's t-tests: $^{*}P < 0.05$, $^{**}P < 0.01$, $^{***}P < 0.005$.

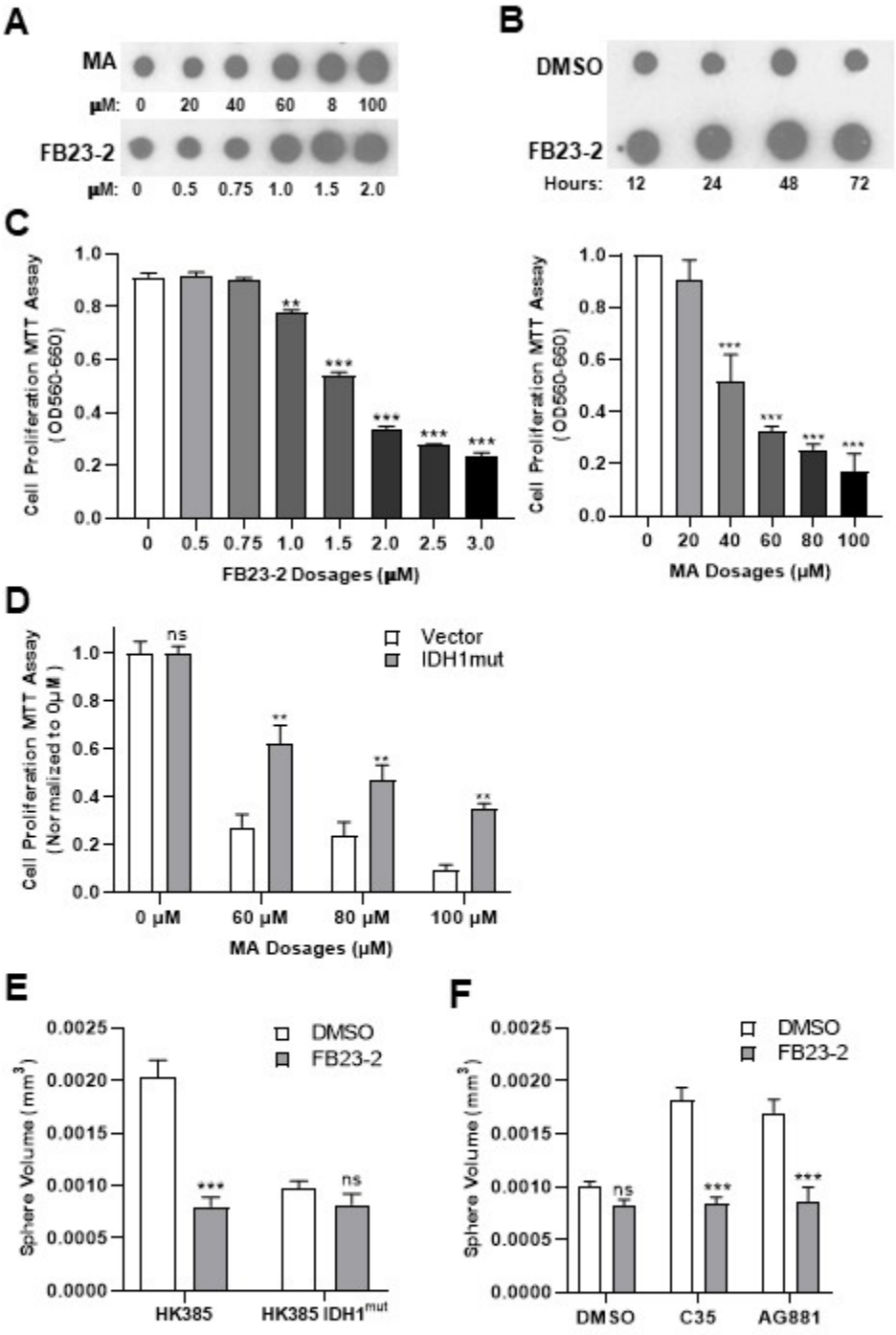
A
MA
μM: 0 20 40 60 8 100
FB23-2
μM: 0 0.5 0.75 1.0 1.5 2.0
B
DMSO
FB23-2
Hours: 12 24 48 72
C
Cell Proliferation MTT Assay (OD560-660)
FB23-2 Dosages (μM)
MA Dosages (μM)
D
Cell Proliferation MTT Assay (Normalized to 0μM)
Vector
IDH1mut
ns
0 μM
60 μM
80 μM
100 μM
MA Dosages (μM)
E
Sphere Volume (mm3)
DMSO
FB23-2
HK385
HK385 IDH1mut
F
Sphere Volume (mm3)
DMSO
FB23-2
DMSO
C35
AG881

G

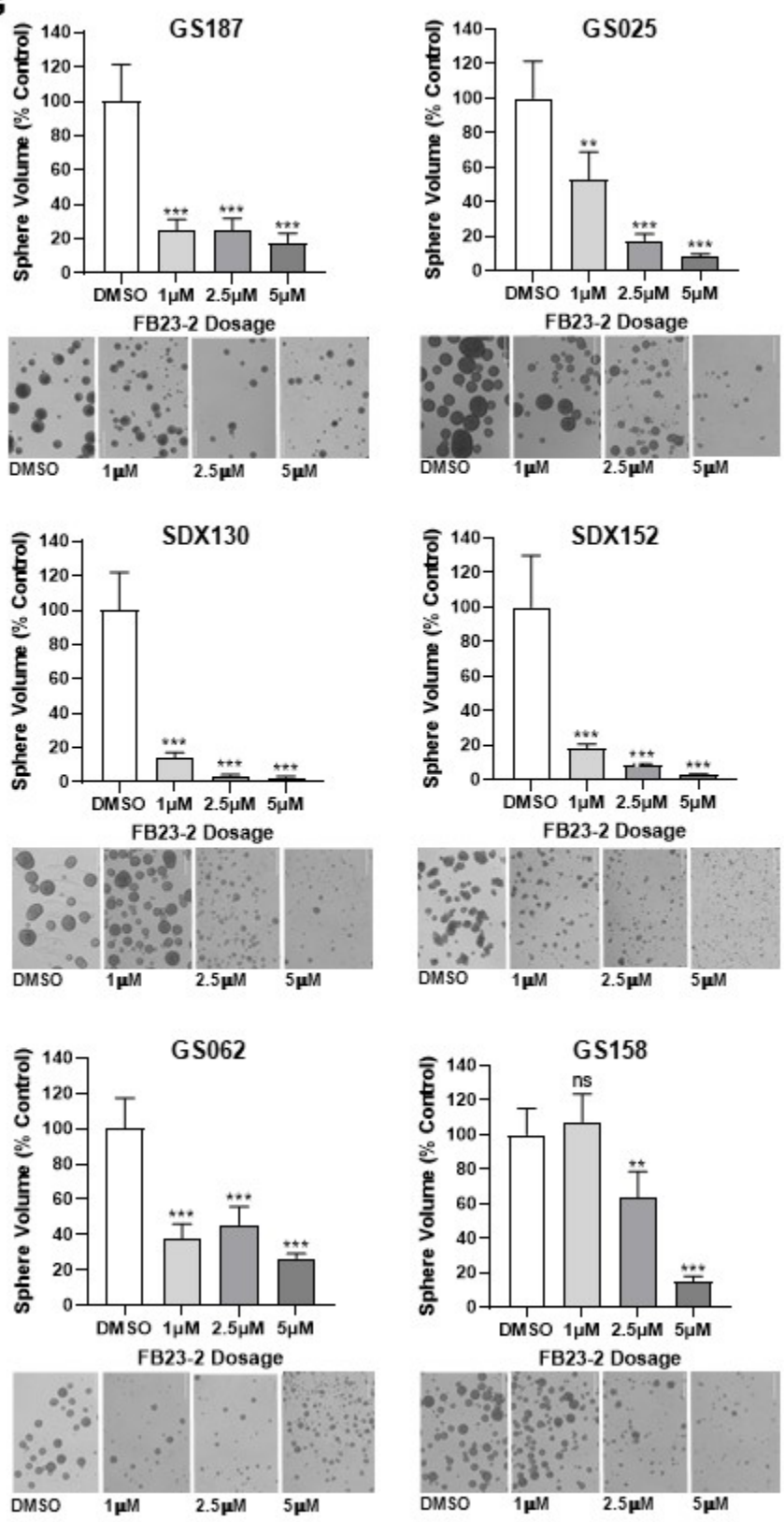
GS187
Sphere Volume (% Control)
140
120
100
80
60
40
20
0
***
***
***
DMSO 1μM 2.5μM 5μM
FB23-2 Dosage
DMSO 1μM 2.5μM 5μM
GS025
Sphere Volume (% Control)
**
***
***
DMSO 1μM 2.5μM 5μM
FB23-2 Dosage
DMSO 1μM 2.5μM 5μM
SDX130
Sphere Volume (% Control)
***
***
***
DMSO 1μM 2.5μM 5μM
FB23-2 Dosage
DMSO 1μM 2.5μM 5μM
SDX152
Sphere Volume (% Control)
***
***
***
DMSO 1μM 2.5μM 5μM
FB23-2 Dosage
DMSO 1μM 2.5μM 5μM
GS062
Sphere Volume (% Control)
***
***
***
DMSO 1μM 2.5μM 5μM
FB23-2 Dosage
DMSO 1μM 2.5μM 5μM
GS158
Sphere Volume (% Control)
ns
**
***
DMSO 1μM 2.5μM 5μM
FB23-2 Dosage
DMSO 1μM 2.5μM 5μM

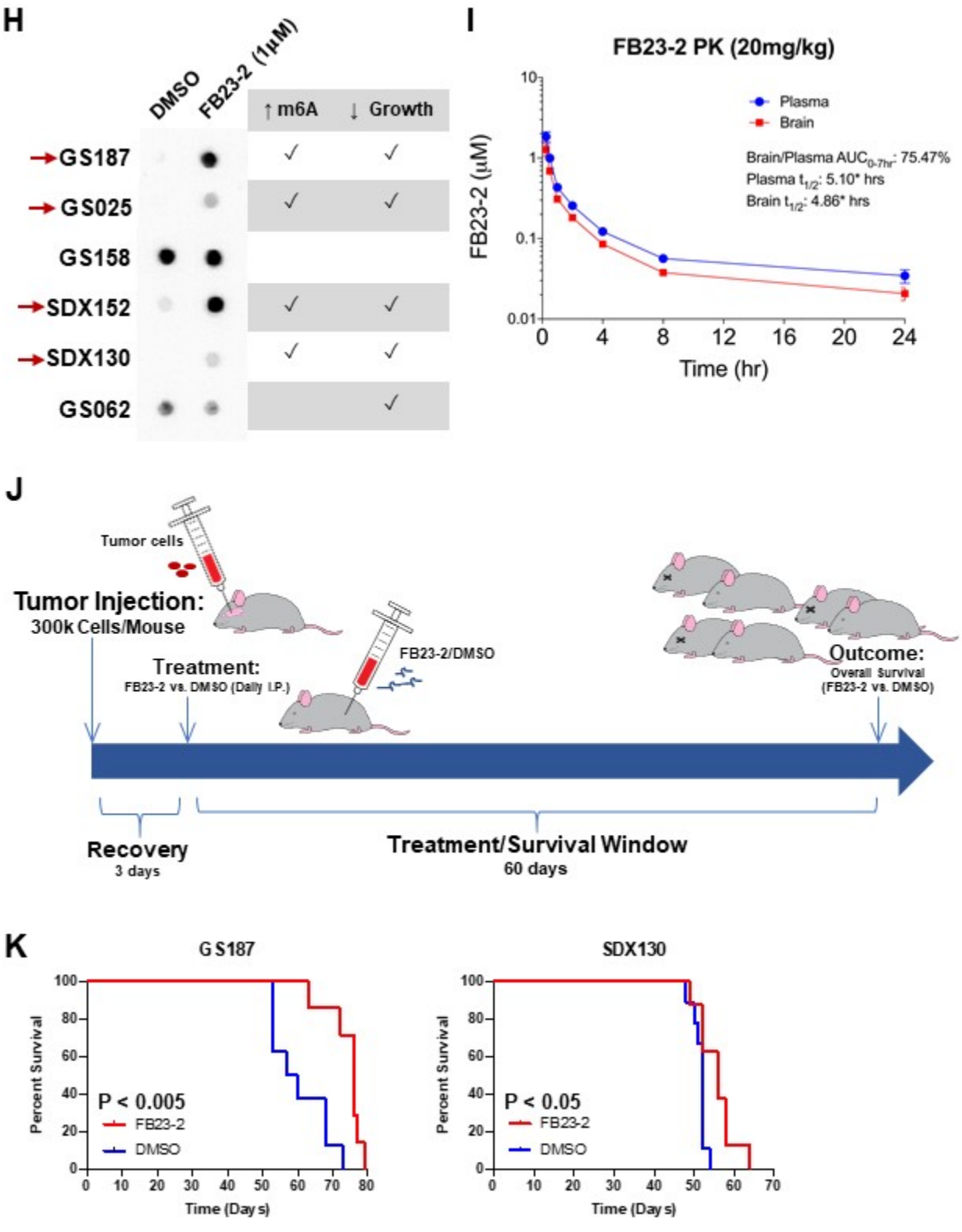

Figure 1-5. Pharmacologic inhibition of FTO leads to m6A enrichment and reduces glioma cell growth *in vitro* and *in vivo*. A) Qualitative m6A dot blots comparing MA and FB23-2

treatments in different dose concentration in U87 glioma cells. B) Qualitative m6A dot blots comparing different durations of FB23-2 and DMSO treatment in U87 glioma cells. C) MTT cell proliferation assays comparing dose responses to FB23-2 and MA in U87 glioma cells. D) MTT assays comparing MA dose responses in U87 cells transduced with *IDH1*^{mut} or empty vector control, normalized to 0 μM MA treatment. E) Sphere volumes measuring proliferative potential in *IDH1*^{wt} HK385 and *IDH1*^{mut} HK385 gliomaspheres treated with FB23-2 or DMSO control. F) Sphere volumes measuring proliferative potential in *IDH1*^{mut}-expressing HK385 gliomaspheres treated with FB23-2 or DMSO control, pre-treated with *IDH1*^{mut} inhibitors C35 or AG881 . G) Sphere volumes and representative images measuring proliferation in *IDH1*^{wt} gliomaspheres (GS187, GS025, SDX130, SDX152, GS062, GS158) comparing treatment effects of different concentrations of FB23-2 versus DMSO control. H) Representative m6A dot blots depicting changes in m6A enrichment in *IDH1*^{wt} gliomaspheres treated with 1 μM FB23-2 versus DMSO control. I) Pharmacokinetic studies performed in mice (2 mice per timepoint) showing brain and plasma concentrations of FB23-2 over time following 20 mg/kg doses of FB23-2 delivered via intraperitoneal injection. J) Schematic depicting the experimental protocol for *in vivo* studies of FB23-2 treatment efficacy in *IDH1*^{wt} gliomasphere intracranial xenografts. K) Kaplan-Meier survival curves comparing overall survival in GS187 and SDX130 xenografted mice treated with FB23-2 or DMSO control. Outside of *in vivo* experiments, all experiments were conducted in triplicate. Results are presented as Mean ± S.E.M. Pairwise Student's t-tests: $^{*}P < 0.05$, $^{**}P < 0.01$, $^{***}P < 0.005$. Mantel-Cox and Gehan-Breslow-Wilcoxon tests were utilized in calculating survival statistics.

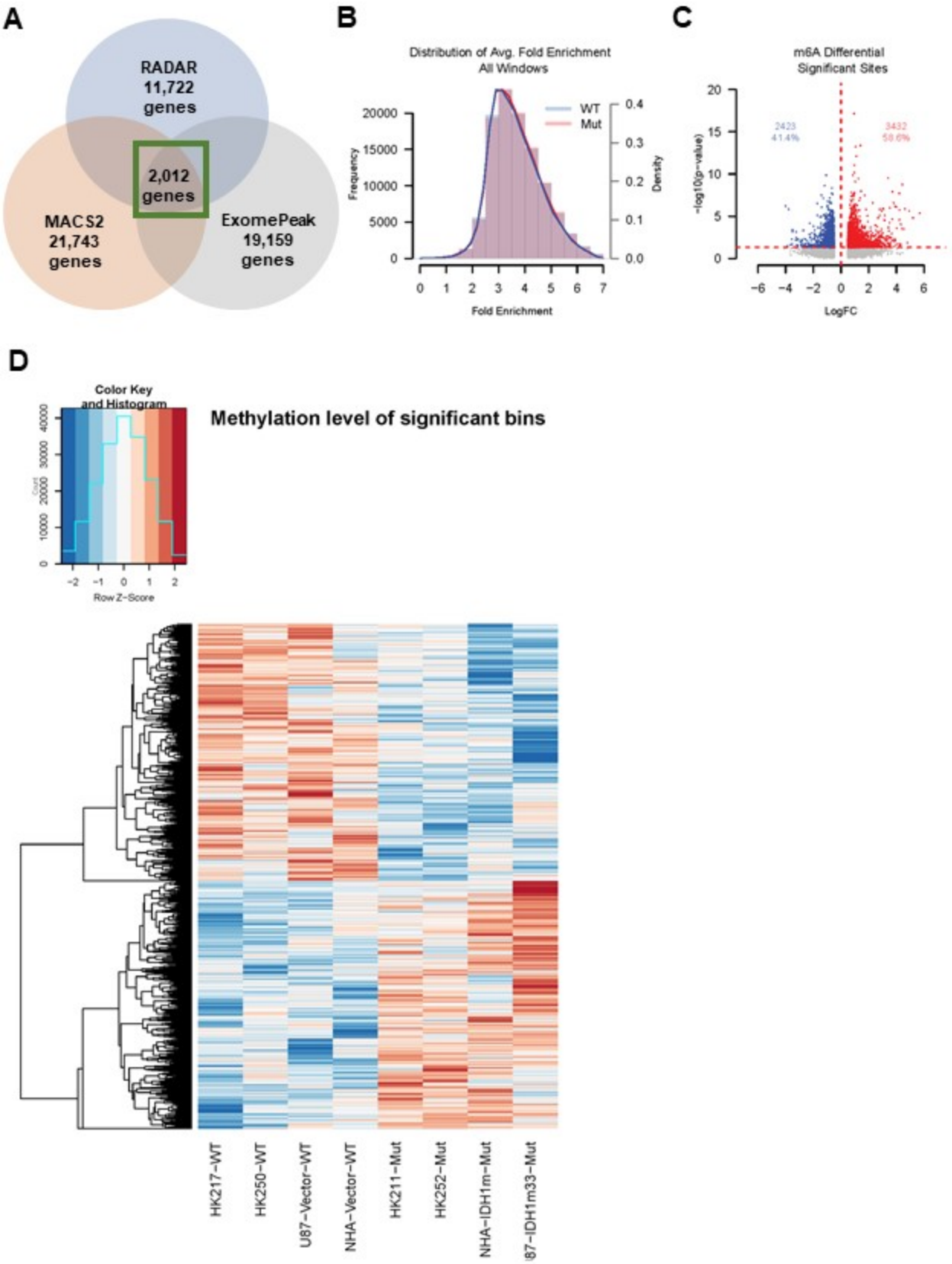
A
RADAR
11,722
genes
2,012
genes
MACS2
21,743
genes
ExomePeak
19,159
genes
B
Distribution of Avg. Fold Enrichment
All Windows
WT
Mut
Frequency
Density
Fold Enrichment
C
m6A Differential
Significant Sites
2423
41.4%
3432
58.6%
-log10(p-value)
LogFC
D
Color Key
and Histogram
Count
Row Z-Score
Methylation level of significant bins
HK217-WT
HK250-WT
U87-Vector-WT
NHA-Vector-WT
HK211-Mut
HK252-Mut
NHA-IDH1m-Mut
87-IDH1m33-Mut

E

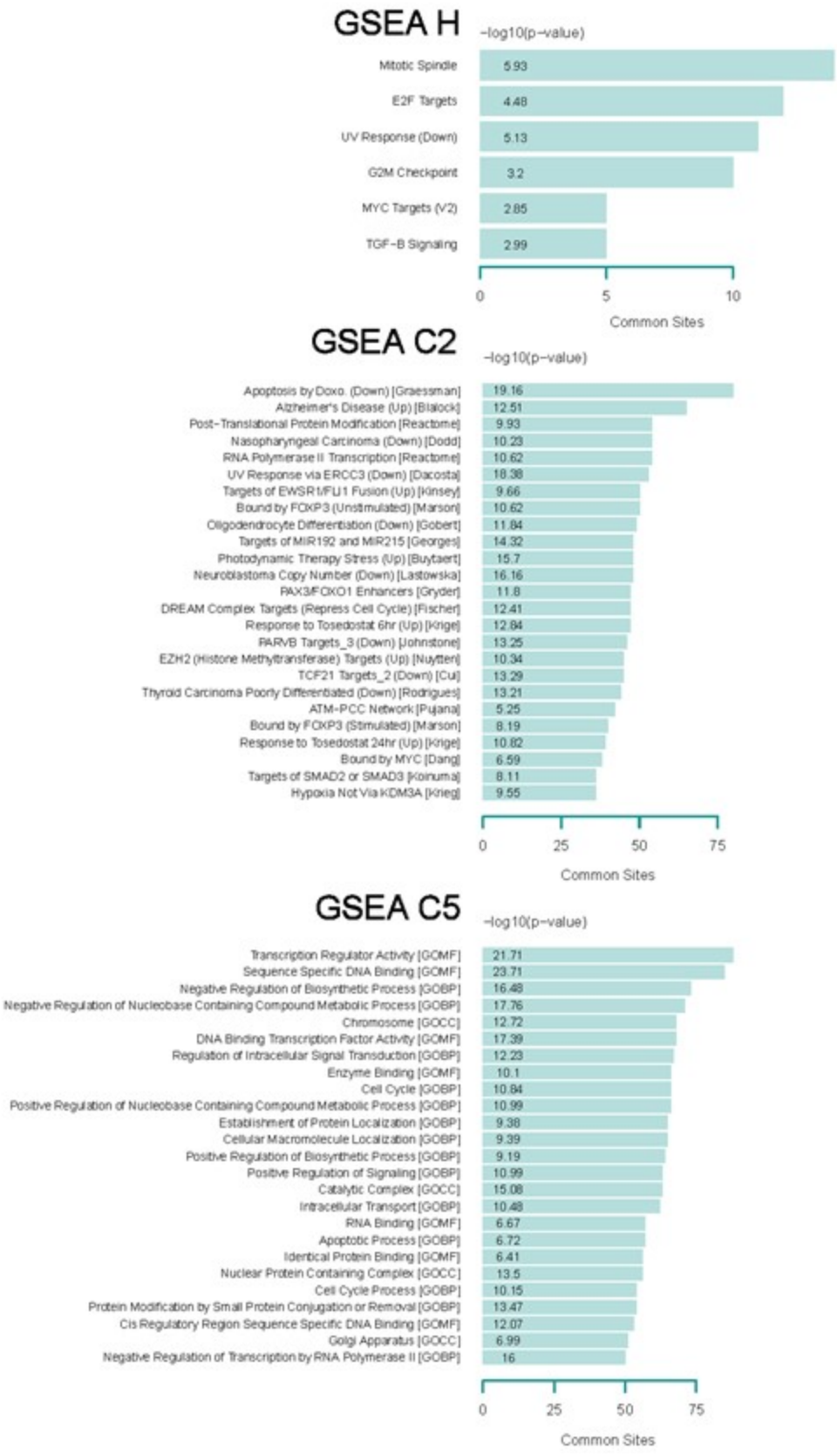
GSEA H
-log10(p-value)
Mitotic Spindle
5.93
E2F Targets
4.48
UV Response (Down)
5.13
G2M Checkpoint
3.2
MYC Targets (V2)
2.85
TGF-B Signaling
2.99
0
5
10
Common Sites
GSEA C2
-log10(p-value)
Apoptosis by Doxo. (Down) [Graessman]
19.16
Alzheimer's Disease (Up) [Blalock]
12.51
Post-Translational Protein Modification [Reactome]
9.93
Nasopharyngeal Carcinoma (Down) [Dodd]
10.23
RNA Polymerase II Transcription [Reactome]
10.62
UV Response via ERCC3 (Down) [Dacosta]
18.38
Targets of EWSR1/FLI1 Fusion (Up) [Kinsey]
9.66
Bound by FOXP3 (Unstimulated) [Marson]
10.62
Oligodendrocyte Differentiation (Down) [Gobert]
11.84
Targets of MIR192 and MIR215 [Georges]
14.32
Photodynamic Therapy Stress (Up) [Buytaert]
15.7
Neuroblastoma Copy Number (Down) [Lastowska]
16.16
PAX3/FOXO1 Enhancers [Gryder]
11.8
DREAM Complex Targets (Repress Cell Cycle) [Fischer]
12.41
Response to Tosedostat 6hr (Up) [Krige]
12.84
PARVB Targets_3 (Down) [Johnstone]
13.25
EZH2 (Histone Methyltransferase) Targets (Up) [Nuytten]
10.34
TCF21 Targets_2 (Down) [Cui]
13.29
Thyroid Carcinoma Poorly Differentiated (Down) [Rodrigues]
13.21
ATM-PCC Network [Pujana]
5.25
Bound by FOXP3 (Stimulated) [Marson]
8.19
Response to Tosedostat 24hr (Up) [Krige]
10.82
Bound by MYC [Dang]
6.59
Targets of SMAD2 or SMAD3 [Koinuma]
8.11
Hypoxia Not Via KDM3A [Krieg]
9.55
0
25
50
75
Common Sites
GSEA C5
-log10(p-value)
Transcription Regulator Activity [GOMF]
21.71
Sequence Specific DNA Binding [GOMF]
23.71
Negative Regulation of Biosynthetic Process [GOBP]
16.48
Negative Regulation of Nucleobase Containing Compound Metabolic Process [GOBP]
17.76
Chromosome [GOCC]
12.72
DNA Binding Transcription Factor Activity [GOMF]
17.39
Regulation of Intracellular Signal Transduction [GOBP]
12.23
Enzyme Binding [GOMF]
10.1
Cell Cycle [GOBP]
10.84
Positive Regulation of Nucleobase Containing Compound Metabolic Process [GOBP]
10.99
Establishment of Protein Localization [GOBP]
9.38
Cellular Macromolecule Localization [GOBP]
9.39
Positive Regulation of Biosynthetic Process [GOBP]
9.19
Positive Regulation of Signaling [GOBP]
10.99
Catalytic Complex [GOCC]
15.08
Intracellular Transport [GOBP]
10.48
RNA Binding [GOMF]
6.67
Apoptotic Process [GOBP]
6.72
Identical Protein Binding [GOMF]
6.41
Nuclear Protein Containing Complex [GOCC]
13.5
Cell Cycle Process [GOBP]
10.15
Protein Modification by Small Protein Conjugation or Removal [GOBP]
13.47
Cis Regulatory Region Sequence Specific DNA Binding [GOMF]
12.07
Golgi Apparatus [GOCC]
6.99
Negative Regulation of Transcription by RNA Polymerase II [GOBP]
16
0
25
50
75
Common Sites

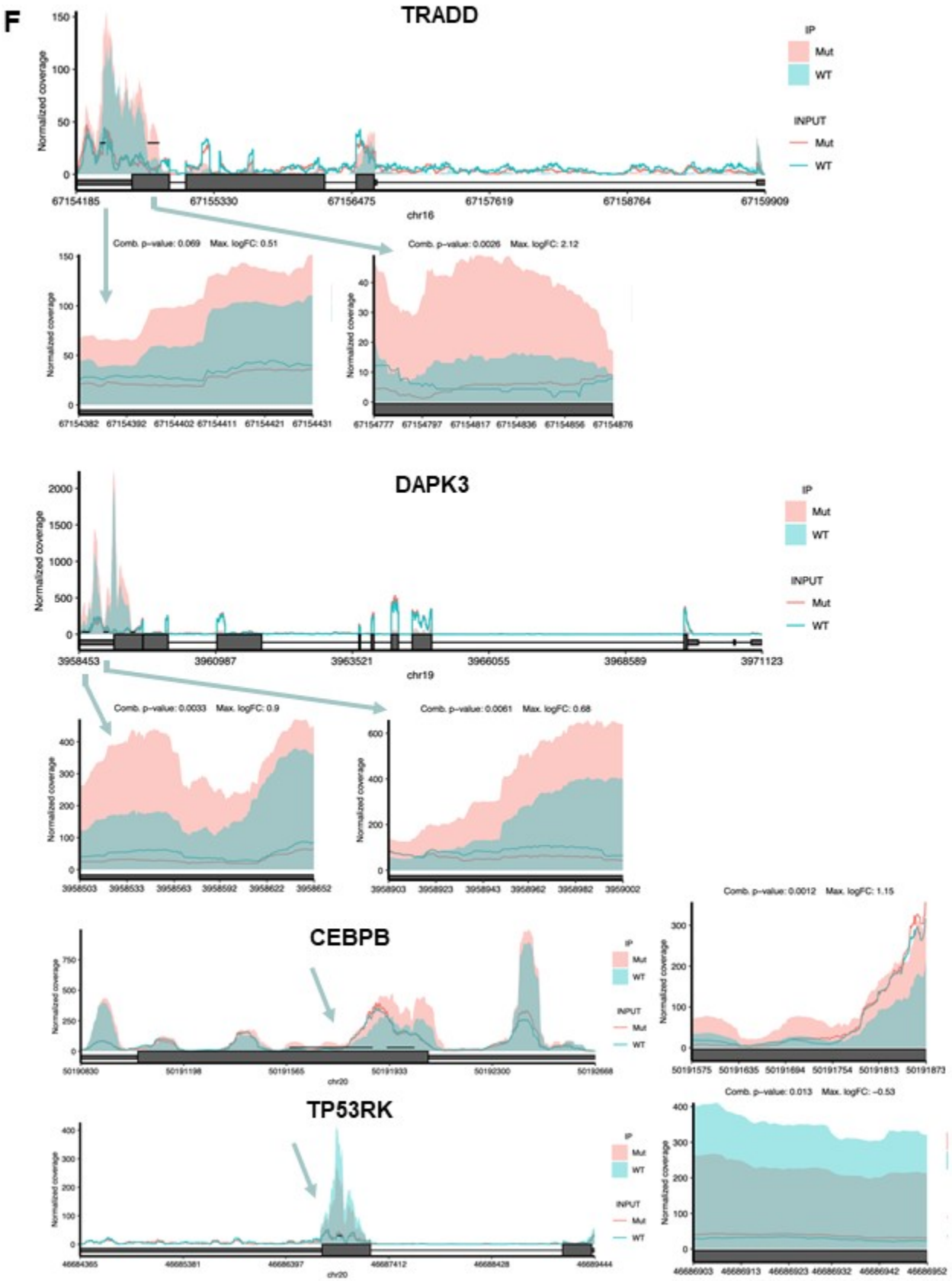
F
TRADD
Normalized coverage
IP
Mut
WT
INPUT
Mut
WT
67154185
67155330
67156475
67157619
67158764
67159909
chr16
Comb. p-value: 0.069 Max. logFC: 0.51
Comb. p-value: 0.0026 Max. logFC: 2.12
DAPK3
3958453
3960987
3963521
3966055
3968589
3971123
chr19
Comb. p-value: 0.0033 Max. logFC: 0.9
Comb. p-value: 0.0061 Max. logFC: 0.68
CEBPB
chr20
Comb. p-value: 0.0012 Max. logFC: 1.15
TP53RK
chr20
Comb. p-value: 0.013 Max. logFC: −0.53

G

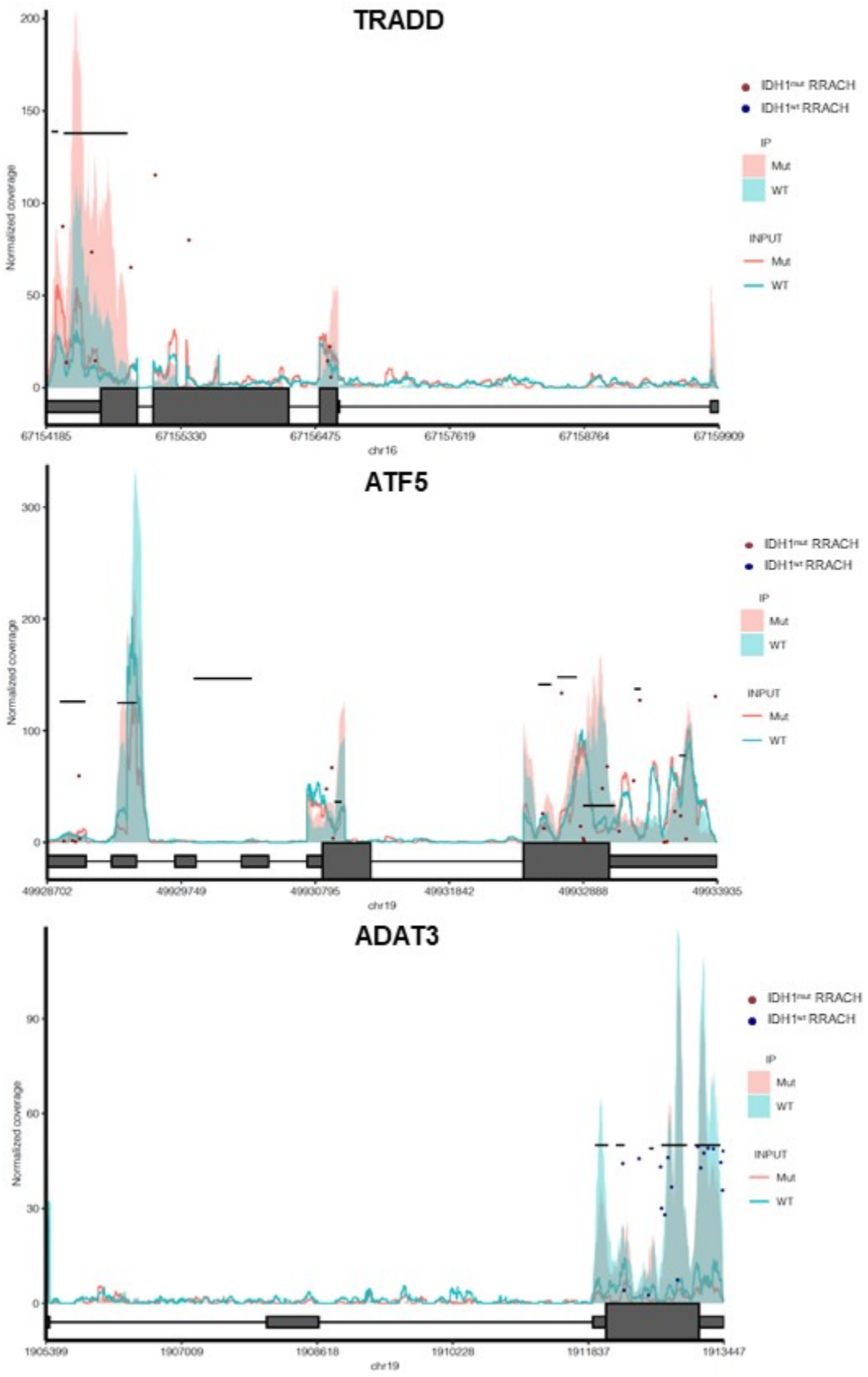
TRADD
Normalized coverage
200
150
100
50
0
67154185
67155330
67156475
67157619
67158764
67159909
chr16
IDH1mut RRACH
IDH1wt RRACH
IP
Mut
WT
INPUT
Mut
WT
ATF5
Normalized coverage
300
200
100
0
49928702
49929749
49930795
49931842
49932888
49933935
chr19
IDH1mut RRACH
IDH1wt RRACH
IP
Mut
WT
INPUT
Mut
WT
ADAT3
Normalized coverage
90
60
30
0
1905399
1907009
1908618
1910228
1911837
1913447
chr19
IDH1mut RRACH
IDH1wt RRACH
IP
Mut
WT
INPUT
Mut
WT

Figure 1-6. MeRIP-Seq reveals distinct epitranscriptomic profiles between *IDH1^{mut}* and *IDH1^{mut}* gliomas. A) Schematic Venn diagram showing genes exhibiting significantly differential m6A methylation in *IDH1^{mut}* gliomas, identified using RADAR, MACS2, and ExomePeak m6A bioinformatic analyses. B) Distributions of average fold enrichments stratified by frequency and density in *IDH1^{mut}* and *IDH1^{wt}* gliomas. C) Volcano plot depicting positive (red) and negative (blue) changes in fold enrichment for m6A sites in *IDH1^{mut}* gliomas. D) Heatmaps of significantly differentially methylated m6A sites across *IDH1^{mut}* and *IDH1^{wt}* MeRIP-Seq samples. E) GSEA analysis results for consensus differentially m6A methylated transcripts, compared to GSEA-H, GSEA-C2, and GSEA-C5 Molecular Signature Databases. F) Sequence coverage plots for representative G-RAMP gene transcripts showing m6A localization and abundance (IP) and total transcript reads (INPUT) at both the transcript level and the level of select significant bins. G) Transcript-level display of RRACH motif m6A sites identified through Nanopore direct RNA sequencing exhibiting differential methylation between *IDH1^{mut}* and *IDH1^{wt}* overlaying sequence coverage plots.

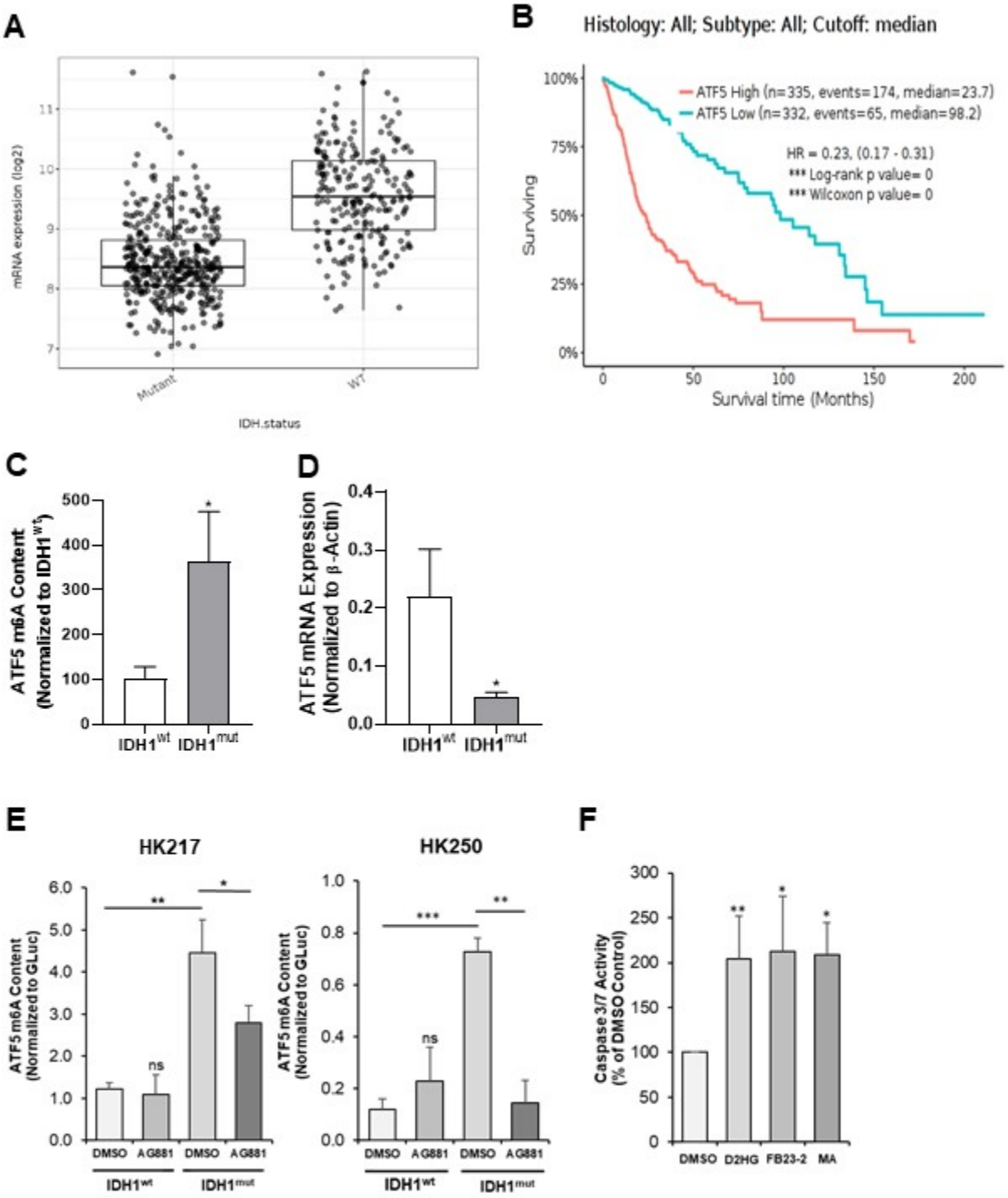
A
mRNA expression (log2)
Mutant
WT
IDH.status
B
Histology: All; Subtype: All; Cutoff: median
ATF5 High (n=335, events=174, median=23.7)
ATF5 Low (n=332, events=65, median=98.2)
HR = 0.23, (0.17 - 0.31)
*** Log-rank p value= 0
*** Wilcoxon p value= 0
Surviving
Survival time (Months)
C
ATF5 m6A Content (Normalized to IDH1wt)
IDH1wt
IDH1mut
D
ATF5 mRNA Expression (Normalized to β-Actin)
IDH1wt
IDH1mut
E
HK217
HK250
ATF5 m6A Content (Normalized to GLuc)
DMSO
AG881
IDH1wt
IDH1mut
ns
F
Caspase 3/7 Activity (% of DMSO Control)
DMSO
D2HG
FB23-2
MA

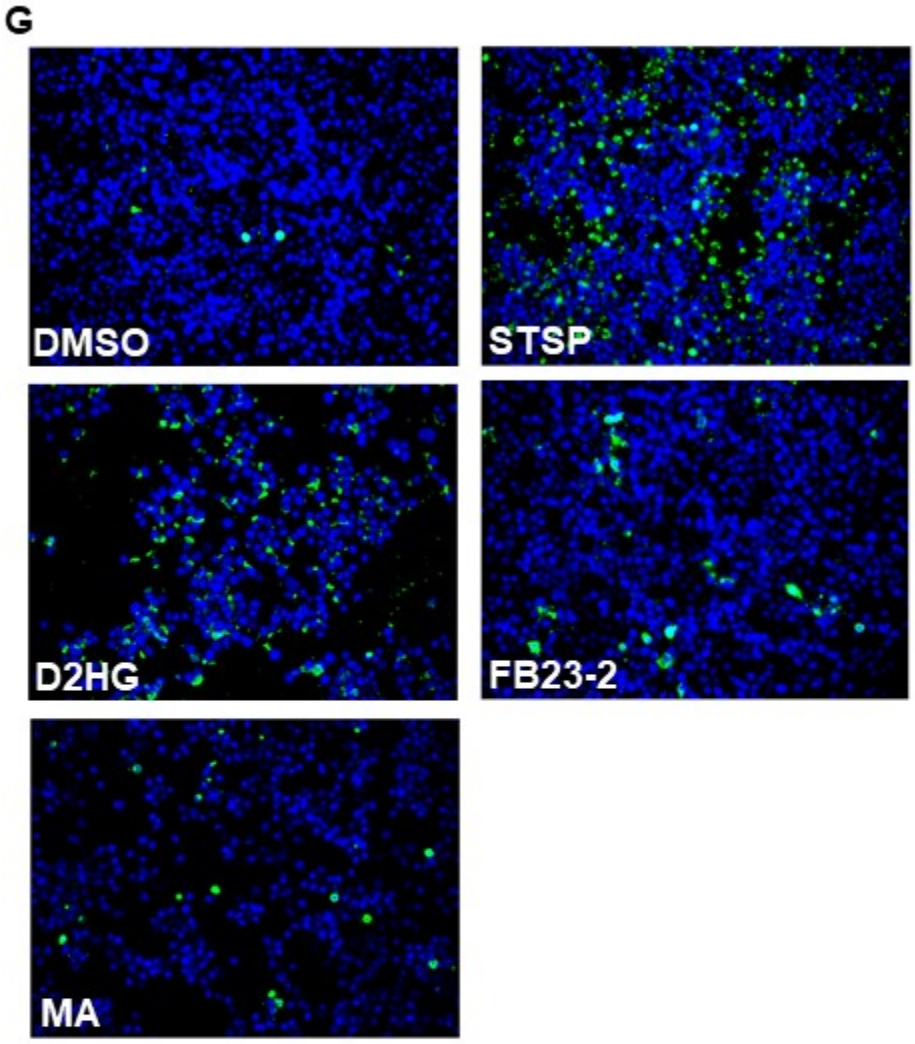

Figure 1-7. Changes in m6A enrichment in ATF5 mediate reductions in ATF5 expression associated with increased apoptotic activity. A) GlioVis ATF5 expression data of ATF5, stratified by *IDH1* mutational status. B) GlioVis Kaplan-Meier survival data for ATF5-High and ATF5-Low expressing patient tumors. C) Targeted MeRIP-Seq validation showing levels of m6A-enriched ATF5 transcripts in $IDH1^{wt}$ and $IDH1^{mut}$ glioma patient tumor samples, normalized to GLuc positive m6A control. D) Targeted MeRIP-Seq validation showing total ATF5 mRNA expression levels in $IDH1^{wt}$ and $IDH1^{mut}$ glioma patient tumor samples, normalized to β-actin. E) Levels of m6A-enriched ATF5 transcripts in $IDH1^{wt}$ and $IDH1^{mut}$-expressing gliomaspheres (HK217, HK250) treated with AG881 or DMSO control, normalized to GLuc. F) Caspase 3/7

activity in *IDH1*^{wt} gliomaspheres treated with D-2-HG, FB23-2, and MA versus DMSO control. G) Green fluorescent labeling of apoptotic U87 cells in DMSO negative control, staurosporine (STSP) positive control, and D-2-HG, FB23-2, and MA treated cells. All experiments were conducted in triplicate. Results are presented as Mean ± S.E.M. Pairwise Student's t-tests: $*P < 0.05$, $**P < 0.01$, $***P < 0.005$.

SUPPLEMENTARY FIGURES & TABLES

Supplementary Table 1-1. Glioma Patient Tumor Diagnosis (WHO 2007) and *IDH1* Status

Sample #	*IDH1* Status*	Tumor Classification†	Tumor Grade	Sample #	*IDH1* Status*	Tumor Classification†	Tumor Grade
1	WT	GBM	IV	14	MUT	GBM	IV
2	WT	GBM	IV	15	MUT	GBM	IV
3	WT	GBM	IV	16	MUT	GBM	IV
4	WT	AA	III	17	MUT	LGA	II
5	WT	GBM	IV	18	MUT	AO	III
6	WT	GBM	IV	19	MUT	AO	III
7	WT	GBM	IV	20	MUT	LGA	II
8	WT	GBM	IV	21	MUT	AO	III
9	WT	GBM	IV	22	MUT	AAO	III
10	WT	GBM	IV	23	MUT	AA	III
11	WT	GBM	IV	24	MUT	AA	III
12	WT	GBM	IV	25	MUT	AA	III
13	WT	GBM	IV				

*WT = Wildtype, MUT = Mutant

†GBM = Glioblastoma, AA = Anaplastic Astrocytoma, LGA = Low Grade Astrocytoma, AO = Anaplastic Oligodendroglioma, AAO = Anaplastic Oligoastrocytoma

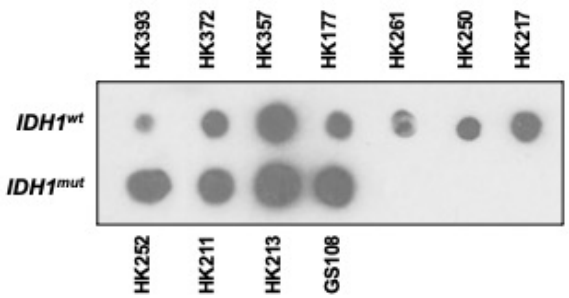

Supplementary Figure 1-1. Dot blots measuring m6A content in patient-derived gliomaspheres. Dot blots performed on *IDH1*^{mut} (*n* = 4) and *IDH1*^{wt} (*n* = 7) RNA using m6A-specific antibody.

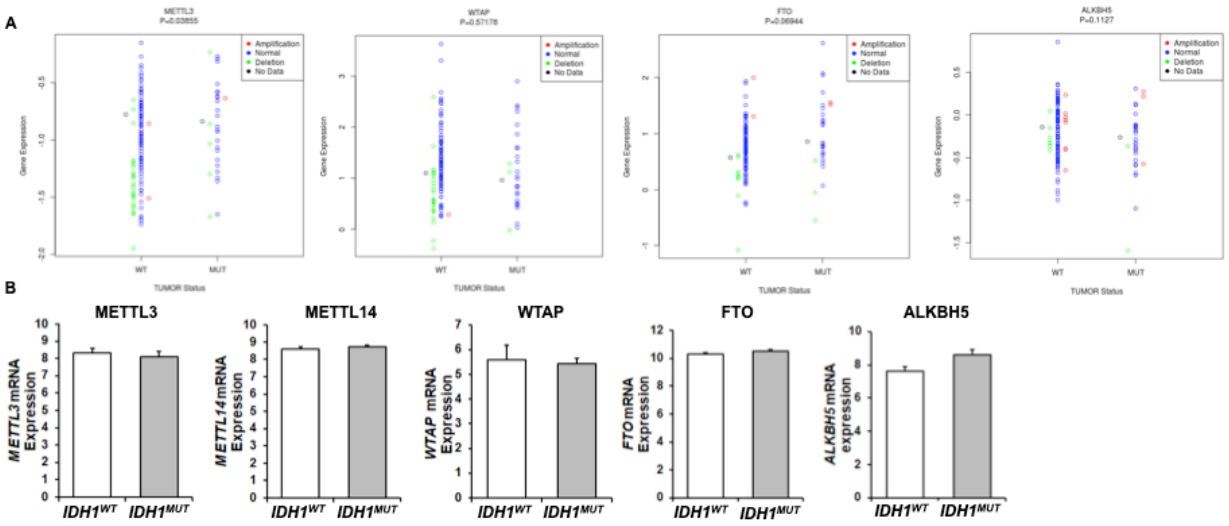

Supplementary Figure 1-2. Expression of m6A writers and erasers in patient tumors and gliomaspheres. A) TCGA data showing expression levels of m6A writers (*METTL3*, *WTAP*) and erasers (*FTO*, *ALKBH5*) across $IDH1^{mut}$ and $IDH1^{wt}$ patient glioma samples. B) Microarray results for gliomaspheres showing no differences in expression levels of m6A writers (*METTL3*, *METTL14*, *WTAP*) or erasers (*FTO*, *ALKBH5*) between $IDH1^{MUT}$ and $IDH1^{WT}$ gliomaspheres. *$p < 0.05$ expressed as Mean ± S.E.M.

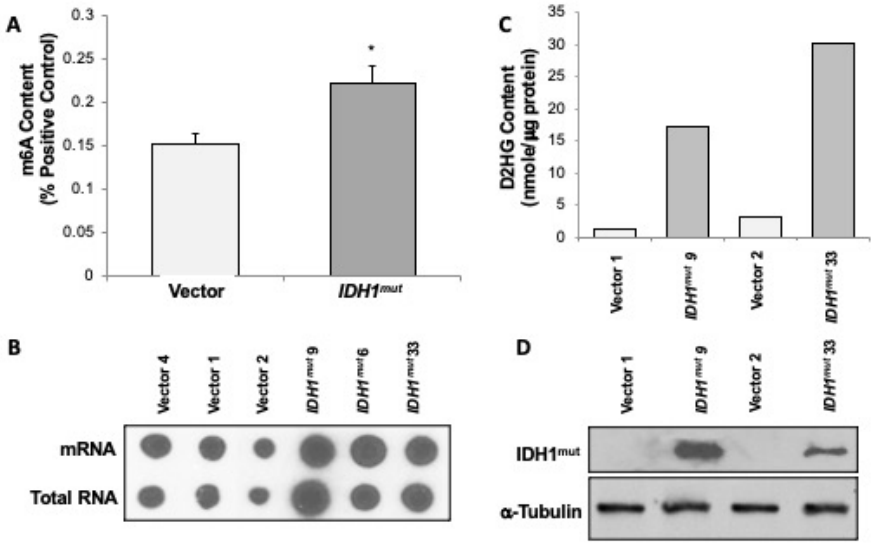

Supplementary Figure 1-3. Dot blots measuring m6A content in HEK293T cells. A) HEK293T cell lines transduced with lentivirus expressing *IDH1*^{mut} (3 independent lines) or empty vector control (3 independent lines) subjected to EpiQuik m6A quantification of total RNA. B) m6A dot blot analyses for *IDH1*^{mut} and vector control lines comparing total RNA (400 ng input) and poly A^{+} purified mRNA (2 ng input). C) D-2-HG levels quantified via enzymatic assay (upper panel) in *IDH1*^{mut} and vector control HEK293T cells, with Western blots showing stable expressing of *IDH1*^{mut}. *$p < 0.05$ expressed as Mean ± S.E.M.

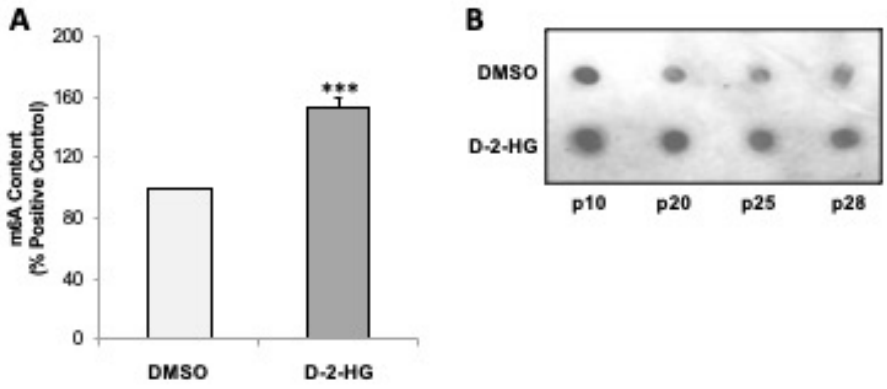

Supplementary Figure 1-4. Octyl-D-2-HG treatment significantly increases m6A content in HEK293T versus DMSO control treatment. A) HEK293T cells treated with 1.0 mM octyl-D-2-HG for 72 hours (3 independent repeats) showing significant m6A enrichment versus DMSO control treatment measured via EpiQuik m6A quantification. B) Long term treatment of HEK293T cells with 1.0 mM octyl-D-2-HG (3 independent repeats per time point) demonstrates stable m6A enrichment across 10, 20, 25, and 28 passages (approximately 3 days between each passage event) visualized via m6A dot blot. ***p <0.001 expressed as Mean ± S.E.M.

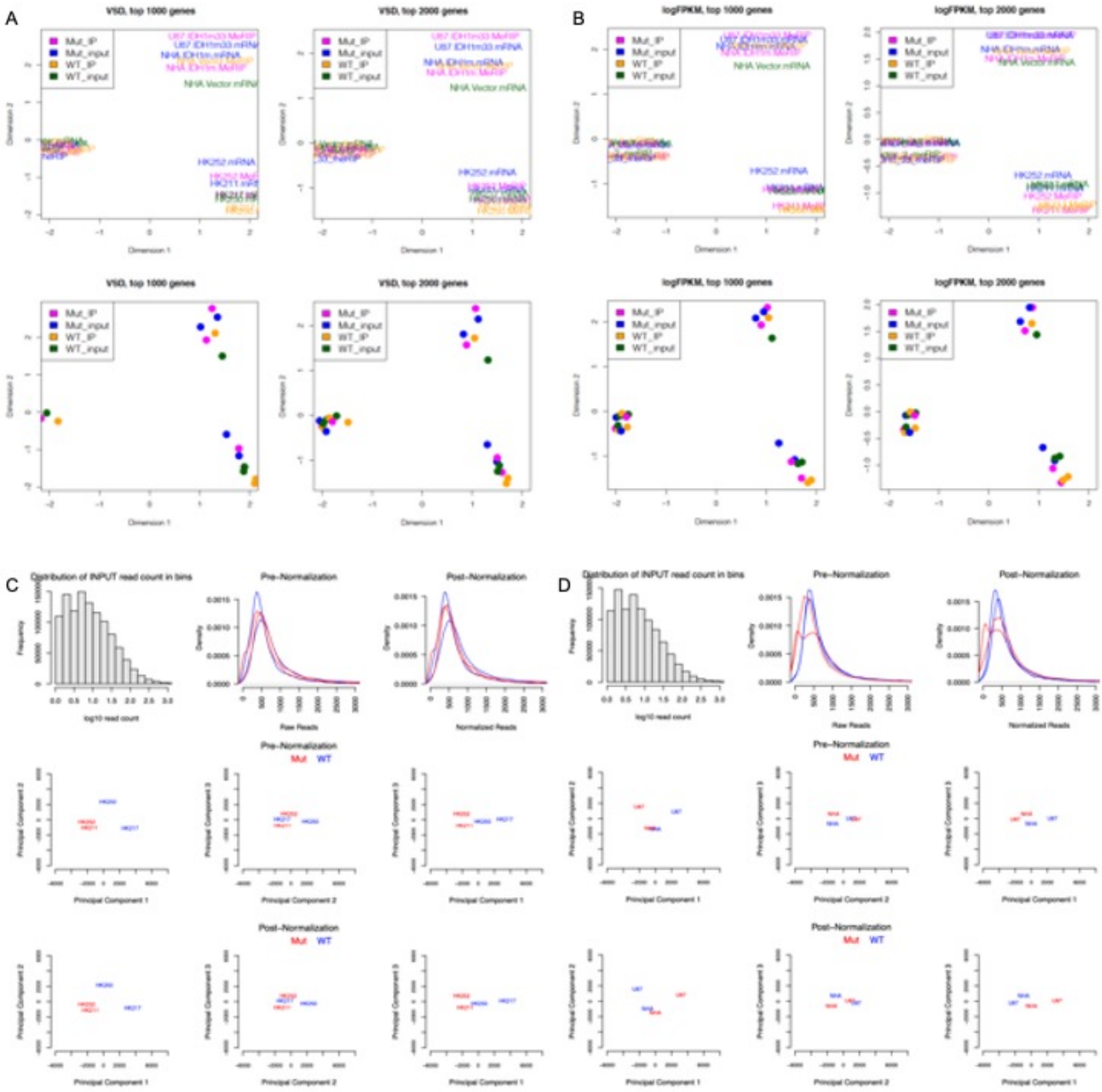

Supplementary Figure 1-5. RADAR quality control and PCA analysis of MeRIP-Seq samples. A) Multidimensional scaling analysis of variance-stabilizing transformation for top 1000 and 2000 differentially expressed genes in *IDH1*^{mut} and *IDH1*^{wt} glioma MeRIP-Seq samples. B) Multidimensional scaling analysis of FPKM scores in *IDH1*^{mut} and *IDH1*^{wt} glioma MeRIP-Seq samples. C) Total mRNA read count bins, pre- and post-normalization read density distributions, and pre- and post-normalization PCA for *IDH1*^{mut} (HK211, HK252) and *IDH1*^{wt} (HK217, HK250)

patient-derived gliomasphere MeRIP-Seq samples. D) Total mRNA read count bins, pre- and post-normalization read density distributions, and pre- and post-normalization PCA for IHA (i.e., NHA) and U87 MeRIP-Seq samples. Mut = *IDH1*^{mut}; WT = *IDH1*^{wt}; IP = m6A-immunoprecipitated mRNA fraction; Input = total mRNA fraction.

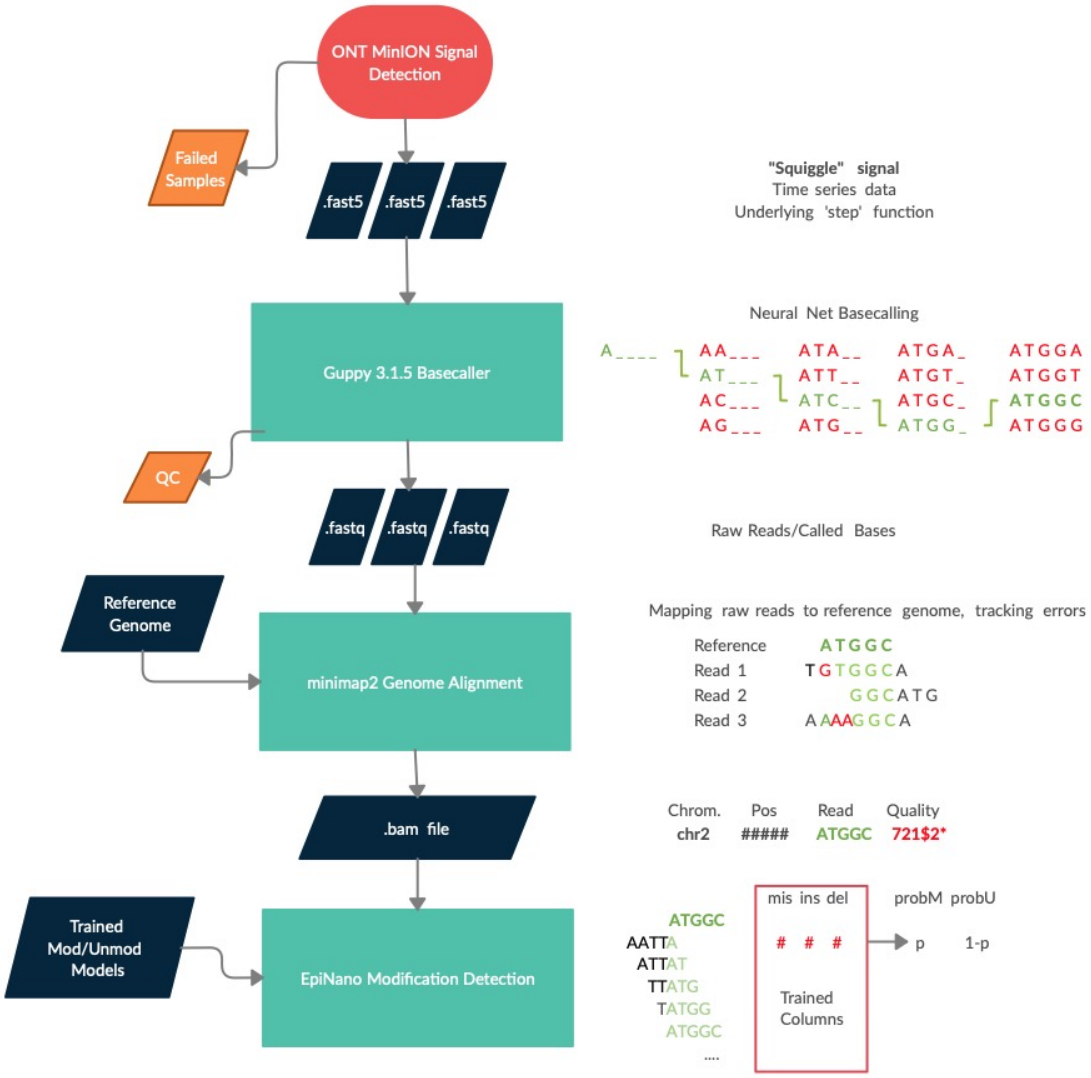

Supplementary Figure 1-6. EpiNano workflow schematic for Direct RNA Sequencing performed. A workflow schematic of the EpiNano m6A peak calling pipeline to identify differentially m6A-methylated RRACH motif sites from direct RNA sequencing performed on an ONT MinION MK1B platform.

SUPPLEMENTARY m6A BIOINFORMATICS MARKDOWN

MeRIP-Seq (m6A) RNA Differential Methylation Tool

Bryan Kevan

5/23/2021

Introduction

This is documentation for a MeRIP-seq tool which identifies differential m6A RNA methylation across IDH1 Mutant and Wild Type (WT) biological samples.

The program achieves its goals by intersecting the significantly DM genomic ranges of three leading RNA DM identification methods. The goal is to not only identify peaks but search for agreement among the three leading methods. These three models are `RADAR`, `ExomePeak`, and ChIP-seq method `MACS2`. These three methods have their own strengths and weaknesses in the identification of DM sites in RNA, so agreement is desirable. This intersection of the three main MeRIP methods is further narrowed using a standard gene-level RNAseq analysis.

The primacy of RADAR as a method deserves mentioning. From a numerical standpoint, the intersection process in this workflow is mostly a matter of narrowing down false-positive-rich RADAR sites using ExomePeak and MACS2, and finally RNAseq rather than the reverse.

There are six major components to this workflow, from reading in data and defining the files through to presentation:

1. **Define files and set parameters**

   The raw files and caches for this workflow are stored on the Lai Lab Server. Paths to the files are assigned in this step, parameters are set, and the study design (grouping samples into Mut. vs WT) is defined.

2. **Count Data**

   All of these models concern the same Poisson or Negative Binomial statistical framework: counting events (modifications) in bins (usually around 50bp length) and calculating significant differences in those individual bins across samples. While all three sources rely on the same MeRIP-seq .bam files, ExomePeak and RADAR have their own counting algorithm, while the ChIPseq program MACS2 relies on RADAR's counting procedure.

   The counting procedures use their own normalization and low-count filtering techniques to improve comparability across the samples. Further, in methods where consecutive bins are identified, an algorithm is deployed which merges adjacent bins into larger 3-10x50bp regions.

3. **Run Models**

   The three models are:

   - `RADAR` - 'RNA methylAtion Differential Analysis in R'
   - `ExomePeak` - 'Exome-based anlaysis of MeRIP-Seq data'
   - `MACS2` - ChIPseq method

4. **Intersect Results**

   After saving the results from the counting processes, the intervals of significant bins are identified and intersected. This intersection method is strict, only allowing ranges in which all three methods agree. Further cross-reference is provided from:

   a. **Gene-level RNAseq**

      DESeq2 is a gene-level RNA-seq method which runs on the INPUT (control) counts from RADAR.

5. **Oxford Nanopore/EpiNano**

   The results from the m6A pipeline are further compared to output from an Oxford Nanopore MinION sequencer, using different raw samples.The Oxford Nanopore neural net approach, uses patterns in errors from basecalling performed by ONT's Guppy 3.1.5 neural net basecaller. The package (https://github.com/enovoa/EpiNano) includes models designed to identify m6A-specific basecalling errors, and results in a probability of methylation for each sliding 5-mer window. These 5-mer windows are filtered to retain and analyze only RRACH motifs.

6. **Present Results**

   Create .pdfs of heatmaps, stacked bar charts, lists of sites, etc.

Code here is presented in three colors, giving some indication of the time required and necessity of running the block to generating results:

Code in **Red** is for package installation. If you need to update packages, this is where that might happen. Otherwise, **no need to run blocks in red.**

Code in **Yellow** is mostly counting algorithms and model evaluation. Time-consuming steps that **do not need to be run more than once for a comparison or parameterization.** Its output is archived on the server at periodic checkpoints in the process and at completion. If you are adding samples or are interested in changing RADAR's bin resolution from 50bp to 100bp in an already-run comparison, it would be necessary to run a counting process again to do this.

Code in **Green** is low-computing-power output generation. Green code is for defining paths, assigning parameters, and generating output. Every task after the counting processes have been done and respective peaks have been identified is in green. This code is flexible, presentation-focused, and runs independent of the counting algorithms. This allows for charts to be created and edited quickly. If further analysis is needed, add modules at the bottom of the file and color them green.

Define files and set Parameters

The following block of code defines the filestructure of the project and assigns output locations. Currently, there are two sets of files that the paper depends on. HK IDH1 WT vs IDH1 Mut. and HK/NHA/U86 IDH1 WT vs. IDH1 Mut. The study design for these two comparisons is:

```
## HK/NHA/U87 Comparison
```

```
##      [,1]            [,2]
## [1,] "HK217-WT"      "HK211-Mut"
## [2,] "HK250-WT"      "HK252-Mut"
## [3,] "U87-Vector-WT" "U87-IDHlm33-Mut"
## [4,] "NHA-Vector-WT" "NHA-IDHlm-Mut"
```

```
## HK Comparison
```

```
##      [,1]       [,2]
## [1,] "HK217-WT" "HK211-Mut"
## [2,] "HK250-WT" "HK252-Mut"
```

Here is a list of the .bam files

```
## total 115436164
## -rwxrwx--- 1 spianka spianka 4020613887 May 23  2020 HEK293-IDH-Mut-6.input.bam
## -rwxrwx--- 1 spianka spianka    4966896 Jun 11  2020 HEK293-IDH-Mut-6.input.bam.bai
## -rwxrwx--- 1 spianka spianka 4207432325 May 23  2020 HEK293-IDH-Mut-6.m6A.bam
## -rwxrwx--- 1 spianka spianka    5007120 Jun 11  2020 HEK293-IDH-Mut-6.m6A.bam.bai
## -rwxrwx--- 1 spianka spianka 3727066780 May 23  2020 HEK293-IDH-Mut-9.input.bam
## -rwxrwx--- 1 spianka spianka    6143336 Jun 11  2020 HEK293-IDH-Mut-9.input.bam.bai
## -rwxrwx--- 1 spianka spianka 3607850734 May 23  2020 HEK293-IDH-Mut-9.m6A.bam
## -rwxrwx--- 1 spianka spianka    6165520 Jun 11  2020 HEK293-IDH-Mut-9.m6A.bam.bai
## -rwxrwx--- 1 spianka spianka 3718858024 May 23  2020 HEK293-IDH-WT-1.input.bam
## -rwxrwx--- 1 spianka spianka    5951872 Jun 11  2020 HEK293-IDH-WT-1.input.bam.bai
## -rwxrwx--- 1 spianka spianka 2291815111 May 23  2020 HEK293-IDH-WT-1.m6A.bam
## -rwxrwx--- 1 spianka spianka    5845480 Jun 11  2020 HEK293-IDH-WT-1.m6A.bam.bai
## -rwxrwx--- 1 spianka spianka 4381115787 May 23  2020 HEK293-IDH-WT-4.input.bam
## -rwxrwx--- 1 spianka spianka    5648296 Jun 11  2020 HEK293-IDH-WT-4.input.bam.bai
## -rwxrwx--- 1 spianka spianka 1961603945 May 23  2020 HEK293-IDH-WT-4.m6A.bam
## -rwxrwx--- 1 spianka spianka    4544744 Jun 11  2020 HEK293-IDH-WT-4.m6A.bam.bai
## -rwxrwx--- 1 spianka spianka 5570597598 May 23  2020 HK211-Mut.input.bam
## -rwxrwx--- 1 spianka spianka    6926560 May 25  2020 HK211-Mut.input.bam.bai
## -rwxrwx--- 1 spianka spianka 2037982896 May 23  2020 HK211-Mut.m6A.bam
## -rwxrwx--- 1 spianka spianka    6182440 May 25  2020 HK211-Mut.m6A.bam.bai
## -rwxrwx--- 1 spianka spianka 5905174748 May 23  2020 HK217-WT.input.bam
## -rwxrwx--- 1 spianka spianka    7294784 May 25  2020 HK217-WT.input.bam.bai
## -rwxrwx--- 1 spianka spianka 1962668594 May 23  2020 HK217-WT.m6A.bam
## -rwxrwx--- 1 spianka spianka    6385912 May 25  2020 HK217-WT.m6A.bam.bai
## -rwxrwx--- 1 spianka spianka 6050133153 May 23  2020 HK250-WT.input.bam
## -rwxrwx--- 1 spianka spianka    6501888 May 25  2020 HK250-WT.input.bam.bai
## -rwxrwx--- 1 spianka spianka 2050465155 May 23  2020 HK250-WT.m6A.bam
## -rwxrwx--- 1 spianka spianka    5690928 May 25  2020 HK250-WT.m6A.bam.bai
## -rwxrwx--- 1 spianka spianka 6225930033 May 23  2020 HK252-Mut.input.bam
## -rwxrwx--- 1 spianka spianka    6667792 May 25  2020 HK252-Mut.input.bam.bai
## -rwxrwx--- 1 spianka spianka 1974149831 May 23  2020 HK252-Mut.m6A.bam
## -rwxrwx--- 1 spianka spianka    5091496 May 25  2020 HK252-Mut.m6A.bam.bai
## -rwxrwx--- 1 spianka spianka 8861521203 May 23  2020 IDH1_33-Mut.input.bam
## -rwxrwx--- 1 spianka spianka    6534168 Jun 11  2020 IDH1_33-Mut.input.bam.bai
## -rwxrwx--- 1 spianka spianka 7433408486 May 23  2020 IDH1_33-Mut.m6A.bam
## -rwxrwx--- 1 spianka spianka    5034888 Jun 11  2020 IDH1_33-Mut.m6A.bam.bai
## -rwxrwx--- 1 spianka spianka 4954557752 May 23  2020 NHA-IDHlm-Mut.input.bam
## -rwxrwx--- 1 spianka spianka    7267192 May 25  2020 NHA-IDHlm-Mut.input.bam.bai
## -rwxrwx--- 1 spianka spianka 2984151324 May 23  2020 NHA-IDHlm-Mut.m6A.bam
## -rwxrwx--- 1 spianka spianka    5065320 May 25  2020 NHA-IDHlm-Mut.m6A.bam.bai
## -rwxrwx--- 1 spianka spianka 4166684587 May 23  2020 NHA-Vector-WT.input.bam
## -rwxrwx--- 1 spianka spianka    7476648 May 25  2020 NHA-Vector-WT.input.bam.bai
## -rwxrwx--- 1 spianka spianka 3189767596 May 23  2020 NHA-Vector-WT.m6A.bam
## -rwxrwx--- 1 spianka spianka    6256016 May 25  2020 NHA-Vector-WT.m6A.bam.bai
## -rwxrwx--- 1 spianka spianka 3723796323 May 23  2020 U87-IDHlm33-Mut.input.bam
## -rwxrwx--- 1 spianka spianka    6478488 May 25  2020 U87-IDHlm33-Mut.input.bam.bai
## -rwxrwx--- 1 spianka spianka 2512081301 May 23  2020 U87-IDHlm33-Mut.m6A.bam
## -rwxrwx--- 1 spianka spianka    4932152 May 25  2020 U87-IDHlm33-Mut.m6A.bam.bai
## -rwxrwx--- 1 spianka spianka 5353782341 May 23  2020 U87-Vector-WT.input.bam
## -rwxrwx--- 1 spianka spianka    6111336 May 25  2020 U87-Vector-WT.input.bam.bai
```

```
## -rwxrwx--- 1 spianka spianka 2982344548 May 23  2020 U87-Vector-WT.m6A.bam
## -rwxrwx--- 1 spianka spianka    6023800 May 25  2020 U87-Vector-WT.m6A.bam.bai
## -rwxrwx--- 1 spianka spianka 4832649880 May 23  2020 Vector_2-WT.input.bam
## -rwxrwx--- 1 spianka spianka    6012728 Jun 11  2020 Vector_2-WT.input.bam.bai
## -rwxrwx--- 1 spianka spianka 7350887480 May 23  2020 Vector_2-WT.m6A.bam
## -rwxrwx--- 1 spianka spianka    5088784 Jun 11  2020 Vector_2-WT.m6A.bam.bai
```

```
knitr::opts_chunk$set(echo = TRUE,
                      eval = FALSE,
                      error = TRUE)
## Sample choice variables

# HK_NHA_U87 (Uncomment for this run)

sample <- "HK_NHA_U87"
cutoff.fdr <- .25
samples <- c("HK217-WT",
             "HK250-WT",
             "U87-Vector-WT",
             "NHA-Vector-WT",
             "HK211-Mut",
             "HK252-Mut",
             "U87-IDH1m33-Mut",
             "NHA-IDH1m-Mut")

# HK (Uncomment for this RADAR run)

# sample <- "HK"
# cutoff.fdr <- .25
# samples <- c("HK217-WT",
#              "HK250-WT",
#              "HK211-Mut",
#              "HK252-Mut")

# Important directories

alignment <- "/home/spianka/Desktop/ont/mpores/master_of_pores/output/alignment"
radara <- "/home/spianka/Desktop/radar/loci/"
radar2 <- "/home/spianka/Desktop/radar/radarfull/"
radar_charts <- "/home/spianka/Desktop/radar/charts/"
rnaseq <- "/home/spianka/Desktop/macs/rnaseq/"
macs <- "/home/spianka/Desktop/macs"
gtf <- "/home/spianka/Desktop/ont/mpores/master_of_pores/gencode.v35.annotation.gtf"
bam_files <- "/home/spianka/Desktop/bam_files/"

#knitr::opts_knit$set(root.dir = macs)
```

Required Packages

These packages are installed already, on the machine. Bioconductor, a repository for genomics R packages, uses a separate install function from base R.

```
BiocManager::install("biomaRt")
install_github("scottzijiezhang/RADAR")
BiocManager::install("GenomicRanges")
BiocManager::install("DESeq2")
BiocManager::install("edgeR")
BiocManager::install("tximeta")
BiocManager::install("limma")
BiocManager::install("minfi")
install.packages("remotes")
```

This is where all the necessary packages are loaded into R. This needs to happen any time you run code in this program.

```
library(GenomicFeatures)
library(GenomicRanges)
library(DESeq2)
library(edgeR)
library(tximeta)
library(readxl)
library(ggplot2)
```

```
# RADAR
library(remotes)
library("RADAR")
library("biomaRt")
library("limma")
library("minfi")
library(rtracklayer)

#ExomePeak
library("exomePeak")
library("dplyr")

# Intersect
library(org.Hs.eg.db)
library(annotate)

# Plot grids
library(gridExtra)
library("gplots")
library("RColorBrewer")

# Manual RADAR charts
source("/home/spianka/Desktop/radar/radar_charts.R")
```

Model 1: RADAR

RADAR is an R package which counts modifications in bins across the genome using the `countReads()` function in R. This model is the most time-intensive, particularly the read counting and normalization steps. I have implemented a checkpoint after the reads counting, which saves the counted reads object. You can start with the saved file, otherwise the `countReads` function takes a few hours.

```
filename <- sample
length <- length(samples)
wtlist <- data.frame(c(rep("WT", length/2),
                       rep("Mut", length/2)))

radar <- countReads(samplenames = samples,
                    gtf="~/Desktop/radar/gencode.v34.primary_assembly.annotation.gtf",
                    bamFolder = "~/Desktop/bam_files",
                    outputDir = "global",
                    modification = "m6A",
                    paired = TRUE,
                    threads = 20,
                    binSize = 25)
```

Save the counted reads image. This is the most simple version of the RADAR object, with just the raw counts in 50bp bins. Further code in the RADAR section will act upon this object, adding components which describe the model and results. But the core object stays intact.

```
save(radar, paste0(radar2, "radar_", sample, ".RData"))
```

Command to load the checkpoint

```
load(paste0(radar2, "radar_", sample, ".RData"))
```

Normalize and adjust the levels for better comparison between samples.

```
# Normalize and Adjust
radar <- normalizeLibrary(radar, boxPlot=FALSE)
radar <- adjustExprLevel(radar)
```

Filter low-count bins (under 15)

```
# Define Variables
variable(radar) <- wtlist

# Filter bins subject to cutoff
radar <- filterBins(radar, minCountsCutOff = 15)

# Give to RNA-seq
RNA_seq <- radar
```

Run the model. `diffIP_parallel` runs the model, `PrepCoveragePlot` adds visual data to the radar object. `reportResult` cuts off the results at a particular false discovery rate and binds consecutive bins into regions.

```
# Run Differential Methylation model
radar <- diffIP_parallel(radar, thread = 20, fdrBy = "fdr")

# Prep coverage plot
radar <- PrepCoveragePlot(radar,
                          gtf = "~/Desktop/radar/gencode.v34.primary_assembly.annotation.gtf")

# Report Results
radar_post <- reportResult(radar, cutoff = 2,Beta_cutoff = 0, threads = 20)

# Merge with gene names
# Convert Gene IDs
res <- RADAR::results(radar_post)
```

Save the fully executed model image. `radar post` is the complete version of the RADAR run, with everything from raw counts to results from the differential expression model.

```
save(radar_post, file = paste0(radar2, "radar", sample, "_counted.RData"))
```

RADAR output

Load the checkpoint image.

```
load(paste0(radar2, "radar_", sample, "_counted.RData"))
```

This is a block of code which matches the results from RADAR with gene names from the GTF file with which the results were annotated.

```
G_list <- data.frame(gene = radar_post@GTF@elementMetadata@listData$gene_id,
                     ensembl_gene_id = radar_post@GTF@elementMetadata@listData$gene_name,
                     gene_type = radar_post@GTF@elementMetadata@listData$gene_type)
G_list <- unique(G_list)

res <- merge(res,G_list,by.x="name",by.y="gene", all.y = FALSE)
```

Write the output from RADAR to a .csv file.

```
res <- res[order(res$p_value),]
row.names(res) <- c(1:nrow(res))

write.csv(res, paste0("radar/loci/differential_loci_fdr_", sample,".csv"), row.names = FALSE)
```

The top 10 RADAR sites

Heatmap

```
pdf(paste0(radar_charts,"RADAR_charts_heatmap_", sample, ".pdf"),
    width = 8.5, height = 11,
    title = "RNA Differential Methylation Using RADAR, MACS2, ExomePeak")

heatmap.radar() # built in radar_charts.R

dev.off()
```

Example Heatmap

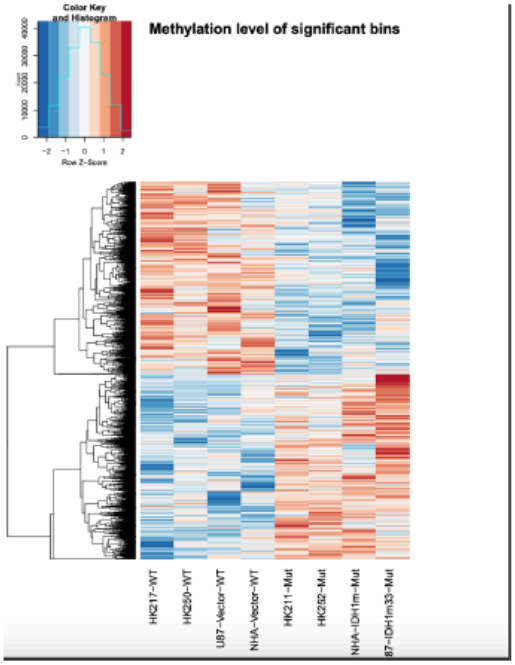

Peak charts, stacked bars in a loop.

```
# Get top bins
colors <- unlist(variable(radar_post))
colors <- ifelse(colors == "Mut", "red", "blue")

top_bins_post <- extractIP(radar_post,
                           filtered = T,
                           normalized = T)[order(rowMeans(extractIP(radar_post,
                                                                    filtered = T,
                                                                    normalized = T)),
                                                 decreasing = T)[1:5000],]
```

```
## Returning normalized IP read counts.
## Returning normalized IP read counts.
```

```
attr(top_bins_post, "color") <- colors

top_bins_pre <-  extractIP(radar_post,
                           filtered = T,
                           normalized = F)[order(rowMeans(extractIP(radar_post,
                                                                    filtered = T,
                                                                    normalized = F)),
                                                 decreasing = T)[1:5000],]
```

```
## Returning raw IP read counts.
## Returning raw IP read counts.
```

```
attr(top_bins_pre, "color") <- colors
```

Create RADAR Charts PDF

```
pdf(paste0("radar/charts/RADAR_charts_", filename, ".pdf"),
    width = 8.5, height = 11,
    title = "RNA Differential Methylation Using RADAR")

par(mfrow = c(4,3),
    mai = c(.75,.75,.5,.25))

dist.reads(radar_post)
```

```
par(mgp=c(4,1,0))
normalization(top_bins_pre, top_bins_post)
par(mgp=c(3,1,0))

pca(top_bins_pre, 1, 2)
pca(top_bins_pre, 2, 3)
mtext("Pre-Normalization",
      cex = .8,
      line = 2.25)

mtext("Mut", col = "red", side = 3, cex = .8, line = .75)
mtext("\t\t\t\t\t\t\t\t\t\tWT", col = "blue", side = 3, cex = .8, line = .75)
pca(top_bins_pre, 1, 3)

pca(top_bins_post, 1, 2)
pca(top_bins_post, 2, 3)
mtext("Post-Normalization",
      cex = .8,
      line = 2.25)

mtext("Mut", col = "red", side = 3, cex = .8, line = .75)
mtext("\t\t\t\t\t\t\t\t\t\tWT", col = "blue", side = 3, cex = .8, line = .75)
pca(top_bins_post, 1, 3)

#heatmap.radar()

page_1 <- lapply(seq(1,8,1), coverage_plot)
page_2 <- lapply(seq(9,16,1), coverage_plot)
page_3 <- lapply(seq(17,24,1), coverage_plot)
page_4 <- lapply(seq(25,32,1), coverage_plot)
page_5 <- lapply(seq(33,40,1), coverage_plot)
page_6 <- lapply(seq(41,48,1), coverage_plot)
page_7 <- lapply(seq(49,56,1), coverage_plot)
page_8 <- lapply(seq(57,64,1), coverage_plot)
page_9 <- lapply(seq(65,72,1), coverage_plot)
page_10 <- lapply(seq(73,80,1), coverage_plot)

# Top overall
plot.new()

do.call("grid.arrange", c(page_1, ncol = 2, nrow = 4))
do.call("grid.arrange", c(page_2, ncol = 2, nrow = 4))
do.call("grid.arrange", c(page_3, ncol = 2, nrow = 4))
do.call("grid.arrange", c(page_4, ncol = 2, nrow = 4))
do.call("grid.arrange", c(page_5, ncol = 2, nrow = 4))
do.call("grid.arrange", c(page_6, ncol = 2, nrow = 4))
do.call("grid.arrange", c(page_7, ncol = 2, nrow = 4))
do.call("grid.arrange", c(page_8, ncol = 2, nrow = 4))
do.call("grid.arrange", c(page_9, ncol = 2, nrow = 4))
do.call("grid.arrange", c(page_10, ncol = 2, nrow = 4))

dev.off()
```

Visualization of Normalization

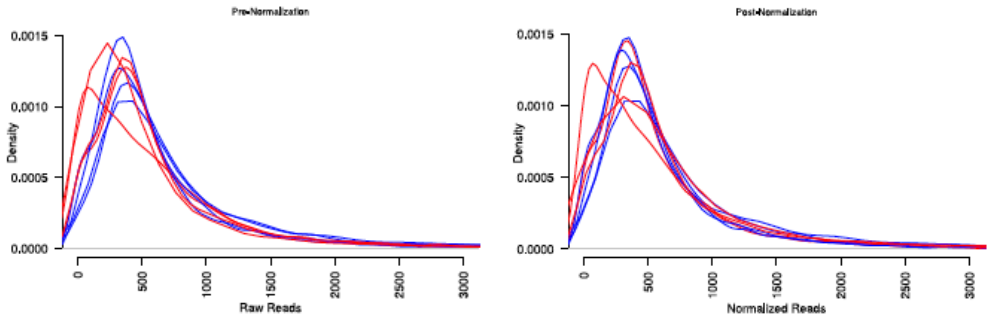

Visualization of Peaks

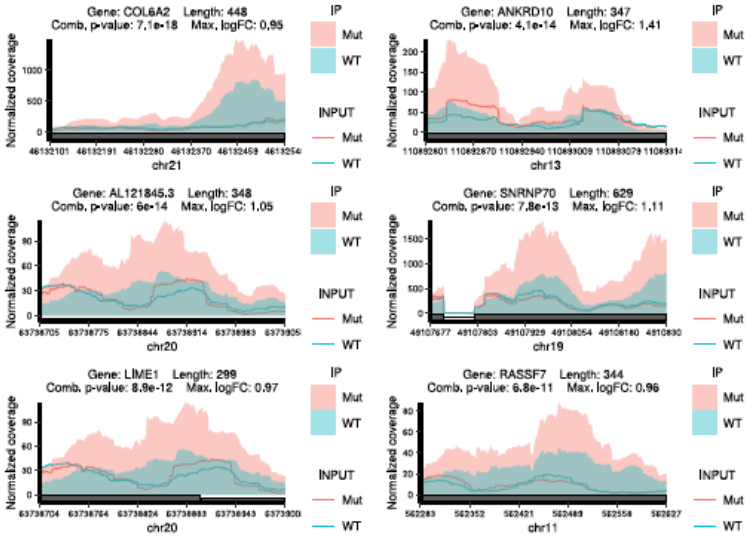

Model 2: MACS2

MACS2 is written in Python, but interfaces with shell. RMarkdown allows you to run shell code straight from the markdown file. Here are the two runs which correspond to the two desired comparisons. The macs2 program runs in two different modes, `callpeak` which calls peaks, and `bdgdiff` which runs the differential expression model.

Here are the `callpeak` runs:

```
cd /home/spianka/Desktop/macs/macs_peaks/macs2_hk_nha_u87_wt
/home/spianka/miniconda3/bin/macs2 callpeak -t \
                  /home/spianka/Desktop/bam_files/HK217-WT.m6A.bam  \
                  /home/spianka/Desktop/bam_files/HK250-WT.m6A.bam  \
                  /home/spianka/Desktop/bam_files/U87-Vector-WT.m6A.bam \
                  /home/spianka/Desktop/bam_files/NHA-Vector-WT.m6A.bam -c  \
                  /home/spianka/Desktop/bam_files/HK217-WT.input.bam \
                  /home/spianka/Desktop/bam_files/HK250-WT.input.bam \
                  /home/spianka/Desktop/bam_files/U87-Vector-WT.input.bam \
                  /home/spianka/Desktop/bam_files/NHA-Vector-WT.input.bam \
                  -f BAMPE -g hs -n HK_WT -B -q 0.05

cd /home/spianka/Desktop/macs/macs_peaks/macs2_hk_nha_u87_mut
/home/spianka/miniconda3/bin/macs2  callpeak -t \
                  /home/spianka/Desktop/bam_files/HK211-Mut.m6A.bam \
                  /home/spianka/Desktop/bam_files/HK252-Mut.m6A.bam \
                  /home/spianka/Desktop/bam_files/NHA-IDH1m-Mut.m6A.bam \
                  /home/spianka/Desktop/bam_files/U87-IDH1m33-Mut.m6A.bam -c \
                  /home/spianka/Desktop/bam_files/HK211-Mut.input.bam \
                  /home/spianka/Desktop/bam_files/HK252-Mut.input.bam \
                  /home/spianka/Desktop/bam_files/NHA-IDH1m-Mut.input.bam \
                  /home/spianka/Desktop/bam_files/U87-IDH1m33-Mut.input.bam \
                  -f BAMPE -g hs -n HK_Mut -B -q 0.05
```

```
cd /home/spianka/Desktop/macs/macs_peaks/macs2_hk_wt
/home/spianka/miniconda3/bin/macs2 callpeak -t \
                  /home/spianka/Desktop/bam_files/HK217-WT.m6A.bam  \
                  /home/spianka/Desktop/bam_files/HK250-WT.m6A.bam  \
                  /home/spianka/Desktop/bam_files/U87-Vector-WT.m6A.bam \
                  /home/spianka/Desktop/bam_files/NHA-Vector-WT.m6A.bam -c  \
                  /home/spianka/Desktop/bam_files/HK217-WT.input.bam \
                  /home/spianka/Desktop/bam_files/HK250-WT.input.bam \
                  /home/spianka/Desktop/bam_files/U87-Vector-WT.input.bam \
                  /home/spianka/Desktop/bam_files/NHA-Vector-WT.input.bam -f \
                  BAMPE -g hs -n HK_WT -B -q 0.05

cd /home/spianka/Desktop/macs/macs_peaks/macs2_hk_mut
```

```
/home/spianka/miniconda3/bin/macs2  callpeak -t \
                /home/spianka/Desktop/bam_files/HK211-Mut.m6A.bam  \
                /home/spianka/Desktop/bam_files/HK252-Mut.m6A.bam \
                /home/spianka/Desktop/bam_files/NHA-IDH1m-Mut.m6A.bam \
                /home/spianka/Desktop/bam_files/U87-IDH1m33-Mut.m6A.bam -c  \
                /home/spianka/Desktop/bam_files/HK211-Mut.input.bam \
                /home/spianka/Desktop/bam_files/HK252-Mut.input.bam \
                /home/spianka/Desktop/bam_files/NHA-IDH1m-Mut.input.bam \
                /home/spianka/Desktop/bam_files/U87-IDH1m33-Mut.input.bam \
                -f BAMPE -g hs -n HK_Mut -B -q 0.05
```

MACS2 output

Here are the `bdgdiff` model runs:

```
/home/spianka/miniconda3/bin/macs2 bdgdiff \
    --t1 /home/spianka/Desktop/macs/macs_peaks/macs2_hk_nha_u87_mut/HK_Mut_treat_pileup.bdg \
    --c1 /home/spianka/Desktop/macs/macs_peaks/macs2_hk_nha_u87_wt/HK_WT_control_lambda.bdg \
    --t2 /home/spianka/Desktop/macs/macs_peaks/macs2_hk_nha_u87_mut/HK_Mut_treat_pileup.bdg \
    --c2 /home/spianka/Desktop/macs/macs_peaks/macs2_hk_nha_u87_wt/HK_WT_control_lambda.bdg \
    --o-prefix HK_NHA_U87_diff -g 60 -l 120
```

```
/home/spianka/miniconda3/bin/macs2 bdgdiff
    --t1 /home/spianka/Desktop/macs/macs_peaks/macs2_hk_mut/HK_Mut_treat_pileup.bdg \
    --c1 /home/spianka/Desktop/macs/macs_peaks/macs2_hk_wt/HK_WT_control_lambda.bdg \
    --t2 /home/spianka/Desktop/macs/macs_peaks/macs2_hk_mut/HK_Mut_treat_pileup.bdg \
    --c2 /home/spianka/Desktop/macs/macs_peaks/macs2_hk_wt/HK_WT_control_lambda.bdg \
    --o-prefix HK_diff -g 60 -l 120
```

Top 10 MACS2 sites

```
## UCSC track 'common (peaks)'
## UCSCData object with 10 ranges and 2 metadata columns:
##          seqnames        ranges strand |                    name     score
##             <Rle>     <IRanges>  <Rle> |             <character> <numeric>
##    [1] GL000008.2     1954-2122      * |  HK_NHA_U86_diff_common_1         0
##    [2] GL000008.2     2195-2496      * |  HK_NHA_U86_diff_common_2         0
##    [3] GL000008.2     2588-2898      * |  HK_NHA_U86_diff_common_3         0
##    [4] GL000008.2     2987-5549      * |  HK_NHA_U86_diff_common_4         0
##    [5] GL000008.2 151783-151951      * |  HK_NHA_U86_diff_common_5         0
##    [6] GL000008.2 154168-154356      * |  HK_NHA_U86_diff_common_6         0
##    [7] GL000009.2   60618-60919      * |  HK_NHA_U86_diff_common_7         0
##    [8] GL000194.1   54737-55497      * |  HK_NHA_U86_diff_common_8         0
##    [9] GL000194.1  55660-115046      * |  HK_NHA_U86_diff_common_9         0
##   [10] GL000195.1   30761-30929      * | HK_NHA_U86_diff_common_10         0
##   -------
##   seqinfo: 55 sequences from an unspecified genome; no seqlengths
```

Model 3: ExomePeak

ExomePeak is run in R, using one command for peak calling through output. Changing the selection of files in the introduction will determine which set of files are created using this block of code.

```
samples.m6a <- paste0(bam_files, samples,".m6A.bam")
samples.inp <- paste0(bam_files, samples,".input.bam")

result.ep <- exomepeak(GENE_ANNO_GTF=gtf,
                       IP_BAM=samples.m6a[grepl("WT", samples.m6a)],
                       TREATED_IP_BAM = samples.m6a[grepl("Mut", samples.m6a)],
                       INPUT_BAM=samples.inp[grepl("WT", samples.m6a)],
                       OUTPUT_DIR=paste0(macs,"/exomePeak_output_", sample),
                       TREATED_INPUT_BAM = samples.m6a[grepl("Mut", samples.m6a)])
```

```
## GRanges object with 10 ranges and 5 metadata columns:
##        seqnames          ranges strand |              name     score
##           <Rle>       <IRanges>  <Rle> |       <character> <numeric>
##    [1]     chr1 1054949-1055698      + | ENSG00000188157.15  3.3e-189
##    [2]     chr1 1055033-1056030      + |  ENSG00000242590.1  3.3e-189
##    [3]     chr1 1232565-1233579      + |  ENSG00000176022.7  3.6e-143
##    [4]     chr1 1233639-1234206      + |  ENSG00000176022.7  4.5e-114
##    [5]     chr1 1234355-1235041      + |  ENSG00000176022.7  6.7e-155
```

```
##    [6]     chr1 1327322-1328896      + |  ENSG00000224051.7  3.3e-189
##    [7]     chr1 1400560-1401392      + |  ENSG00000224870.7  9.3e-166
##    [8]     chr1 2229336-2232587      + | ENSG00000157933.10  1.2e-123
##    [9]     chr1 2306953-2308060      + | ENSG00000157933.10  3.3e-189
##   [10]     chr1 2308120-2308419      + | ENSG00000157933.10     5e-78
##            itemRgb           thick          blocks
##        <character>       <IRanges>   <IRangesList>
##    [1]        <NA> 1054949-1055698          1-750
##    [2]        <NA> 1055033-1056030   1-183,866-998
##    [3]        <NA> 1232565-1233579         1-1015
##    [4]        <NA> 1233639-1234206          1-568
##    [5]        <NA> 1234355-1235041          1-687
##    [6]        <NA> 1327322-1328896         1-1575
##    [7]        <NA> 1400560-1401392          1-833
##    [8]        <NA> 2229336-2232587 1-400,3144-3252
##    [9]        <NA> 2306953-2308060         1-1108
##   [10]        <NA> 2308120-2308419          1-300
##   -------
##   seqinfo: 23 sequences from an unspecified genome; no seqlengths
```

Gene-level RNAseq using DESeq2

RNAseq here is gene-level, using INPUT counts from RADAR.

```
# Find gene counts
counts_hk <- RNA_seq@geneSum #INPUT counts from RADAR
#counts_hk <- as.data.frame(radar@ip_adjExpr_filtered) #IP counts from RADAR

filter <- as.character(dimnames(RNA_seq@ip_adjExpr_filtered)[[1]])
filter <- unique(gsub("\\,[0-9]*","",filter))
counts_filter <- round(counts_hk[dimnames(counts_hk)[[1]] %in% filter,])
```

Build the model, including an experiment matrix and column definitions.

```
length <- ncol(counts_hk)
treatment <- c(rep("WT", length/2), rep("Mut", length/2))
coldata <- DataFrame(Treatment = treatment,
                     row.names = dimnames(counts_filter)[[2]])

# Experiment matrix
ddsMat <- DESeqDataSetFromMatrix(countData = counts_filter,
                                 colData = coldata,
                                 ~ Treatment)
```

Run the model using R function `DESeq()` and extract results

```
# DESeq runs model
DESeq <- DESeq(ddsMat)
res <- results(DESeq,
               contrast = c("Treatment", "Mut", "WT"))

# Extract results from model
RNAseq <- data.frame(name = res@rownames,
                     log2fc = res@listData$log2FoldChange,
                     p = res@listData$pvalue)
```

RNAseq Output

```
RNAseq <- merge(RNAseq,G_list,
                by.x="name",
                by.y="gene")

write.csv(RNAseq, paste0(rnaseq, sample,"_RNAseq.csv"), row.names = FALSE)
```

```
cat /home/spianka/Desktop/ont/mpores/master_of_pores/NanoPreprocess/params.config
```

```
## params {
##     kit                 = "SQK-RNA002"
##     flowcell            = "FLO-MIN106"
##     fast5               = "/home/spianka/Desktop/Nanopore_Data/data/FAM95931/*.fast5"
##     reference           = "/home/spianka/Desktop/ont/mpores/master_of_pores/GRCh38.primary_assembly.
genome.fa"
##     annotation          = "/home/spianka/Desktop/ont/mpores/master_of_pores/output/FAM95931/gencode.
v38.chr_patch_hapl_scaff_annotation.gtf"
##     ref_type            = "genome"
##
##     seq_type            = "RNA"
##     output              = "/home/spianka/Desktop/ont/mpores/master_of_pores/output/FAM95931/gluc"
##     qualityqc           = 5
##     granularity         = "200"
##
##     basecaller          = "guppy"
##     basecaller_opt      = ""
##     GPU                 = "OFF"
##     demultiplexing      = "OFF"
##     demultiplexing_opt  = "-m pAmps-final-actrun_newdata_nanopore_UResNet20v2_model.030.h5"
##
##     filter              = ""
##     filter_opt          = ""
##
##     mapper              = "minimap2"
##     mapper_opt          = "-uf -k14"
##     map_type            = "spliced"
##
##     counter             = "YES"
##     counter_opt         = ""
##     email               = ""
## }
```

NanoPreprocess.nf controls the processing of files from raw signial (.fast5 files) through to aligned reads (.bam). This is a computationally intensive task, which is sped up 10x by using a strong GPU. Running NanoPreprocess looks like this:

```
nextflow nanopreprocess.nf
```

Nanopreprocess creates a number of output files, including the all-important aligned .bam file, aligned to the reference genome using minimap2. This next section isolates chromosome 1 and

```
cd /home/spianka/Desktop/ont/mpores/master_of_pores/output/FAM95931/alignment
samtools view -b FAM95931.minimap2.sorted.bam chr1 > bam/chr1.bam
```

`Epinano_Variants.py` is a Python script which processes the bam file and basecalling quality data and transforms the .bam file into a per-base .csv file for + and - strand with per-base read quality statistics. These quality statistics are based on overall read quality, number of mismatches, insertions, and deletions across the aligned reads at a site on the genome.

```
cd /home/spianka/Desktop/ont/mpores/master_of_pores
python /home/spianka/Desktop/ont/mpores/epinano/EpiNano/Epinano_Variants.py -n 20 \
      -R GRCh38.primary_assembly.genome.fa \
      -b output/FAM95931/alignment/bam/chr1.bam \
      -s /home/spianka/Desktop/ont/mpores/jvarkit/dist/sam2tsv.jar --type g
```

The + and - strand files are large, and to aggregate the data into 5-mer windows a Python script (`Slide_Variants.py`) must be slid through the per-base files to change from per-base to per-5mer output.

```
cd /home/spianka/Desktop/ont/mpores/master_of_pores
python /home/spianka/Desktop/ont/mpores/epinano/EpiNano/misc/Slide_Variants.py per_site/chr1.plus_stran
d.per.site.csv 5
python /home/spianka/Desktop/ont/mpores/epinano/EpiNano/misc/Slide_Variants.py per_site/chr1.minus_stra
nd.per.site.csv 5
```

These sites are filtered to only include RRACH motifs at this stage, otherwise the machine learning error detection takes a long time.

```
awk -F"," 'NR==1; NR > 1{if($1=="AAACA" || $1=="AAACT" || $1=="GAACT" || $1=="GGACA" || $1=="AGACT" ||
$1=="GGACT" || \
          $1=="AAACC" || $1=="AGACC" || $1=="GAACC" || $1=="GAACA" || $1=="AGACA" || $1=="GGACC") prin
t}' \
      chr1.plus_strand.per.site.csv.per_site.5mer.csv > chr_1_plus_RRACH.csv
```

```
awk -F"," 'NR==1; NR > 1{if($1=="AAACA" || $1=="AAACT" || $1=="GAACT" || $1=="GGACA" || $1=="AGACT" || $1=="GGACT" || \
          $1=="AAACC" || $1=="AGACC" || $1=="GAACC" || $1=="GAACA" || $1=="AGACA" || $1=="GGACC") print t}' \
      chr1.minus_strand.per.site.csv.per_site.5mer.csv > chr_1_minus_RRACH.csv
```

Error detection is performed by `Epinano_Predict.py` uses trained models to predict methylated sites in the list of slid 5-mer windows. `rrach.q3.mis3.del3.linear.dump` indicates that the training models used have been trained on column 3, which indicate errors that predict m6A sites in particular.

```
cd /home/spianka/Desktop/ont/mpores/master_of_pores/output/FAM95931/alignment
python /home/spianka/Desktop/ont/mpores/epinano/EpiNano/Epinano_Predict.py \
      --model /home/spianka/Desktop/ont/mpores/epinano/EpiNano/models/rrach.q3.mis3.del3.linear.dump \
      --predict kmer/chr_1_plus_RRACH.csv \
      --out_prefix chr_1_plus \
      --columns 8,13,23

python /home/spianka/Desktop/ont/mpores/epinano/EpiNano/Epinano_Predict.py \
      --model /home/spianka/Desktop/ont/mpores/epinano/EpiNano/models/rrach.q3.mis3.del3.linear.dump \
      --predict kmer/chr_1_minus_RRACH.csv \
      --out_prefix chr_1_minus \
      --columns 8,13,23
```

A list of EpiNano sites looks like this.

```
cd /home/spianka/Desktop/ont/mpores/master_of_pores/output/FAM95931/alignment/net
cat chr_1_plus.q3.mis3.del3.MODEL.rrach.q3.mis3.del3.linear.dump.csv | awk 'NR < 5'| awk '{print $1, $2, $4, $3, $28, $29 }'| column -t -s,
```

```
## #Kmer  Window         Ref  Strand  Coverage   q1    q2    q3        q4        q5    mis1  mis2  mis3
mis4  mis5     ins1  ins2  ins3  ins4  ins5  del1  del2  del3  del4  del5     prediction  dist
ProbM               ProbU
## AAACA  629744-629748  0    +       5:5:5:5:5  24.0  21.2  17.6      15.2      4.0   1.0   1.0   1.0
1.0   0.4      0.0   0.0   0.0   0.0   0.0   0.0   0.0   0.0   0.6      unm         0.37008187463
93608   0.3402664067452102   0.6597335932547899
## AAACC  629783-629787  0    +       5:5:5:5:5  24.8  21.2  20.8      15.25     18.0  1.0   1.0   1.0
0.8   1.0      0.0   0.0   0.0   0.0   0.0   0.0   0.0   0.0   0.2   0.0      unm         1.36914044441
17765   0.10742333451782397  0.8925766654821758
## GGACA  629883-629887  0    +       3:3:3:3:3  18.0  18.0  12.66667  12.33333  25.5  1.0   1.0   1.0
1.0   0.66667  0.0   0.0   0.0   0.0   0.0   0.0   0.0   0.0   0.33333  mod         -1.1701323797
394778  0.8290366059912101   0.1709633940087901
```

Read Files After Runs

This is a checkpoint, before which all files are saved in anticipation of intersecting the ranges. This section proceeds by reading files in from the three peak calling models and converting them to genomic ranges objects for intersection. If the counting and models have already been run, this is essentially the start of the program. We start here with peaks identified for each model, and proceed to intersect them.

First, read the RADAR results.

```
RADAR_HK <- read.csv(paste0(radara, "differential_loci_fdr_HK.csv"))
RADAR_HK_NHA_U87 <- read.csv(paste0(radara, "differential_loci_fdr_HK_NHA_U87.csv"))

RADAR_HK_grange <- GRanges(seqnames = RADAR_HK$chr,
                           IRanges(RADAR_HK$start, RADAR_HK$end),
                           strand = RADAR_HK$strand)

RADAR_HK_NHA_U87_grange <- GRanges(seqnames = RADAR_HK$chr,
                                   IRanges(RADAR_HK$start, RADAR_HK$end),
                                   strand = RADAR_HK$strand)
```

Second, read the MACS2 results.

```
macs2_hk_nha_u87_granges <- import.bed("/home/spianka/Desktop/macs/macs2_hk_nha_u87_diff/HK_NHA_U87_diff_c3.0_common.bed")
macs2_hk_granges <- import.bed("/home/spianka/Desktop/macs/macs2_hk_diff/HK_diff_c3.0_common.bed")

write.csv(as.data.frame(macs2_hk_granges),
          "/home/spianka/Desktop/macs/macs2_hk_diff/HK_diff_c3.0_common.csv")
write.csv(as.data.frame(macs2_hk_nha_u87_granges),
          "/home/spianka/Desktop/macs/macs2_hk_nha_u87_diff/HK_NHA_U87_diff_c3.0_common.csv")
```

```
macs2_hk_granges <- GRanges(seqnames = macs2_hk_granges@seqnames,
                            IRanges(macs2_hk_granges@ranges@start,
                                    macs2_hk_granges@ranges@start +
                                      macs2_hk_granges@ranges@width),
                            strand = macs2_hk_granges@strand)

macs2_hk_nha_u87_granges <- GRanges(seqnames = macs2_hk_nha_u87_granges@seqnames,
                                    IRanges(macs2_hk_nha_u87_granges@ranges@start,
                                            macs2_hk_nha_u87_granges@ranges@start +
                                              macs2_hk_nha_u87_granges@ranges@width),
                                    strand = macs2_hk_nha_u87_granges@strand)
```

Third, read the ExomePeak results

```
result.hk.nha.u87 <-
  import.bed("/home/spianka/Desktop/macs/exomePeak_output_hk_nha_u87/con_sig_diff_peak.bed")
result.hk <-
  import.bed("/home/spianka/Desktop/macs/exomePeak_output_hk/con_sig_diff_peak.bed")

result.hk.nha.u87.granges <- GRanges(seqnames = result.hk.nha.u87@seqnames,
                                     IRanges(result.hk.nha.u87@ranges@start,
                                             result.hk.nha.u87@ranges@start +
                                               result.hk.nha.u87@ranges@width),
                                     strand = result.hk.nha.u87@strand)

result.hk.granges <- GRanges(seqnames = result.hk@seqnames,
                             IRanges(result.hk@ranges@start,
                                     result.hk@ranges@start +
                                       result.hk@ranges@width),
                             strand = result.hk@strand)
```

Find Intersection

Intersect the ranges, ignoring strand information.

```
hk.intersect <- GenomicRanges::intersect(RADAR_HK_grange,
                                         result.hk.granges,
                                         ignore.strand = T)

hk.nha.u87.intersect <- GenomicRanges::intersect(RADAR_HK_NHA_U87_grange,
                                                 result.hk.nha.u87.granges,
                                                 ignore.strand = T)

hk.intersect <-  GenomicRanges::intersect(hk.intersect,
                                          macs2_hk_granges,
                                          ignore.strand = T)

hk.nha.u87.intersect <-  GenomicRanges::intersect(hk.intersect,
                                                  macs2_hk_nha_u87_granges,
                                                  ignore.strand = T)
```

Create final .csv files.

```
#HK

bins_hk <- RADAR_HK
bins_hk <- subset(bins_hk, !grepl(",",bins_hk$blockSizes))
bins_hk$blockSizes <- as.numeric(bins_hk$blockSizes)

bins_hk <- subset(bins_hk, select = c(chr, start, end,
                                      logFC, p_value,
                                      ensembl_gene_id, name))
bins_hk <- makeGRangesFromDataFrame(bins_hk,
                                    ignore.strand = TRUE,
                                    keep.extra.columns=TRUE)

p_vals_hk <- mergeByOverlaps(bins_hk, hk.intersect)
output <- as.data.frame(p_vals_hk@listData$bins, row.names = NULL)
write.csv(output, paste0(macs,"/hk_combination.csv"))

#HK-NHA-U87
```

```
bins_hk_plus <- RADAR_HK_NHA_U87
bins_hk_plus <- subset(bins_hk_plus, !grepl(",",bins_hk_plus$blockSizes))
bins_hk_plus$blockSizes <- as.numeric(bins_hk_plus$blockSizes)

bins_hk_plus <- subset(bins_hk_plus, select = c(chr, start, end,
                                        logFC, p_value,
                                        ensembl_gene_id, name))
bins_hk_plus <- makeGRangesFromDataFrame(bins_hk_plus,
                                       ignore.strand = TRUE,
                                       keep.extra.columns=TRUE)

p_vals_hk_plus <- mergeByOverlaps(bins_hk_plus, hk.intersect)
output <- as.data.frame(p_vals_hk_plus@listData$bins, row.names = NULL)
write.csv(output, paste0(macs,"/hk_nha_u87_combination.csv"))
```

The following is a one-off 1600-page pdf with one page for every gene with a significant bin. Each page starts with a stacked bar chart of the overall intensity of methylation according to RADAR, followed by breakout charts for each identified bin, some range within the top chart. The ranges are denoted on the top chart with a black line segment.

```
    results <- read.csv(paste0(rnaseq,"/hk_nha_u87_combo_rna_seq.csv"),
                        stringsAsFactors = F)

    genes <- unique(results$ensembl_gene_id)

    genes <- subset(genes, !(genes %in% c("AC073283.3", "CASP8AP2" )))

    pdf(paste0("peak_charts_hk_nha_u87.pdf"),
        width = 8.5, height = 11,
        title = "")

    for (j in c(1:length(genes))) {
        cat(genes[j], "\n")
        gene <- genes[j]
        #gene <- "AC002310.4"
        gene_bins <- subset(results, results$ensembl_gene_id == gene)[]
        if(nrow(gene_bins) != 0) {
            gene_bins <- gene_bins[order(gene_bins$start),]
            segment_data = data.frame(
                x = gene_bins$start,
                xend = gene_bins$end,
                y = rep(30, nrow(gene_bins)),
                yend = rep(30, nrow(gene_bins))
            )

            if(nrow(gene_bins)>6) {gene_bins <- gene_bins[c(1:6),]}
            tryCatch({
                p <- plotGeneCov(radar_post,
                                 geneName = unique(gene_bins$name),
                                 center = mean,
                                 adjustExprLevel = FALSE,
                                 libraryType = "opposite") +
                    theme(plot.title = element_text(size = 8, face = "plain"),
                          legend.text = element_text(size = 8, face = "plain"),
                          axis.title = element_text(size = 8, face = "plain"),
                          axis.text = element_text(size = 8, face = "plain"),
                          legend.title = element_text(size = 8, face = "plain"),
                          axis.line = element_line(size = 1, colour = "black")) +
                    geom_segment(data = segment_data,
                                 aes(x = x,
                                     y = y,
                                     xend = xend,
                                     yend = yend)) +
                    ggtitle(paste0("Gene: ",
                                   unique(gene_bins$ensembl_gene_id),
                                   "\nRNAseq INPUT p-value: ",
                                   unique(signif(gene_bins$p, 2)),
                                   "\nRNAseq INPUT LogFC: ",
                                   unique(round(gene_bins$log2fc, 2))))
            }, error=function(e){cat("ERROR :",conditionMessage(e), "\n")})

            plots <- list(p)

            for(k in 1:nrow(gene_bins)) {
                tryCatch({
```

```
                p_sub <- plotGeneCov(radar_post,
                                     geneName = unique(gene_bins$name),
                                     center = mean,
                                     adjustExprLevel = FALSE,
                                     ZoomIn = c(gene_bins$start[k],
                                                gene_bins$end[k]),
                                     libraryType = "opposite") +
                    theme(plot.title = element_text(size = 8, face = "plain"),
                          legend.text = element_text(size = 8, face = "plain"),
                          axis.title = element_text(size = 8, face = "plain"),
                          axis.text = element_text(size = 8, face = "plain"),
                          legend.title = element_text(size = 8, face = "plain"),
                          axis.line = element_line(size = 1, colour = "black"))  +
                    ggtitle(paste0("Gene: ", unique(gene_bins$ensembl_gene_id),
                                   "\nComb. p-value: ",
                                   signif(gene_bins[k,]$p_value, 2),
                                   "    Max. logFC: ",
                                   as.character(round(gene_bins[k,]$logFC, 2))))
            }, error=function(e){cat("ERROR :",conditionMessage(e), "\n")})

            p_sub <- list(p_sub)
            plots <- base::append(plots, p_sub)
        }

        gridl <- c(1,seq(1,7,1))
        gridl <- matrix(gridl, nrow = 4, ncol = 2, byrow = T)

        blanks <- list()
        blank <- list(grid.rect(gp=gpar(col="white")))
        for(l in c(1:(7-length(plots)))) {
            blanks <- append(blanks, blank)
        }

        plots2 <- append(plots, blanks)
        tryCatch({
            grid.arrange(
                grobs = plots,
                layout_matrix = gridl)
        }, error=function(e){cat("ERROR :",conditionMessage(e), "\n")})
    }

}

dev.off()
```

Example Page for gene ADAT3

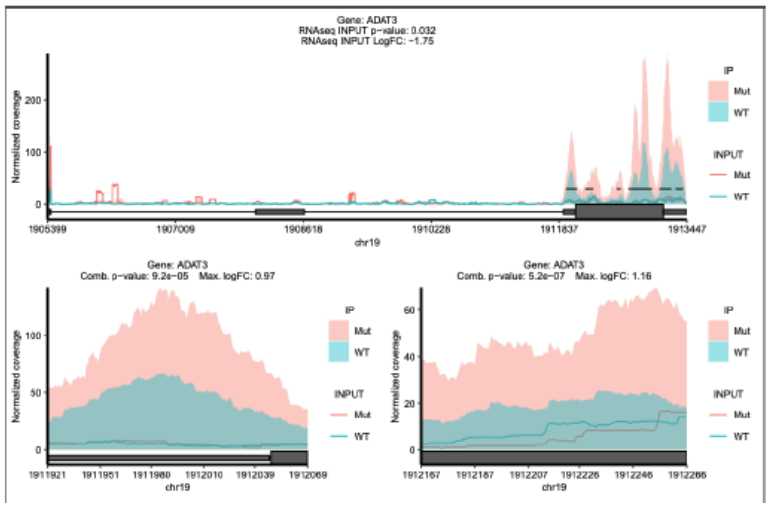

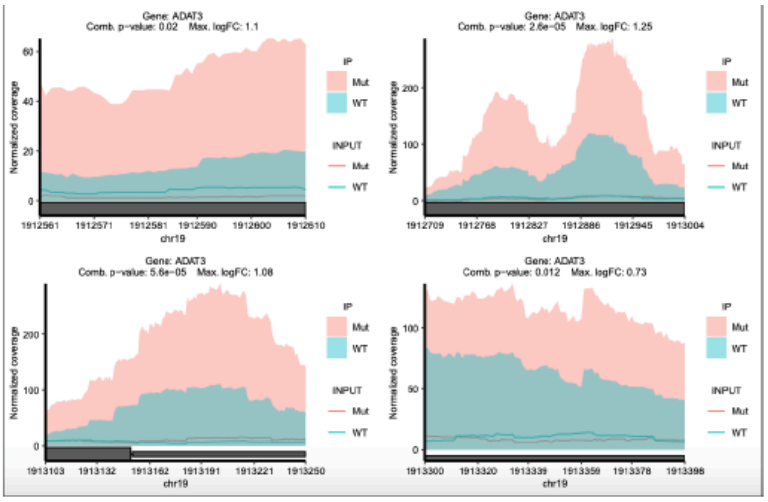

Gene CEBPB with basecalling errors included alongside RADAR bins, height indicates significance.

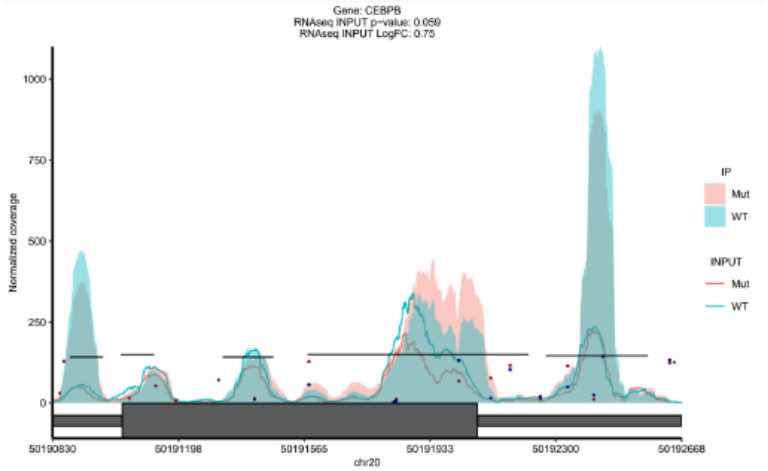

REFERENCES

Aas, A., Isakson, P., Bindesbøll, C., Alemu, E.A., Klungland, A., and Simonsen, A. (2017). Nucleocytoplasmic Shuttling of FTO Does Not Affect Starvation-Induced Autophagy. PLOS ONE *12*, e0168182.

Aik, W., Scotti, J.S., Choi, H., Gong, L., Demetriades, M., Schofield, C.J., and McDonough, M.A. (2014). Structure of human RNA N^6-methyladenine demethylase ALKBH5 provides insights into its mechanisms of nucleic acid recognition and demethylation. Nucleic Acids Res *42*, 4741–4754.

Alarcón, C.R., Lee, H., Goodarzi, H., Halberg, N., and Tavazoie, S.F. (2015). N6-methyladenosine marks primary microRNAs for processing. Nature *519*, 482–485.

Alikhani, M., Alikhani, Z., and Graves, D.T. (2005). FOXO1 functions as a master switch that regulates gene expression necessary for tumor necrosis factor-induced fibroblast apoptosis. J Biol Chem *280*, 12096–12102.

Anders, M., Chelysheva, I., Goebel, I., Trenkner, T., Zhou, J., Mao, Y., Verzini, S., Qian, S.-B., and Ignatova, Z. (2018). Dynamic m6A methylation facilitates mRNA triaging to stress granules. Life Science Alliance *1*.

Angelastro, J.M., Ignatova, T.N., Kukekov, V.G., Steindler, D.A., Stengren, G.B., Mendelsohn, C., and Greene, L.A. (2003). Regulated expression of ATF5 is required for the progression of neural progenitor cells to neurons. J Neurosci *23*, 4590–4600.

Angelastro, J.M., Mason, J.L., Ignatova, T.N., Kukekov, V.G., Stengren, G.B., Goldman, J.E., and Greene, L.A. (2005). Downregulation of activating transcription factor 5 is required for differentiation of neural progenitor cells into astrocytes. J Neurosci *25*, 3889–3899.

Angelastro, J.M., Canoll, P.D., Kuo, J., Weicker, M., Costa, A., Bruce, J.N., and Greene, L.A. (2006). Selective destruction of glioblastoma cells by interference with the activity or expression of ATF5. Oncogene *25*, 907–916.

Balss, J., Meyer, J., Mueller, W., Korshunov, A., Hartmann, C., and von Deimling, A. (2008). Analysis of the IDH1 codon 132 mutation in brain tumors. Acta Neuropathol *116*, 597–602.

Balss, J., Pusch, S., Beck, A.-C., Herold-Mende, C., Krämer, A., Thiede, C., Buckel, W., Langhans, C.-D., Okun, J.G., and von Deimling, A. (2012). Enzymatic assay for quantitative analysis of (d)-2-hydroxyglutarate. Acta Neuropathol *124*, 883–891.

Begik, O., Lucas, M.C., Pryszcz, L.P., Ramirez, J.M., Medina, R., Milenkovic, I., Cruciani, S., Liu, H., Vieira, H.G.S., Sas-Chen, A., et al. (2021). Quantitative profiling of native RNA modifications and their dynamics using nanopore sequencing. BioRxiv 2020.07.06.189969.

Berger, J., Hauber, J., Hauber, R., Geiger, R., and Cullen, B.R. (1988). Secreted placental alkaline phosphatase: a powerful new quantitative indicator of gene expression in eukaryotic cells. Gene *66*, 1–10.

Bokar, J.A., Shambaugh, M.E., Polayes, D., Matera, A.G., and Rottman, F.M. (1997). Purification and cDNA cloning of the AdoMet-binding subunit of the human mRNA (N6-adenosine)-methyltransferase. RNA *3*, 1233–1247.

Bowman, R.L., Wang, Q., Carro, A., Verhaak, R.G.W., and Squatrito, M. (2017). GlioVis data portal for visualization and analysis of brain tumor expression datasets. Neuro Oncol *19*, 139–141.

Brennan, C.W., Verhaak, R.G.W., McKenna, A., Campos, B., Noushmehr, H., Salama, S.R., Zheng, S., Chakravarty, D., Sanborn, J.Z., Berman, S.H., et al. (2013). The Somatic Genomic Landscape of Glioblastoma. Cell *155*, 462–477.

Bunse, L., Pusch, S., Bunse, T., Sahm, F., Sanghvi, K., Friedrich, M., Alansary, D., Sonner, J.K., Green, E., Deumelandt, K., et al. (2018). Suppression of antitumor T cell immunity by the oncometabolite (R)-2-hydroxyglutarate. Nat Med *24*, 1192–1203.

Cancer Genome Atlas Research Network, Brat, D.J., Verhaak, R.G.W., Aldape, K.D., Yung, W.K.A., Salama, S.R., Cooper, L.A.D., Rheinbay, E., Miller, C.R., Vitucci, M., et al. (2015). Comprehensive, Integrative Genomic Analysis of Diffuse Lower-Grade Gliomas. N Engl J Med *372*, 2481–2498.

Cates, C.C., Arias, A.D., Nakayama Wong, L.S., Lamé, M.W., Sidorov, M., Cayanan, G., Rowland, D.J., Fung, J., Karpel-Massler, G., Siegelin, M.D., et al. (2016). Regression/eradication of gliomas in mice by a systemically-deliverable ATF5 dominant-negative peptide. Oncotarget *7*, 12718–12730.

Ceccarelli, M., Barthel, F.P., Malta, T.M., Sabedot, T.S., Salama, S.R., Murray, B.A., Morozova, O., Newton, Y., Radenbaugh, A., Pagnotta, S.M., et al. (2016). Molecular Profiling Reveals Biologically Discrete Subsets and Pathways of Progression in Diffuse Glioma. Cell *164*, 550–563.

Chen, T., Hao, Y.-J., Zhang, Y., Li, M.-M., Wang, M., Han, W., Wu, Y., Lv, Y., Hao, J., Wang, L., et al. (2015). m(6)A RNA methylation is regulated by microRNAs and promotes reprogramming to pluripotency. Cell Stem Cell *16*, 289–301.

Chipuk, J.E., Moldoveanu, T., Llambi, F., Parsons, M.J., and Green, D.R. (2010). The BCL-2 family reunion. Mol Cell *37*, 299–310.

Chowdhury, R., Yeoh, K.K., Tian, Y., Hillringhaus, L., Bagg, E.A., Rose, N.R., Leung, I.K.H., Li, X.S., Woon, E.C.Y., Yang, M., et al. (2011). The oncometabolite 2-hydroxyglutarate inhibits histone lysine demethylases. EMBO Rep *12*, 463–469.

Clifton, I.J., McDonough, M.A., Ehrismann, D., Kershaw, N.J., Granatino, N., and Schofield, C.J. (2006). Structural studies on 2-oxoglutarate oxygenases and related double-stranded β-helix fold proteins. Journal of Inorganic Biochemistry *100*, 644–669.

Cobrinik, D. (2005). Pocket proteins and cell cycle control. Oncogene *24*, 2796–2809.

Cui, Q., Shi, H., Ye, P., Li, L., Qu, Q., Sun, G., Sun, G., Lu, Z., Huang, Y., Yang, C.-G., et al. (2017). m6A RNA Methylation Regulates the Self-Renewal and Tumorigenesis of Glioblastoma Stem Cells. Cell Rep *18*, 2622–2634.

Dang, L., and Su, S.-S.M. (2017). Isocitrate Dehydrogenase Mutation and (R)-2-Hydroxyglutarate: From Basic Discovery to Therapeutics Development. Annu Rev Biochem *86*, 305–331.

Dang, L., White, D.W., Gross, S., Bennett, B.D., Bittinger, M.A., Driggers, E.M., Fantin, V.R., Jang, H.G., Jin, S., Keenan, M.C., et al. (2009). Cancer-associated IDH1 mutations produce 2-hydroxyglutarate. Nature *462*, 739–744.

Deng, G., Shen, J., Yin, M., McManus, J., Mathieu, M., Gee, P., He, T., Shi, C., Bedel, O., McLean, L.R., et al. (2015). Selective inhibition of mutant isocitrate dehydrogenase 1 (IDH1) via disruption of a metal binding network by an allosteric small molecule. J Biol Chem *290*, 762–774.

Deng, X., Su, R., Weng, H., Huang, H., Li, Z., and Chen, J. (2018a). RNA N6-methyladenosine modification in cancers: current status and perspectives. Cell Res *28*, 507–517.

Deng, X., Su, R., Feng, X., Wei, M., and Chen, J. (2018b). Role of N6-methyladenosine modification in cancer. Curr Opin Genet Dev *48*, 1–7.

Desrosiers, R., Friderici, K., and Rottman, F. (1974). Identification of methylated nucleosides in messenger RNA from Novikoff hepatoma cells. Proc Natl Acad Sci U S A *71*, 3971–3975.

Dluzen, D., Li, G., Tacelosky, D., Moreau, M., and Liu, D.X. (2011). BCL-2 Is a Downstream Target of ATF5 That Mediates the Prosurvival Function of ATF5 in a Cell Type-dependent Manner. Journal of Biological Chemistry *286*, 7705–7713.

Dobin, A., Davis, C.A., Schlesinger, F., Drenkow, J., Zaleski, C., Jha, S., Batut, P., Chaisson, M., and Gingeras, T.R. (2013). STAR: ultrafast universal RNA-seq aligner. Bioinformatics *29*, 15–21.

Dominissini, D., Moshitch-Moshkovitz, S., Schwartz, S., Salmon-Divon, M., Ungar, L., Osenberg, S., Cesarkas, K., Jacob-Hirsch, J., Amariglio, N., Kupiec, M., et al. (2012). Topology of the human and mouse m6A RNA methylomes revealed by m6A-seq. Nature *485*, 201–206.

Du, H., Zhao, Y., He, J., Zhang, Y., Xi, H., Liu, M., Ma, J., and Wu, L. (2016). YTHDF2 destabilizes m(6)A-containing RNA through direct recruitment of the CCR4-NOT deadenylase complex. Nat Commun *7*, 12626.

Du, T., Li, G., Yang, J., and Ma, K. (2020). RNA demethylase Alkbh5 is widely expressed in neurons and decreased during brain development. Brain Research Bulletin *163*, 150–159.

Eckel-Passow, J.E., Lachance, D.H., Molinaro, A.M., Walsh, K.M., Decker, P.A., Sicotte, H., Pekmezci, M., Rice, T., Kosel, M.L., Smirnov, I.V., et al. (2015). Glioma Groups Based on 1p/19q, IDH, and TERT Promoter Mutations in Tumors. N Engl J Med *372*, 2499–2508.

Feng, C., Liu, Y., Wang, G., Deng, Z., Zhang, Q., Wu, W., Tong, Y., Cheng, C., and Chen, Z. (2014). Crystal structures of the human RNA demethylase Alkbh5 reveal basis for substrate recognition. J Biol Chem *289*, 11571–11583.

Feng, J.-H., Guo, X.-P., Chen, Y.-Y., Wang, Z.-J., Cheng, Y.-P., and Tang, Y.-M. (2012). Prognostic significance of IDH1 mutations in acute myeloid leukemia: a meta-analysis. Am J Blood Res *2*, 254–264.

Ferenc, K., Pilžys, T., Garbicz, D., Marcinkowski, M., Skorobogatov, O., Dylewska, M., Gajewski, Z., Grzesiuk, E., and Zabielski, R. (2020). Intracellular and tissue specific expression of FTO protein in pig: changes with age, energy intake and metabolic status. Sci Rep *10*, 13029.

Fischer, M., and Müller, G.A. (2017). Cell cycle transcription control: DREAM/MuvB and RB-E2F complexes. Critical Reviews in Biochemistry and Molecular Biology *52*, 638–662.

Fischer, M., Grossmann, P., Padi, M., and DeCaprio, J.A. (2016). Integration of TP53, DREAM, MMB-FOXM1 and RB-E2F target gene analyses identifies cell cycle gene regulatory networks. Nucleic Acids Res *44*, 6070–6086.

Franken, N.A.P., Rodermond, H.M., Stap, J., Haveman, J., and van Bree, C. (2006). Clonogenic assay of cells in vitro. Nat Protoc *1*, 2315–2319.

Fu, Y., Zheng, Y., Li, K., Huang, R., Zheng, S., An, N., and Liang, A. (2012). Mutations in isocitrate dehydrogenase 2 accelerate glioma cell migration via matrix metalloproteinase-2 and 9. Biotechnol Lett *34*, 441–446.

Fu, Y., Jia, G., Pang, X., Wang, R.N., Wang, X., Li, C.J., Smemo, S., Dai, Q., Bailey, K.A., Nobrega, M.A., et al. (2013). FTO-mediated formation of N6-hydroxymethyladenosine and N6-formyladenosine in mammalian RNA. Nat Commun *4*, 1798.

Fustin, J.-M., Doi, M., Yamaguchi, Y., Hida, H., Nishimura, S., Yoshida, M., Isagawa, T., Morioka, M.S., Kakeya, H., Manabe, I., et al. (2013). RNA-Methylation-Dependent RNA Processing Controls the Speed of the Circadian Clock. Cell *155*, 793–806.

Garrett, M., Sperry, J., Braas, D., Yan, W., Le, T.M., Mottahedeh, J., Ludwig, K., Eskin, A., Qin, Y., Levy, R., et al. (2018). Metabolic characterization of isocitrate dehydrogenase (IDH) mutant and IDH wildtype gliomaspheres uncovers cell type-specific vulnerabilities. Cancer Metab *6*, 4.

Gelman, S.J., Naser, F., Mahieu, N.G., McKenzie, L.D., Dunn, G.P., Chheda, M.G., and Patti, G.J. (2018). Consumption of NADPH for 2-HG Synthesis Increases Pentose Phosphate Pathway Flux and Sensitizes Cells to Oxidative Stress. Cell Rep *22*, 512–522.

Gerken, T., Girard, C.A., Tung, Y.-C.L., Webby, C.J., Saudek, V., Hewitson, K.S., Yeo, G.S.H., McDonough, M.A., Cunliffe, S., McNeill, L.A., et al. (2007). The obesity-associated FTO gene encodes a 2-oxoglutarate-dependent nucleic acid demethylase. Science *318*, 1469–1472.

Geula, S., Moshitch-Moshkovitz, S., Dominissini, D., Mansour, A.A., Kol, N., Salmon-Divon, M., Hershkovitz, V., Peer, E., Mor, N., Manor, Y.S., et al. (2015). Stem cells. m6A mRNA methylation facilitates resolution of naïve pluripotency toward differentiation. Science *347*, 1002–1006.

Gobert, R.P., Joubert, L., Curchod, M.-L., Salvat, C., Foucault, I., Jorand-Lebrun, C., Lamarine, M., Peixoto, H., Vignaud, C., Frémaux, C., et al. (2009). Convergent functional genomics of oligodendrocyte differentiation identifies multiple autoinhibitory signaling circuits. Mol Cell Biol *29*, 1538–1553.

Graessmann, M., Berg, B., Fuchs, B., Klein, A., and Graessmann, A. (2007). Chemotherapy resistance of mouse WAP-SVT/t breast cancer cells is mediated by osteopontin, inhibiting apoptosis downstream of caspase-3. Oncogene *26*, 2840–2850.

Gryder, B.E., Yohe, M.E., Chou, H.-C., Zhang, X., Marques, J., Wachtel, M., Schaefer, B., Sen, N., Song, Y., Gualtieri, A., et al. (2017). PAX3-FOXO1 Establishes Myogenic Super Enhancers and Confers BET Bromodomain Vulnerability. Cancer Discov *7*, 884–899.

Gulati, P., Avezov, E., Ma, M., Antrobus, R., Lehner, P., O'Rahilly, S., and Yeo, G.S.H. (2014). Fat mass and obesity-related (FTO) shuttles between the nucleus and cytoplasm. Biosci Rep *34*, e00144.

Hai, T.W., Liu, F., Coukos, W.J., and Green, M.R. (1989). Transcription factor ATF cDNA clones: an extensive family of leucine zipper proteins able to selectively form DNA-binding heterodimers. Genes Dev *3*, 2083–2090.

Han, D., Liu, J., Chen, C., Dong, L., Liu, Y., Chang, R., Huang, X., Liu, Y., Wang, J., Dougherty, U., et al. (2019). Anti-tumour immunity controlled through mRNA m 6 A methylation and YTHDF1 in dendritic cells. Nature *566*, 270–274.

Hannon, G.J. (2010). FASTX-Toolkit.

Harper, J.E., Miceli, S.M., Roberts, R.J., and Manley, J.L. (1990). Sequence specificity of the human mRNA N6-adenosine methylase in vitro. Nucleic Acids Research *18*, 5735–5741.

Harris, M.H., and Thompson, C.B. (2000). The role of the Bcl-2 family in the regulation of outer mitochondrial membrane permeability. Cell Death Differ *7*, 1182–1191.

Hausinger, R.P. (2004). Fe(II)/α-Ketoglutarate-Dependent Hydroxylases and Related Enzymes. Critical Reviews in Biochemistry and Molecular Biology *39*, 21–68.

Hermisson, M., Klumpp, A., Wick, W., Wischhusen, J., Nagel, G., Roos, W., Kaina, B., and Weller, M. (2006). O6-methylguanine DNA methyltransferase and p53 status predict temozolomide sensitivity in human malignant glioma cells. Journal of Neurochemistry *96*, 766–776.

Hesser, C.R., Karijolich, J., Dominissini, D., He, C., and Glaunsinger, B.A. (2018). N6-methyladenosine modification and the YTHDF2 reader protein play cell type specific roles in lytic viral gene expression during Kaposi's sarcoma-associated herpesvirus infection. PLOS Pathogens *14*, e1006995.

Huang, L.E. (2019). Friend or foe-IDH1 mutations in glioma 10 years on. Carcinogenesis *40*, 1299–1307.

Huang, Y., Yan, J., Li, Q., Li, J., Gong, S., Zhou, H., Gan, J., Jiang, H., Jia, G.-F., Luo, C., et al. (2015). Meclofenamic acid selectively inhibits FTO demethylation of m6A over ALKBH5. Nucleic Acids Research *43*, 373–384.

Huang, Y., Su, R., Sheng, Y., Dong, L., Dong, Z., Xu, H., Ni, T., Zhang, Z.S., Zhang, T., Li, C., et al. (2019). Small-Molecule Targeting of Oncogenic FTO Demethylase in Acute Myeloid Leukemia. Cancer Cell *35*, 677-691.e10.

Ichimura, K., Pearson, D.M., Kocialkowski, S., Bäcklund, L.M., Chan, R., Jones, D.T.W., and Collins, V.P. (2009). IDH1 mutations are present in the majority of common adult gliomas but rare in primary glioblastomas. Neuro Oncol *11*, 341–347.

Jia, G., Fu, Y., Zhao, X., Dai, Q., Zheng, G., Yang, Y., Yi, C., Lindahl, T., Pan, T., Yang, Y.-G., et al. (2011). N6-Methyladenosine in nuclear RNA is a major substrate of the obesity-associated FTO. Nat Chem Biol *7*, 885–887.

Kang, M.R., Kim, M.S., Oh, J.E., Kim, Y.R., Song, S.Y., Seo, S.I., Lee, J.Y., Yoo, N.J., and Lee, S.H. (2009). Mutational analysis of IDH1 codon 132 in glioblastomas and other common cancers. Int J Cancer *125*, 353–355.

Khurshed, M., Aarnoudse, N., Hulsbos, R., Hira, V.V.V., van Laarhoven, H.W.M., Wilmink, J.W., Molenaar, R.J., and van Noorden, C.J.F. (2018). IDH1-mutant cancer cells are sensitive to cisplatin and an IDH1-mutant inhibitor counteracts this sensitivity. FASEB J fj201800547R.

Kinsey, M., Smith, R., and Lessnick, S.L. (2006). NR0B1 is required for the oncogenic phenotype mediated by EWS/FLI in Ewing's sarcoma. Mol Cancer Res *4*, 851–859.

Knuckles, P., Lence, T., Haussmann, I.U., Jacob, D., Kreim, N., Carl, S.H., Masiello, I., Hares, T., Villaseñor, R., Hess, D., et al. (2018). Zc3h13/Flacc is required for adenosine methylation by bridging the mRNA-binding factor Rbm15/Spenito to the m6A machinery component Wtap/Fl(2)d. Genes Dev *32*, 415–429.

Koinuma, D., Tsutsumi, S., Kamimura, N., Taniguchi, H., Miyazawa, K., Sunamura, M., Imamura, T., Miyazono, K., and Aburatani, H. (2009). Chromatin Immunoprecipitation on Microarray Analysis of Smad2/3 Binding Sites Reveals Roles of ETS1 and TFAP2A in Transforming Growth Factor β Signaling. Mol Cell Biol *29*, 172–186.

Kölker, S., Pawlak, V., Ahlemeyer, B., Okun, J.G., Hörster, F., Mayatepek, E., Krieglstein, J., Hoffmann, G.F., and Köhr, G. (2002). NMDA receptor activation and respiratory chain complex V inhibition contribute to neurodegeneration in d-2-hydroxyglutaric aciduria. Eur J Neurosci *16*, 21–28.

Konteatis, Z., Artin, E., Nicolay, B., Straley, K., Padyana, A.K., Jin, L., Chen, Y., Narayaraswamy, R., Tong, S., Wang, F., et al. (2020). Vorasidenib (AG-881): A First-in-Class, Brain-Penetrant Dual Inhibitor of Mutant IDH1 and 2 for Treatment of Glioma. ACS Med Chem Lett *11*, 101–107.

Kopinja, J., Sevilla, R.S., Levitan, D., Dai, D., Vanko, A., Spooner, E., Ware, C., Forget, R., Hu, K., Kral, A., et al. (2017). A Brain Penetrant Mutant IDH1 Inhibitor Provides In Vivo Survival Benefit. Sci Rep *7*, 13853.

Kopylova, E., Noé, L., and Touzet, H. (2012). SortMeRNA: fast and accurate filtering of ribosomal RNAs in metatranscriptomic data. Bioinformatics *28*, 3211–3217.

Kranendijk, M., Struys, E.A., van Schaftingen, E., Gibson, K.M., Kanhai, W.A., van der Knaap, M.S., Amiel, J., Buist, N.R., Das, A.M., de Klerk, J.B., et al. (2010). IDH2 mutations in patients with D-2-hydroxyglutaric aciduria. Science *330*, 336.

Kurowski, M.A., Bhagwat, A.S., Papaj, G., and Bujnicki, J.M. (2003). Phylogenomic identification of five new human homologs of the DNA repair enzyme AlkB. BMC Genomics *4*, 48.

Lai, A., Kharbanda, S., Pope, W.B., Tran, A., Solis, O.E., Peale, F., Forrest, W.F., Pujara, K., Carrillo, J.A., Pandita, A., et al. (2011). Evidence for Sequenced Molecular Evolution of IDH1 Mutant Glioblastoma From a Distinct Cell of Origin. JCO *29*, 4482–4490.

Laks, D.R., Crisman, T.J., Shih, M.Y.S., Mottahedeh, J., Gao, F., Sperry, J., Garrett, M.C., Yong, W.H., Cloughesy, T.F., Liau, L.M., et al. (2016). Large-scale assessment of the gliomasphere model system. NEUONC *18*, 1367–1378.

Latini, A., Scussiato, K., Rosa, R.B., Llesuy, S., Belló-Klein, A., Dutra-Filho, C.S., and Wajner, M. (2003). D-2-hydroxyglutaric acid induces oxidative stress in cerebral cortex of young rats. Eur J Neurosci *17*, 2017–2022.

Lazovic, J., Soto, H., Piccioni, D., Lo Ru, J.R., Li, S., Mirsadraei, L., Yong, W., Prins, R., Liau, L.M., Ellingson, B.M., et al. (2012). Detection of 2-hydroxyglutaric acid in vivo by proton magnetic resonance spectroscopy in U87 glioma cells overexpressing isocitrate dehydrogenase-1 mutation. Neuro-Oncology *14*, 1465–1472.

Leng, N., Dawson, J.A., Thomson, J.A., Ruotti, V., Rissman, A.I., Smits, B.M.G., Haag, J.D., Gould, M.N., Stewart, R.M., and Kendziorski, C. (2013). EBSeq: an empirical Bayes hierarchical model for inference in RNA-seq experiments. Bioinformatics *29*, 1035–1043.

Li, B., and Dewey, C.N. (2011). RSEM: accurate transcript quantification from RNA-Seq data with or without a reference genome. BMC Bioinformatics *12*, 323.

Li, A., Chen, Y.-S., Ping, X.-L., Yang, X., Xiao, W., Yang, Y., Sun, H.-Y., Zhu, Q., Baidya, P., Wang, X., et al. (2017a). Cytoplasmic m 6 A reader YTHDF3 promotes mRNA translation. Cell Res *27*, 444–447.

Li, G., Li, W., Angelastro, J.M., Greene, L.A., and Liu, D.X. (2009). Identification of a novel DNA binding site and a transcriptional target for activating transcription factor 5 in c6 glioma and mcf-7 breast cancer cells. Mol Cancer Res *7*, 933–943.

Li, S., Chou, A.P., Chen, W., Chen, R., Deng, Y., Phillips, H.S., Selfridge, J., Zurayk, M., Lou, J.J., Everson, R.G., et al. (2013). Overexpression of isocitrate dehydrogenase mutant proteins renders glioma cells more sensitive to radiation. Neuro-Oncology *15*, 57–68.

Li, S., Chowdhury, R., Liu, F., Chou, A.P., Li, T., Mody, R.R., Lou, J.J., Chen, W., Reiss, J., Soto, H., et al. (2014). Tumor-Suppressive miR148a Is Silenced by CpG Island Hypermethylation in IDH1-Mutant Gliomas. Clin Cancer Res *20*, 5808–5822.

Li, Z., Weng, H., Su, R., Weng, X., Zuo, Z., Li, C., Huang, H., Nachtergaele, S., Dong, L., Hu, C., et al. (2017b). FTO plays an oncogenic role in acute myeloid leukemia as a N6-methyladenosine RNA demethylase. Cancer Cell *31*, 127–141.

Lin, Y.S., and Green, M.R. (1988). Interaction of a common cellular transcription factor, ATF, with regulatory elements in both E1a- and cyclic AMP-inducible promoters. PNAS *85*, 3396–3400.

Linder, B., Grozhik, A.V., Olarerin-George, A.O., Meydan, C., Mason, C.E., and Jaffrey, S.R. (2015). Single-nucleotide-resolution mapping of m6A and m6Am throughout the transcriptome. Nat Methods *12*, 767–772.

Liu, H., Begik, O., Lucas, M.C., Ramirez, J.M., Mason, C.E., Wiener, D., Schwartz, S., Mattick, J.S., Smith, M.A., and Novoa, E.M. (2019a). Accurate detection of m6A RNA modifications in native RNA sequences. Nature Communications *10*, 4079.

Liu, J., Yue, Y., Han, D., Wang, X., Fu, Y., Zhang, L., Jia, G., Yu, M., Lu, Z., Deng, X., et al. (2014). A METTL3–METTL14 complex mediates mammalian nuclear RNA N6-adenosine methylation. Nat Chem Biol *10*, 93–95.

Liu, N., Dai, Q., Zheng, G., He, C., Parisien, M., and Pan, T. (2015). N6-methyladenosine-dependent RNA structural switches regulate RNA–protein interactions. Nature *518*, 560–564.

Liu, W., Sun, M., Jiang, J., Shen, X., Sun, Q., Liu, W., Shen, H., and Gu, J. (2004). Cyclin D3 interacts with human activating transcription factor 5 and potentiates its transcription activity. Biochemical and Biophysical Research Communications *321*, 954–960.

Liu, X.-M., Zhou, J., Mao, Y., Ji, Q., and Qian, S.-B. (2019b). Programmable RNA N6-methyladenosine editing by CRISPR-Cas9 conjugates. Nat Chem Biol *15*, 865–871.

Lorenz, D.A., Sathe, S., Einstein, J.M., and Yeo, G.W. (2020). Direct RNA sequencing enables m6A detection in endogenous transcript isoforms at base-specific resolution. RNA *26*, 19–28.

Love, M.I., Huber, W., and Anders, S. (2014). Moderated estimation of fold change and dispersion for RNA-seq data with DESeq2. Genome Biology *15*, 550.

Lu, C., Ward, P.S., Kapoor, G.S., Rohle, D., Turcan, S., Abdel-Wahab, O., Edwards, C.R., Khanin, R., Figueroa, M.E., Melnick, A., et al. (2012). IDH mutation impairs histone demethylation and results in a block to cell differentiation. Nature *483*, 474–478.

Ma, R., and Yun, C.-H. (2018). Crystal structures of pan-IDH inhibitor AG-881 in complex with mutant human IDH1 and IDH2. Biochemical and Biophysical Research Communications *503*, 2912–2917.

Maiti, B., Li, J., Bruin, A. de, Gordon, F., Timmers, C., Opavsky, R., Patil, K., Tuttle, J., Cleghorn, W., and Leone, G. (2005). Cloning and Characterization of Mouse E2F8, a Novel Mammalian E2F Family Member Capable of Blocking Cellular Proliferation *. Journal of Biological Chemistry *280*, 18211–18220.

Malta, T.M., de Souza, C.F., Sabedot, T.S., Silva, T.C., Mosella, M.S., Kalkanis, S.N., Snyder, J., Castro, A.V.B., and Noushmehr, H. (2018). Glioma CpG island methylator phenotype (G-CIMP): biological and clinical implications. Neuro-Oncology *20*, 608–620.

Mardis, E.R., Ding, L., Dooling, D.J., Larson, D.E., McLellan, M.D., Chen, K., Koboldt, D.C., Fulton, R.S., Delehaunty, K.D., McGrath, S.D., et al. (2009). Recurring Mutations Found by Sequencing an Acute Myeloid Leukemia Genome. N Engl J Med *361*, 1058–1066.

Mason, J.L., Angelastro, J.M., Ignatova, T.N., Kukekov, V.G., Lin, G., Greene, L.A., and Goldman, J.E. (2005). ATF5 regulates the proliferation and differentiation of oligodendrocytes. Mol Cell Neurosci *29*, 372–380.

Mauer, J., Luo, X., Blanjoie, A., Jiao, X., Grozhik, A.V., Patil, D.P., Linder, B., Pickering, B.F., Vasseur, J.-J., Chen, Q., et al. (2017). Reversible methylation of m6Am in the 5’ cap controls mRNA stability. Nature *541*, 371–375.

McTaggart, J.S., Lee, S., Iberl, M., Church, C., Cox, R.D., and Ashcroft, F.M. (2011). FTO Is Expressed in Neurones throughout the Brain and Its Expression Is Unaltered by Fasting. PLoS ONE *6*, e27968.

Meng, J., Lu, Z., Liu, H., Zhang, L., Zhang, S., Chen, Y., Rao, M.K., and Huang, Y. (2014). A protocol for RNA methylation differential analysis with MeRIP-Seq data and exomePeak R/Bioconductor package. Methods *69*, 274–281.

Meyer, K.D., Saletore, Y., Zumbo, P., Elemento, O., Mason, C.E., and Jaffrey, S.R. (2012). Comprehensive Analysis of mRNA Methylation Reveals Enrichment in 3' UTRs and Near Stop Codons. Cell *149*, 1635–1646.

Meyer, K.D., Patil, D.P., Zhou, J., Zinoviev, A., Skabkin, M.A., Elemento, O., Pestova, T.V., Qian, S.-B., and Jaffrey, S.R. (2015). 5' UTR m6A Promotes Cap-Independent Translation. Cell *163*, 999–1010.

Molenaar, R.J., Botman, D., Smits, M.A., Hira, V.V., van Lith, S.A., Stap, J., Henneman, P., Khurshed, M., Lenting, K., Mul, A.N., et al. (2015). Radioprotection of IDH1-Mutated Cancer Cells by the IDH1-Mutant Inhibitor AGI-5198. Cancer Res *75*, 4790–4802.

Molinie, B., Wang, J., Lim, K.S., Hillebrand, R., Lu, Z., Van Wittenberghe, N., Howard, B.D., Daneshvar, K., Mullen, A.C., Dedon, P., et al. (2016). m6A-LAIC-seq reveals the census and complexity of the m6A epitranscriptome. Nat Methods *13*, 692–698.

Molinie, B., Giallourakis, C.C., and Lusser, Alexandra (2017). RNA Methylation: Methods and Protocols (Springer New York).

Monaco, S.E., Angelastro, J.M., Szabolcs, M., and Greene, L.A. (2007). The transcription factor ATF5 is widely expressed in carcinomas, and interference with its function selectively kills neoplastic, but not nontransformed, breast cell lines. Int J Cancer *120*, 1883–1890.

Natsume, A., Wakabayashi, T., Miyakita, Y., Narita, Y., Mineharu, Y., Arakawa, Y., Yamasaki, F., Sugiyama, K., Hata, N., Muragaki, Y., et al. (2019). Phase I study of a brain penetrant mutant IDH1 inhibitor DS-1001b in patients with recurrent or progressive IDH1 mutant gliomas. JCO *37*, 2004–2004.

Nobusawa, S., Watanabe, T., Kleihues, P., and Ohgaki, H. (2009). IDH1 mutations as molecular signature and predictive factor of secondary glioblastomas. Clin Cancer Res *15*, 6002–6007.

Nomura, M., Saito, K., Aihara, K., Nagae, G., Yamamoto, S., Tatsuno, K., Ueda, H., Fukuda, S., Umeda, T., Tanaka, S., et al. (2019). DNA demethylation is associated with malignant progression of lower-grade gliomas. Sci Rep *9*, 1903.

Noushmehr, H., Weisenberger, D.J., Diefes, K., Phillips, H.S., Pujara, K., Berman, B.P., Pan, F., Pelloski, C.E., Sulman, E.P., Bhat, K.P., et al. (2010). Identification of a CpG Island Methylator Phenotype that Defines a Distinct Subgroup of Glioma. Cancer Cell *17*, 510–522.

Ogawa, H., Ishiguro, K., Gaubatz, S., Livingston, D.M., and Nakatani, Y. (2002). A Complex with Chromatin Modifiers That Occupies E2F- and Myc-Responsive Genes in G0 Cells. Science *296*, 1132–1136.

Ostrom, Q.T., Gittleman, H., Liao, P., Vecchione-Koval, T., Wolinsky, Y., Kruchko, C., and Barnholtz-Sloan, J.S. (2017). CBTRUS Statistical Report: Primary brain and other central nervous system tumors diagnosed in the United States in 2010-2014. Neuro Oncol *19*, v1–v88.

Papaemmanuil, E., Gerstung, M., Bullinger, L., Gaidzik, V.I., Paschka, P., Roberts, N.D., Potter, N.E., Heuser, M., Thol, F., Bolli, N., et al. (2016). Genomic Classification and Prognosis in Acute Myeloid Leukemia. N Engl J Med *374*, 2209–2221.

Paris, J., Morgan, M., Campos, J., Spencer, G.J., Shmakova, A., Ivanova, I., Mapperley, C., Lawson, H., Wotherspoon, D.A., Sepulveda, C., et al. (2019). Targeting the RNA m6A Reader YTHDF2 Selectively Compromises Cancer Stem Cells in Acute Myeloid Leukemia. Cell Stem Cell *25*, 137-148.e6.

Park, O.H., Ha, H., Lee, Y., Boo, S.H., Kwon, D.H., Song, H.K., and Kim, Y.K. (2019). Endoribonucleolytic Cleavage of m6A-Containing RNAs by RNase P/MRP Complex. Mol Cell *74*, 494-507.e8.

Parsons, D.W., Jones, S., Zhang, X., Lin, J.C.-H., Leary, R.J., Angenendt, P., Mankoo, P., Carter, H., Siu, I.-M., Gallia, G.L., et al. (2008). An Integrated Genomic Analysis of Human Glioblastoma Multiforme. Science *321*, 1807.

Pati, D., Meistrich, M.L., and Plon, S.E. (1999). Human Cdc34 and Rad6B ubiquitin-conjugating enzymes target repressors of cyclic AMP-induced transcription for proteolysis. Mol Cell Biol *19*, 5001–5013.

Patil, D.P., Pickering, B.F., and Jaffrey, S.R. (2018). Reading m6A in the Transcriptome: m6A-Binding Proteins. Trends in Cell Biology *28*, 113–127.

Perry, R.P., and Kelley, D.E. (1974). Existence of methylated messenger RNA in mouse L cells. Cell *1*, 37–42.

Persengiev, S.P., Devireddy, L.R., and Green, M.R. (2002). Inhibition of apoptosis by ATFx: a novel role for a member of the ATF/CREB family of mammalian bZIP transcription factors. Genes Dev *16*, 1806–1814.

Peters, C.S., Liang, X., Li, S., Kannan, S., Peng, Y., Taub, R., and Diamond, R.H. (2001). ATF-7, a novel bZIP protein, interacts with the PRL-1 protein-tyrosine phosphatase. J Biol Chem *276*, 13718–13726.

Phillips, H.S., Kharbanda, S., Chen, R., Forrest, W.F., Soriano, R.H., Wu, T.D., Misra, A., Nigro, J.M., Colman, H., Soroceanu, L., et al. (2006). Molecular subclasses of high-grade glioma predict prognosis, delineate a pattern of disease progression, and resemble stages in neurogenesis. Cancer Cell *9*, 157–173.

Piaskowski, S., Bienkowski, M., Stoczynska-Fidelus, E., Stawski, R., Sieruta, M., Szybka, M., Papierz, W., Wolanczyk, M., Jaskolski, D.J., Liberski, P.P., et al. (2011). Glioma cells showing

IDH1 mutation cannot be propagated in standard cell culture conditions. Br J Cancer *104*, 968–970.

Ping, X.-L., Sun, B.-F., Wang, L., Xiao, W., Yang, X., Wang, W.-J., Adhikari, S., Shi, Y., Lv, Y., Chen, Y.-S., et al. (2014). Mammalian WTAP is a regulatory subunit of the RNA N6-methyladenosine methyltransferase. Cell Res *24*, 177–189.

Popovici-Muller, J., Saunders, J.O., Salituro, F.G., Travins, J.M., Yan, S., Zhao, F., Gross, S., Dang, L., Yen, K.E., Yang, H., et al. (2012). Discovery of the First Potent Inhibitors of Mutant IDH1 That Lower Tumor 2-HG in Vivo. ACS Med Chem Lett *3*, 850–855.

Pujana, M.A., Han, J.-D.J., Starita, L.M., Stevens, K.N., Tewari, M., Ahn, J.S., Rennert, G., Moreno, V., Kirchhoff, T., Gold, B., et al. (2007). Network modeling links breast cancer susceptibility and centrosome dysfunction. Nat Genet *39*, 1338–1349.

Pusch, S., Krausert, S., Fischer, V., Balss, J., Ott, M., Schrimpf, D., Capper, D., Sahm, F., Eisel, J., Beck, A.-C., et al. (2017). Pan-mutant IDH1 inhibitor BAY 1436032 for effective treatment of IDH1 mutant astrocytoma in vivo. Acta Neuropathol *133*, 629–644.

Remington, M., Chtchetinin, J., Ancheta, K., Nghiemphu, P.L., Cloughesy, T., and Lai, A. (2009). The L84F polymorphic variant of human O6-methylguanine-DNA methyltransferase alters stability in U87MG glioma cells but not temozolomide sensitivity. Neuro Oncol *11*, 22–32.

Richardson, L.G., Choi, B.D., and Curry, W.T. (2019). (R)-2-hydroxyglutarate drives immune quiescence in the tumor microenvironment of IDH-mutant gliomas. Transl Cancer Res *8*, S167–S170.

Rohle, D., Popovici-Muller, J., Palaskas, N., Turcan, S., Grommes, C., Campos, C., Tsoi, J., Clark, O., Oldrini, B., Komisopoulou, E., et al. (2013). An Inhibitor of Mutant IDH1 Delays Growth and Promotes Differentiation of Glioma Cells. Science *340*, 626–630.

Sadasivam, S., and DeCaprio, J.A. (2013). The DREAM complex: master coordinator of cell cycle-dependent gene expression. Nat Rev Cancer *13*, 585–595.

Schmidt, M.C., Antweiler, S., Urban, N., Mueller, W., Kuklik, A., Meyer-Puttlitz, B., Wiestler, O.D., Louis, D.N., Fimmers, R., and von Deimling, A. (2002). Impact of Genotype and Morphology on the Prognosis of Glioblastoma. Journal of Neuropathology & Experimental Neurology *61*, 321–328.

Schnittger, S., Haferlach, C., Ulke, M., Alpermann, T., Kern, W., and Haferlach, T. (2010). IDH1 mutations are detected in 6.6% of 1414 AML patients and are associated with intermediate risk karyotype and unfavorable prognosis in adults younger than 60 years and unmutated NPM1 status. Blood *116*, 5486–5496.

Shi, H., Wang, X., Lu, Z., Zhao, B.S., Ma, H., Hsu, P.J., Liu, C., and He, C. (2017). YTHDF3 facilitates translation and decay of N 6 -methyladenosine-modified RNA. Cell Res *27*, 315–328.

Shi, H., Zhang, X., Weng, Y.-L., Lu, Z., Liu, Y., Lu, Z., Li, J., Hao, P., Zhang, Y., Zhang, F., et al. (2018). m 6 A facilitates hippocampus-dependent learning and memory through YTHDF1. Nature *563*, 249–253.

Shi, H., Wei, J., and He, C. (2019). Where, When, and How: Context-Dependent Functions of RNA Methylation Writers, Readers, and Erasers. Molecular Cell *74*, 640–650.

Siegel, P.M., and Massagué, J. (2003). Cytostatic and apoptotic actions of TGF-beta in homeostasis and cancer. Nat Rev Cancer *3*, 807–821.

Sonoda, Y., Ozawa, T., Hirose, Y., Aldape, K.D., McMahon, M., Berger, M.S., and Pieper, R.O. (2001). Formation of intracranial tumors by genetically modified human astrocytes defines four pathways critical in the development of human anaplastic astrocytoma. Cancer Res *61*, 4956–4960.

Struys, E.A. (2006). D-2-Hydroxyglutaric aciduria: unravelling the biochemical pathway and the genetic defect. J Inherit Metab Dis *29*, 21–29.

Sturm, D., Witt, H., Hovestadt, V., Khuong-Quang, D.-A., Jones, D.T.W., Konermann, C., Pfaff, E., Tönjes, M., Sill, M., Bender, S., et al. (2012). Hotspot Mutations in H3F3A and IDH1 Define Distinct Epigenetic and Biological Subgroups of Glioblastoma. Cancer Cell *22*, 425–437.

Su, R., Dong, L., Li, C., Nachtergaele, S., Wunderlich, M., Qing, Y., Deng, X., Wang, Y., Weng, X., Hu, C., et al. (2018). R-2HG Exhibits Anti-tumor Activity by Targeting FTO/m6A/MYC/CEBPA Signaling. Cell *172*, 90-105.e23.

Su, R., Dong, L., Li, Y., Gao, M., Han, L., Wunderlich, M., Deng, X., Li, H., Huang, Y., Gao, L., et al. (2020). Targeting FTO Suppresses Cancer Stem Cell Maintenance and Immune Evasion. Cancer Cell *38*, 79-96.e11.

Sulkowski, P.L., Corso, C.D., Robinson, N.D., Scanlon, S.E., Purshouse, K.R., Bai, H., Liu, Y., Sundaram, R.K., Hegan, D.C., Fons, N.R., et al. (2017). 2-Hydroxyglutarate produced by neomorphic IDH mutations suppresses homologous recombination and induces PARP inhibitor sensitivity. Sci Transl Med *9*, eaal2463.

Tan, A., Dang, Y., Chen, G., and Mo, Z. (2015). Overexpression of the fat mass and obesity associated gene (FTO) in breast cancer and its clinical implications. Int J Clin Exp Pathol *8*, 13405–13410.

Tang, C., Klukovich, R., Peng, H., Wang, Z., Yu, T., Zhang, Y., Zheng, H., Klungland, A., and Yan, W. (2018). ALKBH5-dependent m6A demethylation controls splicing and stability of long 3'-UTR mRNAs in male germ cells. PNAS *115*, E325–E333.

Tannous, B.A. (2009). Gaussia luciferase reporter assay for monitoring biological processes in culture and in vivo. Nat Protoc *4*, 582–591.

Tategu, M., Arauchi, T., Tanaka, R., Nakagawa, H., and Yoshida, K. (2007). Systems Biology-Based Identification of Crosstalk between E2F Transcription Factors and the Fanconi Anemia Pathway. Gene Regul Syst Bio *1*, 117762500700100000.

Tateishi, K., Wakimoto, H., Iafrate, A.J., Tanaka, S., Loebel, F., Lelic, N., Wiederschain, D., Bedel, O., Deng, G., Zhang, B., et al. (2015). Extreme Vulnerability of IDH1 Mutant Cancers to NAD+ Depletion. Cancer Cell *28*, 773–784.

Thalhammer, A., Bencokova, Z., Poole, R., Loenarz, C., Adam, J., O'Flaherty, L., Schödel, J., Mole, D., Giaslakiotis, K., Schofield, C.J., et al. (2011). Human AlkB Homologue 5 Is a Nuclear 2-Oxoglutarate Dependent Oxygenase and a Direct Target of Hypoxia-Inducible Factor 1α (HIF-1α). PLOS ONE *6*, e16210.

Toh, J.D.W., Crossley, S.W.M., Bruemmer, K.J., Ge, E.J., He, D., Iovan, D.A., and Chang, C.J. (2020). Distinct RNA N-demethylation pathways catalyzed by nonheme iron ALKBH5 and FTO enzymes enable regulation of formaldehyde release rates. PNAS *117*, 25284–25292.

Tommasi, S., and Pfeifer, G.P. (1995). In vivo structure of the human cdc2 promoter: release of a p130-E2F-4 complex from sequences immediately upstream of the transcription initiation site coincides with induction of cdc2 expression. Molecular and Cellular Biology *15*, 6901–6913.

Turcan, S., Rohle, D., Goenka, A., Walsh, L.A., Fang, F., Yilmaz, E., Campos, C., Fabius, A.W.M., Lu, C., Ward, P.S., et al. (2012). IDH1 mutation is sufficient to establish the glioma hypermethylator phenotype. Nature *483*, 479–483.

Turcan, S., Fabius, A.W.M., Borodovsky, A., Pedraza, A., Brennan, C., Huse, J., Viale, A., Riggins, G.J., and Chan, T.A. (2013). Efficient induction of differentiation and growth inhibition in IDH1 mutant glioma cells by the DNMT Inhibitor Decitabine. Oncotarget *4*, 1729–1736.

Waitkus, M.S., Diplas, B.H., and Yan, H. (2018). Biological Role and Therapeutic Potential of IDH Mutations in Cancer. Cancer Cell *34*, 186–195.

Wang, X., and He, C. (2014). Reading RNA methylation codes through methyl-specific binding proteins. RNA Biology *11*, 669–672.

Wang, Y., and Zhao, J.C. (2016). Update: Mechanisms Underlying N 6 -Methyladenosine Modification of Eukaryotic mRNA. Trends in Genetics *32*, 763–773.

Wang, S., Sun, C., Li, J., Zhang, E., Ma, Z., Xu, W., Li, H., Qiu, M., Xu, Y., Xia, W., et al. (2017). Roles of RNA methylation by means of N6-methyladenosine (m6A) in human cancers. Cancer Letters *408*, 112–120.

Wang, T., Hong, T., Huang, Y., Su, H., Wu, F., Chen, Y., Wei, L., Huang, W., Hua, X., Xia, Y., et al. (2015a). Fluorescein Derivatives as Bifunctional Molecules for the Simultaneous Inhibiting and Labeling of FTO Protein. J Am Chem Soc *137*, 13736–13739.

Wang, X., Lu, Z., Gomez, A., Hon, G.C., Yue, Y., Han, D., Fu, Y., Parisien, M., Dai, Q., Jia, G., et al. (2014a). N6-methyladenosine-dependent regulation of messenger RNA stability. Nature *505*, 117–120.

Wang, X., Zhao, B.S., Roundtree, I.A., Lu, Z., Han, D., Ma, H., Weng, X., Chen, K., Shi, H., and He, C. (2015b). N6-methyladenosine Modulates Messenger RNA Translation Efficiency. Cell *161*, 1388–1399.

Wang, Y., Li, Y., Toth, J.I., Petroski, M.D., Zhang, Z., and Zhao, J.C. (2014b). N6-methyladenosine modification destabilizes developmental regulators in embryonic stem cells. Nat Cell Biol *16*, 191–198.

Watanabe, T., Nobusawa, S., Kleihues, P., and Ohgaki, H. (2009). IDH1 Mutations Are Early Events in the Development of Astrocytomas and Oligodendrogliomas. Am J Pathol *174*, 1149–1153.

Wei, C.-M., and Moss, B. (2002). Nucleotide sequences at the N6-methyladenosine sites of HeLa cell messenger ribonucleic acid (American Chemical Society).

Wei, J., Liu, F., Lu, Z., Fei, Q., Ai, Y., He, P.C., Shi, H., Cui, X., Su, R., Klungland, A., et al. (2018). Differential m6A, m6Am, and m1A Demethylation Mediated by FTO in the Cell Nucleus and Cytoplasm. Mol Cell *71*, 973-985.e5.

Xiang, Y., Laurent, B., Hsu, C.-H., Nachtergaele, S., Lu, Z., Sheng, W., Xu, C., Chen, H., Ouyang, J., Wang, S., et al. (2017). RNA m6A methylation regulates the ultraviolet-induced DNA damage response. Nature *543*, 573–576.

Xu, C., Liu, K., Tempel, W., Demetriades, M., Aik, W., Schofield, C.J., and Min, J. (2014). Structures of human ALKBH5 demethylase reveal a unique binding mode for specific single-stranded N6-methyladenosine RNA demethylation. J Biol Chem *289*, 17299–17311.

Xu, W., Yang, H., Liu, Y., Yang, Y., Wang, P., Kim, S.-H., Ito, S., Yang, C., Wang, P., Xiao, M.-T., et al. (2011). Oncometabolite 2-Hydroxyglutarate Is a Competitive Inhibitor of α-Ketoglutarate-Dependent Dioxygenases. Cancer Cell *19*, 17–30.

Yalaza, C., Ak, H., Cagli, M.S., Ozgiray, E., Atay, S., and Aydin, H.H. (2017). R132H Mutation in IDH1 Gene is Associated with Increased Tumor HIF1-Alpha and Serum VEGF Levels in Primary Glioblastoma Multiforme. Ann Clin Lab Sci *47*, 362–364.

Yamazaki, T., Ohmi, A., Kurumaya, H., Kato, K., Abe, T., Yamamoto, H., Nakanishi, N., Okuyama, R., Umemura, M., Kaise, T., et al. (2010). Regulation of the human CHOP gene promoter by the stress response transcription factor ATF5 via the AARE1 site in human hepatoma HepG2 cells. Life Sci *87*, 294–301.

Yan, F., Al-Kali, A., Zhang, Z., Liu, J., Pang, J., Zhao, N., He, C., Litzow, M.R., and Liu, S. (2018). A dynamic N6-methyladenosine methylome regulates intrinsic and acquired resistance to tyrosine kinase inhibitors. Cell Res *28*, 1062–1076.

Yan, H., Parsons, D.W., Jin, G., McLendon, R., Rasheed, B.A., Yuan, W., Kos, I., Batinic-Haberle, I., Jones, S., Riggins, G.J., et al. (2009). IDH1 and IDH2 Mutations in Gliomas. N Engl J Med *360*, 765–773.

Yu, F., Wei, J., Cui, X., Yu, C., Ni, W., Bungert, J., Wu, L., He, C., and Qian, Z. (2021). Post-translational modification of RNA m6A demethylase ALKBH5 regulates ROS-induced DNA damage response. Nucleic Acids Research *49*, 5779–5797.

Zaccara, S., and Jaffrey, S.R. (2020). A Unified Model for the Function of YTHDF Proteins in Regulating m6A-Modified mRNA. Cell *181*, 1582-1595.e18.

Zeller, K.I., Jegga, A.G., Aronow, B.J., O'Donnell, K.A., and Dang, C.V. (2003). An integrated database of genes responsive to the Myc oncogenic transcription factor: identification of direct genomic targets. Genome Biol *4*, R69.

Zhang, H., Shi, X., Huang, T., Zhao, X., Chen, W., Gu, N., and Zhang, R. (2020). Dynamic landscape and evolution of m6A methylation in human. Nucleic Acids Research *48*, 6251–6264.

Zhang, L., Sorensen, M.D., Kristensen, B.W., Reifenberger, G., McIntyre, T.M., and Lin, F. (2018). D-2-Hydroxyglutarate Is an Intercellular Mediator in IDH-Mutant Gliomas Inhibiting Complement and T Cells. Clin Cancer Res *24*, 5381–5391.

Zhang, S., Zhao, B.S., Zhou, A., Lin, K., Zheng, S., Lu, Z., Chen, Y., Sulman, E.P., Xie, K., Bögler, O., et al. (2017). m6A Demethylase ALKBH5 Maintains Tumorigenicity of Glioblastoma Stem-like Cells by Sustaining FOXM1 Expression and Cell Proliferation Program. Cancer Cell *31*, 591-606.e6.

Zhang, Y., Liu, T., Meyer, C.A., Eeckhoute, J., Johnson, D.S., Bernstein, B.E., Nusbaum, C., Myers, R.M., Brown, M., Li, W., et al. (2008). Model-based Analysis of ChIP-Seq (MACS). Genome Biology *9*, R137.

Zhang, Z., Zhan, Q., Eckert, M., Zhu, A., Chryplewicz, A., De Jesus, D.F., Ren, D., Kulkarni, R.N., Lengyel, E., He, C., et al. (2019). RADAR: differential analysis of MeRIP-seq data with a random effect model. Genome Biology *20*, 294.

Zhao, B.S., Wang, X., Beadell, A.V., Lu, Z., Shi, H., Kuuspalu, A., Ho, R.K., and He, C. (2017). m6A-dependent maternal mRNA clearance facilitates zebrafish maternal-to-zygotic transition. Nature *542*, 475–478.

Zhao, S., Lin, Y., Xu, W., Jiang, W., Zha, Z., Wang, P., Yu, W., Li, Z., Gong, L., Peng, Y., et al. (2009). Glioma-Derived Mutations in IDH1 Dominantly Inhibit IDH1 Catalytic Activity and Induce HIF-1α. Science *324*, 261–265.

Zhao, X., Yang, Y., Sun, B.-F., Shi, Y., Yang, X., Xiao, W., Hao, Y.-J., Ping, X.-L., Chen, Y.-S., Wang, W.-J., et al. (2014). FTO-dependent demethylation of N6-methyladenosine regulates mRNA splicing and is required for adipogenesis. Cell Res *24*, 1403–1419.

Zheng, G., Dahl, J.A., Niu, Y., Fedorcsak, P., Huang, C.-M., Li, C.J., Vågbø, C.B., Shi, Y., Wang, W.-L., Song, S.-H., et al. (2013). ALKBH5 Is a Mammalian RNA Demethylase that Impacts RNA Metabolism and Mouse Fertility. Molecular Cell *49*, 18–29.

Zhou, J., Wan, J., Gao, X., Zhang, X., Jaffrey, S.R., and Qian, S.-B. (2015). Dynamic m(6)A mRNA methylation directs translational control of heat shock response. Nature *526*, 591–594.

Zhou, J., Wan, J., Shu, X.E., Mao, Y., Liu, X.-M., Yuan, X., Zhang, X., Hess, M.E., Brüning, J.C., and Qian, S.-B. (2018). N6-Methyladenosine Guides mRNA Alternative Translation during Integrated Stress Response. Mol Cell *69*, 636-647.e7.

Zhu, C., and Yi, C. (2014). Switching Demethylation Activities between AlkB Family RNA/DNA Demethylases through Exchange of Active-Site Residues. Angewandte Chemie International Edition *53*, 3659–3662.

Zou, S., Toh, J.D.W., Wong, K.H.Q., Gao, Y.-G., Hong, W., and Woon, E.C.Y. (2016). N 6 -Methyladenosine: a conformational marker that regulates the substrate specificity of human demethylases FTO and ALKBH5. Sci Rep *6*, 25677.

Zwicker, J., Liu, N., Engeland, K., Lucibello, F.C., and Müller, R. (1996). Cell Cycle Regulation of E2F Site Occupation in Vivo. Science *271*, 1595–1597.

CHAPTER 2

Targeted Epigenetic Engineering of *MGMT* Represents a New Approach to Effecting Chemotherapeutic Sensitization in Glioma

ABSTRACT

Glioblastoma is a deadly form of brain cancer affecting some 20,000 individuals a year in the US alone. Standard-of-care consists of tumor resection followed by temozolomide chemotherapy and radiation, however, prognoses for the average patient seldom extends beyond 12 months. Treatment responses are improved in patients with tumors exhibiting methylation-mediated silencing of *MGMT*, a gene encoding a DNA damage repair enzyme. Nevertheless, most patients present with *MGMT* unmethylated tumors, and derive limited clinical benefits from temozolomide therapy. In this study, we explore how targeted epigenetic editing achieved using recently developed dCas9 systems can effect precise changes in *MGMT* methylation profiles and temozolomide responses *in vitro*. We employed a dCas9 fusion protein linked to a DNMT3a methyltransferase to induce methylation of the *MGMT* promoter and first exon region, resulting in reduced MGMT expression and temozolomide sensitization. These findings provide the first example of how we might achieve 'treatment equity' between *MGMT* methylated and unmethylated glioma patients using targeted epigenetic engineering as a synergistic complement to standard-of-care temozolomide therapy.

INTRODUCTION

Glioma is the most common primary adult brain cancer and remains incurable in nearly all patients (Ricard et al., 2012). Glioma has an average age-adjusted annual incidence rate of 6.0 per 100,000 people, and of the approximately 20,000 individuals receiving a glioma diagnosis each year in the United States, close to 50% are diagnosed with GBM (glioblastoma) (Ostrom et al., 2017). GBM is the most aggressive form of glioma, with an average 5-year survival rate of 5% making it one of the most lethal of all known human cancers (Ostrom et al., 2017). Standard-of-care treatment includes surgical resection followed by radiation and TMZ (temozolomide) chemotherapy (Stupp et al., 2005, 2007). Varying, and often poor, patient responses to these treatments owes much to the genetic and molecular diversity of gliomas. Nearly two decades of large scale and systematic study has succeeded in identifying distinct genetically- and molecularly-defined glioma subtypes with different degrees of malignancy and amenability to treatment (Phillips et al., 2006; Schmidt et al., 2002). Extensive characterization has also defined glioma subtypes based on a number of epigenetic aberrations predictive of patient survival, including those arising as a result of mutations in *IDH1* (isocitrate dehydrogenase 1) that establishes a hypermethylated DNA phenotype known as G-CIMP (glioma-associated CpG island hypermethylator phenotype) (Balss et al., 2008; Cancer Genome Atlas Research Network et al., 2015; Eckel-Passow et al., 2015; Ichimura et al., 2009; Kang et al., 2009; Nobusawa et al., 2009; Parsons et al., 2008; Yan et al., 2009), as well as in glioma patients with different *de novo* methylation patterns of an important DNA damage repair enzyme known as *MGMT* (O-6-methylguanine-DNA methyltransferase) (Ceccarelli et al., 2016; Hegi et al., 2005, 2008; Ostrom et al., 2017; Reifenberger et al., 2012; Stupp et al., 2005, 2007; Wick et al., 2013). Despite these advances in our understanding of glioma, current treatment approaches continue to demonstrate limited efficacy and remain 'one size fits all.' This makes the development of effective, molecularly tailored therapies the greatest area of unmet need in the field. The goal of this study is to capitalize

on our knowledge of the prognostic value of *MGMT* methylation to explore the utilization of targeted epigenetic editing as a novel therapeutic strategy in the treatment of malignant GBM.

MGMT promoter methylation status is routinely tested for in all GBM patients during clinical assessment due to its established role as a robust prognostic indicator (Ceccarelli et al., 2016; Hegi et al., 2005, 2008; Ostrom et al., 2017; Reifenberger et al., 2012; Stupp et al., 2005, 2007; Wick et al., 2013). *MGMT* promoter methylation occurs in ~40% of GBM patients and is associated with more efficacious responses to chemotherapeutic intervention. However, the remaining 60% of GBM patients with unmethylated *MGMT* appear to derive only limited treatment benefits. Gliomas with unmethylated *MGMT* promoters have high MGMT expression, leading to increased DNA damage repair capabilities conferring significant resistance to standard-of-care TMZ therapy (Brandes et al., 2009; Ceccarelli et al., 2016; Hegi et al., 2005, 2008; Malmström et al., 2012; Reifenberger et al., 2012; Rivera et al., 2010; Stupp et al., 2005, 2007; Wick et al., 2013; Wiestler et al., 2013). TMZ is an alkylating chemotherapeutic that introduces DNA double-strand breaks to damage rapidly dividing cells, and it is the only FDA-approved drug shown to significantly increase survival in glioma patients (Stupp et al., 2005, 2007). The clinical utility of TMZ is markedly enhanced in patients with methylated *MGMT* promoters, as methylation suppresses *MGMT* transcription and inhibits the DNA repair pathway responsible for producing TMZ resistance (Hegi et al., 2005, 2008). Patients with methylated *MGMT* exhibit median PFS (progression-free survival) and OS (overall survival) durations of 10.3 months and 21.7 months, respectively (Hegi et al., 2005). Unfortunately, the majority of GBM patients possess tumors lacking *MGMT* methylation, and experience devastating reductions in survival compared to their methylated *MGMT* counterparts (PFS = 5.3 months, OS = 12.7 months) (Hegi et al., 2005). Clinical trials using the direct MGMT inhibitor O-6-benzylguanine showed some limited benefits, however, this strategy is not clinically employed due to severe dose-limiting toxicities, particularly with respect to bone marrow suppression (Quinn et al., 2009; Schilsky et al., 2000). Unmethylated

MGMT glioma patients thus represent an easily identifiable clinical population that may stand to derive tremendous benefit from new treatment strategies targeting mechanisms of epigenetic modulation. Finding a way to achieve 'treatment equity' between unmethylated and methylated *MGMT* glioma patients could theoretically serve to double survival times in the majority of GBM patients lacking this positive prognostic signature.

Recently developed epigenetic editing technologies fuse a deactivated Cas9 (dCas9) gene-targeting system with epigenetic editors such as the CpG methylator DNMT3a (de novo DNA methyltransferase 3a) or the CpG demethylase TET1 (Tet methylcytosine dioxygenase 1) (Liu et al., 2016). The dCas9-DNMT3a fusion protein uses single guide RNAs (sgRNAs) to induce loci-specific methylation or demethylation in mammalian cell genomes (Anton and Bultmann, 2017; Liu et al., 2016). Additional derivations on the dCas9-DNMT3a model include a DNMT3a catalytic domain-only iteration we used for the current study (Pflueger et al., 2018), as well as others fusing an additional DNMT3L (de novo DNA methyltransferase 3l) constituent that recruits endogenous DNMT3a to enhance methylation at target loci (Stepper et al., 2017), and a dCas9-MQ1 iteration utilizing a prokaryotic methyltransferase first characterized in *Mollicutes spiroplasma* (M. Sss1) (Lei et al., 2017; Renbaum et al., 1990). Few studies have probed the direct clinical utility of these novel system. Given what is known about the clinical effects of unmethylated *MGMT*, it stands to reason that inducing targeted methylation of the *MGMT* promoter and first exon region identified in prognostic studies may present a novel treatment opportunity. Modifying methylation profiles using epigenetic editors represents a breakthrough approach to altering gene expression, as other methodologies to suppress gene expression *in vivo* carry important limitations that impede their utilization in clinical settings. For example, RNA interference (RNAi) is an older approach to silencing the activity of gene products. RNAi is limiting in that sequences are rapidly cleared *in vivo*, only partially suppress targets, exhibit modest specificity, show cytotoxicity at high doses, and at saturation can induce potentially harmful activation of the mammalian immune system

(Fedorov et al., 2006; Grimm et al., 2006; Hornung et al., 2005; Jackson et al., 2003; Marques and Williams, 2005). Another approach to altering gene expression is via standard CRISPR/Cas9 activity, where a Cas9 endonuclease under sgRNA guidance induces DNA double-strand breaks in a gene locus of interest to permanently silence its expression (Cong et al., 2013; Deltcheva et al., 2011; Gasiunas et al., 2012; Jinek et al., 2012; Mali et al., 2013). Compared to the permanent genetic alterations produced by Cas9, targeted epigenetic editing represents a theoretically safer approach to modifying gene expression. This is primarily because of its reversibility and the lower potential for unexpected phenotypic alterations in the case of off-target actions. For example, if dCas9-DNMT3a binds to an off-target site, the locus must exhibit susceptibility to methylation (i.e., be unmethylated) to produce a measurable off-target effect or phenotype. Additionally, any unintended methylation events are potentially reversible due to endogenous mechanisms of epigenetic regulation that remain unperturbed. Targeted epigenetic editing is unique in that it uses deactivated Cas9 (dCas9) to capitalize on the specificity of CRISPR-based genetic engineering systems, while enhancing/suppressing target genes via epigenetic mechanisms such as CpG methylation.

Manipulating the epigenetic landscape of gliomas using targeted epigenetic editing represents a cutting-edge approach to probing fundamental cancer biology and revolutionizing therapeutic design. Recent advances in this field make it both possible and imperative that we develop tailored therapies for glioma patients who remain in acute and pressing need of new treatments. In this study, we attempt to harness targeted epigenetic editing approaches to induce methylation of the *MGMT* promoter and exon 1 region in order to downregulate the expression of MGMT in glioma model systems and effect TMZ sensitization. This represents a groundbreaking application of epigenetic editing tools in service of artificially inducing a clinically validated epigenetic phenotype known to enhance the efficacy of standard-of-care therapies in glioma.

RESULTS

dCas9-DNMT3a and sgRNAs Targeting MGMT are Stably Expressed in LN18 GBM Cells

The first goal of this study was to establish a model of dCas9-DNMT3a-mediated methylation of CpG target sites in the *MGMT* gene in GBM cells. We utilized LN18 cells for this study because, among commonly utilized glioma model systems tested in our laboratory, LN18 GBM cells exhibit no CpG methylation in our region of interest and show high levels of *de novo* MGMT expression. Additionally, LN18 cells demonstrate some of the highest TMZ EC_{50} values of all glioma model systems (EC_{50} = 400 μM) and are capable of developing resistance after repeated TMZ exposures (Happold et al., 2012). These factors combine to make the LN18 line a significantly challenging glioma model within which to test our epigenetic editing approach. We considered several fusion proteins as candidate epigenetic editors in this study, all shown to be cable of achieving loci-specific targeting and demonstrating efficacy as potent CpG methylators in mammalian cells (Amabile et al., 2016; Liu et al., 2016; McDonald et al., 2016; Pflueger et al., 2018; Stepper et al., 2017; Vojta et al., 2016). Targeted epigenetic editing was ultimately achieved using the dCas9-DNMT3a iteration developed by Pflueger *et al*. containing only the DNMT3a catalytic domain fused to dCas9 via a flexible linker (Pflueger et al., 2018). We selected this system due to the homology with endogenous DNMT3a, and for comprising a smaller plasmid construct that made it more amenable to lentiviral vector transduction methods. A final consideration for this study was the design of sgRNAs targeting dCas9-DNMT3a to the *MGMT* regions of interest. Studies have shown that methylation-mediated suppression of gene expression was possible even when methylating a single critical CpG site (Ben-Hattar and Jiricny, 1988; Gonzalgo et al., 1998; Jones and Chen, 2006; Pogribny et al., 2000; Robertson and Jones, 1998; Sohn et al., 2010; Wicki et al., 1997). Multiplexed approaches with multiple sgRNAs can also be used to broaden the region targeted for epigenetic editing (Amabile et al., 2016; Liu et al., 2016; McDonald et al., 2016; Pflueger et al., 2018; Stepper et al., 2017; Vojta et al., 2016). We developed a series of sgRNAs with appropriate sequence homology to the *MGMT* promoter and Exon 1 region identified by

Lalezari *et. al.* as being predictive of improved patient survival (Lalezari et al., 2013). This area aligns with the DMR2 (differentially methylated region 2) region identified by Malley *et al* as being the most highly associated with MGMT mRNA suppression when methylated in GBM cell lines, xenografts, and normal brain tissue (Malley et al., 2011). This region falls within the *MGMT* CpG island, and we focused our sgRNA design on this area such that we were able to target 27 CpG sites that could be verified using the MSP (methylation specific primer) and bisulfite sequencing methods commonly employed in clinical practice to characterize gliomas and stratify patients by *MGMT* methylation status (Hegi et al., 2005; Lalezari et al., 2013). A schematic of the *MGMT* regions of interest as well as the sgRNA and bisulfite sequencing primer sites are shown (Figure 2-1a).

We established numerous LN18 cell lines stably expressing dCas9-DNMT3a epigenetic editing machinery to use in subsequent experiments. RT-qPCR performed on RNA isolated from these cells showed no differences in MGMT mRNA expression across LN18 lines containing the construct (Figure 2-1b). Only transduced lines exhibited dCas9-DNMT3a expression, while LN18 native cells did not (Figure 2-1b). Direct DNA sequencing as well as RT-qPCR of the dCas9, fusion linker, and DNMT3a regions confirmed the presence of all dCas9-DNMT3a plasmid construct elements (Figure 2-1c). Additional immunohistochemistry experiments showed that dCas9 and DNMT3a were co-localized within the cell lines established (Figure 2-1d). We next performed transductions using lentiviral vectors delivering one of three *MGMT*-targeting sgRNAs (I, II, III) or a combination of all three (I-III) in LN18 cells stably expressing dCas9-DNMT3a. RT-qPCR was used to verify suppression of *MGMT* mRNA, and we found that only combination sgRNA treatment significantly reduced gene expression (Figure 2-1e). These experiments show that the dCas9-DNMT3a epigenetic editor can reliably attenuate *MGMT* mRNA expression when coupled with a combinatorial sgRNA paradigm providing coverage of the promoter and Exon 1 region.

dCas9-DNMT3a Under sgRNA Guidance Methylates the MGMT Promoter and Exon 1 Region and Suppresses MGMT Expression

We next sought to establish the efficacy of our targeted methylation approach through bisulfite sequencing and protein assays to confirm methylation of our target sites and meaningful suppression of MGMT protein synthesis. For this purpose, we established additional LN18-dCas9-DNMT3a lines expressing a scrambled gRNA (scRNA) to use as negative controls in experimental comparisons. The scRNA we employed has no sequence homology to any regions of the mammalian genome, providing a negative control to demonstrate the specificity of our targeted methylation approach. Bisulfite sequencing is a technique that parses unmethylated and methylated CpG sites with base-resolution through a process that begins with bisulfite conversion of purified DNA followed by methylation-specific sequencing using specially designed primers (Herman et al., 1996). The bisulfite conversion reaction converts unmethylated cytosine residues to uracil, while leaving methylated cytosines intact. The persistent presence of a cytosine at a particular locus upon sequencing therefore indicates that the site exhibits methylation. We utilized the *EZ DNA Methylation-Gold* (*Zymo Research*, Catalog #D5005, Irvine, CA, USA) kit according to the manufacturer's instructions for all bisulfite conversion reactions.

Bisulfite sequencing results from LN18 cells expressing dCas9-DNMT3a and a quad-sgRNA (I-IV) construct showed successful methylation of all 27 CpG sites within the *MGMT* promoter and Exon 1 region (Figure 2-2a). Cells expressing the scRNA negative control exhibited no changes in methylation compared to LN18 lines, demonstrating the specificity of our approach. We next performed immunoblotting experiments using protein isolated from LN18 GBM cells one week after construct transduction and puromycin selection. The results show that MGMT protein levels are reduced in epigenetically edited LN18 cells, but not in those exhibiting a lack of methylation in the *MGMT* target region (Figure 2-2b). The effect of targeted methylation on suppressing

MGMT protein expression was robust and persistent, with consistent reductions in expression observed even after 2 months of normal cell growth and regular passaging without the application of additional selection measures or rounds of dCas9-DNMT3a or sgRNA I-IV construct transduction (Figure 2-2c). Our findings providing strong evidence that achieving targeted methylation of the *MGMT* promoter and Exon 1 region is capable of meaningfully suppressing MGMT protein expression in LN18 GBM cells.

Targeted Methylation of MGMT Enhances TMZ Sensitization in LN18 GBM Cells In Vitro

The final goal of the current study was to demonstrate that *MGMT* methylation effected through targeted epigenetic editing can sensitive glioma cells to TMZ treatment. We evaluated TMZ treatment effects in LN18 GBM cells expressing dCas9-DNMT3a and sgRNAs I-IV or scRNA constructs. We also generated Cas9-mediated knockout lines to draw comparisons between LN18 cells wherein MGMT suppression was achieved via direct endonuclease disruption versus targeted methylation. Treatment sensitization was measured using MTT [3-(4,5-dimethyl-2-thiazolyl)-2,5-diphenyl-2H-tetrazolium bromide] and clonogenic assays, both as previously described (Franken et al., 2006; Hermisson et al., 2006; Remington et al., 2009). We compared the percentage of surviving cells subjected to either 100 μM or 250 μM TMZ treatments, evaluated against a DMSO control treatment condition. MTT assays were conducted after 6 days of continuous treatment. Clonogenic assays were conducted following 12 days of continuous treatment, after which cells were fixed and stained with 0.5% crystal violet before being imaged and assessed using the ImageJ plug-in ColonyArea (Guzmán et al., 2014). MTT results reveal a highly significant TMZ sensitization effect in LN18 GBM cells successfully targeted for *MGMT* methylation (Figure 2-3a). Clonogenic assays confirmed this finding, showing that epigenetically edited LN18 cells achieved sensitization parity with *MGMT* Cas9-mediated knockout lines within the 250 μM TMZ dose condition. Few to no changes in TMZ sensitivity were observed in LN18

dCas9-DNMT3a cells expressing the scRNA negative control construct. These results clearly demonstrate that inducing targeted *MGMT* methylation is a viable strategy to enhance TMZ chemotherapeutic effects in treatment resistant GBM cells.

DISCUSSION

Here we establish 'proof-of-principle' that targeted epigenetic editing represents a novel approach to enhancing glioma treatment. We successfully achieved robust methylation of 27 CpG sites in the *MGMT* promoter and Exon 1 region in LN18 GBM models using dCas9-DNMT3a coupled with four sgRNAs targeting our region of interest. This approach consistently suppressed MGMT protein expression and effected drastic sensitization to TMZ chemotherapeutic challenges similar to those achieved with a Cas9-mediated MGMT knockout. This novel approach represents a groundbreaking step towards realizing a new avenue of currently untapped therapeutic potential.

Our long-term goal is to harness the power of targeted epigenetic editing to spearhead improved treatment paradigms for glioma. Effecting TMZ sensitization through targeted *MGMT* methylation would bring us one step closer to achieving treatment equity between *MGMT* methylated and unmethylated gliomas and could drastically improve outcomes for a significant majority of GBM patients. Further studies are actively underway in our laboratory with the aim of providing a pre-clinical evidentiary basis for eventual therapeutic adoption. Primary among them is replicating our LN18 findings in patient-derived gliomaspheres and preparing those cell lines for *ex vivo* and *in vivo* TMZ sensitization experiments. We have screened a bank of patient-derived gliomaspheres and identified several candidates that are *MGMT* unmethylated and able to engraft in mice (GS028, GS104, and GS227) (Table 2-1). The *MGMT* methylation statuses for these samples were obtained at the time of surgical resection, where tumor tissues underwent next generation sequencing and were confirmed to have a low tumor mutational burden with no other mutations in the mismatch repair pathway. Clinical *MGMT* status was determined from bulk tumor, using conventional methylation-specific PCR. Each sample listed was originally classified as *MGMT* unmethylated, although validation experiments in gliomaspheres isolated from the bulk tumors show some variability in methylation degrees. One cell line, GS142, was in fact found to be methylated; and two such cell lines, GS242 and GS084, were predominantly unmethylated in the

region we assayed, but exhibited trace methylation in the 5' end of our tested region. This variability will be used to the benefit of understanding whether gradations in *MGMT* methylation lead to corresponding degrees of gene expression suppression and TMZ sensitivity, or if there are critical sites within the promoter and Exon 1 region that are the primary drivers of transcriptional attenuation. This will allow us to determine whether there is a hierarchy of biological significance to various CpG sites within the region of interest, as measured by TMZ sensitivity and survival data from both the relevant patients and intracranial xenograft experiments in animal models. We will use our current dCas9-DNMT3a and sgRNA I-IV epigenetic editing constructs to systematically target select CpG sites for methylation to address these questions. *Ex vivo* experiments will be performed using gliomaspheres expressing our *MGMT*-targeting platform, and overall survival will be determined in the context of TMZ treatment and compared to negative control lines not under sgRNA guidance (i.e., scRNA-containing lines). Achieving optimized *in vivo* experimental validation is also a necessary step to maximize the translational potential of this work. Lentiviral vectors are a common tool for delivering genome-editing payloads *in vivo* and is one option we plan to explore. Another approach will be to test the efficacy of high efficiency lipid-based nanoparticle that have been shown to effectively deliver Cas9-sgRNA complexes (Wang et al., 2016). Additional delivery mechanisms include the use of hydrodynamic injections of lipid-based nanoparticles capable of crossing the blood brain barrier. Other studies have demonstrated this to be an effective route for intracranial delivery of genome-editing ribonucleoproteins, making it a promising avenue for the delivery of epigenetic editing platforms as well (Kim et al., 2014; Zuris et al., 2015). Finally, we seek to characterize any off-target methylation effects in glioma cells containing dCas9-DNMT3a and sgRNA constructs. Reduced representation bisulfite sequencing (RRBS) methods is one approach we are using to catalogue differences in methylation patterns across the genomes of native and epigenetically engineered cell lines (Meissner et al., 2005). We are also utilizing methylation arrays (*Illumina*, Catalog #WG-

317-1001, San Diego, CA, USA), which are designed to cover >850,000 CpG sites throughout the genome, as an off-target orthogonal validation screen.

We believe that targeted epigenetic editing represents a novel approach to enhancing glioma treatment. The sustained impact of our current and future work will be to establish targeted epigenetic editing as an effective approach to selectively altering *MGMT* promoter methylation statuses in glioma. If successful, we hope to devise efficacious methods to deliver this intervention directly to patients to develop a synergistic therapeutic option for *MGMT* unmethylated GBM patients undergoing standard-of-care TMZ therapy.

METHODS

Cell Culture and Treatments

LN18 cells were maintained in DMEM cell culture medium supplemented with 10% fetal bovine serum and penicillin/streptomycin, cultured at 37 °C and 5% CO_2. TMZ was obtained from Santa Cruz Biotechnology (*Santa Cruz Biotechnology*, Catalog #85622-93-1, Dallas, TX, USA) and dissolved in DMSO.

Plasmids and Lentiviral Transduction

dCas9-DNMT3a catalytic domain plasmids were originally constructed by Pflueger *et* al. (*Addgene*, Catalog #100936, Watertown, MA, USA). Cas9 plasmids were obtained from Addgene (*Addgene*, Catalog #108100, Watertown, MA, USA). Sequences for sgRNAs were determined using the Broad Institute Genetic Perturbation Platform and the following input sequence mapping to the *MGMT* region of interest: TGCCCCTCGGCCCCGCCCCCGCGCCCCGGATATGCTGGGACAGCCCGCGCCCCTAGAACGCTTTGCGTCCCGACGCCCGCAGGTCCTCGCGGTGCGCACCGTTTGCGACTTGGTGAGTGTCTGGGTCGCCTCGCTCCCGGAAGAGTGCGGAGCTCTCCCTCGGGACGGTGGCAGCCTCGAGTGGTCCTGCAGGCGCCCTCACTTCGCCGTCGGGTGTGGGGCCGCCCTGACCCCCACCCATCCCGGGCGA. Sequences for sgRNA I-IV utilized in this study are as follows:

- sgRNA I (5’ – GGTGCGCACCGTTTGCGACT – 3’, PAM = TGG)
- sgRNA II (5’ – AGGCGCCCTCACTTCGCCGT – 3’, PAM = CGG)
- sgRNA III (5’ – CTTTGCGTCCCGACGCCCGC – 3’, PAM = AGG)
- sgRNA IV (5’ – AGGGCATGCGCCGACCCGGT – 3’, PAM = CGG)
- Scrambled guide RNA (scRNA) (5’ – GTATTACTGATATTGGTGGG – 3’)

All sgRNA and scRNA constructs were mounted on lentivirus-compatible plasmids by through Vector Builder (*Vector Builder*, Chicago, IL, USA).

Plasmids were packaged with pMD2.G VSV-G envelope plasmid (*Addgene*, Catalog #12259, Watertown, MA, USA) and pCMVR8.74 packaging plasmid (*Addgene*, Catalog #22036, Watertown, MA, USA) in HEK293T cells cultured in regular DMEM. Plasmids were transfected into HEK293T using X-tremeGENE HP DNA Transfection Reagent (*MilliporeSigma*, Catalog #XTGHP-RO, Burlington, MA, USA). HEK293T cells were allowed to incubate for 48 hours, at which time the lentivirus-containing media was harvested, aliquoted, and stored at -80 °C. LN18 cells were disassociated to and seeded at ~70% confluence in 6-well cell culture plates. Cells were transduced with lentivirus-containing media and regular culture media in a 1:3 ratio. 1.0 μg/mL of polybrene was added to facilitate transduction efficiency. Cells remained in lentivirus-containing media for no more than 48 hours, at which point media was replaced with standard culture media. After an additional day, transduced cells were subjected to 0.8 μg/mL puromycin selection. Sequencing and western blot analyses provided orthogonal confirmation of stable expression.

Reverse Transcription and Quantitative PCR (RT-qPCR)

RT-qPCR was performed on RNA purified from LN18 cells using RNeasy Kits (*Qiagen*, Catalog #74104, Hilden, Germany). First-strand cDNA synthesis was performed using SuperScript II Reverse Transcriptase Kit with oligo-dT primers (*Thermo Fisher Scientific*, Catalog# 18064014, Waltham, MA, USA). Briefly, 1 μL of Oligo(dT) was combined with 1 μL of 10mM dNTP mix, 500 ng of m6A-immunoprecipitated or total mRNA from samples, and sterile nuclease-free water for a final volume of 12 μL. The mixture was heated to 65 °C for 5 minutes and chilled on ice. 4 μL of 5X First-Strand Buffer, 2 μL of 0.1 M DTT, and 1 μL of RNaseOUT was then added to the mixture. The contents were mixed and then incubated at 42 °C for 2 minutes. 1 μL of SuperScript II RT was then added to the mixture, with sterile nuclease-free water added to achieve a final volume of 20 μL. The mixture was incubated at 42 °C for 50 minutes. The RT reaction was then inactivated

at 70 °C for 15 minutes. Next, 2 μL of the RT product was added to a PCR reaction mixture of 5 μL of 10X PCR Buffer (200 mM Tris-HCL (pH 8.4), 500 mM KCl), 1.5 μL of 50 mM $MgCl_2$, 1 μL of 10 mM dNTP mix, 1 μL of forward primer (10 μM), 1 μL of reverse primer (10 μM), 0.4 μL of Taq DNA polymerase, and sterile nuclease-free water for a final volume of 50 μL. The mixture was then added in triplicate to a 96-well plate, and a denaturing step was performed by heating the mixture to 94 °C for 2 minutes. Real-time quantitative PCR data collection and analysis were performed on a CFX Connect Real-Time PCR Detection System (*Bio-Rad Laboratories*, Hercules, CA, USA).

Primers utilized in these experiments include the following:

Gene	Forward Primer	Reverse Primer
ACTB	5'- CCAGAGGCGTACAGGGATAG-3'	5'-CCAACCGCGAGAAGATGA-3'
MGMT	5'- CGAAATAAAGCTCCTGGGCA -3'	5'- GAACTCTTCGATAGCCTCGGG -3'

Bisulfite Sequencing

DNA was isolated from cells using QIAmp DNA Kits (*Qiagen*, Catalog #51304, Hilden, Germany). Bisulfite conversion was accomplished using *EZ DNA Methylation-Gold* (*Zymo Research*, Catalog #D5005, Irvine, CA, USA) per the manufacturer's instructions. Methylation-specific PCR to amplify and sequence the *MGMT* promoter and Exon 1 region was performed as previously described (Hegi et al., 2005; Lalezari et al., 2013).

Immunoblotting

Cells or tissues were lysed in 1x Pierce RIPA lysis buffer (*Thermo Fisher Scientific,* Catalog #89900, Waltham, MA, USA) with proteinase inhibitor in a 1:100 dilution (*Thermo Fisher Scientific,* Catalog #EO0491, Waltham, MA, USA). Purified protein from the lysates was measured using

the Pierce BCA Protein Assay Kit (*Thermo Fisher Scientific,* Catalog #23225, Waltham, MA, USA). Protein was denatured at 100 °C for 10 minutes with Laemmli Sample Buffer. Equal concentrations of protein were then electrophoretically fractionated in 4–15% precast polyacrylamide gels (8.6 x 6.7 cm, for use with Mini-PROTEAN Electrophoresis Cells) (*Bio-Rad Laboratories*, Catalog #4568084, Hercules, CA, USA) and transferred to nitrocellulose membranes. The membranes were then subjected to immunoblot assays following a similar protocol as described above for m6A dot blots. One alteration was that blocking buffer was performed in TBST with 5% dry milk. Specific primary antibodies include mouse anti-MGMT (1:1000) (*Thermo Fisher Scientific,* Catalog #35-7000, Waltham, MA, USA) and mouse anti-α-tubulin (1:2000) (*MilliporeSigma*, Catalog #T6199, Burlington, MA, USA). Secondary antibodies used include goat anti-mouse IgG-HRP (1:5000) (*Thermo Fisher Scientific,* Catalog #62-6520, Waltham, MA, USA).

Cell Survival Assays

MTT assays were employed to test cell proliferation rates as previously described (Franken et al., 2006; Hermisson et al., 2006; Remington et al., 2009). Briefly, a uniform number of cells were cultured in 24-well plates for 6 days undergoing temozolomide (100 μM or 250 μM) or DMSO control treatment, and then exposed to pre-mixed 3-(4,5-dimethylthiazol-2-yl)-2,5-diphenyltetrazolium bromide (MTT) solution (0.5 mg/mL in regular culture media). Cells were incubated at 37 °C for 1 hour. The MTT solution was then removed, and the MTT-reduced formazan product was extracted from the cells following lysing with 300 mL of DMSO. Formazan concentrations were measured at 560 nm absorbance using a Wallac Victor2 microplate reader (*Perkin Elmer*, Waltham, MA, USA) with a background subtraction of 660 nm absorbance. Three independent experiments were performed for each experimental condition. Data were analyzed in Prism 9 and results presented as a 'mean$\pm$SEM,' and significant differences determined using

pairwise two-tailed Student's *t*-tests. Clonogenic assays were also conducted as previously described (Franken et al., 2006; Hermisson et al., 2006; Remington et al., 2009). Briefly, 250 cells were seeded in 60 mm cell culture plates and cultured for 12 days 6 days undergoing temozolomide (100 μM or 250 μM) or DMSO control treatment. Cells were then washed gently with cold PBS and covered with ice-cold 100% methanol to a depth of 2-3 mm. Cells were allowed to fix for 15 minutes at -20 °C before staining with 0.5% crystal violet solution in 25% methanol. Following 30 minutes of incubation at room temperature, the crystal violet solution was disposed of and cells were submerged in dH2O to rinse off excess staining solution. Cells were then allowed to dry overnight at room temperature, before being digitally scanned and uploaded into ImageJ. The ColonyArea plug-in was used to calculate the percentage of each 60 mm culture plate exhibiting colony formation (Guzmán et al., 2014). All experiments were performed in triplicate. Data were analyzed in Prism 9 and results presented as a 'mean±SEM,' and significant differences determined using pairwise two-tailed Student's *t*-tests.

FIGURES & TABLES

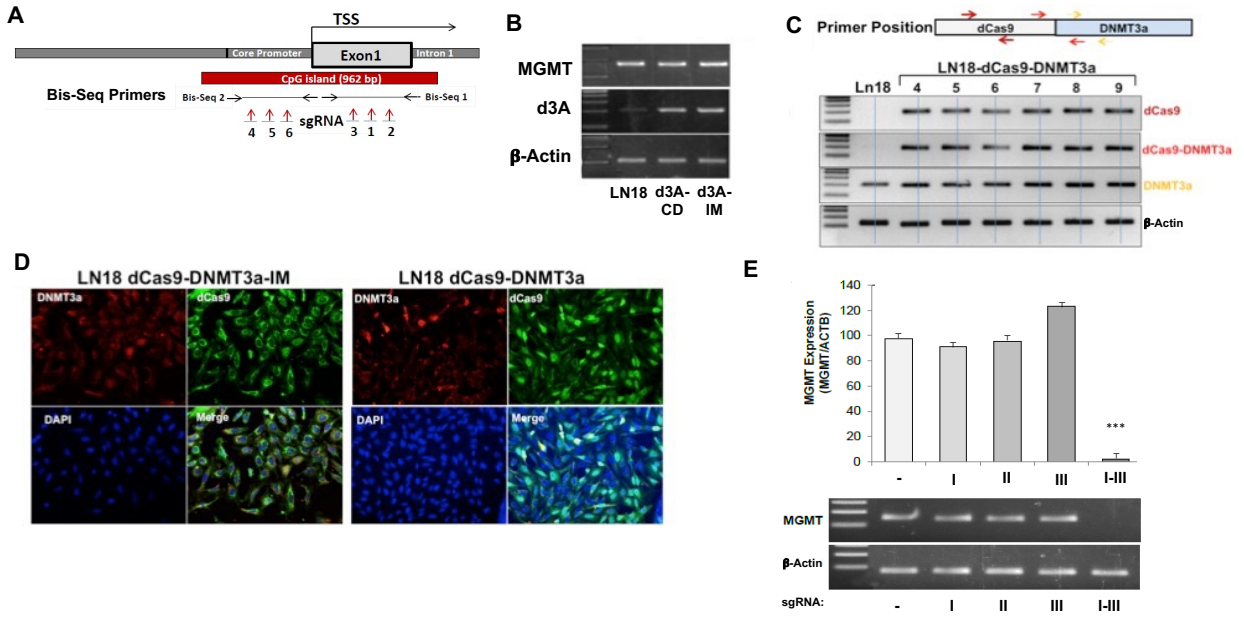

Figure 2-1. dCas9-DNMT3a and sgRNAs targeting *MGMT* can be stably expressed in LN18 glioma cells. A) Schematic of the *MGMT* gene containing a CpG island that is methylated in a subset of glioma patients and cell lines. *MGMT* gene structure, bisulfite sequencing regions, and sgRNA homology regions targeting the *MGMT* promoter and Exon 1 region are also shown. The transcription start site (TSS) occurs at the beginning of Exon 1. **B)** Gel of RT-qPCR products showing the presence of MGMT in LN18 cells following transduction with dCas9-DNMT3a constructs (d3A-CD = active, d3A-IM = inactivating methyltransferase mutation) compared to **β**-actin control. **C)** Gel of RT-qPCR products showing fragments for all components of the dCas9-DNMT3a fusion protein in LN18 clones #4-9 following transduction. **β**-actin and native LN18 RT-qPCR products are shown for comparison. A schematic of the dCas9-DNMT3a plasmid and associated primers are also shown. **D)** Immunohistochemistry showing fluorescence co-localization of dCas9 and DNMT3a in LN18 cells. **E)** Bar graph showing MGMT mRNA levels as measured by RT-qPCR in cells treated with control (-) versus individual sgRNAs (I, II, III) or combined sgRNAs (I-III), normalized to **β**-actin (ACTB) control expression. Gel electrophoresis of MGMT and **β**-actin mRNA expression are also shown. All experiments were conducted in

triplicate unless otherwise indicated. Results are presented as Mean ± S.E.M. Pairwise two-tailed Student's *t*-tests: ***$P < 0.001$

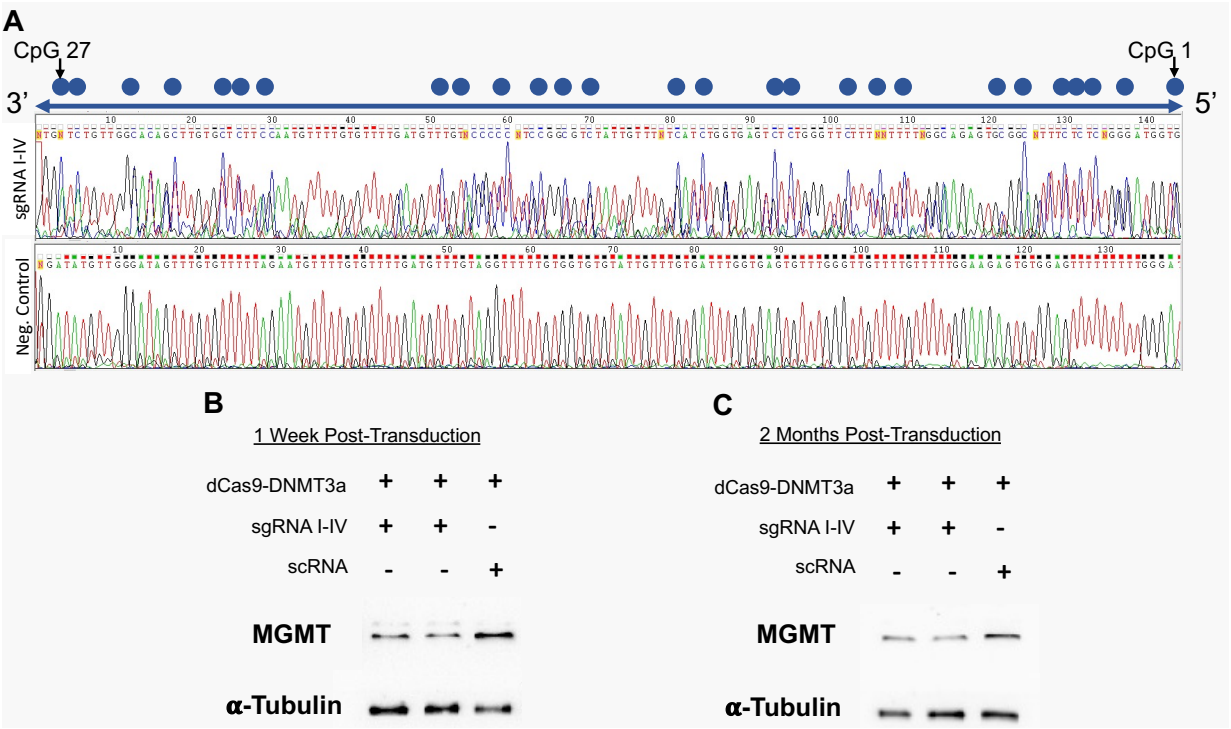

Figure 2-2. dCas9-DNMT3a under sgRNA guidance methylates the *MGMT* promoter and Exon 1 region and suppresses MGMT expression. A) Chromatogram DNA sequencing data showing high levels of CpG methylation sites (blue circles) in LN18 cells stably expressing dCas9-DNMT3a and four non-overlapping sgRNAs (I-IV) targeting the *MGMT* promoter and Exon 1 region. No methylation is seen in the negative control conditions expressing a scrambled gRNA (scRNA) or d3A-only (not shown). The current arrangement of sgRNAs demonstrates the ability to fully methylate the region of interest. Of the potential CpG sites in this region of interest, 100% were successfully and reliably methylated (*n*=8 independent biological replicates). **B)** Western blots showing suppression of MGMT in two independent biological replicates of LN18 lines following lentiviral-mediated expression of d3A and either sgRNAs I-IV or scRNA negative control 1 week after initial transduction and selection. All groups were successfully confirmed as expressing the three components of the d3A construct: dCas9, fusion linker, and DNMT3a. LN18-d3A lines co-expressing sgRNA I-IV targeting the *MGMT* region of interest (lanes 1-2) are shown against those co-expressing scRNA (lane 3), with α-tubulin used as a protein loading control. **C)**

Following confirmation of MGMT downregulation as shown in (B), LN18 cells were maintained in culture by serial passaging without any additional antibiotic selection for 2 months, and protein was subsequently extracted to determine levels of MGMT expression. All experiments were performed in triplicate unless otherwise indicated.

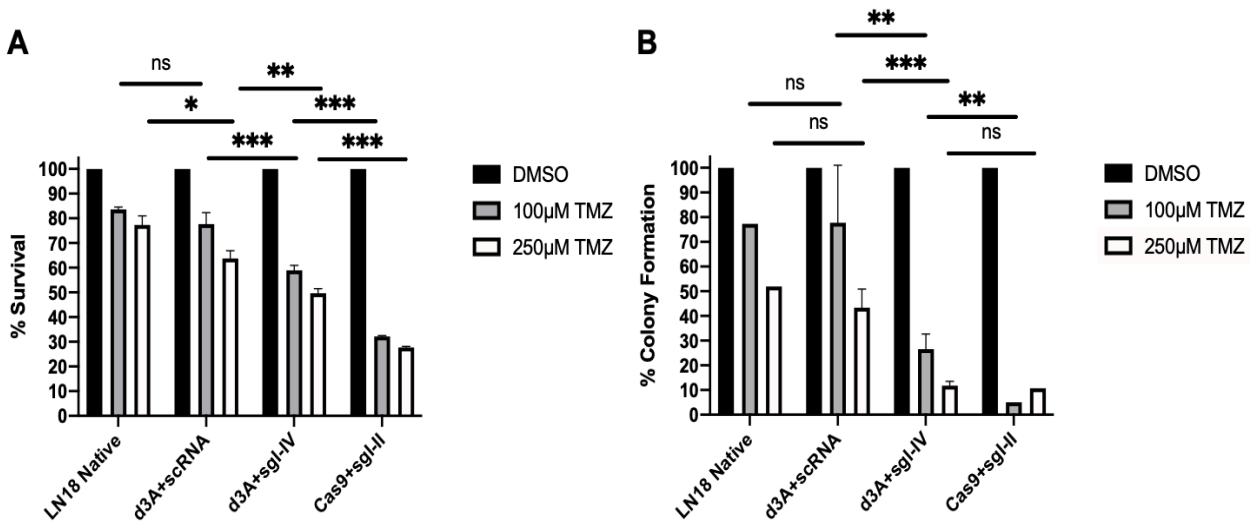

Figure 2-3. Targeted methylation of *MGMT* enhances TMZ sensitization in LN18 glioma cells *in vitro*. A) TMZ sensitivity measured via MTT assays show reduced survival in LN18 cells co-expressing dCas9-DNMT3a (d3A) and *MGMT*-targeting sgRNAs (sgI-IV) compared to LN18 native and scRNA negative control lines. TMZ sensitivity of cell lines methylated by d3A-CD approached the sensitivity of Cas9-mediated MGMT knockout lines (n = 3). MTT cell survival was calculated by subtracting 560 nm readings for TMZ-treated cells (100 μM and 250 μM, 6 days) versus a DMSO treatment control condition. **B)** Clonogenic assay results showing decreased colony formation in methylated lines (n = 3) versus scRNA unmethylated lines treated with 100 μM and 250 μM TMZ for 6 days. LN18 native and scRNA unmethylated lines showed no differences in colony formation, and methylated lines showed comparable TMZ sensitivity to Cas9-mediated *MGMT* knockout lines. Clonogenic assays were performed by seeding 500 cells in 60 mm plates and treating for 12 days, after which the cells were fixed using 0.5% crystal violet. Plates were then digitally scanned. Colonies >30 cells were counted using the ColonyArea plug-in for ImageJ. All experiments were conducted in triplicate unless otherwise indicated. Results are displayed as Mean ± S.E.M. Pairwise two-tailed Student's t-tests: *P < 0.01, **P < 0.005, ***P < 0.001.

Table 2-1. Patient-Derived Gliomaspheres and Clinical/Engraftment Parameters

Patient Cell Line	Overall Survival (Months)	Progression-Free Survival (Months)	Clinical Treatment Summary	Clinical *IDH* Status	Clinical *MGMT* Promoter Status	Bisulfite Sequencing *MGMT* Promoter Verification	Time to Engraftment in Mouse Model (Days)
GS028	13.7	8.54	RT/TMZ/bevacizumab, CCNU, carboplatin	WT	Unmethylated	Unmethylated	50
GS104	10.2	7.09	RT/TMZ, CCNU, lapatinib	WT	Unmethylated	Unmethylated	85.3
GS227	15.9	5.02	RT/TMZ/bevacizumab	WT	Unmethylated	Unmethylated	92
GS084	24.1	11.2	RT/TMZ	WT	Unmethylated	Subset Methylated	129
GS242	18.5	6.21	RT/TMZ/bevacizumab, Somatostatin LAR, pembrolizumab, osimertinib	WT	Unmethylated	Subset Methylated	84
GS142	12.6	NA	RT/TMZ/bevacizumab	WT	Unmethylated	Methylated	TBD

RT=Radiotherapy, TMZ=Temozolomide, CCNU=Lomustine, LAR= Long-Acting Release, WT=Wild type

REFERENCES

Amabile, A., Migliara, A., Capasso, P., Biffi, M., Cittaro, D., Naldini, L., and Lombardo, A. (2016). Inheritable Silencing of Endogenous Genes by Hit-and-Run Targeted Epigenetic Editing. Cell *167*, 219-232.e14.

Anton, T., and Bultmann, S. (2017). Site-specific recruitment of epigenetic factors with a modular CRISPR/Cas system. Nucleus *8*, 279–286.

Balss, J., Meyer, J., Mueller, W., Korshunov, A., Hartmann, C., and von Deimling, A. (2008). Analysis of the IDH1 codon 132 mutation in brain tumors. Acta Neuropathol *116*, 597–602.

Ben-Hattar, J., and Jiricny, J. (1988). Methylation of single CpG dinucleotides within a promoter element of the Herpes simplex virus tk gene reduces its transcription in vivo. Gene *65*, 219–227.

Brandes, A.A., Franceschi, E., Tosoni, A., Benevento, F., Scopece, L., Mazzocchi, V., Bacci, A., Agati, R., Calbucci, F., and Ermani, M. (2009). Temozolomide concomitant and adjuvant to radiotherapy in elderly patients with glioblastoma: correlation with MGMT promoter methylation status. Cancer *115*, 3512–3518.

Cancer Genome Atlas Research Network, Brat, D.J., Verhaak, R.G.W., Aldape, K.D., Yung, W.K.A., Salama, S.R., Cooper, L.A.D., Rheinbay, E., Miller, C.R., Vitucci, M., et al. (2015). Comprehensive, Integrative Genomic Analysis of Diffuse Lower-Grade Gliomas. N Engl J Med *372*, 2481–2498.

Ceccarelli, M., Barthel, F.P., Malta, T.M., Sabedot, T.S., Salama, S.R., Murray, B.A., Morozova, O., Newton, Y., Radenbaugh, A., Pagnotta, S.M., et al. (2016). Molecular Profiling Reveals Biologically Discrete Subsets and Pathways of Progression in Diffuse Glioma. Cell *164*, 550–563.

Cong, L., Ran, F.A., Cox, D., Lin, S., Barretto, R., Habib, N., Hsu, P.D., Wu, X., Jiang, W., Marraffini, L.A., et al. (2013). Multiplex genome engineering using CRISPR/Cas systems. Science *339*, 819–823.

Deltcheva, E., Chylinski, K., Sharma, C.M., Gonzales, K., Chao, Y., Pirzada, Z.A., Eckert, M.R., Vogel, J., and Charpentier, E. (2011). CRISPR RNA maturation by trans-encoded small RNA and host factor RNase III. Nature *471*, 602–607.

Eckel-Passow, J.E., Lachance, D.H., Molinaro, A.M., Walsh, K.M., Decker, P.A., Sicotte, H., Pekmezci, M., Rice, T., Kosel, M.L., Smirnov, I.V., et al. (2015). Glioma Groups Based on 1p/19q, IDH, and TERT Promoter Mutations in Tumors. N Engl J Med *372*, 2499–2508.

Fedorov, Y., Anderson, E.M., Birmingham, A., Reynolds, A., Karpilow, J., Robinson, K., Leake, D., Marshall, W.S., and Khvorova, A. (2006). Off-target effects by siRNA can induce toxic phenotype. RNA *12*, 1188–1196.

Franken, N.A.P., Rodermond, H.M., Stap, J., Haveman, J., and van Bree, C. (2006). Clonogenic assay of cells in vitro. Nat Protoc *1*, 2315–2319.

Gasiunas, G., Barrangou, R., Horvath, P., and Siksnys, V. (2012). Cas9–crRNA ribonucleoprotein complex mediates specific DNA cleavage for adaptive immunity in bacteria. PNAS *109*, E2579–E2586.

Gonzalgo, M.L., Hayashida, T., Bender, C.M., Pao, M.M., Tsai, Y.C., Gonzales, F.A., Nguyen, H.D., Nguyen, T.T., and Jones, P.A. (1998). The role of DNA methylation in expression of the p19/p16 locus in human bladder cancer cell lines. Cancer Res *58*, 1245–1252.

Grimm, D., Streetz, K.L., Jopling, C.L., Storm, T.A., Pandey, K., Davis, C.R., Marion, P., Salazar, F., and Kay, M.A. (2006). Fatality in mice due to oversaturation of cellular microRNA/short hairpin RNA pathways. Nature *441*, 537–541.

Guzmán, C., Bagga, M., Kaur, A., Westermarck, J., and Abankwa, D. (2014). ColonyArea: An ImageJ Plugin to Automatically Quantify Colony Formation in Clonogenic Assays. PLOS ONE *9*, e92444.

Happold, C., Roth, P., Wick, W., Schmidt, N., Florea, A.-M., Silginer, M., Reifenberger, G., and Weller, M. (2012). Distinct molecular mechanisms of acquired resistance to temozolomide in glioblastoma cells. Journal of Neurochemistry *122*, 444–455.

Hegi, M.E., Diserens, A.-C., Gorlia, T., Hamou, M.-F., de Tribolet, N., Weller, M., Kros, J.M., Hainfellner, J.A., Mason, W., Mariani, L., et al. (2005). MGMT gene silencing and benefit from temozolomide in glioblastoma. N Engl J Med *352*, 997–1003.

Hegi, M.E., Liu, L., Herman, J.G., Stupp, R., Wick, W., Weller, M., Mehta, M.P., and Gilbert, M.R. (2008). Correlation of O6-methylguanine methyltransferase (MGMT) promoter methylation with clinical outcomes in glioblastoma and clinical strategies to modulate MGMT activity. J Clin Oncol *26*, 4189–4199.

Herman, J.G., Graff, J.R., Myöhänen, S., Nelkin, B.D., and Baylin, S.B. (1996). Methylation-specific PCR: a novel PCR assay for methylation status of CpG islands. Proc Natl Acad Sci U S A *93*, 9821–9826.

Hermisson, M., Klumpp, A., Wick, W., Wischhusen, J., Nagel, G., Roos, W., Kaina, B., and Weller, M. (2006). O6-methylguanine DNA methyltransferase and p53 status predict temozolomide sensitivity in human malignant glioma cells. Journal of Neurochemistry *96*, 766–776.

Hornung, V., Guenthner-Biller, M., Bourquin, C., Ablasser, A., Schlee, M., Uematsu, S., Noronha, A., Manoharan, M., Akira, S., de Fougerolles, A., et al. (2005). Sequence-specific potent induction of IFN-alpha by short interfering RNA in plasmacytoid dendritic cells through TLR7. Nat Med *11*, 263–270.

Ichimura, K., Pearson, D.M., Kocialkowski, S., Bäcklund, L.M., Chan, R., Jones, D.T.W., and Collins, V.P. (2009). IDH1 mutations are present in the majority of common adult gliomas but rare in primary glioblastomas. Neuro Oncol *11*, 341–347.

Jackson, A.L., Bartz, S.R., Schelter, J., Kobayashi, S.V., Burchard, J., Mao, M., Li, B., Cavet, G., and Linsley, P.S. (2003). Expression profiling reveals off-target gene regulation by RNAi. Nat Biotechnol *21*, 635–637.

Jinek, M., Chylinski, K., Fonfara, I., Hauer, M., Doudna, J.A., and Charpentier, E. (2012). A programmable dual-RNA-guided DNA endonuclease in adaptive bacterial immunity. Science *337*, 816–821.

Jones, B., and Chen, J. (2006). Inhibition of IFN-γ transcription by site-specific methylation during T helper cell development. EMBO J *25*, 2443–2452.

Kang, M.R., Kim, M.S., Oh, J.E., Kim, Y.R., Song, S.Y., Seo, S.I., Lee, J.Y., Yoo, N.J., and Lee, S.H. (2009). Mutational analysis of IDH1 codon 132 in glioblastomas and other common cancers. Int J Cancer *125*, 353–355.

Kim, S., Kim, D., Cho, S.W., Kim, J., and Kim, J.-S. (2014). Highly efficient RNA-guided genome editing in human cells via delivery of purified Cas9 ribonucleoproteins. Genome Res *24*, 1012–1019.

Lalezari, S., Chou, A.P., Tran, A., Solis, O.E., Khanlou, N., Chen, W., Li, S., Carrillo, J.A., Chowdhury, R., Selfridge, J., et al. (2013). Combined analysis of O6-methylguanine-DNA methyltransferase protein expression and promoter methylation provides optimized prognostication of glioblastoma outcome. Neuro Oncol *15*, 370–381.

Lei, Y., Zhang, X., Su, J., Jeong, M., Gundry, M.C., Huang, Y.-H., Zhou, Y., Li, W., and Goodell, M.A. (2017). Targeted DNA methylation in vivo using an engineered dCas9-MQ1 fusion protein. Nat Commun *8*, 16026.

Liu, X.S., Wu, H., Ji, X., Stelzer, Y., Wu, X., Czauderna, S., Shu, J., Dadon, D., Young, R.A., and Jaenisch, R. (2016). Editing DNA Methylation in the Mammalian Genome. Cell *167*, 233-247.e17.

Mali, P., Yang, L., Esvelt, K.M., Aach, J., Guell, M., DiCarlo, J.E., Norville, J.E., and Church, G.M. (2013). RNA-guided human genome engineering via Cas9. Science *339*, 823–826.

Malley, D.S., Hamoudi, R.A., Kocialkowski, S., Pearson, D.M., Collins, V.P., and Ichimura, K. (2011). A distinct region of the MGMT CpG island critical for transcriptional regulation is preferentially methylated in glioblastoma cells and xenografts. Acta Neuropathol *121*, 651–661.

Malmström, A., Grønberg, B.H., Marosi, C., Stupp, R., Frappaz, D., Schultz, H., Abacioglu, U., Tavelin, B., Lhermitte, B., Hegi, M.E., et al. (2012). Temozolomide versus standard 6-week radiotherapy versus hypofractionated radiotherapy in patients older than 60 years with glioblastoma: the Nordic randomised, phase 3 trial. Lancet Oncol *13*, 916–926.

Marques, J.T., and Williams, B.R.G. (2005). Activation of the mammalian immune system by siRNAs. Nat Biotechnol *23*, 1399–1405.

McDonald, J.I., Celik, H., Rois, L.E., Fishberger, G., Fowler, T., Rees, R., Kramer, A., Martens, A., Edwards, J.R., and Challen, G.A. (2016). Reprogrammable CRISPR/Cas9-based system for inducing site-specific DNA methylation. Biol Open *5*, 866–874.

Meissner, A., Gnirke, A., Bell, G.W., Ramsahoye, B., Lander, E.S., and Jaenisch, R. (2005). Reduced representation bisulfite sequencing for comparative high-resolution DNA methylation analysis. Nucleic Acids Res *33*, 5868–5877.

Nobusawa, S., Watanabe, T., Kleihues, P., and Ohgaki, H. (2009). IDH1 mutations as molecular signature and predictive factor of secondary glioblastomas. Clin Cancer Res *15*, 6002–6007.

Ostrom, Q.T., Gittleman, H., Liao, P., Vecchione-Koval, T., Wolinsky, Y., Kruchko, C., and Barnholtz-Sloan, J.S. (2017). CBTRUS Statistical Report: Primary brain and other central nervous system tumors diagnosed in the United States in 2010-2014. Neuro Oncol *19*, v1–v88.

Parsons, D.W., Jones, S., Zhang, X., Lin, J.C.-H., Leary, R.J., Angenendt, P., Mankoo, P., Carter, H., Siu, I.-M., Gallia, G.L., et al. (2008). An Integrated Genomic Analysis of Human Glioblastoma Multiforme. Science *321*, 1807.

Pflueger, C., Tan, D., Swain, T., Nguyen, T., Pflueger, J., Nefzger, C., Polo, J.M., Ford, E., and Lister, R. (2018). A modular dCas9-SunTag DNMT3A epigenome editing system overcomes pervasive off-target activity of direct fusion dCas9-DNMT3A constructs. Genome Res *28*, 1193–1206.

Phillips, H.S., Kharbanda, S., Chen, R., Forrest, W.F., Soriano, R.H., Wu, T.D., Misra, A., Nigro, J.M., Colman, H., Soroceanu, L., et al. (2006). Molecular subclasses of high-grade glioma predict prognosis, delineate a pattern of disease progression, and resemble stages in neurogenesis. Cancer Cell *9*, 157–173.

Pogribny, I.P., Pogribna, M., Christman, J.K., and James, S.J. (2000). Single-site methylation within the p53 promoter region reduces gene expression in a reporter gene construct: possible in vivo relevance during tumorigenesis. Cancer Res *60*, 588–594.

Quinn, J.A., Jiang, S.X., Reardon, D.A., Desjardins, A., Vredenburgh, J.J., Rich, J.N., Gururangan, S., Friedman, A.H., Bigner, D.D., Sampson, J.H., et al. (2009). Phase I trial of temozolomide plus O6-benzylguanine 5-day regimen with recurrent malignant glioma. Neuro Oncol *11*, 556–560.

Reifenberger, G., Hentschel, B., Felsberg, J., Schackert, G., Simon, M., Schnell, O., Westphal, M., Wick, W., Pietsch, T., Loeffler, M., et al. (2012). Predictive impact of MGMT promoter methylation in glioblastoma of the elderly. Int J Cancer *131*, 1342–1350.

Remington, M., Chtchetinin, J., Ancheta, K., Nghiemphu, P.L., Cloughesy, T., and Lai, A. (2009). The L84F polymorphic variant of human O6-methylguanine-DNA methyltransferase alters stability in U87MG glioma cells but not temozolomide sensitivity. Neuro Oncol *11*, 22–32.

Renbaum, P., Abrahamove, D., Fainsod, A., Wilson, G.G., Rottem, S., and Razin, A. (1990). Cloning, characterization, and expression in Escherichia coli of the gene coding for the CpG DNA methylase from Spiroplasma sp. strain MQ1(M Sssl). Nucleic Acids Research *18*, 1145–1152.

Ricard, D., Idbaih, A., Ducray, F., Lahutte, M., Hoang-Xuan, K., and Delattre, J.-Y. (2012). Primary brain tumours in adults. Lancet *379*, 1984–1996.

Rivera, A.L., Pelloski, C.E., Gilbert, M.R., Colman, H., De La Cruz, C., Sulman, E.P., Bekele, B.N., and Aldape, K.D. (2010). MGMT promoter methylation is predictive of response to radiotherapy and prognostic in the absence of adjuvant alkylating chemotherapy for glioblastoma. Neuro Oncol *12*, 116–121.

Robertson, K.D., and Jones, P.A. (1998). The human ARF cell cycle regulatory gene promoter is a CpG island which can be silenced by DNA methylation and down-regulated by wild-type p53. Mol Cell Biol *18*, 6457–6473.

Schilsky, R.L., Dolan, M.E., Bertucci, D., Ewesuedo, R.B., Vogelzang, N.J., Mani, S., Wilson, L.R., and Ratain, M.J. (2000). Phase I clinical and pharmacological study of O6-benzylguanine followed by carmustine in patients with advanced cancer. Clin Cancer Res *6*, 3025–3031.

Schmidt, M.C., Antweiler, S., Urban, N., Mueller, W., Kuklik, A., Meyer-Puttlitz, B., Wiestler, O.D., Louis, D.N., Fimmers, R., and von Deimling, A. (2002). Impact of Genotype and Morphology on the Prognosis of Glioblastoma. Journal of Neuropathology & Experimental Neurology *61*, 321–328.

Sohn, B.H., Park, I.Y., Lee, J.J., Yang, S.-J., Jang, Y.J., Park, K.C., Kim, D.J., Lee, D.C., Sohn, H.A., Kim, T.W., et al. (2010). Functional switching of TGF-beta1 signaling in liver cancer via epigenetic modulation of a single CpG site in TTP promoter. Gastroenterology *138*, 1898–1908.

Stepper, P., Kungulovski, G., Jurkowska, R.Z., Chandra, T., Krueger, F., Reinhardt, R., Reik, W., Jeltsch, A., and Jurkowski, T.P. (2017). Efficient targeted DNA methylation with chimeric dCas9-Dnmt3a-Dnmt3L methyltransferase. Nucleic Acids Res *45*, 1703–1713.

Stupp, R., Mason, W.P., van den Bent, M.J., Weller, M., Fisher, B., Taphoorn, M.J.B., Belanger, K., Brandes, A.A., Marosi, C., Bogdahn, U., et al. (2005). Radiotherapy plus Concomitant and Adjuvant Temozolomide for Glioblastoma. N Engl J Med *352*, 987–996.

Stupp, R., Hegi, M.E., Gilbert, M.R., and Chakravarti, A. (2007). Chemoradiotherapy in malignant glioma: standard of care and future directions. J Clin Oncol *25*, 4127–4136.

Vojta, A., Dobrinić, P., Tadić, V., Bočkor, L., Korać, P., Julg, B., Klasić, M., and Zoldoš, V. (2016). Repurposing the CRISPR-Cas9 system for targeted DNA methylation. Nucleic Acids Res *44*, 5615–5628.

Wang, M., Zuris, J.A., Meng, F., Rees, H., Sun, S., Deng, P., Han, Y., Gao, X., Pouli, D., Wu, Q., et al. (2016). Efficient delivery of genome-editing proteins using bioreducible lipid nanoparticles. PNAS *113*, 2868–2873.

Wick, W., Meisner, C., Hentschel, B., Platten, M., Schilling, A., Wiestler, B., Sabel, M.C., Koeppen, S., Ketter, R., Weiler, M., et al. (2013). Prognostic or predictive value of MGMT promoter methylation in gliomas depends on IDH1 mutation. Neurology *81*, 1515–1522.

Wicki, R., Franz, C., Scholl, F.A., Heizmann, C.W., and Schäfer, B.W. (1997). Repression of the candidate tumor suppressor gene S100A2 in breast cancer is mediated by site-specific hypermethylation. Cell Calcium *22*, 243–254.

Wiestler, B., Claus, R., Hartlieb, S.A., Schliesser, M.G., Weiss, E.K., Hielscher, T., Platten, M., Dittmann, L.M., Meisner, C., Felsberg, J., et al. (2013). Malignant astrocytomas of elderly patients lack favorable molecular markers: an analysis of the NOA-08 study collective. Neuro Oncol *15*, 1017–1026.

Yan, H., Parsons, D.W., Jin, G., McLendon, R., Rasheed, B.A., Yuan, W., Kos, I., Batinic-Haberle, I., Jones, S., Riggins, G.J., et al. (2009). IDH1 and IDH2 Mutations in Gliomas. N Engl J Med *360*, 765–773.

Zuris, J.A., Thompson, D.B., Shu, Y., Guilinger, J.P., Bessen, J.L., Hu, J.H., Maeder, M.L., Joung, J.K., Chen, Z.-Y., and Liu, D.R. (2015). Cationic lipid-mediated delivery of proteins enables efficient protein-based genome editing in vitro and in vivo. Nat Biotechnol *33*, 73–80.

DISSERTATION DISCUSSION

The primary goal of the work contained within these chapters was to demonstrate that treatment-amenable phenotypes can be reconstituted through epitranscriptomic and epigenetic engineering, thereby offering novel approaches to limiting malignancy and enhancing chemotherapeutic responses in glioma. We show that chemical modifications in DNA and RNA act as potent regulators of glioma cell growth and treatment sensitivity, and that manipulating these levers of gene expression control at varying degrees of specificity can have meaningful impacts on reversing malignant phenotypes. Whether these findings will reliably translate into actual therapeutic options remains to be seen, but they bring us one step closer to achieving treatment equity across the wide range of glioma subtypes afflicting our patients, namely, between *IDH1*^{mut} and *IDH1*^{wt} gliomas, and *MGMT* methylated and unmethylated gliomas.

In Chapter 1, we focused on elucidating the mechanisms of the *IDH1*^{mut} → D-2-HG ⊣ FTO axis governing reduced proliferative potential phenotypes observed in *IDH1*^{mut} gliomas, and then harnessed what we learned to recapitulate these anti-tumor pathways in *IDH1*^{wt} tumors through selective FTO inhibition. First, we established that RNA isolated from *IDH1*^{mut} gliomas exhibits m6A enrichment, both in patient tissue samples and patient-derived gliomaspheres. We showed that D-2-HG is the primary mediator of m6A enriched phenotypes, being both necessary for its induction in *IDH1*^{mut} gliomas and sufficient when applied to *IDH1*^{wt} gliomas. D-2-HG and m6A enrichment were also shown to attenuate glioma cell growth, a finding that was reversible when D-2-HG production was inhibited. We further established that D-2-HG-mediated inhibition of FTO was the primary driver of reduced proliferative potential and m6A enrichment in glioma, and that small molecule inhibitors of FTO were capable of reducing *IDH1*^{wt} glioma cell growth both *in vitro* and *in vivo*. MeRIP-Seq unbiased screening of *IDH1*^{mut} and *IDH1*^{wt} glioma cells revealed a unique epitranscriptomic biomarker in *IDH1*^{mut} gliomas that we term G-RAMP, defined by a set of m6A-enriched transcripts involved in a wide range of important biomolecular pathways. Among these

G-RAMP members, we identified the anti-apoptotic regulator ATF5 as a potential modulator of reduced proliferative potential in *IDH1*^{mut} gliomas and found that its transcripts were significantly m6A enriched in *IDH1*^{mut} patient tumor samples and gliomaspheres. M6A enrichment in ATF5 transcripts was also shown to correlate with reduced total expression levels, and attenuated ATF5 expression was associated with increased apoptotic activity. These findings thus provide the first description of an epitranscriptomic signature unique to *IDH1*^{mut} gliomas and identify an apoptotic induction mechanism underlying less malignant phenotypes driven by the *IDH1*^{mut} → D-2-HG ⊣ FTO axis that can also be exploited in the treatment of *IDH1*^{wt} gliomas.

In Chapter 2, we capitalized on long-standing clinical knowledge that *MGMT* methylation predicts improved responses to standard-of-care chemotherapy in glioma patients, and selectively induced this phenotype using dCas9-DNMT3a methylation editors to sensitize previously *MGMT* unmethylated glioma cells to temozolomide treatment. We utilized LN18 glioblastoma lines that are regularly employed in glioma research, and which demonstrate high levels of temozolomide tolerance. We successfully established lines expressing dCas9-DNMT3a constructs and sgRNAs targeting the *MGMT* promoter and exon 1 region most commonly assayed in clinical characterizations of patient tumors. This epigenetic editing platform was able to reliably induce high-density methylation in our region of interest and proved a potent suppressor of *MGMT* expression. *In vitro* studies showed a robust increase in growth attenuation responses to temozolomide in *MGMT* methylated lines, demonstrating that this method is a viable means of achieving treatment sensitization to levels approximating direct *MGMT* knockout.

Even with the relative success of our findings using epitranscriptomic and epigenetic engineering to selectively modulate clinically relevant phenotypes, several obstacles to translational applications remain. Primary among them is the delivery of the biological platforms required to effect these changes in a targeted manner. Delivering precision engineering tools *in vivo* while

minimizing off-target effects is a complex challenge, but potential solutions are available. For example, the biopharmaceutical company Tocagen has tested a replication competent retroviral vector derived from Moloney murine leukemia virus (MoMLV) containing cytosine deaminase (Toca 511) that acts as an adjuvant therapy converting systemically delivered pro-drug flucytosine (5-FC) into the antineoplastic compound 5-fluorouracil (5-FU) (Cloughesy et al., 2020). Unfortunately, the Toca 5 Phase III clinical trials did not meet their primary outcome measure of extending overall survival in recurrent glioblastoma patients (Cloughesy et al., 2020). Nevertheless, the MoMLV vector demonstrates efficacy as a delivery mechanism that, upon injection into the surrounding tumor resection area, demonstrates preferential transfection of tumor cells. While the Toca 511 payload did not result in the intended clinical benefits, one could consider repurposing the MoMLV vector to instead deliver epigenetic editing machinery. A potential application relevant to our work would be the delivery of plasmids encoding dCas9-DNMT3a and sgRNAs targeting *MGMT* via MoMLV into the resection cavity to sensitize residual glioma cells to temozolomide therapy. The importance of testing such an approach is highlighted by the recent failure of another high-profile Phase III clinical trial, CheckMate 143. This randomized clinical trial was the first Phase III immunotherapy study of PD-1 inhibitors (nivolumab) in patients with recurrent glioblastoma, and again, the primary endpoint of increased overall survival was not reached (Reardon et al., 2020). One population that did appear to derive some benefit from nivolumab treatment were patients with methylated *MGMT* promoters (Reardon et al., 2020). Finding a way to effectively deliver *MGMT* methylation platforms into glioma cells may not only improve responses to standard-of-care chemotherapy, but may yet enhance the effects of additional antineoplastic therapeutics developed as either neoadjuvant or mainline therapies. Other delivery approaches besides intracranial viral vectors could include the use of nanoparticles capable of crossing the blood-brain-barrier (Teleanu et al., 2018). Studies have demonstrated the successful delivery of antineoplastic agents to glioma cells *in vivo* using poly(lactide-*co*-glycolic) acid nanoparticles encapsulating therapeutic agents such as doxorubicin (Malinovskaya et al.,

2017) and a combination of cisplatin and boldine (Mondal et al., 2020). A range of such nanoparticles are under active development, including the positively charged poly(ethylene imine) polymer which can be formulated in conjunction with a poly(L-lysine) copolymer to effectively deliver gene therapy platforms in brain cancer. Yet another approach would be the employment of liposomes designed to entrap small molecules and deliver them safely across the blood-brain-barrier to improve the specificity of drug targeting as well as enhance localized concentrations (Teleanu et al., 2018). Several liposomal formulations have already been tested, delivering among other drugs methotrexate (Hu et al., 2017), 5-fluorouracil (Lakkadwala and Singh, 2018), paclitaxel (Peng et al., 2018), doxorubicin (Lakkadwala and Singh, 2019; Zhan and Wang, 2018), and erlotinib (Lakkadwala and Singh, 2019). These nanoparticle and liposomal vectors could easily be repurposed to package ribonucleoproteins or genetic material encoding epigenetic editors or small molecules inhibitors such as FB23-2 that target epitranscriptomic processes, addressing the major limitation of the translational potential of the current studies as far as *in vivo* delivery of epigenetic and epitranscriptomic engineering tools are concerned.

I hope to pursue further studies to develop more translational methods of effecting the glioma subtype conversions described in the current studies. In addition, further research is required in several other areas, mainly to better characterize how healthy tissue may be affected by epigenetic and epitranscriptomic modulations, but also to test exciting new tools that are being developed in this space. For the former, the role of ATF5 in the anti-apoptotic milieu is deserving of further interrogation. As others have previously demonstrated, ATF5 appears to exert its protective effects primarily in breast and glioma cells, while merely serving a redundant role in anti-apoptotic processes in healthy breast epithelial cells and non-cancerous neuronal and glial cells. Disentangling the precise role of ATF5 and its selective impact on preventing apoptosis in glioma remains an open question, especially as it pertains to changes in expression resulting from m6A enrichment in ATF5 transcripts. A combination of approaches will be required to fully

elucidate this mechanism, and an array of new sequencing tools and epitranscriptomic editing platforms will aid in these studies. As was previously described, m6A is deposited on RNA by the m6A methyltransferases METTL3 and METTL14. A recently developed dCas9 fusion protein harnesses the sequence-specific targeting of traditional dCas9 systems to a single strand METTL3-METTL14 complex (Liu et al., 2019). This tool permits targeted epitranscriptomic editing that may shed light on which specific m6A sites are necessary to effect ATF5 transcript degradation. Coupling this tool with new direct m6A sequencing and transcript quantitation methodologies will allow us to investigate how specific m6A modifications affect transcript abundance (Zhou et al., 2018). Studies on the conformational changes induced by enrichment at specific m6A sites may also help us establish a hierarchy of m6A loci exerting the most robust regulatory roles (Zou et al., 2016). Finally, we must continue to investigate how various RNA-binding proteins interact with and determine the fates of any transcripts of interest, G-RAMP members or otherwise. New readers are continuing to be discovered (Edupuganti et al., 2017), and the deployment of PAR-CLIP studies tailored to each reader protein may help us deconvolute the complex network of reader proteins capable of recognizing m6A modified transcripts (Hafner et al., 2010; Zaccara and Jaffrey, 2020). One can easily foresee the possibility of engineering novel reader proteins that selectively target certain transcripts (or groups of transcripts) for degradation to alter cellular phenotypes in a more meticulous fashion while leaving the underlying genetic code intact. The abovementioned tools could all be applied to help us characterize the effects of precise epitranscriptomic alterations and reveal new points of weakness in tumor cell functions that may be exploited for therapeutic purposes.

The application of genetic engineering techniques as therapeutic interventions is an endeavor still in its nascent stages, but we are quickly beginning to see the real-world power of these tools in designing new treatments for intractable and devastating diseases. Epigenetic and epitranscriptomic engineering approaches are at an even earlier stage of development, and

continued investigation of these tools and their utility as therapeutic agents presents us with an exciting new frontier in our ability to more deeply understand and effectively treat diseases such as glioma.

REFERENCES

Alarcón, C.R., Lee, H., Goodarzi, H., Halberg, N., and Tavazoie, S.F. (2015). N6-methyladenosine marks primary microRNAs for processing. Nature *519*, 482–485.

Chen, T., Hao, Y.-J., Zhang, Y., Li, M.-M., Wang, M., Han, W., Wu, Y., Lv, Y., Hao, J., Wang, L., et al. (2015). m(6)A RNA methylation is regulated by microRNAs and promotes reprogramming to pluripotency. Cell Stem Cell *16*, 289–301.

Cloughesy, T.F., Petrecca, K., Walbert, T., Butowski, N., Salacz, M., Perry, J., Damek, D., Bota, D., Bettegowda, C., Zhu, J.-J., et al. (2020). Effect of Vocimagene Amiretrorepvec in Combination With Flucytosine vs Standard of Care on Survival Following Tumor Resection in Patients With Recurrent High-Grade Glioma: A Randomized Clinical Trial. JAMA Oncol *6*, 1939–1946.

Edupuganti, R.R., Geiger, S., Lindeboom, R.G.H., Shi, H., Hsu, P.J., Lu, Z., Wang, S.-Y., Baltissen, M.P.A., Jansen, P.W.T.C., Rossa, M., et al. (2017). N6-methyladenosine (m6A) recruits and repels proteins to regulate mRNA homeostasis. Nat Struct Mol Biol *24*, 870–878.

Geula, S., Moshitch-Moshkovitz, S., Dominissini, D., Mansour, A.A., Kol, N., Salmon-Divon, M., Hershkovitz, V., Peer, E., Mor, N., Manor, Y.S., et al. (2015). Stem cells. m6A mRNA methylation facilitates resolution of naïve pluripotency toward differentiation. Science *347*, 1002–1006.

Hafner, M., Landthaler, M., Burger, L., Khorshid, M., Hausser, J., Berninger, P., Rothballer, A., Ascano, M., Jungkamp, A.-C., Munschauer, M., et al. (2010). Transcriptome-wide identification of RNA-binding protein and microRNA target sites by PAR-CLIP. Cell *141*, 129–141.

Hu, Y., Rip, J., Gaillard, P.J., de Lange, E.C.M., and Hammarlund-Udenaes, M. (2017). The Impact of Liposomal Formulations on the Release and Brain Delivery of Methotrexate: An In Vivo Microdialysis Study. J Pharm Sci *106*, 2606–2613.

Lakkadwala, S., and Singh, J. (2018). Dual Functionalized 5-Fluorouracil Liposomes as Highly Efficient Nanomedicine for Glioblastoma Treatment as Assessed in an In Vitro Brain Tumor Model. J Pharm Sci *107*, 2902–2913.

Lakkadwala, S., and Singh, J. (2019). Co-delivery of doxorubicin and erlotinib through liposomal nanoparticles for glioblastoma tumor regression using an in vitro brain tumor model. Colloids Surf B Biointerfaces *173*, 27–35.

Liu, N., Dai, Q., Zheng, G., He, C., Parisien, M., and Pan, T. (2015). N6-methyladenosine-dependent RNA structural switches regulate RNA–protein interactions. Nature *518*, 560–564.

Liu, X.-M., Zhou, J., Mao, Y., Ji, Q., and Qian, S.-B. (2019). Programmable RNA N6-methyladenosine editing by CRISPR-Cas9 conjugates. Nat Chem Biol *15*, 865–871.

Malinovskaya, Y., Melnikov, P., Baklaushev, V., Gabashvili, A., Osipova, N., Mantrov, S., Ermolenko, Y., Maksimenko, O., Gorshkova, M., Balabanyan, V., et al. (2017). Delivery of doxorubicin-loaded PLGA nanoparticles into U87 human glioblastoma cells. Int J Pharm *524*, 77–90.

Mondal, J., Patra, M., Panigrahi, A.K., and Khuda-Bukhsh, A.R. (2020). Improved drug carriage and protective potential against Cisplatin-induced toxicity using Boldine-loaded PLGA nanoparticles. J Ayurveda Integr Med *11*, 24–36.

Peng, Y., Zhao, Y., Chen, Y., Yang, Z., Zhang, L., Xiao, W., Yang, J., Guo, L., and Wu, Y. (2018). Dual-targeting for brain-specific liposomes drug delivery system: Synthesis and preliminary evaluation. Bioorg Med Chem *26*, 4677–4686.

Reardon, D.A., Brandes, A.A., Omuro, A., Mulholland, P., Lim, M., Wick, A., Baehring, J., Ahluwalia, M.S., Roth, P., Bähr, O., et al. (2020). Effect of Nivolumab vs Bevacizumab in Patients With Recurrent Glioblastoma: The CheckMate 143 Phase 3 Randomized Clinical Trial. JAMA Oncol *6*, 1003.

Teleanu, D.M., Chircov, C., Grumezescu, A.M., Volceanov, A., and Teleanu, R.I. (2018). Blood-Brain Delivery Methods Using Nanotechnology. Pharmaceutics *10*, 269.

Zaccara, S., and Jaffrey, S.R. (2020). A Unified Model for the Function of YTHDF Proteins in Regulating m6A-Modified mRNA. Cell *181*, 1582-1595.e18.

Zhan, W., and Wang, C.-H. (2018). Convection enhanced delivery of liposome encapsulated doxorubicin for brain tumour therapy. J Control Release *285*, 212–229.

Zhou, J., Wan, J., Shu, X.E., Mao, Y., Liu, X.-M., Yuan, X., Zhang, X., Hess, M.E., Brüning, J.C., and Qian, S.-B. (2018). N6-Methyladenosine Guides mRNA Alternative Translation during Integrated Stress Response. Mol Cell *69*, 636-647.e7.

Zou, S., Toh, J.D.W., Wong, K.H.Q., Gao, Y.-G., Hong, W., and Woon, E.C.Y. (2016). N 6 -Methyladenosine: a conformational marker that regulates the substrate specificity of human demethylases FTO and ALKBH5. Sci Rep *6*, 25677.